UNIVERSITY ROMA TRE

ROMA TRE
UNIVERSITÀ DEGLI STUDI

Faculty of Engineering
Doctoral School in Mechanical and Industrial Engineering

Doctoral thesis

Theoretical and numerical modeling of wind instruments: virtual lutherie and time–domain simulations

Author
Francesco Centracchio

.....

Supervisor
Prof. Umberto Iemma .....

Doctoral School Coordinator
Prof. Edoardo Bemporad .....

Rome, June 2015

*« **R**egis **I**ussu **C**antio **E**t **R**eliqua **C**anonica **A**rte **R**esoluta »*

Johann Sebastian Bach, *Musicalisches Opfer*

Contents

List of Figures

List of Tables

Abstract

The present research work deals with the synthesis of the sound produced by a wind instrument through the direct physical modeling. Specifically the purpose is the development theoretical physical models and numerical solution procedures aimed at the time–domain simulations.

The attention is mainly focused on two fundamental topics: the identification of the acoustic response of the resonator as well as the environment in which the performance takes place, and the characterization of the interaction between the resonator and the musician, with particular emphasis to the connection between the mathematical parameters governing the physics of the phenomenon and the properties of the resulting sound.

The acoustical characterization of the resonators and the surroundings is addressed with a prime–principles based approach. The simulation of the acoustic field produced by the instruments alone and in a realistic performing environment is achieved using an integral representation in the frequency–domain. A particular attention is paid to the identification of the transfer functions aimed at the auralized signal propagation.

A simplified model of valve is used to represent the exciter behaviour. The attention has been especially focused on the analysis of a brass instrument during the performance, since the link between the acousto–elastic coupled system and the performed note is crucial.

The transfer functions have been analytically approximated as rational functions in the frequency–domain in order to obtain a block diagram representation of the dynamical system suitable for real–time application. The algorithm has demonstrated to be accurate and efficient in offline calculation, and the observed performance discloses the possibility to implement real–time applications compatible with the consumer devices currently available on the market.

Outline of the work

Part I - Ouverture

- **Chapter 1: Introduction** In the first chapter a brief history of the sound synthesis is outlined, with the purpose of introduce the modern techniques adopted in the musical sound synthesis. Is thus presented the approach developed within this work, with emphasis to the main differences with respect to the commonly used sound synthesis techniques.

Part II - Modeling the instrument in action

- **Chapter 2: Acoustical characterization of resonators and surroundings** The second chapter deals with the description of the *virtual lutherie*, namely the methodologies used to evaluate the acoustic response of the resonators and derive the propagation transfer functions aimed at the signals propagation. Such a characterization is carried out in the frequency–domain.

- **Chapter 3: Interaction with the player and sound propagation** In the third chapter are discussed the methodologies used to model the interaction between the resonator and the exciter in the time–domain, as well as the techniques exploited in order to achieve the time–varying pressure signals radiated by the instruments.

Part III - Time–domain simulations of brasses

- **Chapter 4: From the geometric model to the auralized sounds** The complete time–domain simulation of a natural brass instruments is presented in the fourth chapter, starting from the identification of the characteristics of the resonator up to the auralization of the pressure signal. The attempt to exploit the developed methodologies in real–time applications will be also

outlined, identifying a suitable block diagram representation of the involved acousto–elastic system, and proposing a strategy for the system realization.

- **Chapter 5: Exploration of the physical model parameters** The fifth chapter concerns the characterization of the pressure signals at the inlet section of the brasses during the performance. This part of the work leads to the recognition of the "playability" conditions of the physical model.

- **Chapter 6: The sounds as an optimization problem** In the sixth chapter will be defined an optimization problem with the purpose to identify the physical model parameters aimed at the generation of sounds complying prescribed characteristics.

Part IV - Finale

- **Chapter 7: Conclusions and future works** In the last chapter will be summarized the achievements of this work, outlining the possible developments in the future research works.

Part V - Appendices

- **Appendix A: Kirchhoff-Helmholtz Integral Equation** The integral representation of the wave equation is derived for small acoustic perturbations through a homogeneous, inviscid, non–heat conducting and compressible fluid.

- **Appendix B: Boundary Element Method for acoustic problems** A description of the BEM for acoustic problems is outlined: is derived the source and doublet integrals computation related to the zeroth–order formulation.

- **Appendix C: Optimization problems** Is presented a brief introduction to the problems of constrained and unconstrained optimization.

Part I

Ouverture

CHAPTER 1

Introduction

In this chapter a brief history of the sound synthesis will be outlined, starting from the origins, with the purpose of introduce the modern techniques adopted in the musical sound synthesis. Such historical background has the aim of introduce the approach developed within this work, emphasizing the main differences with respect to the commonly used sound synthesis strategies.

1.1 A brief history of the synthesizer

The connection between the mathematics and the music was known since the 6th century BC. In those times Pythagoras developed a system of tuning starting from the analysis of a monochord, *i.e.* from the physics of the vibrating string: this tuning system is based on the hypothesis that the ratio of the frequencies belonging the musical scale is given by simple rational numbers. Such a link was so deeply rooted that it is interesting to recall that in the Middle Ages the music science, particularly the harmonic theory, was connected with the arithmetic, the geometry and the astronomy in the teaching of the liberal arts: these disciplines constituted the so–called *quadrivium* which, with the *trivium*, *i.e.* grammar, rhetoric and dialectic, represented the seven fundamental disciplines.

Through the ages, and especially with the advent of the modern era, the development of the science and the technology led to the need to put into practice the theoretical basis of the musical physics. The most natural consequence was the birth of that branch today called *sound synthesis*. In the thinking about the musical synthesis the mind, for the most, is addressed to some of the prestigious inventions of the 20th century, such as the *Hammond organ* or the *Moog synthesizer*. Actually very few know that the first attempts to create a synthesizer dates back

to the 18th century, when the Austro–Hungarian inventor Wolfgang von Kempelen designed the *speaking machine*, one of the most important description of the voice production [79, 64, 14, 13].

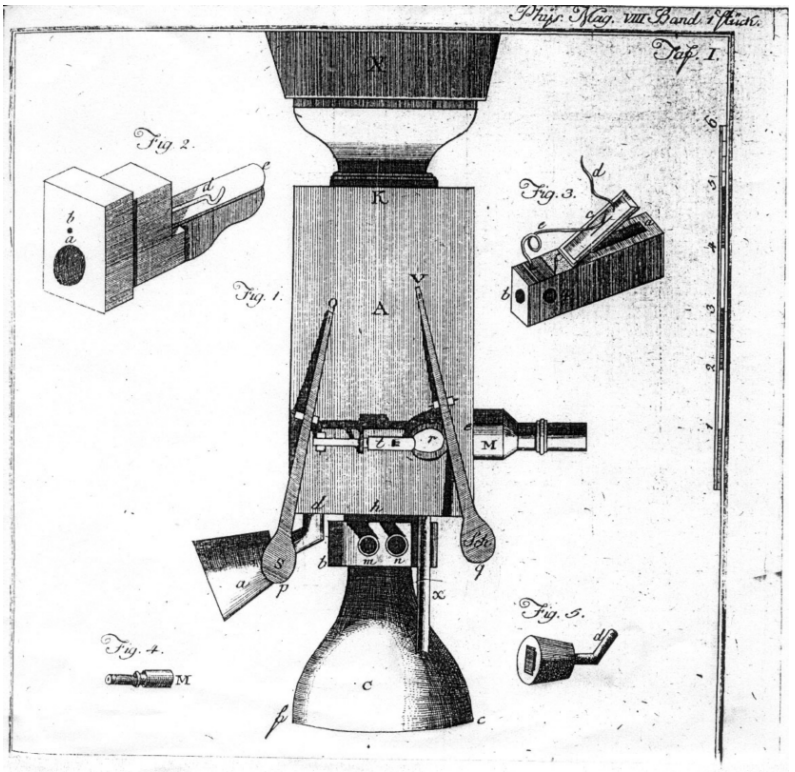

Figure 1.1: Sketch of the Wolfgang von Kempelen's *speaking machine* [64].

The first design of the machine is dated 1769, and is based on a reed pipe, with the aim of simulate the vocal folds, connected with a short rubber horn representing the human mouth. In this configuration the machine produces the vowel "*a*", whereas the other vowels can be approximated by the manual partial closure of the horn with the palm of the hand. Some consonants have to be made through the full closure of the mouth with the hand of the player [13].

From then on have been many precursors of the modern–day analog synthesizers, some of which designed by prominent personalities of the science, as Hermann von Helmholtz, who began the first significant studies concerning the perception of the sounds[1] about a hundred years the *speaking machine*, and was among the first people to use the electricity with musical purpose, building several electro–

[1]It should be recalled that in the introduction of his "*On the sensation of tone as physiological basis for the theory of music*" [41], Helmholtz declares its intention to link the boundaries of the *physical and physiological acoustics* on the one side and the *musical science and esthetics* on the other side.

mechanical oscillators. Shortly afterwards, at the beginning of the 20th century, Thaddeus Cahill presented the *Telharmonium*, developed starting from the 1897: a colossal electro–mechanical musical instrument (the second and the third versions weighed about 200 tons) using tone–wheels for the sound production.

Between the First and the Second World War began the first experiments on the design of innovative musical instruments, as the *Theremin* developed in 1919 and patented in 1928 by the Russian physician and inventor Léon Theremin (was the first musical instrument in history that does not involve the direct contact with the musician) and *hybrid/augmented* musical instruments, such as the *Neo–Bechstein* electric grand piano [54] invented in 1929 (which can be considered as the precursor of the electric piano). The analog keyboard synthesizers hold the stage, and the American engineer Laurens Hammond in 1935 introduced the first model of the organ (the *Model A*) still associated with his name. The mechanism of the sound production is completely electromagnetic and is based on the additive synthesis[2] exploiting several rotating contoured tone–wheels.[3] It is worth noting that the success of the *Hammond organ* is also attributable to its compact size and the low weight compared with the pipe organs. Indeed the compactness of the instruments was a matter to be reckoned with: in those times the electronic components were bulky and frangible, and this issue was solved with the coming of the transistors.

In fact, in the early '50s the transistors became available on the market and the technology of the analog sound synthesis has been revolutionized: the voltage–controlled technique allows to set the output characteristics of an oscillator simply by varying the input voltage. An excellent example of the exploitation of these potentialities is the *Melochord*, made by the German engineer Harald Bode. The same technology has been used by the American engineer Robert Moog who designed, starting from 1964, a complex system of synthesizers based on voltage-controlled oscillators and amplifiers. The technological revolution represented by the components miniaturization has made possible the reducing of the size of the synthesizers, making them compact and easy–to–use.

Is clear how the need of the "imitation" of the sounds produced by existing musical instruments was developed in parallel to the need of the "exploration" of new sound *visions*. Such two points of view, apparently unrelated but often converging, found several benefit from the coming of the digital era.

1.2 The modern approaches to sound synthesis

Simultaneously with the birth of electronic music have been outlined the different strategies for the musical sounds synthesis. Such techniques can be differentiated according to their ultimate purpose: on one hand there are the so–called **signal models**, on the other hand the **source models**.

[2]For details concerning the additive synthesis see below.

[3]The mechanism of the sound generation was the same as the *Telharmonium*.

As suggested by the designation itself, the aim of the signal models is the generation of complex waveforms, instead the source models propose to describe the physical phenomena that produce the sound event.

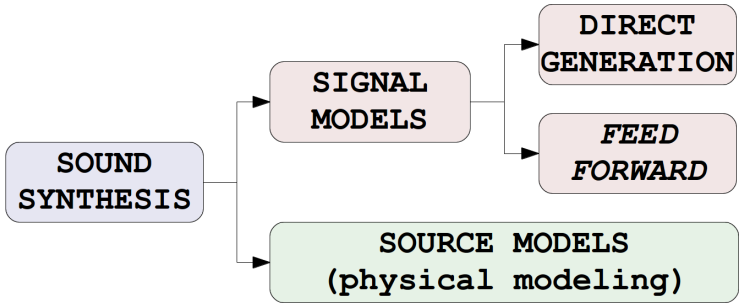

Figure 1.2: The signal models and the source models as branches of the sound synthesis.

1.2.1 Signals models

Two classes of methodologies pertain to the signal models, as shown in Fig. 1.2, *i.e.* the *direct generation* methods and the *feed–forward* techniques. The methods based on the direct generation of the signal rely on the direct creation of the waveforms. Such waveforms can be created from theoretical bases, or else generated from recording of the real sounds [10, 74, 84, 18, 27]. The *feed–forward* techniques are instead based on the alteration *a posteriori* of existing waveforms produced by oscillators: the input waveforms may have a high level of complexity and subsequently are simplified, or can be simple and then combined to each other as well as filtered [17, 7, 68, 77].

It is worth noting that the waveform can not characterize by itself the timbre of a complex sound. The time envelope of the waveform allows to discern the nature of the sound differentiating the percussive from the non–percussive sounds, and all the intermediate gradations. For this reason the musical sound synthesis based on signal models employs an envelope control, often an ADSR control (**A**ttack, **D**ecay, **S**ustain, **R**elease) which allows to set the amplitude envelope of the sound, by setting the following four parameters:

- **attack** time: is the time that the sound takes for the initial slide from zero to the maximum value of the volume;
- **decay** time: determines the duration of the falling from the full volume to the sustain level;
- **sustain** level: represents the steady level, *i.e.* the amplitude at "key–down";
- **release** time: is the time that the sound takes to vary its volume up to zero.

Out below, a brief description of the most commonly used techniques belonging to the signals models is proposed.

The *direct generation* synthesis

Sample–based synthesis The sample–based synthesis is probably the most common form of sound synthesis. It is not properly a synthesis method, since a real sound is digitally recorded, and the recording is played back. The problem of this kind of synthesis is in the impossibility to know *a priori* the length of the sound that the musician will want to perform. On the other hand the memory required to store long sounds could be very wide. In order to overcome this drawback, few periods of the wave in its steady–state are recorded, and by a suitable choosing of the initial and the final sample, the recording is played in closed–loop, with the purpose of create a continuous waveform. This technique, the *looping*, ensures the extension of the sampled sound duration.

The limitation of the sample–based synthesis is that the waveforms are rather static due to the *looping*, making difficult to add expression and dynamics to the performance: indeed the perfect periodicity is perceived as "artificial", since the microfluctuations of the sound pitch turn out to be pleasing to the human ears.

Additive synthesis The Fourier analysis ensures that each signal can be considered as sum of monochromatic, *i.e.* sinusoidal, components at different frequencies and different amplitudes. In the event that the signal is periodic, the expression of the sum is such that only the sinusoids with frequencies equal to multiples of to the fundamental periodicity of the signal are involved. In this view a sound is the superposition of its harmonic components, and this seems to be consistent with the Helmholtz theory of the timbre [41]. This perspective suggests a technique for the conversely usage of the Fourier analysis, and such technique is the additive synthesis, through which a purposeful number of sine waves is combined to produce a complex waveform.

It is interesting to point up that such method is computationally inexpensive and can provide, in the more general formulation, both harmonic and inharmonic time–dependent partials with time–dependent amplitudes.

Granular synthesis The granular representation of the sounds seems to be a way to interpret a complex sound phenomenon as the superposition of elementary units of the duration of around 1 to 100 ms called *grains*, being the latter exactly bounded in both the time–domain and in the frequency–domain. Introduced by the electrical engineer and physicist Dannis Gabor in 1946 is based on the same principles of the sample–based synthesis: the *grains* are properly overlapped and sequence of them are played back, following the selection a number of parameters as the volume or the speed.

The *Feed–forward* synthesis

Subtractive synthesis The subtractive synthesis had great popularity between the '60s and the 70s, with the rising of the analog synthesizers. The principle on which it is based may seem the reverse with respect to the additive synthesis: a waveform rich in harmonic components, as a sawtooth or a square wave, is generated by an oscillator and is subsequently filtered in order to modify its spectrum. Specifically the resonant voltage–controlled filter can be low–pass, high–pass, band–pass, band–reject or all–pass:[4] it is clear how the resulting waveform can gain color and complexity.

Nonlinear distorsions The synthesis of she sounds through nonlinear distortion is based on the modification of an existing sound using nonlinear filters in order to obtain a richer frequency spectrum. The input waveform is often a monochromatic signal, as a simple sinusoid, hence it is easy to understand that the harmonic components of the output signal are entirely attributable to the effect of the nonlinear transfer function. It is interesting to mention the possibility of dynamic filters with the purpose of achieve a time–varying envelope of both the amplitude and the harmonic component of the signal.

Frequency modulation synthesis The frequency modulation synthesis, also referred to as the FM synthesis, was introduced by John Chowning in 1973, with the aim of extend the well–understood radio transmission technique to the generation of audio signals. This method simply consists in change an input waveform, such as a square wave or a triangle wave, by modulating its frequency. Substantially an oscillator generates an audio signal with a carrier frequency f_c, then a modulating audio signal with a frequency f_m is applied, and the rate at with the carrier wave varies is the modulating frequency.

It is interesting to highlight that the FM synthesis can produce both harmonic and inharmonic sounds. The generation of harmonic sounds is achieved by imposing an harmonic relationship between the modulating wave and the carrier signal, whereas by dropping the assumption of integer ratio between f_m and f_c, can be progressively reached percussive atonal sounds.

1.2.2 Physical modeling

The sound synthesis through the physical modeling has a relatively short history. Differs from the signal model for the purpose of reconstruct the physical phenomenon on the basis of the sound generation instead of the sound waveform: often referred to as the *source models*, the physical modeling seems to have begun with the attempts to reduce the data-flows in the telecommunications.

[4]The all–pass filter leaves unchanged the amplitude of the spectrum, but alters the phases.

The basic idea is to consider the production sounds as the effect of the interaction between an vibrating element, the **exciter**, and a **resonator** which provide the harmonic content of the signal, *e.g.* a string of an air column. The interaction strictly depends on the instrument, and can be both impulsive, as an hammer that hit a string or a membrane, as well as *feedback–like*, as in the case of a wind instrument.

Historically, the first approach to the solution of the interaction between the exciter and the resonator is represented by the *waveguides*. This approach consists in describing the dynamics of the oscillations in the musical instruments with a bi-dimensional wave equation, whose solution can be considered as the superposition of a progressive wave and a regressive wave (the D'Alembert solution): in this view the acoustic perturbation can be evaluated starting from the initial conditions, being the latter indefinitely propagated through the resonator. The first implementation of such a waveguide [47, 46] was computationally inexpensive, but the formulation did not yet provide the exciter model. In the event that complex excitations, even time–variant, force the resonator, it becomes necessary to introduce a contribution to both the progressive wave and regressive wave, by the exploitation of two waveguides with the aim of describe the phenomenon. It is worth noting that both the models implementations described above describe a conservative system, meaning that the produced sounds involve infinite duration and constant amplitude, as well as infinitely increasing amplitude in the event that the excitation is repetitive [72].

These drawbacks suggest to introduce dissipative terms in the equations describing the physical models and the waveguide models began going towards a more detailed description of the mechanisms of the sound production.

1.3 The proposed approach

This work deals with the time–domain simulation of wind instruments, *i.e.* the woodwind and the brasses, through a physical–models–based direct simulation. The purpose is the development of a methodology that allows to reconstruct the timbre of a given musical instrument (not necessarily existing) starting just from the geometric model of the instrument itself and from the knowledge of the type of excitation, focusing on the interaction of the player with the instrument, and of the instrument with the performance environment and the listener. The usefulness of this approach lies on the possibility not only to achieve valuable sounds for electronic music compositions, but also to explore new features of the design of *hybrid* and *augmented* musical instruments as well as the implement real–time applications compatible with the consumer devices.

The novelty of the present approach is in the integrated modeling of the instrument response and the propagation and scattering within the hall where the performance takes place: this will be referred to as **virtual lutherie**. The pro-

posed technique allows to derive the time–varying perceived[5] signals starting from the knowledge of the frequency–dependent acoustical characteristics of the field inside and outside the resonator, and the instrument excitation type. The acoustical characterization of the field inside the instrument is evaluated with the aim of compute the time–varying signals inside the embouchure of the instrument (otherwise called mouthpiece) by solving the acousto–elastic coupling between the resonator and the exciter, whereas the knowledge of the acoustic field outside the resonator enables the evaluation of the sound radiated by the instrument.

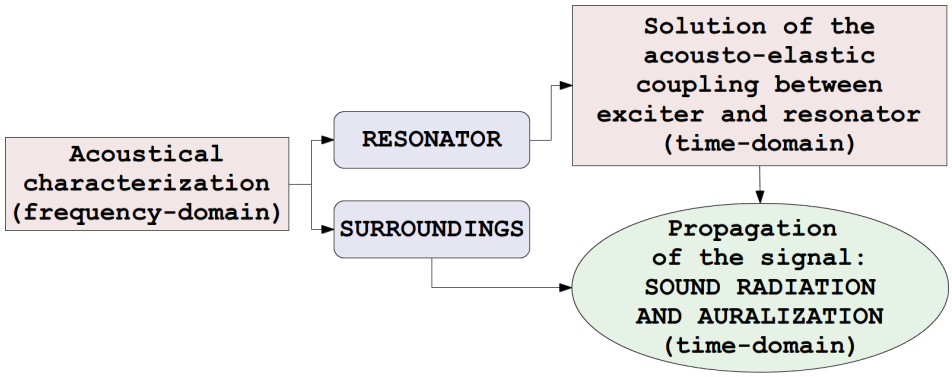

Figure 1.3: Acoustical characterization of the field inside and outside the resonator with the purpose of evaluate the radiated sound.

The strength of this method is in the simultaneous evaluation of both the acoustic fields inside and outside the resonator, by exploiting a single frequency–domain simulation. Indeed it is notorious that a satisfactory[6] identification of the acoustical characteristics of resonators can be achieved even theoretically,[7] *i.e.* making use of the Webster's *horn equation*, but the characterization of the acoustic fields produced by the instrument during the performance provides an additional contribution to obtain coherent radiated waveforms.

1.3.1 Acoustical characterization

The approach proposed in this work is based, as mentioned above, on the simultaneous acoustical characterization the resonators, *i.e.* the musical instruments, and the surroundings, *i.e.* the environment where the performance takes place.

The acoustical characterization, carried out through prime–principle methods, is achieved in the frequency–domain, and this method allows to derive simultaneously, and for each frequency the transfer functions relating the instrument inflow with

[5] Perceived by an acoustical transducer, *i.e.* a virtual microphone in the field, or perceived by a listener even in presence of other scattering objects.

[6] With the purpose of solve the acousto–elastic coupling between the exciter and the resonator.

[7] As long as the resonator is axisymmetrical.

the pressure perturbation inside the resonator and at an arbitrary location in the surroundings, *i.e.*

- the **input impedance** of the resonator, namely the ratio between the pressure at the inlet section of the instrument and the resulting inflow. The knowledge of the input impedance is aimed to model the *acousto–elastic feedback* between the exciter and the resonator itself. The importance of the input impedance is in its use for the complete identification of the acoustical characteristic of the musical instrument, since provides information on the sound pressure intensity at a given frequency. In fact the harmonic content of a sound produced by a wind instrument is strictly dependent on its frequency response;

- the **propagation transfer functions**, *i.e.* the ratio between the acoustic pressure at any point in of the field and the inflow at the inlet section of the instrument, by means of which it is possible to compute the time–varying signal radiated by the instrument once the acousto–elastic coupling between the exciter and the resonator is solved.

The frequency–domain simulations are carried out by exploiting the integral representation of the acoustic field through the **Kirchhoff–Helmholtz Integral Equation** (KHIE). The latter is solved numerically using a zeroth–order **Boundary Element Method** (BEM) by imposing a constant inflow at the inlet section of the resonator at all the frequencies of the simulation.[8] This is equivalent to consider the acoustical system forced by a constant spectrum *i.e.* imitating the frequency behaviour a time–impulsive force at the inlet section, that is compliant with the definition of frequency response.

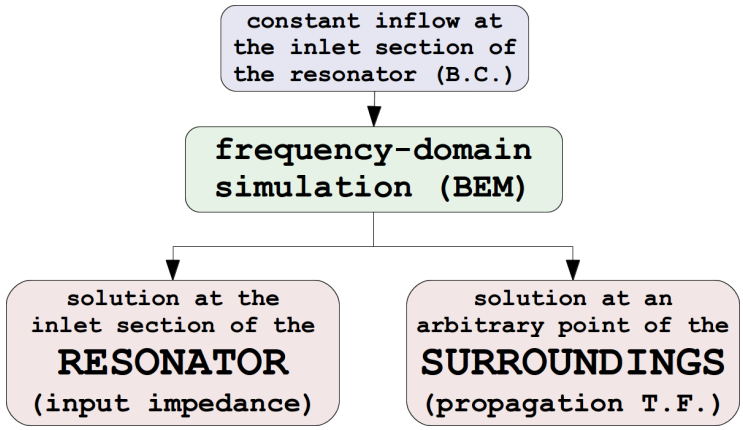

Figure 1.4: Simultaneous characterization of the acoustical characteristics of resonators and surroundings in the frequency–domain.

[8]The numerical results have been obtained using the open–source BEM code `AcouSTO` [45].

The velocity potential field is solved on the boundary of the acoustic field, and the solution is evaluated at the inlet section of the instrument with the aim of derive the input impedance, and in several points of interest, such virtual microphones, with the purpose of estimate the propagation transfer functions.

The BEM method for the evaluation of broad acoustic frequency responses turns out to be quite expensive in computational terms. In order to overcome this drawback several strategies will be adopted, as the exploitation of axisymmetric problems through the modeling of straight resonators.

1.3.2 Excitation mechanism and sound propagation

Once the acoustic characteristics of the resonator and the surroundings are evaluated through a unique frequency–domain numerical (BEM) simulation, the proposed method allows the evaluation of the time–dependent state variables (displacement, pressure and inflow) at the inlet section of the instrument through the solution of the acousto–elastic coupling between the resonator and the excitation mechanism, with the aim of radiate the signal outside the instrument and reconstruct the waveform.

The solution of the acousto–elastic coupling between the exciter and the resonator is performed in the time–domain, as well as the sound propagation.

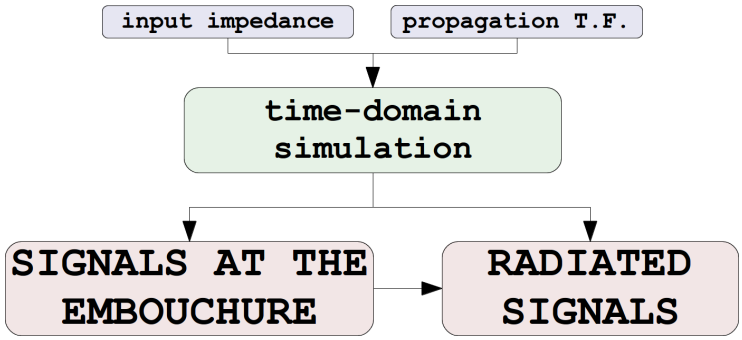

Figure 1.5: Solution of the acousto–elastic coupling between the exciter and the resonator and sound propagation in the time–domain.

The mechanism of the sound production of the wind instruments can be considered as a constant interaction between an exciter and a resonator, and such interaction turns out to be *feedback–like*, meaning that the change in variables inside the resonator,[9] *i.e.* the pressure and the flow, modifies the dynamic response of the exciter. The *exciter* is the "mechanical device" with which the musician let vibrate the air column inside the instrument and can be a piece (or two pieces) of cane in the case of reed–driven instruments, an unstable jet for the air–jet–driven instruments or the lips in the brasses. The *control parameters* of the exciter are

[9]The *resonator*, is the musical instrument, and by its acoustical properties depends the harmonic content of the signal, as mentioned above.

provided by the musician, which represent the energy source of the system: such parameters substantially consist in the blowing pressure and everything with which the act of blowing is related, *e.g.* the pronunciation of vowels.[10]

Modeling of the exciter is crucial aspect of the physical modeling, since the perceived acoustic signature of the wind instruments primarily depends by the excitation mechanism. In fact it is useful to recall that *i.e.* a flute played with a clarinet mouthpiece will be sensed like a clarinet and *vice–versa*. Thus it could be argued that the acoustical characteristics of the resonators are mainly responsible of the tuning of the instruments. A wide literature provides suitable models to describe the acousto–elastic coupling between the exciter and the resonator for both the woodwinds (single–reed, double–reed and jets) and the brasses. Most of these models are based on the introduction of several simplification of the phenomenon, *e.g.* using one degree–of–freedom models of valve for describe the reed and the lip motion. Instead other models, making use of multiple degree–of–freedoms mechanical systems, provide a meticulous description of the dynamics of the exciter. Obviously the more rigorous is the model, the more accurate is the reconstruction of the exciter dynamics. On the other hand, the link between the accuracy of the model and the quality sounds is still unclear, at least according to the knowledge of the author.

1.3.3 Exploration of the brass physical model

Another issue that will be analysed is the connection between the parameters governing the equation of the lip motion and the musically–relevant characteristics of the produced sound by the brass instruments. This aspects turns out to be crucial since the physical model must be somehow "routed" toward the desired sounds. In fact the input of the physical model is a combination of parameters of some equations and the output is the sound. Assuming a prescribed acoustical behaviour of the instrument, such parameters are related to the mechanical characteristics of the exciter. Regarding the brasses it is worth noting that the mechanical characteristics of the exciter, *i.e.* the lip, are difficult to quantify since are strictly dependent on the performance condition: the player varies the mechanical behaviour of the lips depending upon both the note and the musical emphasis, such the dynamics, the accents and the articulation.

Nevertheless an attempt to define several objective criteria aimed at the sound identification will be presented. Under the hypothesis that a solution must be considered as "sound" only if its periodicity fall within the hearing–range, several subspaces belonging the solutions of the brass physical model will be identified:

- the sustained solutions, *i.e.* the set of all the solution that admit a sustained steady–state;

[10] It is interesting to note that in the cases of the brasses, the frontier between the *control parameters* and the *exciter* is not is not clearly defined, since is the musician himself that provide the mechanical characteristics of the *exciter*.

- the feasible solution, which involve physical quantities consistent with the case study;
- the musical solutions, characterized by prescribed timbrical characteristics.

It was noticed that the identified subspaces are independent: accordingly, the intersection of the latter will be considered as the set of the sounds mirroring a realistic performance.

It is interesting to note that the criteria aimed at the identification of the abovementioned subspaces are suitable for the formulation of an optimization problem, with the purpose of find the combination of the parameters of the physical model leading to a sound with prescribed characteristics in terms of both the physics and the timbrical properties.

Part II

Modeling the instrument in action

CHAPTER 2

Acoustical characterization of resonators and surroundings

In this chapter, the *virtual lutherie* will be presented. It should be pointed out that the used expression must be understood as an "augmented locution' due to two reasons. The first one is that, historically, the luthier (lutist, lute–maker) is someone who builds or repair string instruments, while this work dealing with the wind instruments. The second plea concerns the fact that the lutherie is not confined to the instrument since the proposed approach give the possibility of characterize the instrument response contextually to the propagation and scattering within the hall where the performance takes place, by exploiting a single frequency–domain simulation.

Below the methodologies used to evaluate the acoustic response of the resonators and derive the propagation transfer functions will be presented. The acoustical characterization is with the aim of reconstruct the timbre of wind instrument and obtain the auralization of the signals. These methodologies are based on prime–principles and consist in the solution of the acoustic field inside and outside the pipe, even in presence of scattering phenomena within the hall where the performance takes place. The numerical simulations aimed at the acoustical characterizations are achieved using the *Boundary Element Method*, BEM.

2.1 On the timbrical characteristics

The timbre is the peculiarity of a sound that make it different form another one, such as musical instruments or voices. The *American Standards Association*, ASA,[1] define the timbre as "[...] that attribute of sensation in terms of which a listener

[1]From 1928, previously *American Engineering Standards Committee*, AESC, and in 1969, following a reorganization became the *United States of America Standards Institute*, USASI.

can judge that two sounds having the same loudness and pitch are dissimilar" and, in addition, "[...] depends primarily upon the spectrum of the stimulus, but it also depends upon the waveform, the sound pressure, the frequency location of the spectrum, and the temporal characteristics of the stimulus.". In addition, it is crucial to note that the above–mentioned characteristics are, in the most general case, time–varying.

The complexity of the topic led both scientists and musicians, *e.g.* Hermann von Helmholtz and Arnold Schoenberg, to question about the timbre of the sounds.[2] Strong *multidimensionality* characterize, in fact, the sound events due to the fact that the perception of a sound is related to both the spectral dynamic and psycho-cognitive phenomena [41].

The physical modeling of musical instruments has the objective of generating appropriated waveforms.[3] Since the harmonic content and the partials envelope of the sounds produced by the wind instruments, *i.e.* the timbre, comes from the acoustic characteristics of the resonator, the first step is to determine the properties of the instrument in terms of its frequency response. The fundamental tone produced by the instrument during playing, the *pitch*, as well as the harmonic overtones, are strictly depended by the input impedance spectrum. Reed-driven and brass instruments sound close peaks of the input impedance spectrum (high pressure, low inflow), whereas jet-driven instruments play near the minima (high inflow, low pressure). This distinction directly comes from the notion of input impedance $\mathcal{Z}_{in}$,

$$\mathcal{Z}_{in} = \frac{p - p_0}{\bar{v} \cdot n} \tag{2.1}$$

defined as the ratio beween the pressure jump across the input section and the resulting inflow throught the same section. The unit of acoustic impedance is the acoustic Ohm, being

$$[\Omega] = \left[\frac{\mathrm{Pa}}{\mathrm{s} \cdot \mathrm{m}^3}\right] \tag{2.2}$$

The input impedance is an intrinsic property of the resonator and is a function of the geometry and the characteristics of the medium. In the frequency–domain

$$\mathcal{Z}_{in}(\omega) = \frac{\tilde{p}_{in}(\omega)}{\tilde{u}_{in}(\omega)} \tag{2.3}$$

indicates how intense is the sound pressure generated by the air vibration at a given frequency, so represents the acoustic response of the instrument at each frequency. It is a complex function of the angular frequency $\omega = 2\pi f$ and its real part is called *acoustic resistance*, while the imaginary part is called *acoustic reactance*.

[2] The classical distinction between sound and noise is considered outdated, given that the general definition of *timbre* encloses all sound events.

[3] The meaning of the word "appropriate" must be linked to the "consistency" with respect to the model, *i.e.* coherent.

Based on the spectral energy decay analysis related to recorded sounds of the wind instruments, one can note that the pressure spectrum is of interest even at very high frequencies. Seems to be important to earn the acoustical characterization of the resonators up to the highest frequency possible, consistently with the computational resources.

2.2 Modeling the acoustic response of the pipe

The generic acoustic problems can be written, in the frequency–domain, as follow

$$\nabla\tilde{\varphi}(\mathbf{x}) - \kappa^2\tilde{\varphi}(\mathbf{x}) = \tilde{q}, \quad \mathbf{x} \in \mathcal{V} \tag{2.4}$$

being $\tilde{\varphi}$ the scalar velocity potential function, $\kappa = s/c_0$ the complex wave number ($s = \alpha + \iota\omega$ is the Laplace variable and c_0 the speed of sound in reference condition) and $\tilde{q}$ the acoustic sources present in the field. The problem is completed by suitable boundary conditions for $\mathbf{x} \in \mathcal{V}$. Defining the acoustic delay $\theta = r/c_0$, recalling the fundamental solution G for the $3D$ wave equations,

$$G(\mathbf{x}, \mathbf{y}, s) = -\frac{e^{-s\theta}}{4\pi||\mathbf{x} - \mathbf{y}||} = G_0 e^{-s\theta} \tag{2.5}$$

it is possible to provide an integral representation of the Eq. 2.4. Assuming $\tilde{q} = 0$ the integral formulation is

$$E(\mathbf{y})\tilde{\varphi}(\mathbf{y}) = \oint_{\mathcal{S}} \left(G\frac{\partial\tilde{\varphi}}{\partial n} - \tilde{\varphi}\frac{\partial G}{\partial n} \right) d\mathcal{S}(\mathbf{x}) \tag{2.6}$$

with $\mathcal{S} = \partial\mathcal{V}$, being the domain function $E(\mathbf{y})$ such that

$$E(\mathbf{y}) = \begin{cases} 1, & \mathbf{y} \in \mathcal{V} \\ 1/2, & \mathbf{y} \in \partial\mathcal{V} \\ 0, & \mathbf{y} \notin \mathcal{V} \end{cases} \tag{2.7}$$

The Eq. 2.6, integral representation of the Eq. 2.4, is the well–known Kirchhoff–Helmholtz Integral Equation, KHIE (see App. A).

Indeed, when $\mathbf{y} \in \partial V$, KHIE can be solved for the unknown $\tilde{\varphi}$ from the knowledge of the boundary conditions, that can be derived from the relationship between the velocity potential function and its normal derivative as follows

$$\gamma(\mathbf{x}, \omega)\tilde{\varphi}(\mathbf{x}, \omega) + \lambda(\mathbf{x}, \omega)\frac{\partial\tilde{\varphi}(\mathbf{x}, \omega)}{\partial n} = \tilde{f}(\mathbf{x}, \omega) \tag{2.8}$$

Noting that $\gamma(\mathbf{x}, \omega)$, $\lambda(\mathbf{x}, \omega)$ and $\tilde{f}(\mathbf{x}, \omega)$ are complex functions and the can easily provided providing them the appropriate form.[4]

[4]This general formulation allows to easily identify the *Neumann* and *Dirichelet* boundary conditions imposing $\gamma(\mathbf{x}, \omega) = \tilde{f}(\mathbf{x}, \omega)$ and $\lambda(\mathbf{x}, \omega)\partial\tilde{\varphi}(\mathbf{x}, \omega)/\partial n = \tilde{f}(\mathbf{x}, \omega)$ respectively, as well as each linear combination of the latter, obtaining the *Robin* boundary conditions.

In the system theory the frequency response is used to characterize the dynamics of the system: it quantify the frequency–dependent magnitude and phase of the output in comparison to a the input. The frequency response of an acoustical system can be computed by forcing the system with a constant spectrum, and evaluating the complex amplitude of the response for all frequencies. It is easy to note that a constant spectrum can be achieved by exploiting a time–impulsive forcing of the system.[5] The proposed method simulates the frequency behaviour of the time–impulsive forcing [44] by imposing in the Eq. 2.8 a pure Neumann boundary condition on the inlet section $\mathcal{S}_{in}$,

$$\frac{\partial \tilde{\varphi}(\mathbf{x}, \omega)}{\partial n} = \mathbf{u}_{in} \cdot \mathbf{n}, \quad \mathbf{x} \in \mathcal{S}_{in} \tag{2.9}$$

with *hard-wall* boundary conditions on the pipe surface S_p.[6]

$$\frac{\partial \tilde{\varphi}(\mathbf{x}, \omega)}{\partial n} = 0, \quad \mathbf{x} \in \mathcal{S}_{p} \tag{2.10}$$

Note that such a boundary condition is equivalent to considering an ideal piston forcing the pipe in correspondence of the inlet section: as said above, the condition corresponds to consider the response of the instrument to a time-impulsive input inflow. The integral formulation can provide the simultaneous solution of the potential acoustic field inside and outside the pipe.

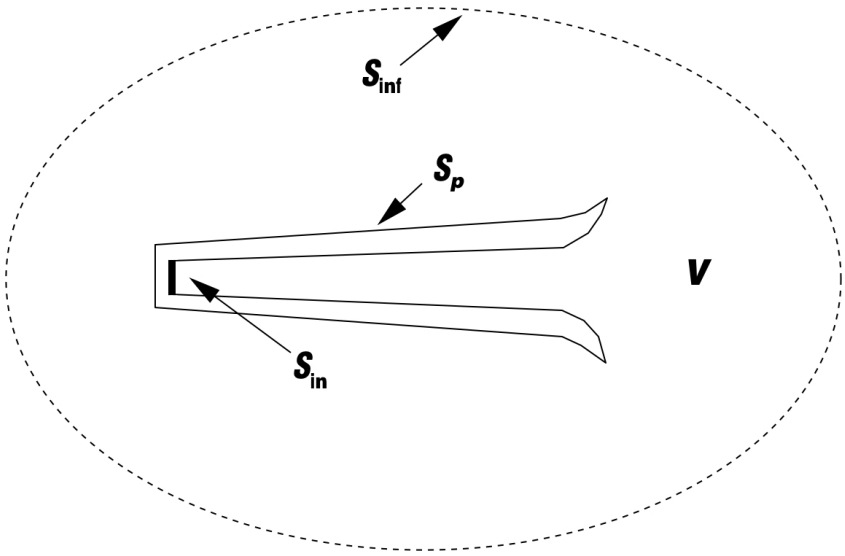

Figure 2.1: Representation of the acoustic field inside and outside the pipe [44].

[5] Flat spectra are also provided by the *sweep* (chirp) and by the *white noise*.

[6] Moreover the Sommerfeld radiation condition must be imposed in order to ensure that $\tilde{\varphi} \to 0$ for $\mathbf{x} \to \infty$.

Recalling the linearised Bernoulli theorem in the frequency–domain

$$\tilde{p} - \tilde{p_0} = -\rho s \tilde{\varphi} \tag{2.11}$$

one can obtain the relationship between the pressure jump across the input section and the velocity potential $\tilde{\varphi}$. Therefore the Eq. 2.3 becomes

$$\mathcal{Z}_{in}(\omega) = -\frac{1}{\mathcal{S}_{in}} \int_{\mathcal{S}_{in}} \frac{j\omega\rho\tilde{\varphi}(\omega)}{\mathbf{u}_{in}(\omega) \cdot \mathbf{n}} d\mathcal{S} \tag{2.12}$$

where $\mathbf{u}_{in}(\omega)$ represents the constant inflow across the intake section, defined by the Eq. 2.9.

2.2.1 Numerical solution

The numerical solution of Eq. 2.6 is provided by a Boundary Element Method (see App. B). In the zeroth–order formulation, one can discretize the boundary in N panels and consider the collocation points y_k located in the centroid of each panel, obtaining

$$\frac{1}{2}\tilde{\varphi}_i = \sum_{j=1}^{N} \left[B_{ij}\tilde{\chi}_j + (C_{ij} + sD_{ij}) \ \tilde{\varphi}_j \right] e^{-s\theta_{ij}} \tag{2.13}$$

where the subscripts indicate the the evaluation at the corresponding collocation point and the integral coefficients have form

$$\begin{aligned} B_{ij} &= \int_{\mathcal{S}_j} G_0 d\mathcal{S} \\ C_{ij} &= -\int_{\mathcal{S}_j} \frac{\partial G_0}{\partial n} d\mathcal{S} \\ D_{ij} &= \int_{\mathcal{S}_j} G_0 \frac{\partial \theta}{\partial n} d\mathcal{S} \end{aligned} \tag{2.14}$$

In matrix form the numerical solution on the boundary is given by

$$\tilde{\varphi} = \mathbf{Y}^{-1}\mathbf{B}\tilde{\chi} \tag{2.15}$$

where

$$\mathbf{Y} = \left(\frac{1}{2}\mathbf{I} - \mathbf{C} - s\mathbf{D} \right) \tag{2.16}$$

The CHIEF regularization

The numerical methodology described above involves an issue, *i.e.* solving the scattered acoustic field in unbounded domains can manifest non–physical resonances. The so–called *fictitious eigenfrequencies* are related to the eigensolutions of the

complementary boundary value problem, *BVP*. Specifically, the exterior Neumann problem, with boundary conditions

$$\frac{\partial\tilde{\varphi}(\mathbf{y},\kappa)}{\partial n} = f(\mathbf{y},\kappa) \quad \text{for} \quad \mathbf{y} \in \partial V$$

is affected by the eigenfrequencies of the interior Dirichlet problem. Similarly, the solution of the exterior problem with Dirichlet boundary conditions

$$\tilde{\varphi}(\mathbf{y},\kappa) = f(\mathbf{y},\kappa) \quad \text{for} \quad \mathbf{y} \in \partial V$$

is singular at the eigenfrequencies of the interior Neumann problem. The CHIEF (Combined Helmholtz Integral Equation Formulation) method [16, 9] is used to circumvent the well–known fictitious eigenfrequencies problem, which arises in the solution of external problems using the KHIE: N_c additional collocation points are added inside V and the resulting over–determined set of $N + N_c$ equation is solved. The solution is now given by

$$\tilde{\varphi} = (\hat{\mathbf{Y}}^T\hat{\mathbf{Y}})^{-1}\tilde{\mathbf{b}}\hat{\mathbf{Y}}^T\tilde{\chi} \tag{2.17}$$

where, indicating with the superscript the coefficients influencing the CHIEF collocation points, the terms $\hat{\mathbf{Y}}$ and $\tilde{\mathbf{b}}$ are defined as follows

$$\hat{\mathbf{Y}} = \begin{bmatrix} \mathbf{Y} \\ -\mathbf{C}^c - s\mathbf{D}^c \end{bmatrix}, \quad \tilde{\mathbf{b}} = \begin{bmatrix} \mathbf{B} \\ \mathbf{B}^c \end{bmatrix} \tag{2.18}$$

and are related to the over–determined problem.

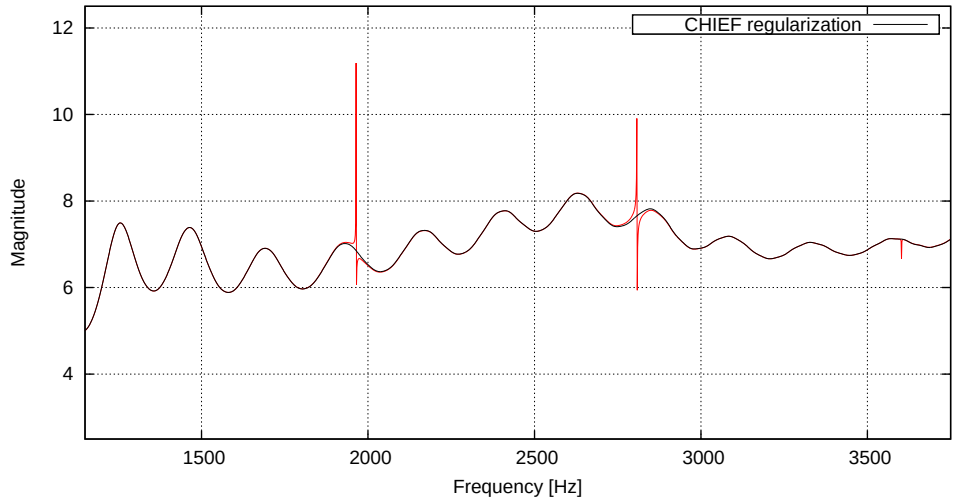

Figure 2.2: CHIEF regularization of the acoustic pressure on the boundary of a rigid sphere of radius $r = 8.75$ cm located at distance $d = 3$ m from the outlet section of a Bessel horn.

The other well–known approaches are the so–called *Burton–Miller* method (also referred to as the *normal derivative* method) and the CONDOR (Composite Outward Normal Derivative Overlap Relation) method [71, 48, 73].

2.2.2 Validation of the methodology

The convergence of the numerical solution obtained with the $3D$ Boundary Element Method [45] will be now investigated, in terms of resonant frequencies as well as the shape of the input impedance spectrum, with respect to the approximated analytical solution of the Webster's *horn equation*. Noting that the i–th resonance must be computed as the zero-crossing of the imaginary part of the complex input impedance spectrum, thus all the resonant frequencies are affected by a systematic error of the order of the frequency step Δf.

In order to derive the Webster's *horn equation*, let us consider the wave equation in the three dimensional Cartesian system

$$\frac{\partial^2 \varphi}{\partial t^2} - c^2 \nabla^2 \varphi = 0 \tag{2.19}$$

In the early twentieth century Webster suggested a simplification of the Eq. 2.19 for the horns [55].

Horns are acoustical transducers consisting of a tube of carrying sectional area. Generally the horns act as impedance adapter between an acoustic source and the free acoustic field: the exploitations of the horns are manifold and in musical wind instruments represent the terminal part of the bell, in brasses, or the full wholeness of the instrument, in the case of woodwinds. Assuming that the acoustic energy is distributed over wavefronts orthogonal to the horn axis, the wave equation become

$$\frac{\partial^2 \varphi}{\partial x^2} - \frac{1}{A}\frac{\partial A}{\partial x}\frac{\partial \varphi}{\partial x} - \frac{1}{c^2}\frac{\partial^2 \varphi}{\partial t^2} = 0 \tag{2.20}$$

The Eq. 2.20 is the so-called Webster's *horn equation*,[7] and its solution [49] can be reached under the assumption

$$\varphi = Au + Bv \tag{2.21}$$

where the terms u and v depend on the horn's type and A and B represent the outgoing and the reflected wave. Note that in the case of an infinite horn $B = 0$ because there is no reflected wave.

By solving the Eq. 2.20 for pressure and velocity at the end section S_2 of the horn, it is possible to make explicit the impedance at the inlet section S_1 as a function of the geometry, the wavenumber and the characteristics of the medium, as follow

$$\mathcal{Z}_1 = \frac{g\mathcal{Z}_2 - b}{a - f\mathcal{Z}_2} \tag{2.22}$$

being $\mathcal{Z}_2$ the acoustical impedance load for a piston set in an infinite baffle, as shown in Fig. 2.3.

[7] Often referred to as the $1.5D$ wave equation.

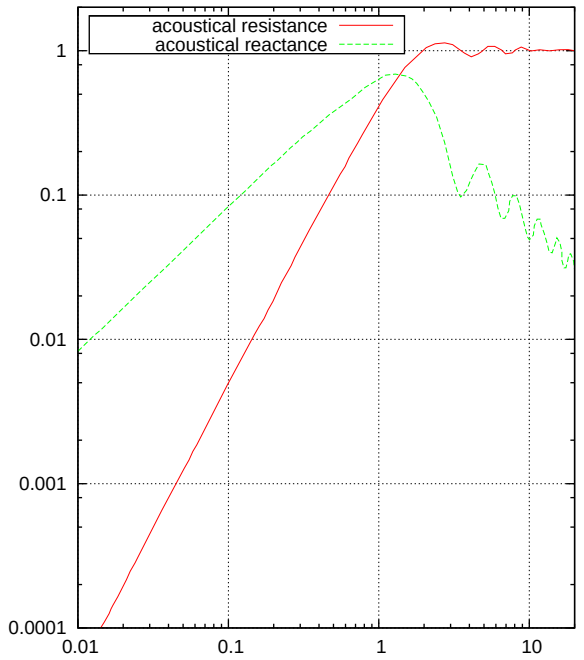

Figure 2.3: Acoustical impedance load per unit area, divided by ρc as a function of kR for a vibrating piston of radius R set in the end of an infinite pipe.

The expression of the coefficients a, b, f and g was given by Stewart and Lindsay [76] for the uniform pipe, the conical horn and the exponential horn, and their analytical (Webster) solutions are presented below.

Let define the relative errors ε^t and ε^w between the BEM solution and respectively the theoretical[8] and the analytical solution (Webster) are defined as follow

$$\varepsilon_n^t = 100 \cdot \frac{\mid f_n^t - f_n^{BEM} \mid}{f_n^t}, \quad \varepsilon_n^w = 100 \cdot \frac{\mid f_n^w - f_n^{BEM} \mid}{f_n^w} \tag{2.23}$$

On the thickness of the resonator and its end Before going ahead it seems necessary to point out, without giving details, an issue typical of the case studies. The link between the acoustical characterization of a resonator via BEM and its thickness turns out to be extremely important. Indeed on the one hand the numerical method requires a not infinitesimal thickness otherwise the matrices (Eq. 2.15) may be ill–conditioned.[9] On the other hand, the unqualified increase in thickness, aimed at the proper numerical solution, may change the acoustical characteristics of the domain, since the unflanged resonators radiate into a solid angle of 4π, while flanged resonators radiate into a solid angle of 2π [59].

[8]The theoretical 1D solution is related only to the uniform pipe.

[9]The topology may be such that two neighbour–opposite panels would have opposite normals.

In those circumstances the adopted strategy was choosing a plentiful thickness, even not compatible with the geometry of the problem,[10] making sharp the end of the geometry (see Fig. 2.4) in order to let it radiate as an unflanged resonator.

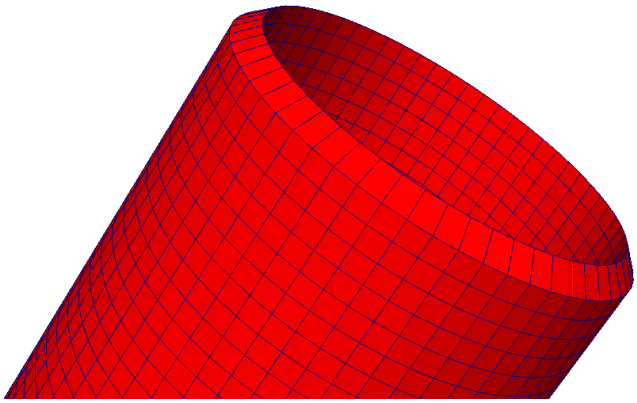

Figure 2.4: Geometry of the end of a cylindrical resonator.

Uniform pipe

Regarding pipes, it is possible to evaluate the $1D$ approximated resonant frequencies, both in the case that is closed at one end and opened at the other end or opened at both ends, as long as the analysis is bounded to a frequency range such that the problem can be considered one-dimensional. The choice of the *cut-off* frequency [67] $f_{cut} = c/2D$ only depend on the sound velocity and the pipe's diameter. For the $1D$ resonant frequencies estimation it is necessary to apply a correction for the length.[11] Defining L the pipe's length, c the sound velocity and λ the wavelength, the approximated fundamental frequency of the pipe closed at one end is

$$f_0 = \frac{c}{\lambda} = \frac{c}{4L} \tag{2.24}$$

and the harmonic overtones, according to the boundary condition at the closed end, are such that $f_n = (2n+1)f_0$.[12] As exhaustively described by Olson [59, 60], in compliance with the foregoing, the expression of the acoustic input impedance (Eq. 2.22) become

$$\mathcal{Z}_1 = \frac{\rho c}{\mathcal{S}} \cdot \frac{S\mathcal{Z}_2 \cos(kL) + j\rho c \sin(kL)}{\rho c \cos(kL) + j\mathcal{S}\mathcal{Z}_2 \sin(kL)} \tag{2.25}$$

being ρ the density of the medium, c the sound velocity, S the section of the pipe, $k = 2\pi/\lambda$ the wavenumber, $\mathcal{Z}_1$ the throat impedance and $\mathcal{Z}_2$ the acoustical impedance load for a piston set in an infinite baffle.

[10] Notice that, as an example, the thickness of a brass instrument is a few tenths of a millimetre, compared with characteristics lengths that can reach several meters.

[11] $0.62R$ for the unflanged pipe, $0.82R$ for flanged pipe, being R the radius.

[12] In the case of the pipe opened at both ends the fundamental frequency is $f_0 = \frac{c}{\lambda} = \frac{c}{2L}$ being the overtones such that $f_n = (n+1)f_0$.

Example Let us consider, as test case, an unflanged pipe of length $L = 85.09$ cm and diameter $D = 2.5$ cm. Setting the sound velocity $c = 343.0$ m/s, the *cut-off* frequency is $f_{cut} = 6.86k$ Hz: the first three $1D$ resonant frequencies are $f_0^t = 100$ Hz, $f_1^t = 300$ Hz and $f_2^t = 500$ Hz, while the resonant frequencies obtained using the Eq. 2.25 are $f_0^w = 99.57$ Hz, $f_1^w = 298.95$ Hz and $f_2^w = 497.83$ Hz. The relative errors are presented in table 2.1, as well as the first three resonant frequencies.

	1D	**Webster**	**BEM**	ε^t	ε^w
I	100 Hz	99.57 Hz	99.81 Hz	0.19 %	0.24 %
II	300 Hz	298.95 Hz	299.00 Hz	0.33 %	0.02 %
III	500 Hz	497.83 Hz	498.03 Hz	0.43 %	0.04 %

Table 2.1: Comparison between theoretical ($1D$), analytical (Webster) and numerical (BEM) solution for the first three resonant frequencies of a uniform pipe.

The convergence analysis highlights that the 3D BEM solution converges to an intermediate solution between the $1D$ theoretical and the resonant frequencies derived from the approximated solution of the Webster's equation, as shown in Figs. 2.5, 2.6 and 2.7, and when the convergence is achieved, the numerical input impedance spectrum overlaps spectrum achieved with Eq. 2.25, as shown in Fig. 2.8.

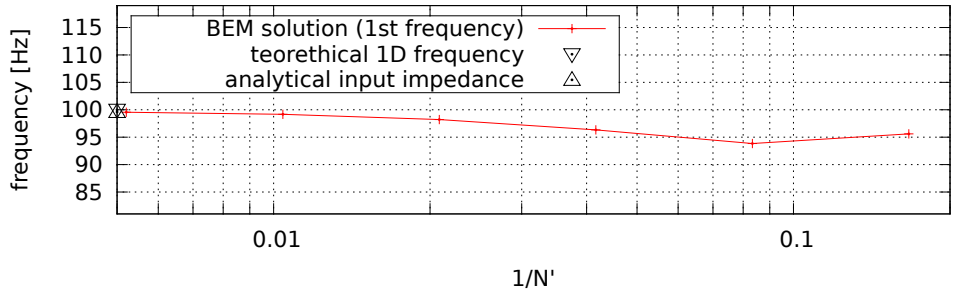

Figure 2.5: Convergence of the first resonant frequency of a uniform pipe, $f_0^t = 100$ Hz and $f_0^w = 99.57$ Hz, as a function of the number of panels per wavelength at the analytical (Webster) frequency.

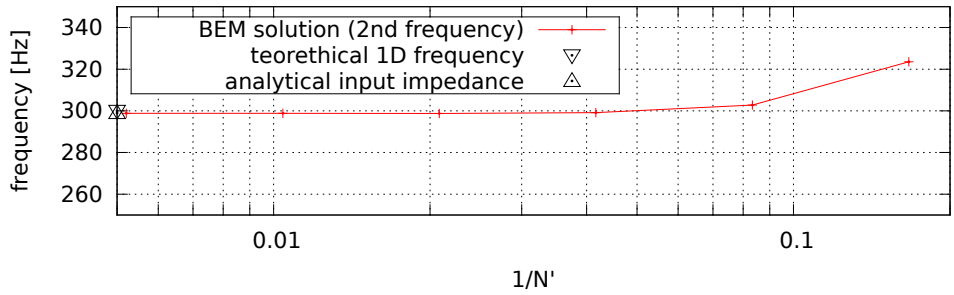

Figure 2.6: Convergence of the second resonant frequency of a uniform pipe, $f_1^t = 300$ Hz and $f_1^w = 298.95$ Hz, as a function of the number of panels per wavelength at the analytical (Webster) frequency.

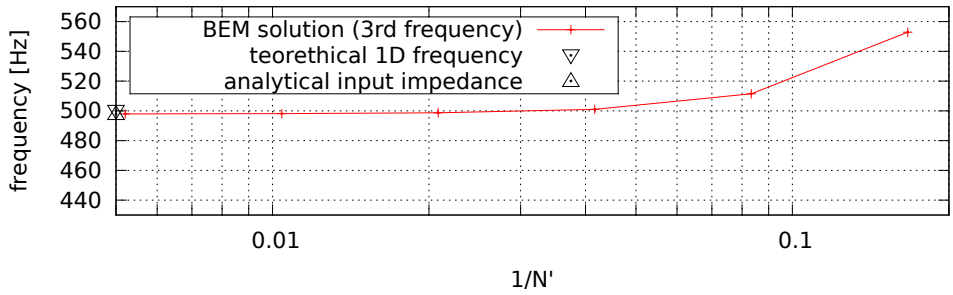

Figure 2.7: Convergence of the third resonant frequency of a uniform pipe, $f_2^t = 500$ Hz and $f_2^w = 497.83$ Hz, as a function of the number of panels per wavelength at the analytical (Webster) frequency.

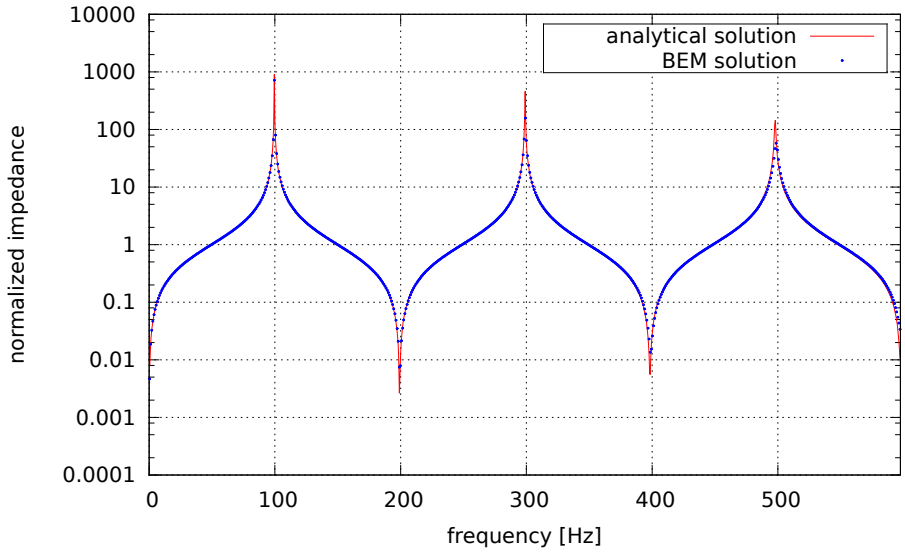

Figure 2.8: Unflanged uniform pipe: analytical (Webster) vs. numerical (BEM) input impedance spectrum divided by $\rho c/\mathcal{S}_{in}$.

Conical horn

For a given conical horn, being ρ the density of the medium, c the sound velocity, S the section of the pipe, $k = 2\pi/\lambda$ the wavenumber, $\mathcal{Z}_1$ the throat impedance, $\mathcal{Z}_2$ the acoustical impedance load for a piston set in an infinite baffle, S_1 the throat section area, S_2 the mouth section area, $\theta_i = \tan^{-1}(kx_i)/k$ with x_i the distance of the $i-th$ section from the apex, the expression of the acoustical input impedance of a conical horn [59, 60] can be evaluated as follows

$$\mathcal{Z}_1 = \frac{\rho c}{\mathcal{S}_1} \cdot \frac{\frac{\rho c}{\mathcal{S}_2}\sin(kL) + j\mathcal{Z}_2 \frac{\sin[k(L-\theta_2)]}{\sin(k\theta_2)}}{\mathcal{Z}_2 \frac{\sin[k(L+\theta_1-\theta_2)]}{\sin(k\theta_1)\sin(k\theta_2)} - j\frac{\rho c}{\mathcal{S}_2}\frac{\sin[k(L+\theta_1)]}{\sin(k\theta_2)}} \tag{2.26}$$

Example Considering a divergent conical horn of lenght $L = 56.73$ cm, which cross section varies from $S_1 = 1.25$ cm to $S_2 = 5$ cm: the first resonant frequencies evaluated using the Eq. 2.26 are $f_0^w = 229.13$ Hz, $f_1^w = 487.17$ Hz and $f_2^w = 764.04$ Hz. The approximated analytical and the numerical (BEM) resonant frequencies are presented in the table 2.2, with the relative errors.

	Webster	**BEM**	ε^w
I	229.13 Hz	228.09 Hz	0.45 %
II	487.17 Hz	487.99 Hz	0.17 %
III	764.04 Hz	764.82 Hz	0.10 %

Table 2.2: Comparison between analytical (Webster) and numerical (BEM) solution for the first three resonant frequencies of a conical horn.

The convergence of the BEM resonances with respect to the approximated analytical resonances is presented in in Figs. 2.9, 2.10 and 2.11, and the convergence numerical input impedance spectrum, in Fig. 2.12, is in remarkable agreement with the approximated analytical solution of the Eq. 2.26.

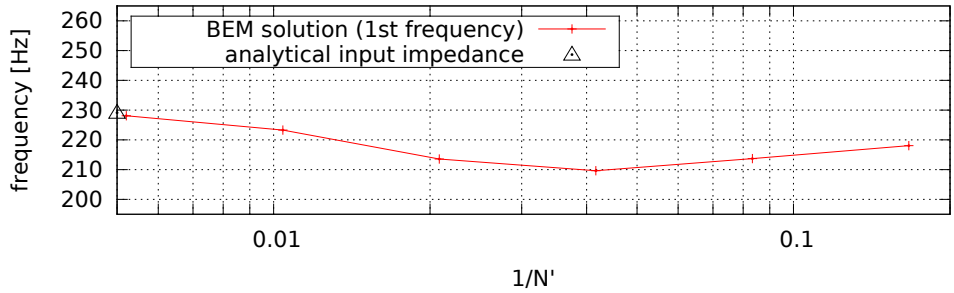

Figure 2.9: Convergence of the first resonant frequency of a conical horn, $f_0^w = 229.13$ Hz, as a function of the number of panels per wavelength at the analytical (Webster) frequency.

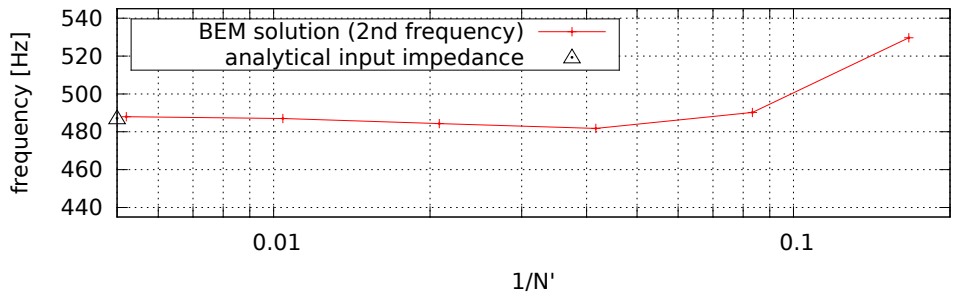

Figure 2.10: Convergence of the second resonant frequency of a conical horn, $f_1^w = 487.17$ Hz, as a function of the number of panels per wavelength at the analytical (Webster) frequency.

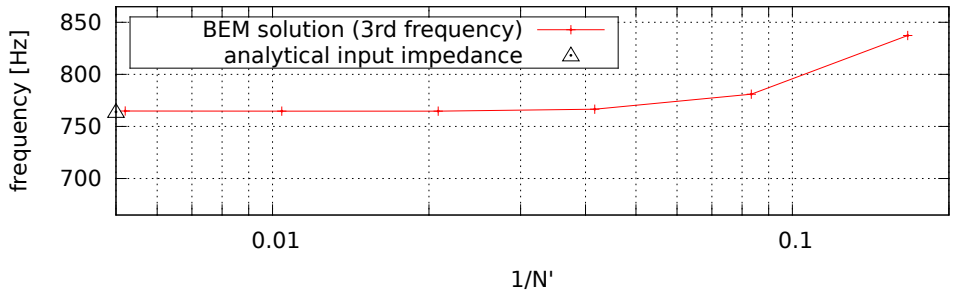

Figure 2.11: Convergence of the third resonant frequency of a conical horn, $f_2^w = 764.04$ Hz, as a function of the number of panels per wavelength at the analytical (Webster) frequency.

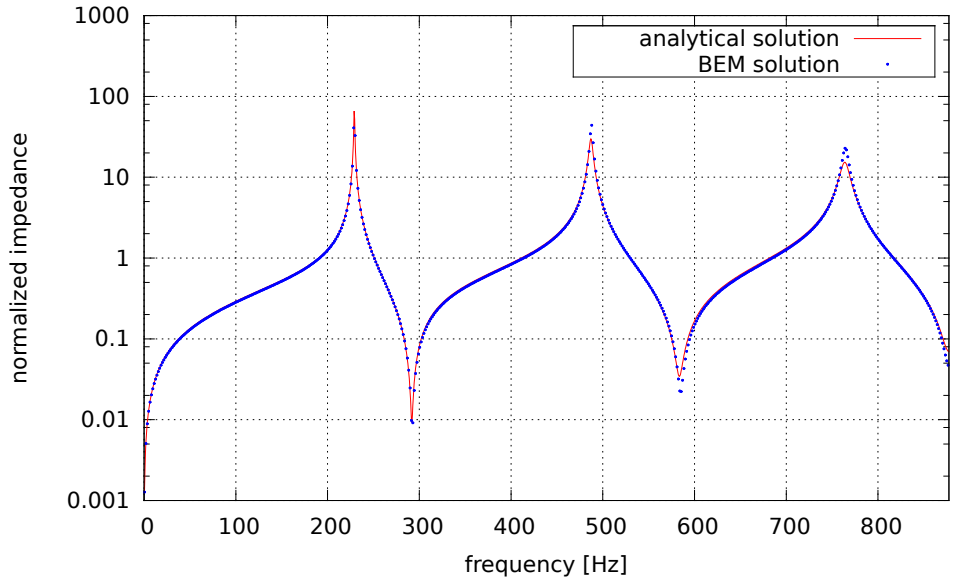

Figure 2.12: Conical horn: analytical (Webster) vs. numerical (BEM) input impedance spectrum divided by $\rho c/\mathcal{S}_{in}$.

Exponential horn

Considering, lastly, the exponential horn: the cross-sectional area varies exponentially with a given flare constant m. The expression of acoustic impedance [59, 60] is given by the following expression

$$\mathcal{Z}_1 = \frac{\rho c}{\mathcal{S}_1} \cdot \frac{\mathcal{S}_2 \mathcal{Z}_2 \cos(bL+\theta) + j\rho c \sin(bL)}{\rho c \cos(bL-\theta) + j\mathcal{S}_2 \mathcal{Z}_2 \sin(bL)} \tag{2.27}$$

being ρ the density of the medium, c the sound velocity, S the section of the pipe, $k = 2\pi/\lambda$ the wavenumber, $\mathcal{Z}_1$ the throat impedance, $\mathcal{Z}_2$ the acoustical impedance

load for a piston set in an infinite baffle, S_1 the throat section area, S_2 the mouth section area, $\theta_i = \tan^{-1}(a/b)$, with $a = m/2$, and $b = \sqrt{4k^2 - m^2}/2$.

Example Let us analyse an exponential horn of length $L = 68.07$ cm, with a throat section $S_1 = 0.625$ cm and a flare constant $m = 0.0676$: the first analytical resonant frequencies, evaluated with Eq. 2.27, are $f_0^a = 259.28$ Hz, $f_1^a = 437.61$ Hz and $f_2^a = 655.94$ Hz. The first three resonant frequencies (Webster) are presented in the table 2.3, with the relative errors.

	Webster	**BEM**	ε^w
I	259.28 Hz	255.79 Hz	1.34 %
II	437.61 Hz	437.59 Hz	0.005 %
III	655.94 Hz	656.03 Hz	0.013 %

Table 2.3: Comparison between analytical (Webster) and numerical (BEM) solution for the first three resonant frequencies of an exponential horn.

The convergence of the numerical (BEM) resonant frequencies is presented in Figs. 2.13, 2.14 and 2.15, whereas the comparison of the input impedance spectra, in Fig. 2.16, highlights a remarkable similarity.

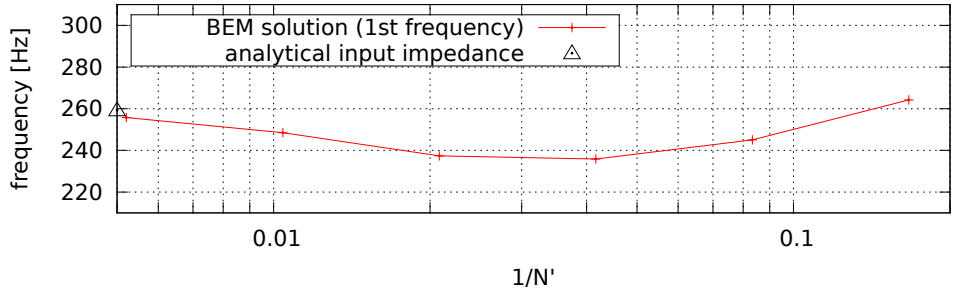

Figure 2.13: Convergence of BEM solution for the first resonant frequency of an exponential horn, $f_0^w = 259.28$ Hz.

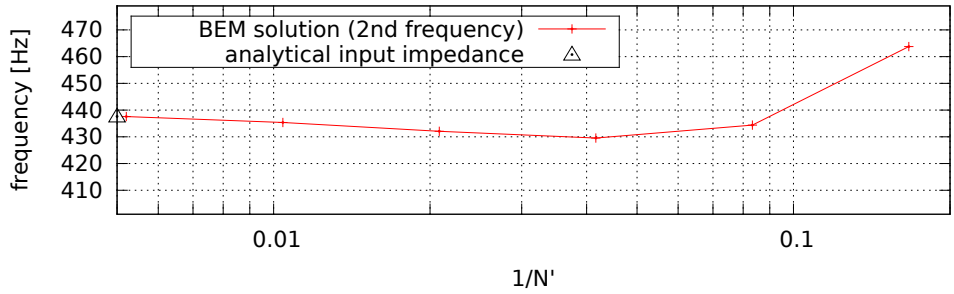

Figure 2.14: Convergence of BEM solution for the second resonant frequency of an exponential horn, $f_1^w = 437.61$ Hz.

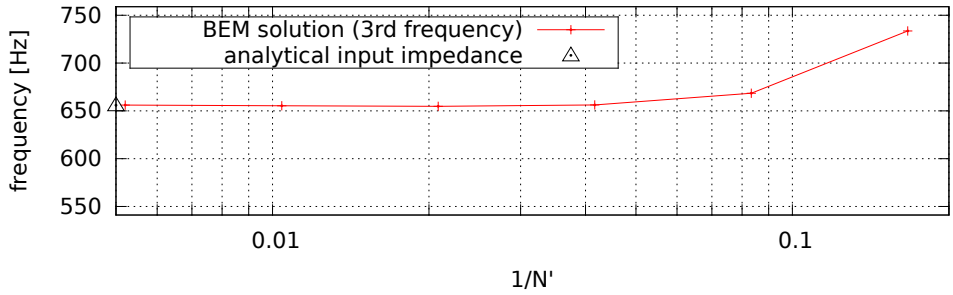

Figure 2.15: Convergence of BEM solution for the third resonant frequency of an exponential horn, $f_2^w = 655.94$ Hz.

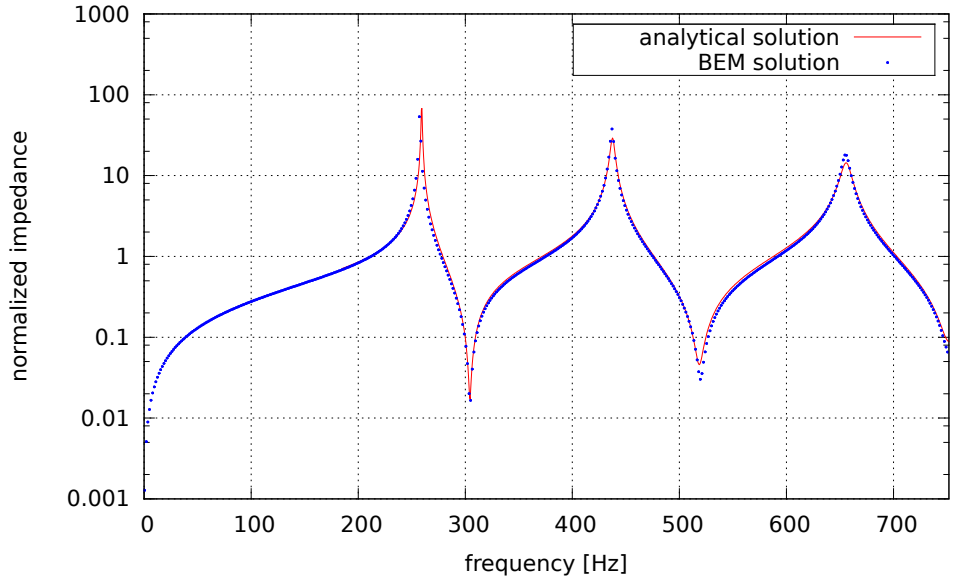

Figure 2.16: Exponential horn: analytical (Webster) vs. numerical (BEM) input impedance spectrum divided by $\rho c/\mathcal{S}_{in}$.

Complex geometries

The acoustical impedance of a complex geometry, considered as superposition of n elementary geometries, can analytically be computed using the Eqs. 2.25, 2.26 and 2.27,[13] taking into account that the i–th input acoustical impedance at the throat matches with the $(i-1)$–th terminating acoustical impedance at the mouth. Note that it is also possible to consider any geometry as superposition or infinitesimal uniform pipes with different cross–sectional areas, as well as superposition of infinitesimal conical horns,[14] imposing the continuity of both pressure and volume

[13] In addition, the input impedance of hyperbolic and parabolic horns can also be analytically computed, but their discussion have been overlooked in this work.

[14] Certainly the uniform pipe can be considered as a special case of the conical horn.

current as boundary conditions for the i–th elementary horn.

Example As an example, without going into details as done in the case of the basic horns, let consider a complex resonator of length L consisting in a uniform pipe of length $L/2$ and diameter d, connected with a divergent conical horn. The the approximated analytical solution, as mentioned above, is provided by the combination of the Eqs. 2.25 and 2.26. The analysis of Fig. 2.17 highlights that the agreement of the numerical solution (BEM) is remarkable.

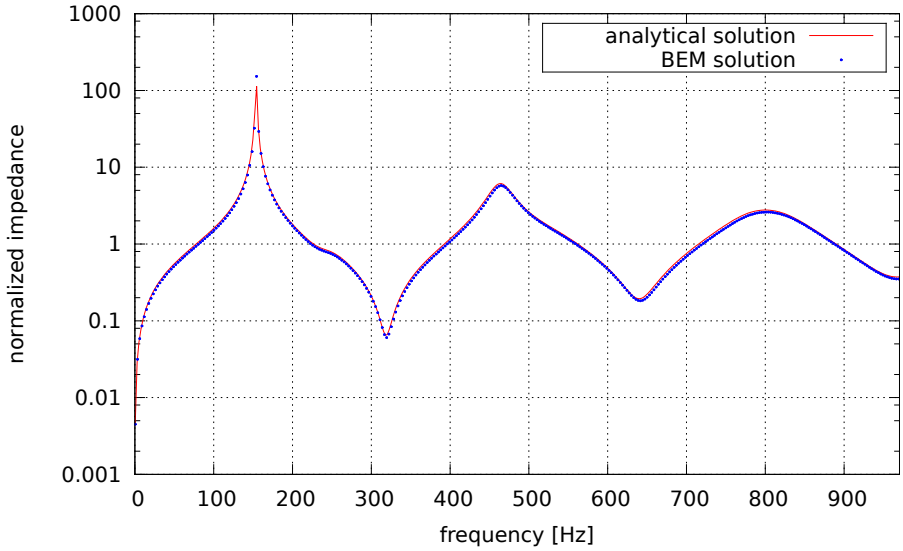

Figure 2.17: Uniform pipe connected to a conical horn: analytical (Webster) vs. numerical (BEM) input impedance spectrum divided by $\rho c/\mathcal{S}_{in}$.

2.3 On the sound propagation

Although an accurate acoustical characterization of resonators is possible, in principle, even availing of analytical formulations (see Eqs. 2.25, 2.26 and 2.27), the strength of the acoustic fields integral representation is in the possibility to derive the transfer functions aimed at the propagation of the signal at any point of the domain: in fact, the representation used in order to obtain the frequency response of the resonator (see Sect. 2.2 and App. A) can be used to evaluate the pressure complex amplitude anywhere in the field.

Indeed the *signature* of a musical instrument, as well as that of any sound source, is highly affected by the propagation pattern of the sound in the space. The spectral components of a complex signal emit, in fact, with different efficiency with respect to both polar and azimuthal angles, and therefore the timbre may be different in relation to the listening area. Moreover, propagation can occur inside closed

spaces, where other objects are present, and therefore occur complex phenomena of reflection and diffusion, among them the reverb is only the most evident.

In the following sections, the propagation transfer functions will be presented, with the purpose of introducing the methodologies that lead to the timbrical reconstruction of wind instruments, as well as the auralization of the signals, which will be discussed hereinafter.

2.3.1 *Embouchure–to–Microphone* transfer function

Let us consider the propagation of the pressure signal in open space, without scattering objects. The integral formulation can be used as a "sound propagator" from the input section $\mathcal{S}_{in}$ to the virtual microphone locate at y^M.

The linearised Bernoulli theorem (see Eq. 2.11) can provide the connection between the frequency–varying velocity potential $\tilde{\varphi}$ at the virtual microphone location and the pressure signal $\tilde{p}$

$$\tilde{p}(y^M, s) = -\rho s \tilde{\varphi}(y^M, s) \tag{2.28}$$

with $\tilde{\varphi}(y^M, s)$ given by the following

$$\tilde{\varphi}(y^M, s) = \sum_{n=1}^{N} \left[B_n^M \frac{\partial \tilde{\varphi}_n}{\partial n} + \left(C_n^M - s D_n^M \right) \tilde{\varphi}_n \right] e^{-s\theta_n^M} \tag{2.29}$$

In matrix form

$$\tilde{\varphi}^M = \mathbf{B}^M \tilde{\chi} + \left(\mathbf{C}^M - s\mathbf{D}^M \right) \tilde{\varphi} \tag{2.30}$$

Coupling the solution on the boundary, given by the Eq. 2.15, with the representation at the virtual microphone location (see Eq. 2.29), with simple steps (for details see App. B) one can obtain the expression of the pressure at the virtual microphone location

$$\tilde{p}(y^M, s) = \mathbf{E_2M}(s) \tilde{\chi}_{in} \tag{2.31}$$

where $\mathbf{E_2M}$, the *Embouchure-to-Microphone* transfer function, is defined by

$$\mathbf{E_2M}(s) = -\rho s \left[\mathbf{B}^M + \left(\mathbf{C}^M - s\mathbf{D}^M \right) \mathbf{Y}^{-1} \mathbf{B} \right] \tag{2.32}$$

and χ_{in} represents the inflow across the intake section of the instrument, calculated as will be shown in the Chap. 3, solving the equations describing the acousto-elastic coupling between the virtual player and the resonator.

Example Considering a Bessel horn with a bottleneck close to the inlet section of total length $L = 70$ cm and inlet diameter $d = 2$ cm, shown in Fig. 2.18.

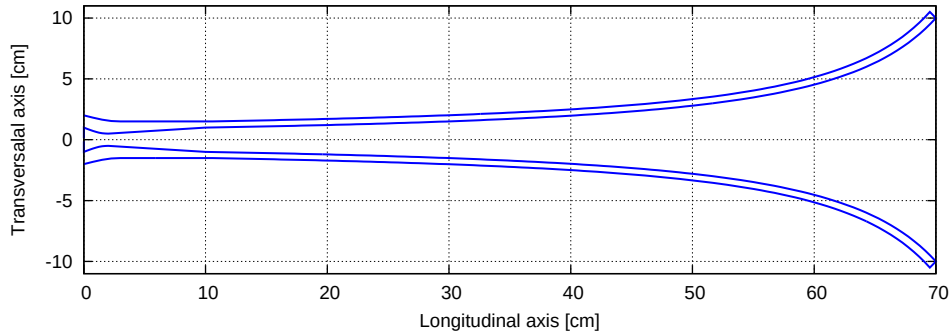

Figure 2.18: Geometric model of the Bessel horn with a bottleneck close to the inlet section.

The acoustical input impedance of the resonator is shown in Fig. 2.19.

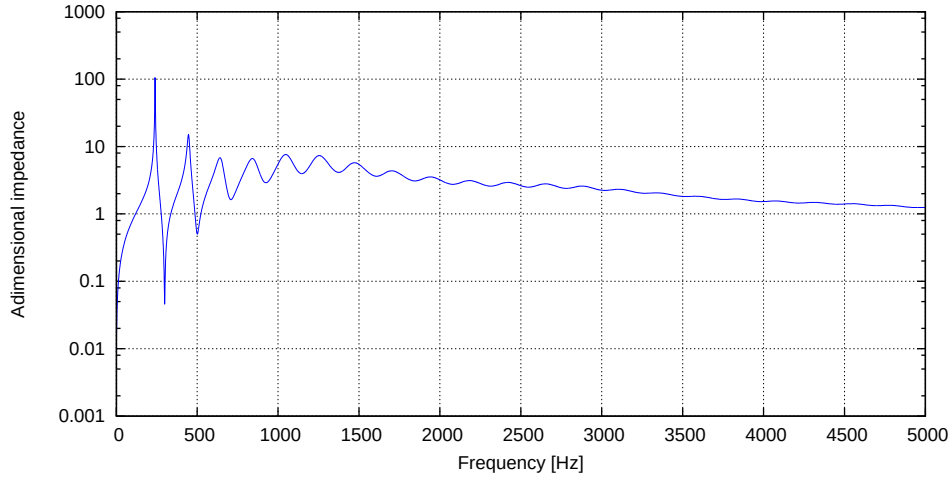

Figure 2.19: Input impedance spectrum divided by $\rho c/\mathcal{S}_{in}$ of the Bessel horn with a bottleneck close to the inlet section.

The input impedance maxima and minima, *i.e.* the resonances and the antiresonances of the resonator, are presented in Tab. 2.4 and 2.4, and are responsible of the harmonic composition of the sounds reproducible with the resonator.

	Frequency	**Note**
f_I	239.88 Hz	Bb_3
f_{II}	447.98 Hz	A$_4$
f_{III}	656.89 Hz	E$_5$
f_{IV}	841.07 Hz	G#$_5$
f_V	1065.97 Hz	C$_6$
f_{VI}	1243.77 Hz	Eb_6

Table 2.4: First resonances of the Bessel horn with a bottleneck close to the inlet section.

	Frequency	**Note**
f_I	299.02 Hz	D_4
f_{II}	498.86 Hz	B_4
f_{III}	690.78 Hz	E_5
f_{IV}	921.72 Hz	$A\#_5$
f_V	1141.49 Hz	D_6

Table 2.5: First antiresonances of the Bessel horn with a bottleneck close to the inlet section.

Instead, the efficiency with which the harmonic component of the sounds are spatially perceived in the field, depends on the directivity pattern of each frequency.

Considering an half–circle of radius $r = 2$ m of virtual microphones centred on the outlet section of the resonator: the evaluation of the *Embouchure–to–Microphone* transfer function $\mathbf{E_2M}$ along such half–circle allows to assess the directivity patterns of the resonator,[15] related to both the resonances and the antiresonances of the instrument, as shown in Figs. 2.20 and 2.21.

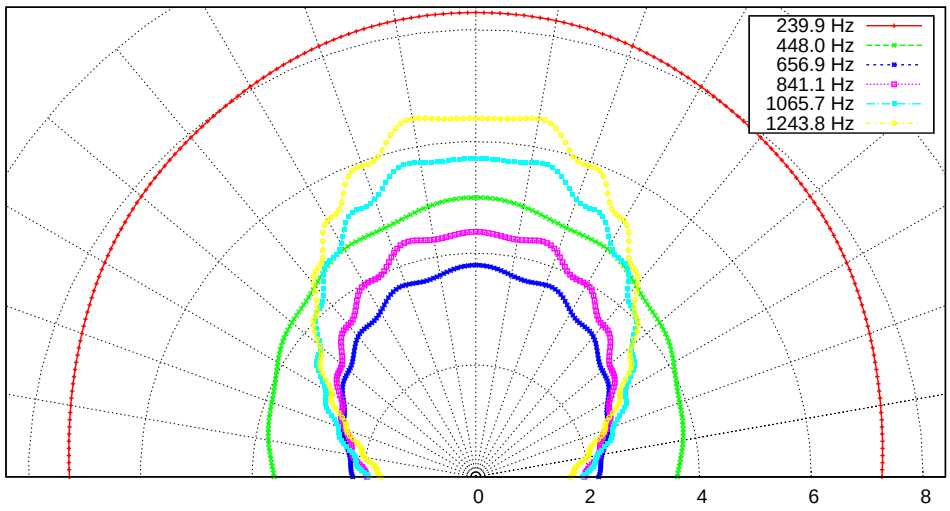

Figure 2.20: Resonances directivity patterns of the Bessel horn with a bottleneck close to the inlet section, evaluated on an half–circle of virtual microphones located at a distance $r = 2$ m from the outlet section.

[15] Obviously one can expect that the directivity is also a function of the distance from the outlet section of the resonator.

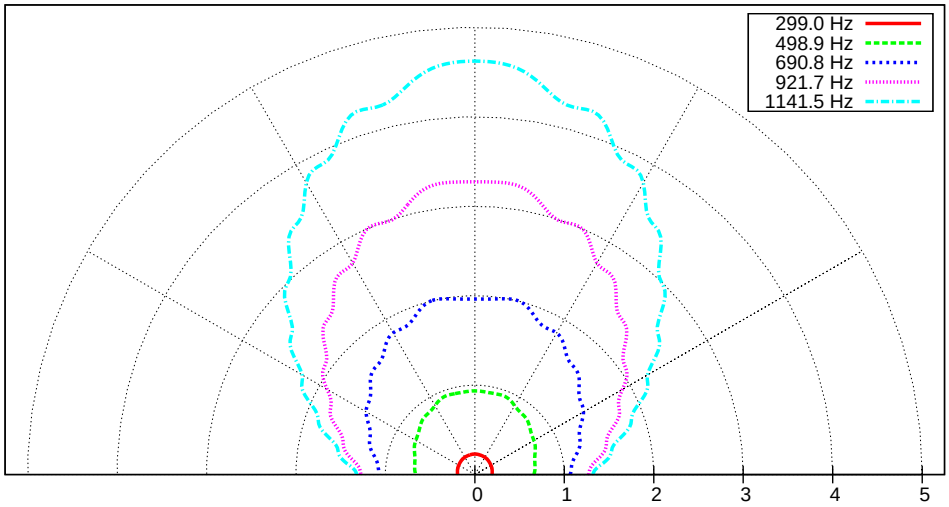

Figure 2.21: Antiresonances directivity patterns of the Bessel horn with a bottleneck close to the inlet section, evaluated on an half–circle of virtual microphones located at a distance $r = 2$ m from the outlet section of the resonator.

The difference in radiation efficiency is even more evident when comparing the transfer functions $\mathbf{E_2M}$ related to the lateral microphone located at $\alpha = 0°$ with respect to the axis of the instrument and the longitudinal microphone located on the axis of the resonator, both at distance $r = 2$ m, in Fig. 2.22.

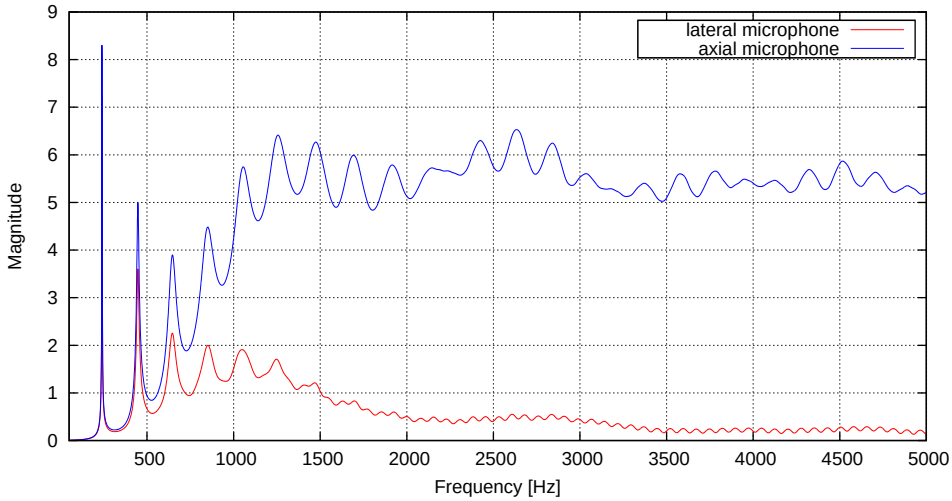

Figure 2.22: Comparison between the *Embouchure–to–Microphone* transfer function divided by $1/S_{in}$ related to the lateral virtual microphone and the longitudinal virtual microphone, both at distance $r = 2$ m from the outlet section of the resonator.

In Fig. 2.23, the bode plot of the *Embouchure–to–Microphone* transfer function $\mathbf{E_2M}$ related to a virtual microphone located at distance $r = 2$ m from the outlet

section of the resonator, with an offset $\alpha = 30°$ with respect to its longitudinal axis.

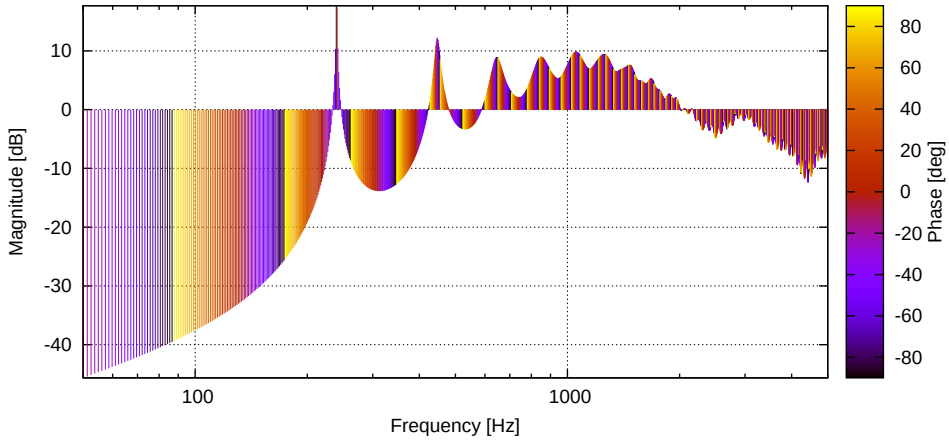

Figure 2.23: Bode plot of the *Embouchure–to–Microphone* transfer function divided by $1/\mathcal{S}_{in}$ related to a virtual microphone located at distance $r = 2$ m from the outlet section of the resonator, with an offset $\alpha = 30°$ with respect to its longitudinal axis.

2.3.2 *Embouchure–to–Listener* transfer function

In order to achieve the auralization of the signal it is important to simulate the spatial effects due to the closed space where the performance take place and where scattering objects, including the listener's head itself, are present. In this condition the total pressure field is sum of incident pressure and scattering pressure

$$\tilde{p}^L(\bar{x}, s) = \tilde{p}^L_{inc}(\bar{x}, s) + \tilde{p}^L_{sc}(\bar{x}, s) = -\rho s \left[\tilde{\varphi}^L_{inc}(\bar{x}, s) + \tilde{\varphi}^L_{sc}(\bar{x}, s)\right] \tag{2.33}$$

For a given acoustic admittance α, one has

$$\frac{\partial \tilde{\varphi}^L_{sc}}{\partial n} = -\left[\frac{\partial \tilde{\varphi}^L_{inc}}{\partial n} + -\rho s \alpha \left(\tilde{\varphi}^L_{inc} + \tilde{\varphi}^L_{sc}\right)\right] \tag{2.34}$$

The incident field is derived from the solution on the instrument

$$\tilde{p}^L_{inc}(s) = \mathbf{Q}(s)\tilde{\chi}_{in} \tag{2.35}$$

where $\mathbf{Q}(s)$, defined by the following expression

$$\mathbf{Q}(s) = -\rho s \left[\mathbf{B}^{inc} + \left(\mathbf{C}^{inc} - s\mathbf{D}^{inc}\right)\mathbf{Y}^{-1}\mathbf{B}\right] \tag{2.36}$$

is the matrix transfer function relating the mouthpiece input velocity to the incident pressure field. The scattering pressure field is derived from definitions of the boundary conditions

$$\chi^L_{sc} = -\chi^L_{inc} - \rho s \alpha \left(\tilde{\varphi^L_{inc}} + \tilde{\varphi^L_{sc}}\right) \tag{2.37}$$

and the scattering component of the potential φ_{sc}^{L} can be expressed as a function of the incident field φ_{inc}^{L} as follows

$$\varphi_{sc}^{L} = -\mathbf{Y}^{-1}\mathbf{B}_{sc}\left(\chi_{inc}^{L} + \rho s\alpha\varphi_{inc}^{L}\right) \tag{2.38}$$

being

$$\mathbf{Y} = \frac{1}{2}\mathbf{I} + \rho s\alpha\mathbf{B}_{sc} - \mathbf{C}_{sc} - s\mathbf{D}_{sc} \tag{2.39}$$

The incident field must be compliant with the compatibility condition on the listener surface

$$-\frac{1}{2}\mathbf{I}\varphi_{inc}^{L} = \mathbf{B}_{sc}\chi_{inc}^{L} + \mathbf{C}_{sc}\varphi_{inc}^{L} + s\mathbf{D}_{sc}\varphi_{inc}^{L} \tag{2.40}$$

namely

$$\chi_{sc}^{L} = \mathbf{B}_{sc}^{-1}\mathbf{Y}\varphi_{inc}^{L} \tag{2.41}$$

being

$$\mathbf{Y} = -\frac{1}{2}\mathbf{I} - \mathbf{C}_{sc} - s\mathbf{D}_{sc} \tag{2.42}$$

Given the above one can express the scattering component of pressure as function of the incident field

$$\tilde{p}_{sc}^{L}(s) = \mathbf{V}(s)\tilde{\chi}_{in} \tag{2.43}$$

where $\mathbf{V}(s)$, defined by the equation

$$\mathbf{V}(s) = \left(\mathbf{Y}^{-1}\mathbf{Y} + \rho s\alpha\mathbf{Y}^{-1} - \mathbf{B}^{sc}\right)\mathbf{Q}(s) \tag{2.44}$$

is the matrix transfer function relating the mouthpiece input velocity to the scattered pressure whereas $\mathbf{Q}(s)$ is the matrix transfer function between the velocity at the inlet section $\mathcal{S}_{in}$ of the resonator and the incident pressure field.

Once that both incident field and scattering field are known, the Eq. 2.33 becomes

$$\tilde{p}(y^{L}, s) = \mathbf{E_2L}(s)\tilde{\chi}_{in} \tag{2.45}$$

where $\mathbf{E_2L}$, the *Embouchure-to-Listener* transfer function, is defined by

$$\mathbf{E_2L}(s) = -\rho s\left[\mathbf{Q}(s) + \mathbf{V}(s)\right] \tag{2.46}$$

It seems essential to specify that the quality of the geometric models of the scattering bodies in the acoustic field, as well as that of the performance environments for which evaluate the *Embouchure-to-Listener* transfer function $\mathbf{E_2L}$, depends exclusively on the available computing resources.

Example With reference to the previous case (the Bessel horn with a bottleneck close to the inlet section, discussed for the $\mathbf{E_2M}$ transfer function), let consider a simple model of head[16] located on the instrument axis at distance $d = 3$ m with respect to the outlet section of the resonator. The *Embouchure–to–Listener* transfer function $\mathbf{E_2L}$ is evaluated for two antipodal location of the head, and is presented in Fig. 2.24.

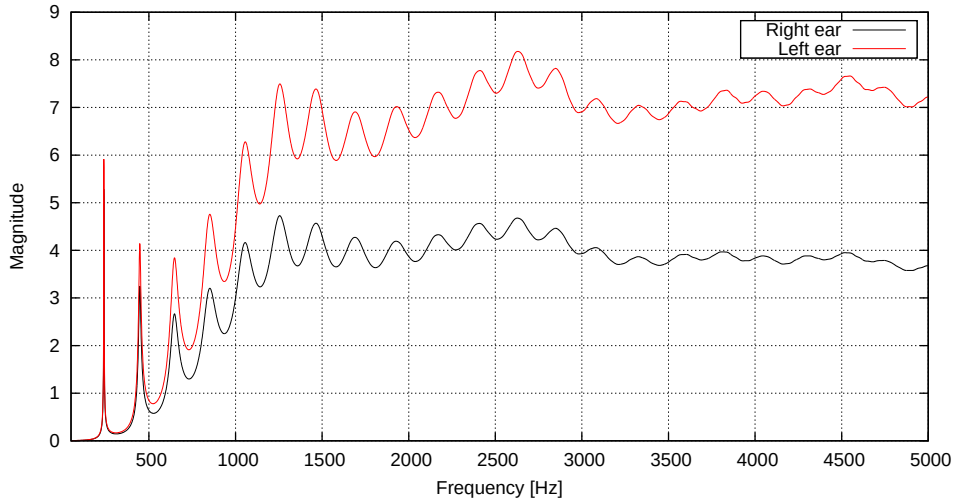

Figure 2.24: *Embouchure–to–Listener* transfer function divided by $1/\mathcal{S}_{in}$ related to a simple model of head located on the instrument axis at distance $d = 3$ m with respect to the outlet section of the Bessel horn with a bottleneck close to the inlet section, being the ears at two antipodal locations.

[16]The head is assumed to be a simple rigid sphere of radius $r_{sph} = 8.75$ cm.

CHAPTER 3

Interaction with the player and sound propagation

The methodologies used to model the interaction between the resonator and the exciter are discussed in this chapter. Once known the acoustic characteristics of the resonators and of the surroundings, provided in the frequency–domain by the methodologies described in the Chap. 2, a model for the coupling with the mechanism of the inflow sustentation is necessary in order to reconstruct in the time–domain the state variables at the inlet section of the instruments. Starting from the latter, the perceived signal anywhere in the field, as well as the auralized acoustic pressure signals are easily achievable.

In what follows, will be shown the models developed in the context of the sound synthesis aimed at the description in the time–domain of the acousto–elastic feedback for the woodwinds and in the brasses, and for some cases will be presented suitable examples.

3.1 The interaction with the player

Playing a resonant aerophone consists in sustain an airflow into a resonating cavity to let the air column vibrate in its interior, and can be envisaged as a constant interaction between the player, an exciter and a resonator. Note that the player represents the energy source, while the exciter and the resonator are respectively the active elastic element and the passive acoustic element of the acousto–elastic feedback (see Fig. 3.1).

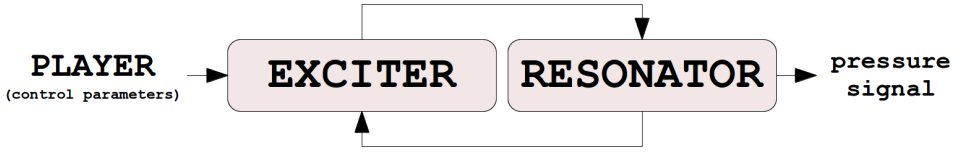

Figure 3.1: Time–domain acousto–elastic feedback for resonant aerophones.

In order to understand the interaction between the exciter and the resonator is essential to formalize the relationship between static pressure and flow inside the embouchure: in the frequency–domain, is given by

$$\tilde{p}_{in}(\omega) = \mathcal{Z}_{in}(\omega)\tilde{u}_{in}(\omega) \tag{3.1}$$

Accordingly to the model of McIntyre, Schumacher and Woodhouse [56] the time–dependent acoustic pressure at the input section of the instrument can be interpreted as the superposition of the outgoing wave $p_{in}^{+}(t)$ and the incoming wave $p_{in}^{-}(t)$

$$p(t) = p_{in}^{+}(t) + p_{in}^{-}(t) \tag{3.2}$$

Exploiting this view the resonator can be described in the time–domain just with $p_{in}^{-}(t)$, *i.e.* the pressure at the inlet section in the time–domain is provided by the convolution between the inflow and the the impulse response

$$p_{in}^{-}(t) = u_{in}(t) * z(t) \tag{3.3}$$

where $z(t)$ is simply the inverse Fourier transform of the input impedance

$$z(t) = \mathcal{F}^{-1}\left[\mathcal{Z}_{in}(\omega)\right] \tag{3.4}$$

and represents the response of the instrument to an incident pressure impulse at the intake section, then considered ideally closed [3].

Remarks In order to focus the acousto–elastic coupling between the exciter and the resonator, in this work some aspects were purposely omitted. These aspects mainly concern three issues:

- Fluid–dynamic effects, *i.e.* the influence of the viscous and thermal boundary layer, as well as the propagation of the shock waves inside the mouthpiece, especially in the brasses, during the playing of *fortissimo* and *sforzatissimo*;[1]
- Structural effects, namely the vibration of the instrument itself during the performance;
- The Helmholtz resonator effect caused by the pronunciation of vowels during the blowing into the embouchure.

Such issues, at least according to the knowledge of the author, should not influence the interaction between the air column and the mechanism of inflow sustentation, that is the objective of the modeling.

[1] In musical language ***ff*** and ***fff***.

3.1.1 The reflection function

The process leading to the simulation of the instrument behaviour consists in solving a convolution integral numerically. The time–domain function $z(t)$ in the Eq. 3.3, which describes the impulse response, consists of a series of multiple reflections of the incident pulse from ends of the pipe. Since the pipe is open at one end, a portion of the energy is radiated outside while the residue energy is inverted and return back to to the input section, so the sign of the pulse alternates, whereas in the case of a pipe closed at both the ends, the the energy remains inside the pipe and the pulses keeps the same sign.

Since the spectrum of $\mathcal{Z}_{in}(\omega)$ is highly rich, its inverse Fourier transform consists in an infinite series of reflections, then its decay time can be highly wide. The complexity of $z(t)$ leads to the limitation of the use of the impulse response in the numerical simulations, because the current $p(t)$ depends not only on $p(t-\tau)$, but also on $p(t-2\tau)$, $p(t-3\tau)$ and so on [43].

Let now consider a pulse that propagates inside the tube and running backwards towards the inlet section, after being inverted: if the input section, rather than being closed, continued with an infinite uniform pipe of section equal to the inlet, the pulse would no longer be reflected. This assumption allows you to draw up a time–domain function, the so–called reflection function $r(t)$, which neglects the multiple reflections subsequent to the first one, therefore isolating only the first as a distinct entity. Is crucial to note that the multiple reflections due to the discontinuities in the pipe[2] will necessarily continue, and this explains the reason why the reflection function of musical instruments is particularly complex.

In order to derive the reflection function $r(t)$, is useful to consider the reflection coefficient $\mathcal{R}(\omega)$ which represents, in terms of physical, the ratio of the amplitude of the reflected wave to the incident wave at a given frequency

$$\mathcal{R}(\omega) = \frac{p^-(\omega)}{p^+(\omega)} \tag{3.5}$$

Considering a plane wave propagating forward in the direction of the axis of the resonator and, once arrived at the interface it reflects propagating backward: the input impedance can be expressed in terms of $\mathcal{R}(\omega)$ as follows

$$\mathcal{Z}_{in}(\omega) = \rho_0 c \frac{1+\mathcal{R}(\omega)}{1-\mathcal{R}(\omega)} \tag{3.6}$$

being ρ_0 the density of the medium and c the sound velocity. With simple steps, knowing the characteristic impedance of the wave guide $\mathcal{Z}_0 = \rho_0 c/\mathcal{S}_{in}$ the frequency–domain representation of the reflection function can be easily computed

$$\mathcal{R}(\omega) = \frac{\mathcal{Z}_{in}(\omega) - \mathcal{Z}_0}{\mathcal{Z}_{in}(\omega) + \mathcal{Z}_0} \tag{3.7}$$

[2] A change in the section has to be considered a discontinuity, since each shape is to be considered as the superposition or infinitesimal uniform pipes, as described in the Sect. 2.2.

where $\mathcal{Z}_{in}(\omega)$ can be evaluated analytically or numerically using the integral formulation, as described above in the Chap. 2.

Note that the condition for which the resonator is energetically passive is

$$\mathrm{Im}\left[\mathcal{R}(\omega)\right] < 1, \quad \forall\omega \neq 0 \tag{3.8}$$

which implies, recalling the Eq. 3.7, that $\mathrm{Re}\left[\mathcal{Z}_{in}(\omega)\right] > 0$, *i.e.* in terms of velocity potential (see Eq. 2.12) is verified if $\mathrm{Im}\left[\tilde{\varphi}(\omega)\right] > 0$ on the inlet section $\mathcal{S}_{in}$ of the resonator.

Example Let now consider a uniform pipe of radius $R = 2.5$ cm and length $L = 40.0$ cm. The input impedance spectrum can be evaluated exploiting the Eq. 2.25 (Webster's *horn equation*) or numerically via BEM, as seen in the Chap. 2.[3]

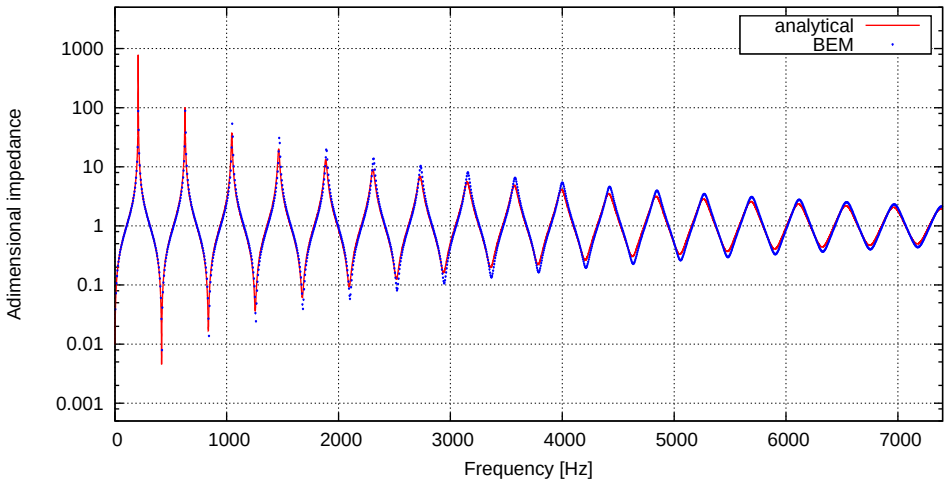

Figure 3.2: Input impedance spectrum divided by $\rho c/\mathcal{S}_{in}$ for a uniform pipe of radius $R = 2.5$ cm and length $L = 40.0$ cm. Superposition of the analytical (Webster) and numerical (BEM) solution.

The comparison between the solution derived by the Eq. 2.25 and the numerical solution highlights a remarkable agreement.

The impulse response, presented in Fig. 3.3, can easily be obtained as the inverse Fourier transform of the input impedance, as described above.

[3] As detaild before, if the cross-sectional area is smaller than the wavelength, the $1D$ theoretical model with the end correction provides the resonances of the pipe.

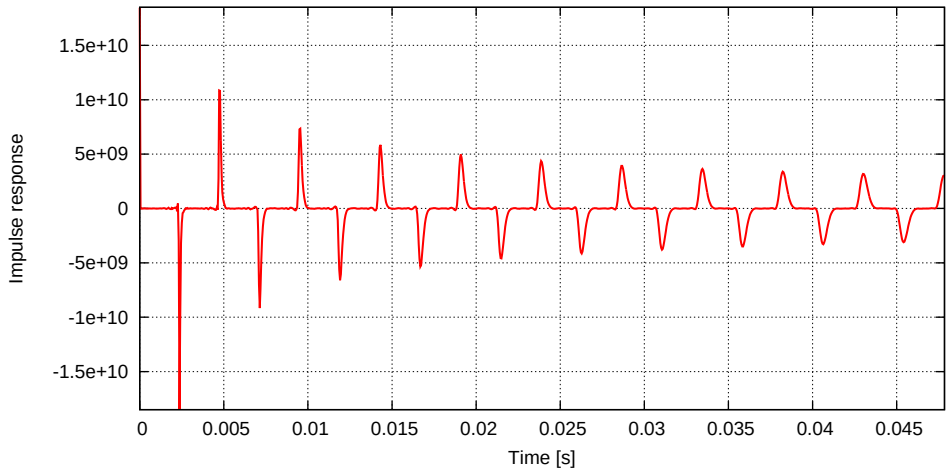

Figure 3.3: Impulse response for a uniform pipe of radius $R = 2.5$ cm and length $L = 40.0$ cm.

The reflection coefficient is obtained with the Eq. 3.7 and, by operating its inverse Fourier transform it is possible to isolate a single reflection, as shown in Fig. 3.4.

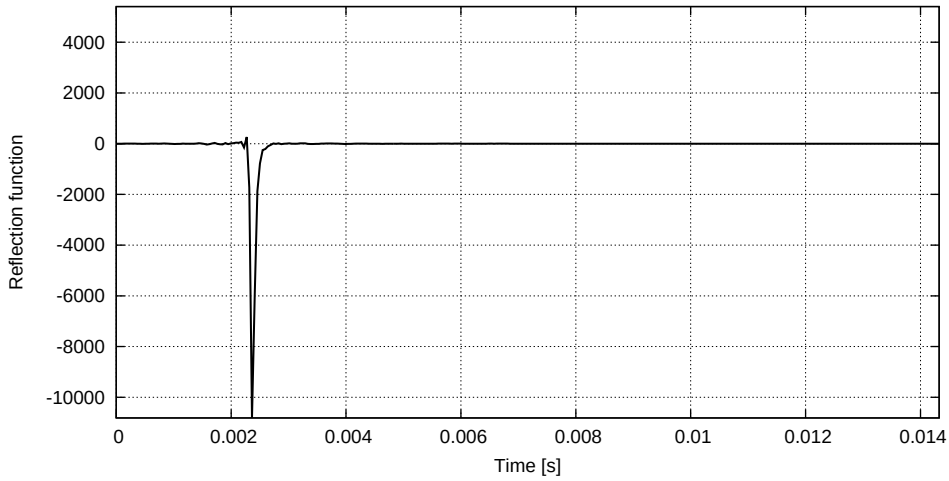

Figure 3.4: Reflection function of a uniform pipe of radius $R = 2.5$ cm and length $L = 40.0$ cm.

It is worth noting that the choice of the frequency sampling can change the shape of the discrete reflection function: as evidenced by Amir et al. [6], if F_{max} is chosen to be on a zero of $\mathcal{Z}_{in}(\omega)$, the discrete reflection function is beset by ripple, while by choosing F_{max} in correspondence of a resonance the ripple tends to disappear.

As evident by the superposition of the impulse response and the reflection function (see Fig. 3.5) the reflection function reproduces the impulse response with respect to the first reflection, otherwise its value is zero.

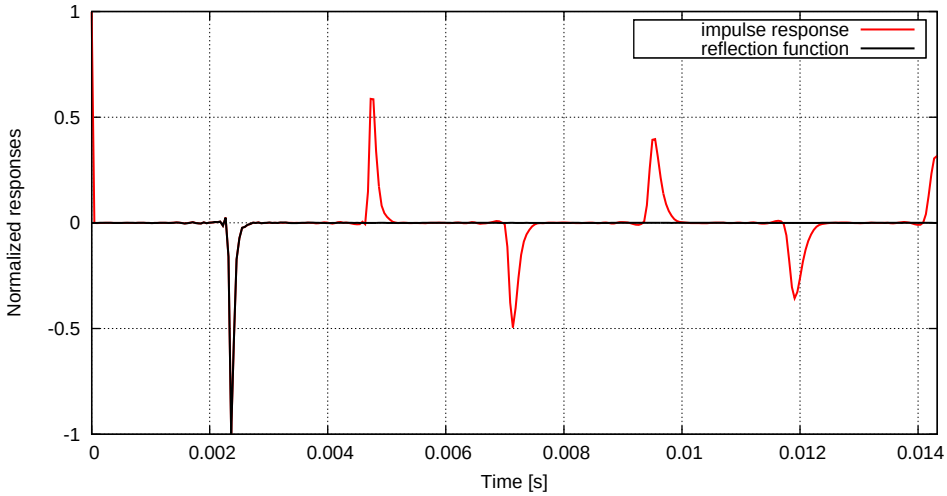

Figure 3.5: Superposition of the normalized impulse response and the normalized reflection function of a uniform pipe of radius $R = 2.5$ cm and length $L = 40.0$ cm.

Lastly it is interesting to point out that, regarding the cylindrical pipe, the decay time, that appears to be extremely long for the impulse response, in the reflection function become comparable to the fundamental period, and such a shortening is relevant indeed in the numerical solution of the convolution integral, as mentioned above.

3.2 The inflow sustentation

Out below, a general discussion concerning the equations governing the dynamics of the reeds (single and double) and the lips will be presented. The air–jets deserve a separate discussion and will be briefly detailed later.

As previously mentioned the dynamics of the exciter, which is represented by an oscillator, is controlled by the energy source with a feedback derived from the acoustic characteristic of the resonator. Such a mechanical system can be depicted by a second–order differential equation

$$m(t)\frac{d^2y(t)}{dt^2} + b(t)\frac{dy(t)}{dt} + k(t)y(t) = S_0 H\left[P_0(t), p(t)\right] \tag{3.9}$$

being $P_0(t)$ the blowing pressure, the coefficients $m(t)$, $g(t)$, $k(t)$ are respectively the inertial, viscous and the stiffness terms, whereas S_0 is the section on which acts the flow and the generic function $H\left[P_0(t), p(t)\right]$ represents the function with which the exciter depends on the resonator.

Note that the term P_0 must be considered as a function of the time in the view of model the intention of the musician to vary the dynamics of the performance, primarily in terms of loudness. Instead the time dependence of the coefficients $m(t)$,

$g(t)$ and $k(t)$ are due to two reasons, *i.e.* the active change of coefficients (aimed at the variation of the note in the brasses, or during the performance of the *vibrato* for the reed–driven instruments) and the passive fluctuations of the mechanical characteristics of the exciters, *e.g* due to the changes in temperature.

Here the pressure is assumed to be constant, and the pressure at the inlet section of the resonators can be described by the Eqs. 3.2 and 3.3. The pressure jump $P_0 - p(t)$ between the player mouth, or the bellow pressure in the case of organ pipes, and the air column inside the resonator can be easily formalized with the Bernoulli law

$$P_0 - p(t) = \frac{1}{2}\rho\frac{u_{in}(t)}{S(t)} \tag{3.10}$$

being $S(t)$ the time-dependent area through which the air-flow passes to the instrument from the musician's mouth. Therefore

$$u_{in}(t) = \sqrt{\frac{2}{\rho}}S(t)\sqrt{\mid P_0 - p(t) \mid} \cdot sgn \tag{3.11}$$

with *sgn* function takes the values 1 or -1 depending on the fact that the sign of $P_0 - p(t)$ is respectively greater or less than zero.

Actually, if the aim of the simulation is the identification and the characterization of a single sustained sound, it is possible to neglect the fluctuations of the mechanical characteristics of the exciter, since in addition it is legitimate to hypothesize that the frequency of these changes are much smaller compared to the frequencies of the generated sounds.

Combining the Eqs. 3.2, 3.3, 3.9 and 3.11, defining the mass ratio $\mu = m/S_0$, the damping factor $g = b/m$ and the exciter angular frequency $\omega = \sqrt{(k/m)}$, one can obtain the system

$$\begin{cases} \ddot{y}(t) + g\dot{y}(t) + \omega^2 y(t) = H\left[P_0, p(t)\right]/\mu \\ p(t) = p_{in}^{+}(t) + p_{in}^{-}(t) \\ p_{in}^{-}(t) = u_{in}(t) * z(t) \\ u_{in}(t) = \sqrt{2/\rho}S(t)\sqrt{\mid P_0 - p(t) \mid} \cdot sgn \end{cases} \tag{3.12}$$

whose solution allows to obtain the complete time–domain simulation.

3.2.1 Woodwinds

Woodwinds [70] are a large family of musical instruments that use feedback from an oscillating air column to control the air flow into the pipe. The valve may be a vibrating reed or an oscillating stream of air. According to the type of the flow-control valve, one can classify woodwinds into two categories:

1. Vibrating–reed: the feedback control (pressure-controlled input) is applied to a vibrating piece of cane. In single-reed instruments only one reed is used to

produce sounds. Belong this class the clarinets and the saxophones (soprano, alto, bass, contra–alto/baritone and contrabass/bass). Regarding double–reed instruments, two pieces of cane vibrate aganist each other in order to establish the acousto-elastic loop during the inflow sustentation. Oboe-like instruments (heckelphones, english horns, etc.) and bassoon-like instruments are the main orchestral double-reed driven musical instruments.

2. Air–jet: an air flow concur with the air column inside the pipe to oscillate producing pressure perturbation. The air stream oscillates back and forth, and the direction of the air flow, due to standing waves, controls the input flow (flow-controlled input). Flutes, recorders and flue organ pipes are part of this category.

The resonances of the air column, except for flue organ pipes and pan flutes, are tuned by tone holes or mechanical keys so the sound is also radiated form the open tone holes and the radiation pattern is very complex.

Single–reed–driven instruments

The attention will be now focused on single–reed instruments (also called *clarinet–like* instruments) *i.e.* clarinets and saxophones. Such instruments consist of a non–uniform holed and keyed pipe, whose section is cylindrical, as in the case of the clarinets, or conical, in the saxophones. Note that the tone holes and the keys modify the characteristics of the resonator in terms of input impedance spectrum, but not the acousto–elastic interaction loop between the air column and the virtual player.

The embouchure of the single–reed instruments consist in is a thin strip, the reed, rigidly clamped in one extreme to the mouthpiece. The reed represents the exciter and the player provides a flow triggering an interaction between the reed and the air column.

By applying a blowing pressure, the puff of air $u(t)$ travels into the pipe and simultaneously the reed starts vibrating, interacting with the wave front reflected by the bell. During such a interaction, reed can be modeled as a simple harmonic oscillator without non-linearity (see Fig. 3.6).

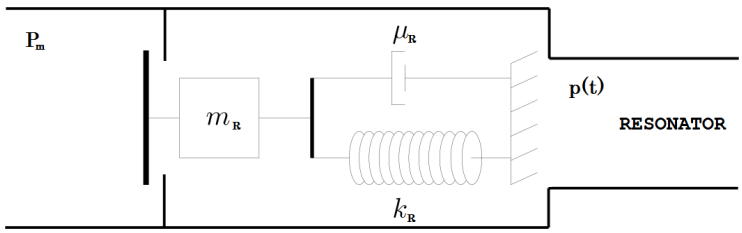

Figure 3.6: Modeling of the single reed as a simple harmonic oscillator.

Its dynamic can be described by the following expression

$$\frac{d^2y(t)}{dt^2} + g_R\frac{dy(t)}{dt} + \omega_R^2 y(t) = \frac{p(t) - P_m}{\mu_R} \tag{3.13}$$

where g_r is the damping factor, ω_R the natural resonance frequency and μ_R represent the ratio between the reed mass m_R and its surface S_R. Note that the abovementioned parameters are peculiarities of the materials of which the reed is made. During the reed movement, total acoustic flow [35] is:

$$u_{in}(t) = u(t) - u_R(t) \tag{3.14}$$

where $u(t)$ is the *Bernoullian* flow, due to the pressure jump between player's mouth and the air column, and the secondary flow $u_R(t)$ is due to the reed movement and can be considered as fallows

$$u_R(t) = S_R\frac{dy(t)}{dt} \tag{3.15}$$

Taking the definitions formalized with the Eqs. 3.14 and 3.15, using the auxiliary displacement variable

$$\xi(t) = y(t) + \frac{P_m}{\mu_R\omega^2}, \tag{3.16}$$

the Eq. 3.13 can be rewritten

$$\begin{pmatrix} \dot{\xi}(t) \\ \dot{u}_R(t) \end{pmatrix} = \begin{bmatrix} 0 & \frac{1}{S_R} \\ -\omega_R^2 S_R & -g_R \end{bmatrix} \begin{pmatrix} \xi(t) \\ u_R(t) \end{pmatrix} + \begin{pmatrix} 0 \\ \frac{S_R}{\mu_R} \end{pmatrix} p(t) \tag{3.17}$$

with

$$\begin{pmatrix} \xi(t) \\ u_R(t) \end{pmatrix} = \begin{pmatrix} -H \\ 0 \end{pmatrix}, \quad \text{if} \quad y(t) \leq -H \tag{3.18}$$

The solution of the system represented by the Eq. 3.17 could be provided numerically. The pressure is given by the convolution between the reflection function and the resulting inflow (see the Eq. 3.12). Once $\xi[n]$ is known, recalling Eq. 3.16, is possible to compute the reed displacement and the knowledge of the inflow composition (see the Eq. 3.14) can give the pressure signal inside the embouchure.[4]

It is interesting to highlight that, since the resonance of the reed is usually greater than the typical fundamental frequencies of the performed notes[5], its dynamics, in quasi–static consitions, can be considered approximatively governed by the pressure jump across the reed

$$k_R(y - y_0) = \Delta p \tag{3.19}$$

[4]Details for the system solution, as well as explanations of the useful numerical schemes, are present in the exhaustive paper [35] of Gazengel et al. (1995).

[5]Typically around 3000 Hz [82].

being k_R the reed stiffness and Δp the pressure jump between the player mouth and the embouchure (see Eq. 3.10). Under this hypothesis, the inflow can be expressed as a function of the pressure jump across the reed

$$u_{in} = \alpha w_R \left(y_0 - \frac{\Delta p}{k_R} \right) \sqrt{\frac{2}{\rho} \Delta p} \tag{3.20}$$

having been introduced the semi–empirical parameter α for jet contraction at the beginning of the reed channel [42, 82], *i.e.* the so–called *vena contracta* effect. The Eq. 3.20 represents the nonlinear characteristic of the single–reed (see Fig. 3.7).

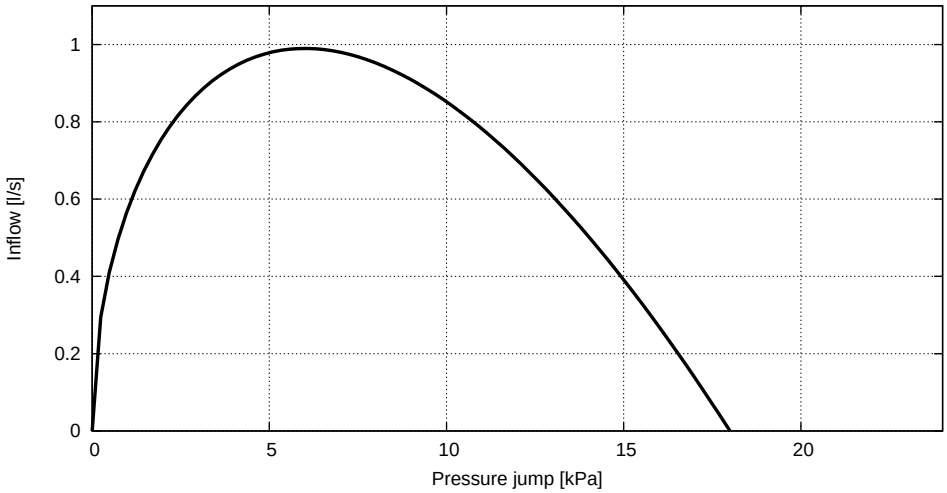

Figure 3.7: A typical nonlinear characteristic of the single–reed: inflow as a function of the pressure jump accross the reed.

The study of the sign of the Eq. 3.20 suggests that when Δp exceeds the value $y_0 k_R$ the reed is closed and the flow passage is inhibited. Instead, the value of pressure jump corresponding to the maximum inflow is given by the annulment of the first derivative, *i.e.* for $\Delta p = y_0 k_R/3$. Lastly it can be proved, by defining the dimensionless inflow, that the shape of the nonlinear characteristic of the single–reed is independent of both the reed characteristics and the blowing pressure [5].

Example As an example let us consider a simulation on a soprano saxophone playing the lowest note. The soprano sax is a transposing instrument[6] pitched in the key of B$\flat$ and is the third smallest member of the saxophone family. Was patented by Adolphe Sax (6 November 1814–February 1894) on March 1846, and is comparable to the B$\flat$ clarinet, but unlike this has a smaller extension and can pan out more energetic sounds on high register.

[6]Transposing instrument are notated at a different pitch from the pitch that actually sounds.

The performed simulation, as mentioned above, refers to the lowest note of a soprano saxophone and the geometrical model, shown in Fig. 3.8, approximates that of a professional high–end concert instrument.

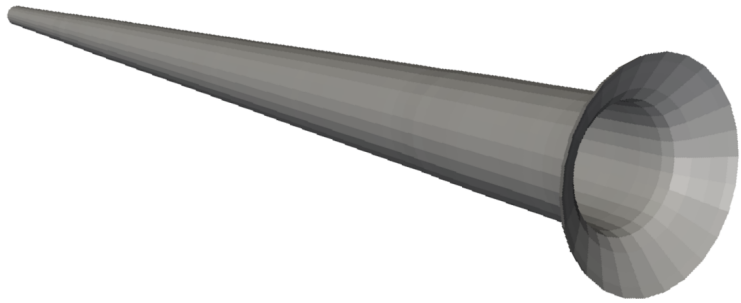

Figure 3.8: Geometric model of the soprano saxophone.

The input impedance spectrum, numerically obtained using the methodology described above, is shown in Fig. 3.9.

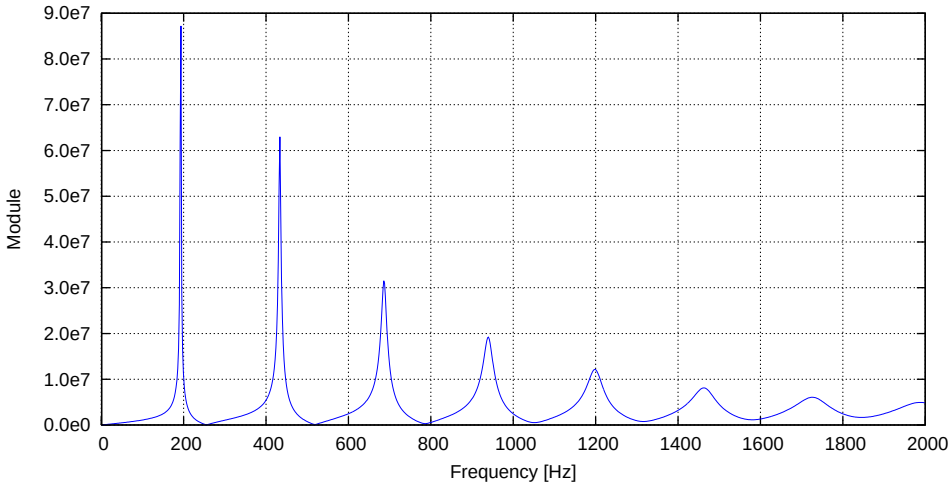

Figure 3.9: Input impedance spectrum of the soprano saxophone.

The analysis of the impedance spectrum shows that the the first resonance frequency of the instruments is close to the B$\flat_3$.[7] Using the Eq. 3.7 is possible to evaluate the reflection coefficient, whose inverse Fourier transform is presented in Fig. 3.10.

[7] A$\flat_3$ in the musical tuning at 440 Hz.

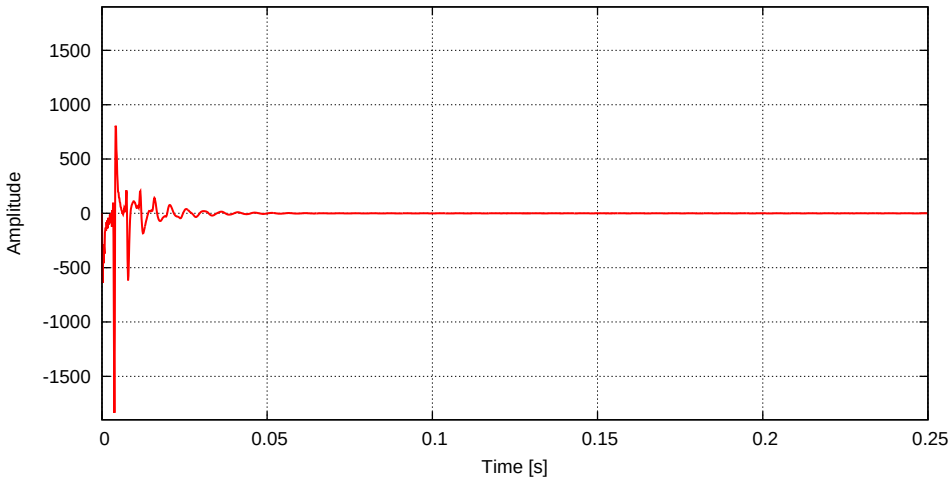

Figure 3.10: Reflection function of the soprano saxophone.

The reflection function, inverse Fourier transform of the reflection coefficient, can be used in order to solve the system represented by the Eq. 3.12 in order to compute the reed displacement, the inflow and the pressure signal, *i.e.* the state variables inside the embouchure (see Fig. 3.11).

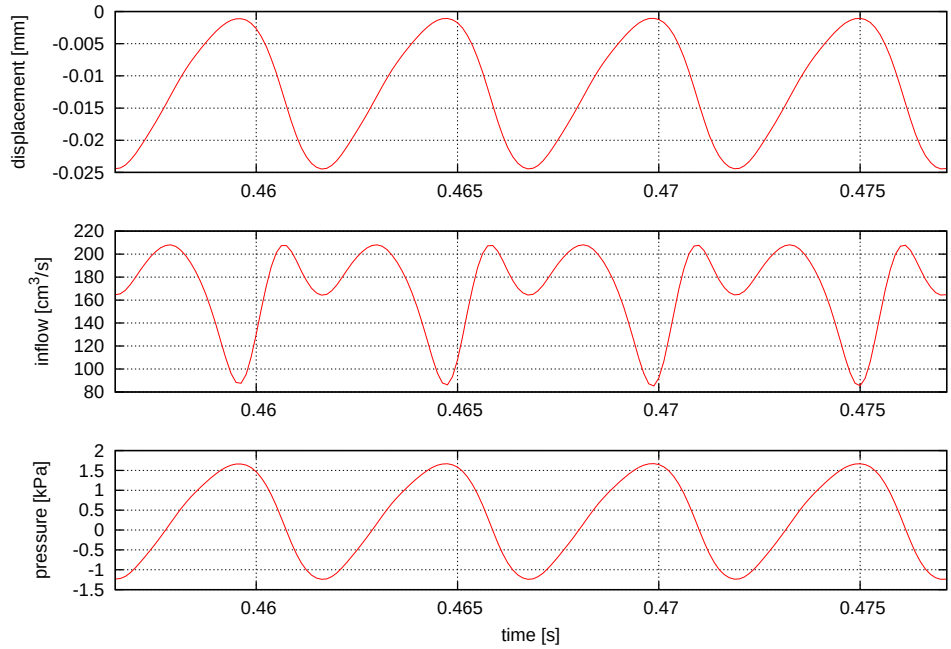

Figure 3.11: Soprano saxophone: reed displacement, inflow and pressure signal inside the embouchure during the performance of the Bb_3.

Double–reed–driven instruments

Double–reed instruments are also called *oboe–like* instruments due to its best–known member, and differ between the single–reed instruments primarily in the excitation mechanism. In fact the exciter is represented by two vibrating pieces of cane.

Several studies [4, 82] have shown that the displacements of the two reeds are symmetrical and the oscillations are synchronous. Given this assumption, the model of the single-reed dynamic (see Eq. 3.13) can be used with the foresight to duplicate the displacement of the single oscillator, with the aim of compute the time–dependent area through which the inflow transits.

Notwithstanding it seems necessary to point up that the particular geometry of the reeds cause inflow separation, hence the nonlinear characteristic would change from single–valued to multi–valued, as shown in Fig. 3.12.

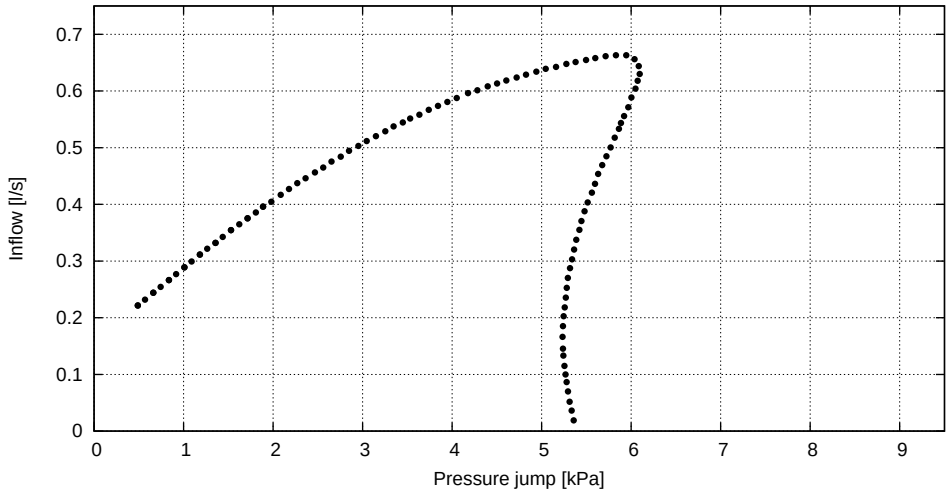

Figure 3.12: A typical nonlinear characteristic of the double–reed: inflow as a function of the pressure jump across the reed.

Air–jet–driven instruments

Air–jet–driven instruments seem to be the most ancient tunable musical instruments. *Flute–like* instruments present a wide variety of geometries and performing techniques, providing both soft and pure tones, like recorders and ocarinas, and loud and noisy sounds, like zampoñas and shakuhachis [23].

It is interesting to note that the studies concerning the physical modeling of these instruments starting with the 17th Century, following the development of the modern fluid dynamics [57, 11, 41, 66].

The sound production of flute–like instruments can be modeled as a nonlinear coupling between an air–jet and an edge, often called labium (see Fig. 3.13).

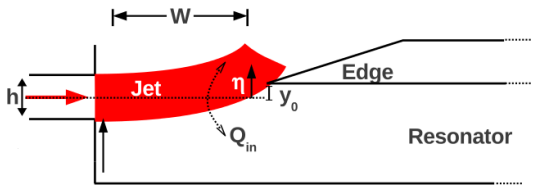

Figure 3.13: Modeling of the mechanism of sound production in flute–like instruments [80].

When the musician starts to play by applying a blowing pressure, an unstable air–jet interacting with the labium is generated. The acoustic perturbation start travelling along the resonator and is reflected by its end, thus the reflected wave goes back to the exciter location and, in turn, perturbs the jet, sustaining the self–oscillations.

The transversal deflection of the air–jet at the labium, can be expressed as follows

$$\eta(W,t) = e^{\alpha_j W}\eta_0(t-\tau) = \frac{h}{u_j}e^{\alpha_j W}v_{ac}(t-\tau) \tag{3.21}$$

being α_j the amplification parameter,[8] W the distance between the channel exit and the labium, η_0 the transversal displacement of the jet, h the height of the channel, u_j the jet central velocity, v_{ac} the oscillating amplitude of the acoustic velocity at the resonator exit and

$$\tau = \frac{W}{c_p} \tag{3.22}$$

the convection delay of the perturbation along the jet, with c_p the convection velocity of perturbations along the jet. It is worth noting that the oscillation of the jet around the labium is responsible of a flow injection inside and outside the pipe and such alternate injection can be modeled as a pressure difference Δp as follows

$$\Delta p(t) = \frac{\rho\delta_d}{S_w}\frac{dQ_{in}}{dt} \tag{3.23}$$

being ρ the air density, δ_d the effective distance between the inflow sources, S_w the area bounded by the channel exit and the labium and Q_{in} the inflow injected in the pipe [81]. The term Q_{in} can be modeled as a function of the jet velocity profile, and the Eq. 3.23 represents the aeroacoustic source that excites the resonator [80].

3.2.2 Brasses

Brasses [8] produce sounds by sympathetic vibration of the air column in the resonator. A lip–energized noise [62] is projected towards the outside of a tube, and is amplified by a bell. The earliest use of trumpet–like instruments seems to date about in the fourth millennium B.C. Mesopotamia, although no instruments have been excavated from archaeological sites, and then only illustrations suggest their

[8]The empirical expression $\alpha_j = 0.4/h$ seems to be suitable [24].

existence. Actually the conscious and extensive, documented by artefacts and paintings, use of brasses came from Egypt during the Egyptian Empire (c. 1550 B.C. - c. 1077 B.C.), when the first trumpet was discovered.

Figure 3.14: Paintings of trumpet–like instruments in the egyptian figurative art.

Modern brasses can be categorized into four classes:

1. Natural brasses: only produce sounds in the instrument's harmonic series. This category include older variants of the trumpet and horn, that were natural brass instrument until about 18th century.

2. Valved brasses: these instruments use a set of valves (piston–valves or rotary–valves) operated by the player's fingers that introduce additional tubing into the instrument, changing its overall length. Such valves allow the players use a single instrument in more than one key. This family includes all of the modern brass instruments (trumpet, french horn, euphonium, tuba, cornet, flugelhorn, tenor horn, baritone horn, sousaphone, mellophone, and the saxhorn) except the trombone.

3. Slide brasses: such instruments use a slide to change the tubing's length, and the main instruments are the trombone family. Occasionally, valve trombones are used especially in jazz.

4. Keyed or Fingered brasses: include the cornet, serpent, ophicleide, keyed bugle and keyed trumpet. Use holes along the body, which are covered by fingers or keys as in the case of woodwind instrument.

Whichever is the type of brass, the player trims the tension of lips, controlling simultaneously the air flow, in order to emit sounds. Lips dynamic can be described, as done for single-reed, with the motion of a simple harmonic oscillator [32, 40, 26],

but unlike what was seen for single reed instruments, the back wavefront arise from the bell leads to close the valve while the flow due to the mouth pressure carries out its opening.

The valve displacement is now governed by the following:

$$\frac{d^2y(t)}{dt^2} + g_L\frac{dy(t)}{dt} + \omega_L^2 y(t) = \frac{P_m - p(t)}{\mu_L} \tag{3.24}$$

where g_L is the damping factor, ω_L the natural resonance frequency of the lips and μ_L is the mass ratio. It is worthy emphasize that all the coefficients of the Eq. 3.24 only depend on musicians lips contraction: the musician acts on the mechanical properties of his lips (accordingly the portion of vibrating mass of lips varies) note by note, and all playable notes are close to input impedance maxima peaks. This is the main difference with reed-driven woodwind instruments, when the player can only slightly alter elastic properties of reed by tightening the mouth around the mouthpiece.

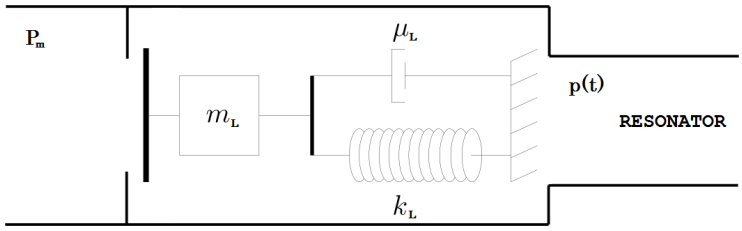

Figure 3.15: Modeling of the lip as a simple harmonic oscillator.

This time is reasonable to neglect the flow due to lips movement, so only the *Bernoullian* one, due to pressure jump between mouth and mouthpiece, is considered. The auxiliary variable can be now defined as

$$\xi(t) = y(t) - \frac{P_m}{\mu_L\omega^2} \tag{3.25}$$

Setting $\dot{y}(t) = v(t)$, one can obtain

$$\begin{pmatrix}\dot{\xi}(t)\\ \dot{v}(t)\end{pmatrix} = \begin{bmatrix}0 & 1\\ -\omega_L^2 & -g_L\end{bmatrix}\begin{pmatrix}\xi(t)\\ v(t)\end{pmatrix} + \begin{pmatrix}0\\ -\frac{1}{\mu_L}\end{pmatrix}p(t) \tag{3.26}$$

with

$$y(t) = 0, \quad \text{if} \quad y(t) \leq 0 \tag{3.27}$$

Knowing $\xi[n]$ for each time step, the displacement $y[n]$ is given by the Eq. 3.25 and the lips opening area can be evaluated by assuming an arbitrary shape.[9]

[9]Typically is used a rectangle whose height is the displacement $y[n]$.

Example Considering now, as a test case, a *B-flat* trumpet with a standard modern mouthpiece, playing the F_4 on first position.[10] The geometric model is presented in Fig. 3.16.

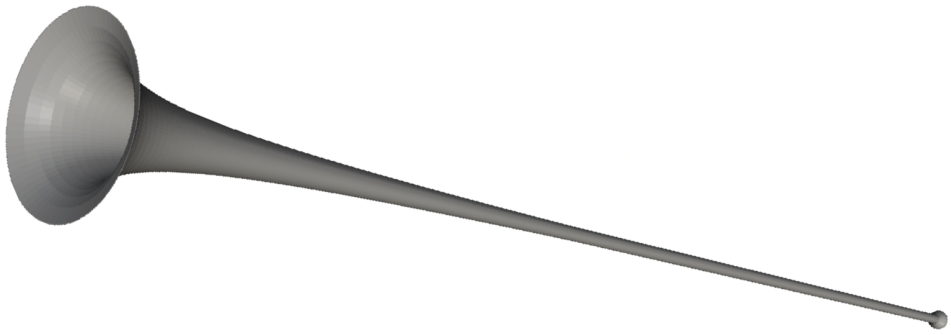

Figure 3.16: Geometric model of the B$\flat$ piston trumpet related to the first position.

The input impedance spectrum of first position is shown in Fig. 3.17 and it is easy to see that the *F4* arises the third impedance peak.[11]

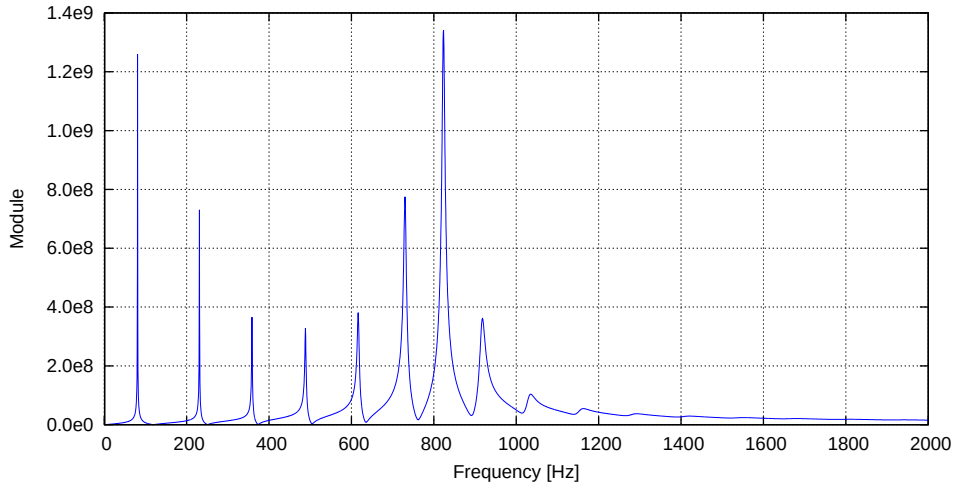

Figure 3.17: Input impedance spectrum of a B$\flat$ piston trumpet.

As well as done before, the inverse Fourier transform of the reflection coefficient (see Eq. 3.7) provide the reflection function, in Fig. 3.18.

[10]First position refers to all key opened.

[11]The analysis of the input impedance spectrum highlights that the trumpet is slightly out of tune, but for the purposes intended at the moment the fine tuning of the instrument is not required. For details concerning the *tuning* of the brass geometry see the Chap. 4 (see Sect. 4.1.2).

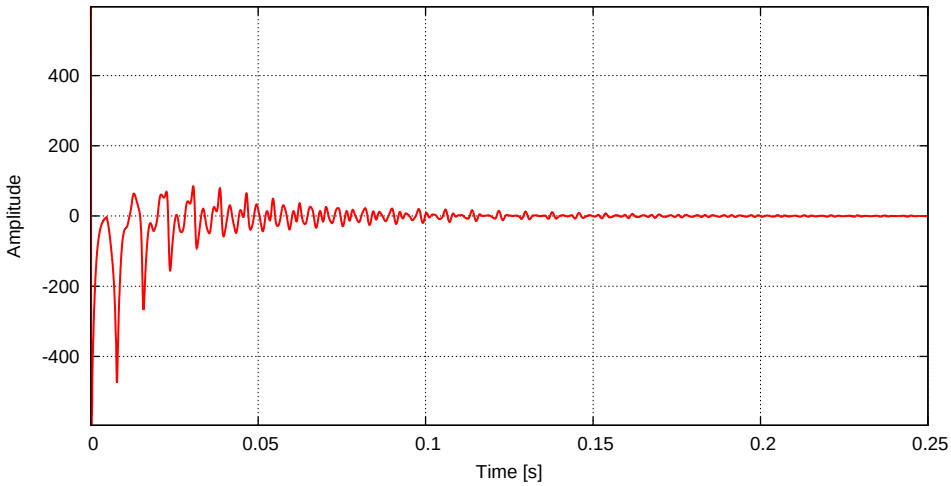

Figure 3.18: Reflection function of a B$\flat$ piston trumpet.

The reflection function is used for the solution of the system represented by the Eq. 3.12, which provides the state variables (lip displacement, inflow and pressure signal) inside the embouchure (see Fig. 3.19).

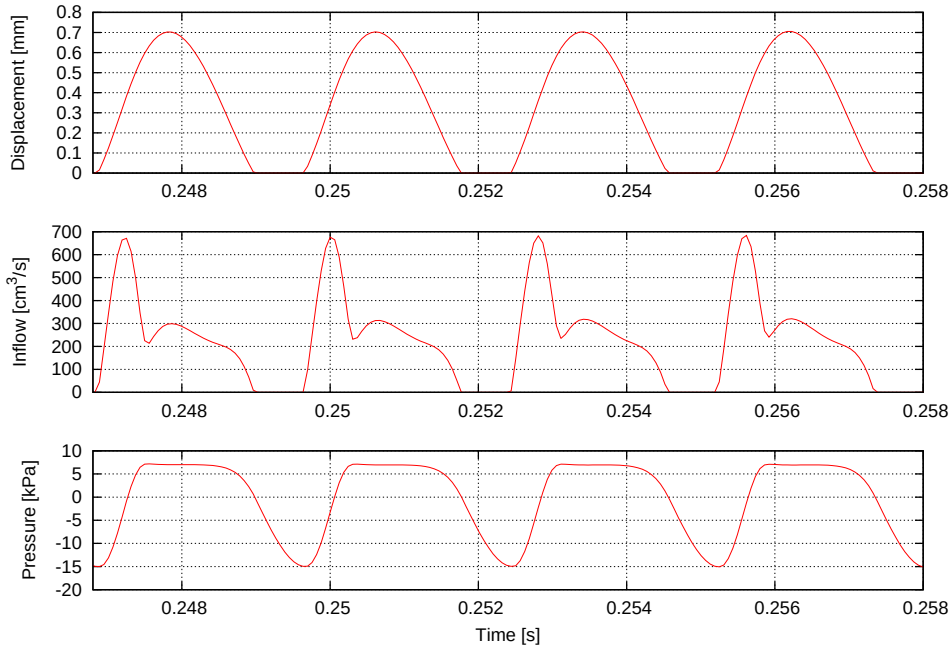

Figure 3.19: B$\flat$ piston trumpet: lips displacement, inflow and pressure signal inside the embouchure during the execution of the F_4.

3.3 The radiation of the signal

As detailed in the Chap. 2 (see Sect. 2.3), the frequency dependent transfer functions related to the sound propagation can be easily obtained with the integral formulation, solving the acoustic fields inside and outside the resonator. Such transfer functions enshrine the connection between the boundary condition $\tilde{\chi}_{in}$ at the inlet section of the resonator the propagated pressure signals $\tilde{p}(y^{ext}, s)$.

In the operating conditions, *i.e.* during the performance of a note, in the frequency–domain one have

$$\tilde{\chi}_{in} \equiv \tilde{u}_{in} \tag{3.28}$$

thus, the propagation of the signal in the time–domain is simply provided by the convolution integral between the inlow $u_{in}(t)$ and the inverse Fourier transform of the *Embouchure–to–Microphone* transfer function $\mathbf{E_2M}$ or of the *Embouchure–to–Listener* transfer function $\mathbf{E_2L}$.

In more detail, the signal at the virtual microphone location is given by the following expression

$$p_m(t) = u_{in}(t) * e_2m(t) \tag{3.29}$$

being $u_{in}(t)$ the inflow across the intake section and $e_2m(t)$ the inverse Fourier transform of $\mathbf{E_2M}$

$$e_2m(t) = \mathcal{F}^{-1}\left[\mathbf{E_2M}(\omega)\right] \tag{3.30}$$

Similarly the pressure signal at the listener's ears is provided by

$$\mathbf{p}_l(t) = u_{in}(t) * \mathbf{e_2l}(t) \tag{3.31}$$

denoting with the superscripts "R" and "L" respectively the right–channel and the left–channel, being the vector $\mathbf{p}_l(t)$ the stereophonic auralized pressure signal at the listener's ears

$$\mathbf{p}_l(t) = \begin{pmatrix} p_l^R(t) \\ p_l^L(t) \end{pmatrix} \tag{3.32}$$

with $u_{in}(t)$, as the first, the inflow across the inlet section of the resonator. The inverse Fourier transform of $\mathbf{E_2L}$ in this case consists in two components

$$\mathbf{e_2l}(t) = \mathcal{F}^{-1}\begin{pmatrix} \mathbf{E_2L}^R(\omega) \\ \mathbf{E_2L}^L(\omega) \end{pmatrix} \tag{3.33}$$

With reference to the Fig. 3.1 it is easy to understand that the inflow $u_{in}(t)$ must be computed by solving the acousto–elastic coupling between the exciter and the resonator.

Example Let consider the example of the Sect 2.3, *i.e.* the Bessel horn with a bottleneck close to the inlet section. Considering, as a test case, a prescribed inflow $u_{in}(t)$ at the inlet surface of the resonator, *e.g.* a translated triangle wave of the type

$$u_{in}(t) = \frac{G}{2}\left[1 + \frac{2}{a}\left(t - a\left\lfloor\frac{t}{a} + \frac{1}{2}\right\rfloor\right)(-1)^{\left\lfloor\frac{t}{a}+\frac{1}{2}\right\rfloor}\right] \tag{3.34}$$

being $a = T^*/2$ the half–period of the wave and G a simple gain. As the frequency of the wave let impose $f^* = 328.6$ Hz, an intermediate frequency between the first maximum and the first minimum of the input impedance spectrum (see Tabs. 2.4 and 2.5).[12] The triangle signal used as prescribed inflow $u_{in}(t)$ at the inlet surface of the resonator is presented in Fig. 3.20.

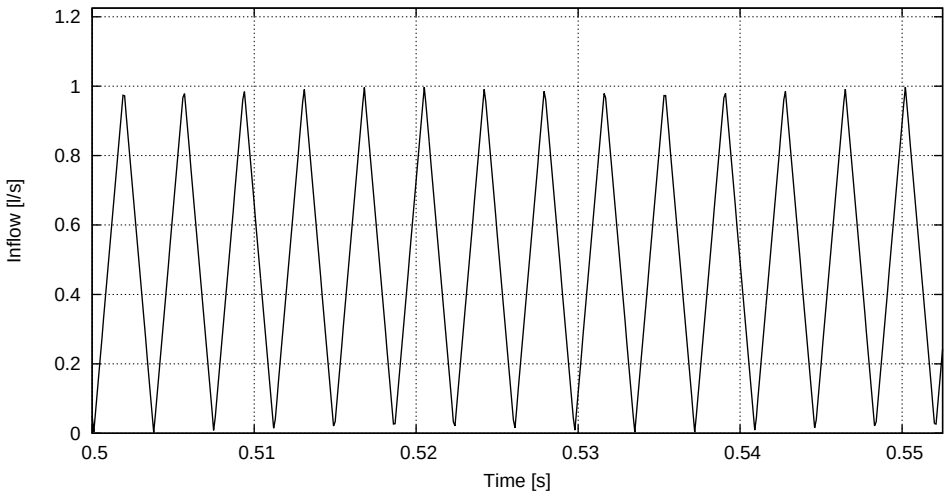

Figure 3.20: Translated triangle wave, used as prescribed inflow $u_{in}(t)$ at the inlet surface of the resonator.

In the following, the signal of Fig. 3.20 will be radiated outside the instrument using the integral representation of the acoustic field (for details see Sect. 2.3). The time–varying pressure signal is evaluated for a virtual microphone located at distance $r = 2$ m with respect to the outlet section, with an offset $\alpha = 30°$ with respect to its longitudinal axis (see Fig. 2.23). The auralized signal is related to a simple model of head located on the instrument axis at distance $d = 3$ m with respect to the outlet section of the resonator (see Fig. 2.24).

The inverse Fourier transform of $\mathbf{E_2M}$ related to the virtual microphone is presented in Fig. 3.21

[12] The choice to use an intermediate frequency between the first maximum and the first minimum of the input impedance spectrum, is in the attempt to generalize the filtering behaviour of transfer functions $\mathbf{E_2M}$ and $\mathbf{E_2L}$, without falling into a specific type of coupling between the exciter and the resonator (see Sect. 2.1).

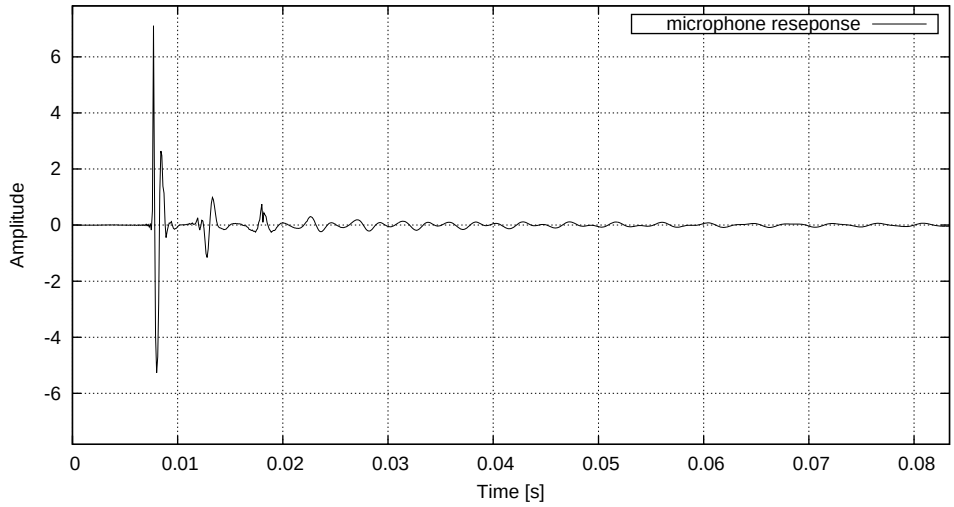

Figure 3.21: Microphone response related to a virtual microphone located at distance $r = 2$ m from the outlet section of the resonator, with an offset $\alpha = 30^\circ$ with respect to its longitudinal axis.

The time shift of the microphone response is related to the distance of the microphone from the inlet section of the resonator. The Eq. 3.29 gives rise to the time–dependent pressure signal at the virtual microphone location, in Figs. 3.22 and 3.23.

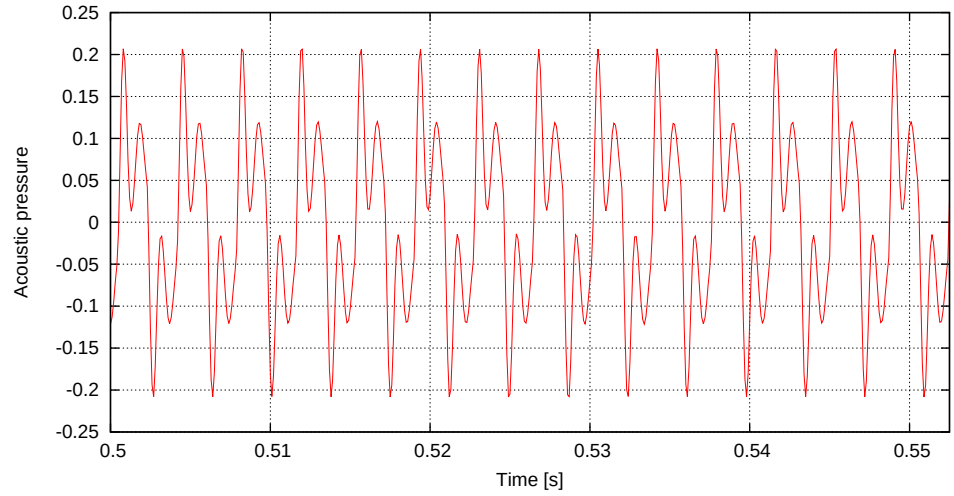

Figure 3.22: Pressure signal at the virtual microphone located at distance $r = 2$ m from the outlet section of the resonator, with an offset $\alpha = 30^\circ$ with respect to its longitudinal axis, evaluated using a prescribed triangle wave as the inflow $u_{in}(t)$ at the inlet surface of the resonator.

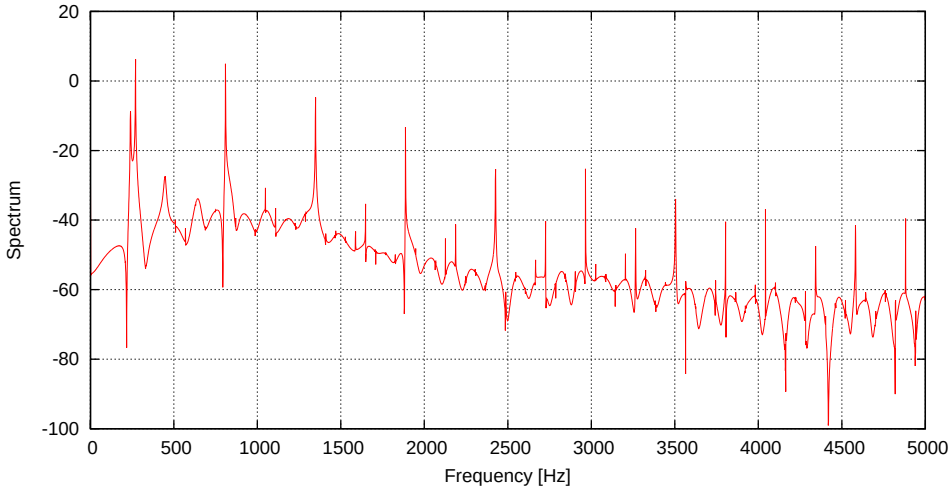

Figure 3.23: Pressure spectrum at the virtual microphone located at distance $r = 2$ m from the outlet section of the resonator, with an offset $\alpha = 30°$ with respect to its longitudinal axis, evaluated using a prescribed triangle wave as the inflow $u_{in}(t)$ at the inlet surface of the resonator.

Let now consider the inverse Fourier transform of the transfer function $\mathbf{E_2L}$, related to two antipodal location of a head model located on the instrument axis at distance $d = 3$ m with respect to the outlet section of the resonator (see Fig. 3.24).

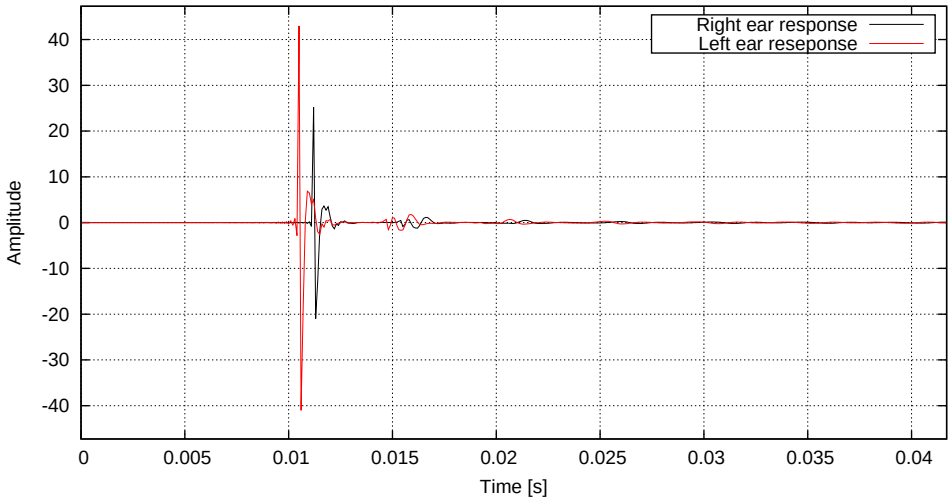

Figure 3.24: Response at the listener's ears, related to a simple model of head located on the instrument axis at distance $d = 3$ m with respect to the outlet section of the resonator.

The time shift between the right ear and the left ear response is related to the time required by the wave to sail around the head, and is responsible of the

stereophonic perception of the sounds.[13] The Eq. 3.31 lead to the stereophonic auralized signal of Figs. 3.25 and 3.26.

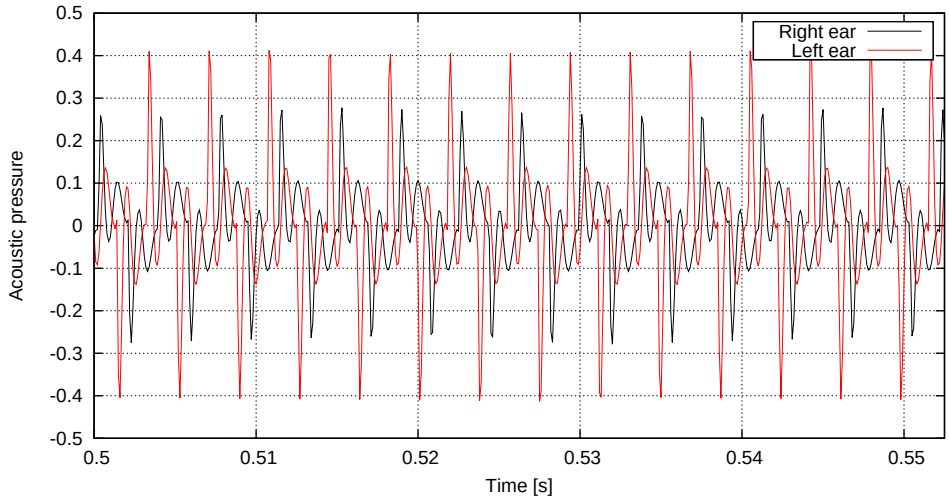

Figure 3.25: Pressure signal at the listener location, related to a simple model of head located on the instrument axis at distance $d = 3$ m with respect to the outlet section of the resonator.

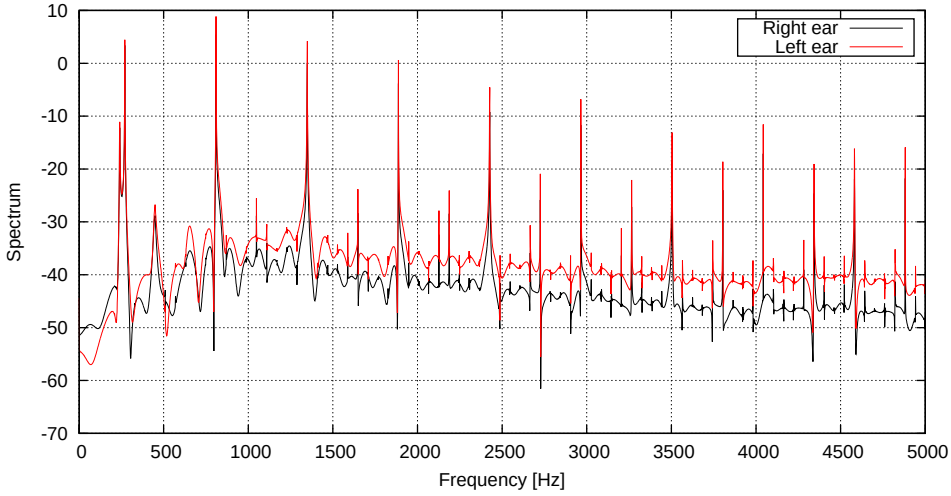

Figure 3.26: Pressure spectrum at the listener location, related to a simple model of head located on the instrument axis at distance $d = 3$ m with respect to the outlet section of the resonator.

[13] Indeed the perception of the provenance of an acoustic source derives by the cerebral interpretation of the phases shift.

Part III

Time–domain simulations of brasses

CHAPTER 4

From the geometric model to the auralized sounds

A complete time–domain simulations of a brass instruments will shown in this chapter. To be noted, as previously mentioned, that the presence or not of the piston does not affect the interaction between the air column inside the resonator and the dynamics of the vibrating lip, hence will be presented the complete simulation of a valveless brass, the natural E$\flat$ trumpet, starting from the identification of the characteristics of the resonator up to the auralization of the pressure signal, using the methodologies previously described in the Chaps. 2 and 3. The technique used in order to obtain the offline real–time utilization of the physical model is also detailed.

4.1 The natural E$\flat$ trumpet

The natural trumpet is one of the most ancient musical instrument. The earliest evidence of its use dates back to the Middle Ages. It reached the widest diffusion in Western music during the Baroque era when important composers like Antonio Vivaldi, Georg Philipp Telemann, Georg Friderich Händel and Johann Sebastian Bach reserved to this instrument a key role in their compositions. For this reason the natural trumpet is commonly referred to as *baroque trumpet*. In that period the trumpet scores were almost written for C and D tuned natural trumpets[1] but eminent exceptions, as the trumpet parts of the first version[2] of the *Magnificat* in E$\flat$ major BWV 243a, by Johann Sebastian Bach, gave glory to the natural E$\flat$ trumpet.

[1] Notice that the tuning frequency of the musical instruments in the baroque era was averagely 415 Hz, hence the compositions today would sound an helf–tone below.

[2] Composed in the 1723 and transposed in D major about ten years later.

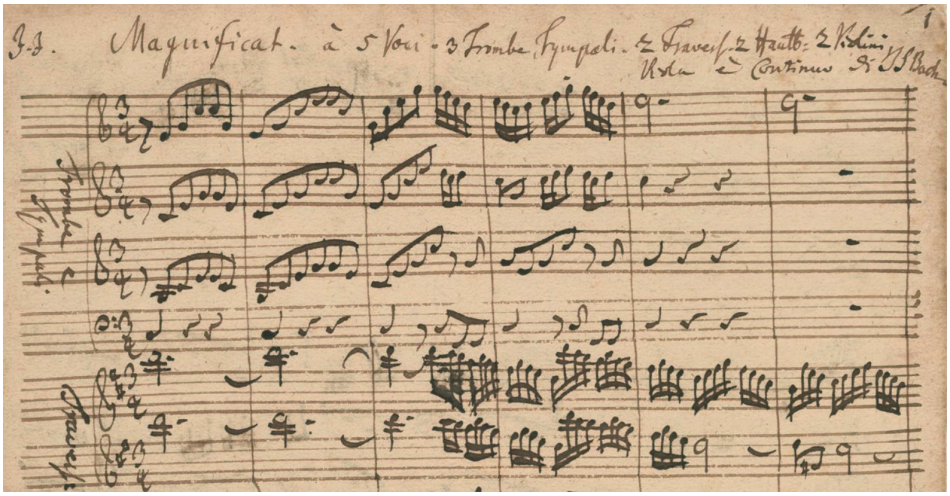

Figure 4.1: First page of the manuscript of the second version (in D major) of the *Magnificat* BWV 243: the first version BWV 243a was in E$\flat$ major. On the top lines of the score, the parts of the three trumpets.

4.1.1 The geometric model

The construction of the geometric model of the E$\flat$ natural trumpet implied an extensive literature survey [28, 65, 63, 53, 29], and the one that has been adopted for the simulations is based a baroque trumpet replica. The global size is comparable with original instruments, but it was chosen to model a modern mouthpiece and the bell has more accentuated flaring.

It is worth noting that due to the high computational cost deriving from the necessity of catch a wide frequency spectrum, a straight geometry was generated. This choice, by exploiting the axial symmetry, allows to reduce the size of the problem and, consequently, the memory that must be allocated by the computer for the simulation. On the other hand should be specified that the natural trumpet was originally built with straight piping, and then the need to keep long instruments compact imposed the bending of portions of the pipe. The influence of the curvatures can be significant, and the study of such effects [31, 38, 30] have proven that the curvatures can both increase and decrease the resonances of the resonator, providing a complex inharmonicity. These effects cannot be considered negligible, since the timbrical perception is highly responsive to the inharmonicity of the sounds: notwithstanding the numerical simulation of a geometry with curvature is too onerous, and hence an axisymmetric resonator was simulated.[3]

[3]In order to understand this difference, considering that the memory requirement of a BEM implementation is related to the square of the number of elements N: for a simulation involving $N = 10^6$ elements,[4] the only storage of the matrix $\mathbf{Y}$ (see Eq. 2.16) is over 100 Gbytes, whereas the corresponding problem, symmetrized by using about a hundred slices, requires little more than 1 Gbytes.

The geometry of the instrument can be roughly divided in three parts: the mouthpiece, the cylindrical pipe and the bell.

The mouthpiece (see Fig. 4.2), whose total length approximately arises 10 centimetres, has a profile generated by imposing the cup diameter and depth, the throat diameter and both the backbore length and slope. It was noticed that that the external profile doesn't affect the acoustical behaviour of the resonator, thus a generic contour has been chosen.

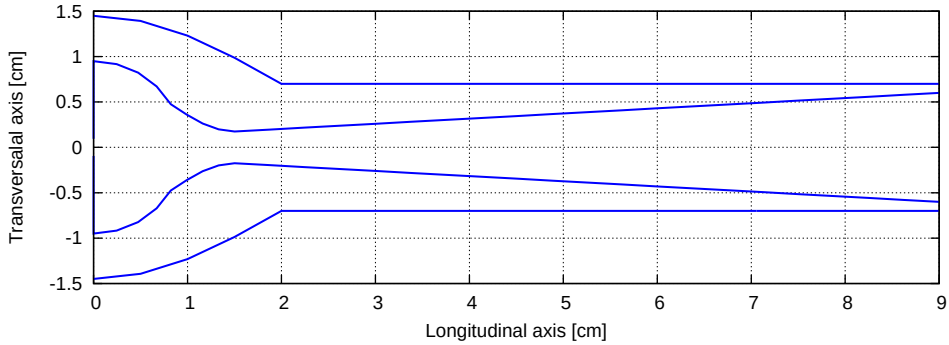

Figure 4.2: Geometric model of the mouthpiece of the E$\flat$ natural trumpet.

The bell, whose profile is shown in Fig. 4.3, consisting in a Bessel horn, with a flaring constant of $\gamma = 0.57$ and a throat–base ratio $TBR = 11.8$: its total length is about 65 centimetres.

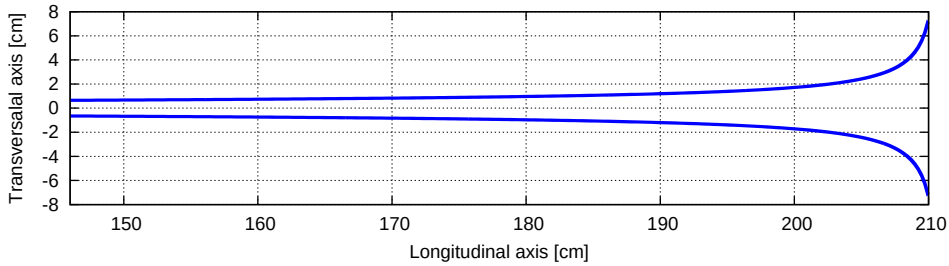

Figure 4.3: Geometric model of the bell of the E$\flat$ natural trumpet.

The total length of the trumpet geometric model, including the mouthpiece is just over 210 centimetres and the diameter of the cylindrical piping is about 12 millimetres. The size is fully in agreement with a real instrument.

It is worth nothing that the tuning of the natural trumpet is highly affected by both the mouthpiece type (and size) and the bell shape. Indeed the effect of the bell is such that the lower resonant frequencies are pulled upward,[5] as well as the mouthpiece forces the upper resonant frequencies downward. The aim of such

[5] And furthermore is produced the *pedal–tone*, which is the lowest, rarely performed, playable note of a brass instrument.

detuning is the achievement of the harmonic sequence of a closed pipe. An accurate selection of the geometric parameters was therefore necessary with a view to get the proper intonation.

Figure 4.4: Jan Vermeer (Delft, 1632 – Delft, December 1675), *The Allegory of Painting* (detail: girl holding a trumpet, the symbol of the glory), 1665-1668, oil on canvas, 130x110 cm, Kunsthistorisches Museum, Vienna.

4.1.2 Acoustical characterization

The BEM simulation was carried out by imposing a constant inflow χ_{in} acting at the inlet section using hard–wall boundary condition on the instrument surface, as shown in the Chap. 2, and solving the acoustic field inside and outside the instrument. The frequency response was evaluated up to 6250 Hz, which is equivalent to having a sampling frequency equal to 12.5 kHz.[6] The simulation was accomplished by introducing a simple model of the head distant $d = 3$ m from the outlet section of the instrument, and the solution was also evaluated on a quarter circle of radius $r = 2$ m of virtual microphones.

[6]The maximum frequency is a slightly higher frequency with respect to the frequency for which the wavefronts can be considered plane. This choice penalizes the quality of the solution at the upper part of the frequency spectrum but is to the benefit of the grade of the reconstructed sounds, since the time discretization Δt is inversely proportional to the sampling frequency.

Input impedance

The complex input impedance spectrum (see Figs. 4.5 and 4.6) is directly derived from the knowledge of the velocity potential function $\tilde{\varphi}$ (see Eq. 2.12).

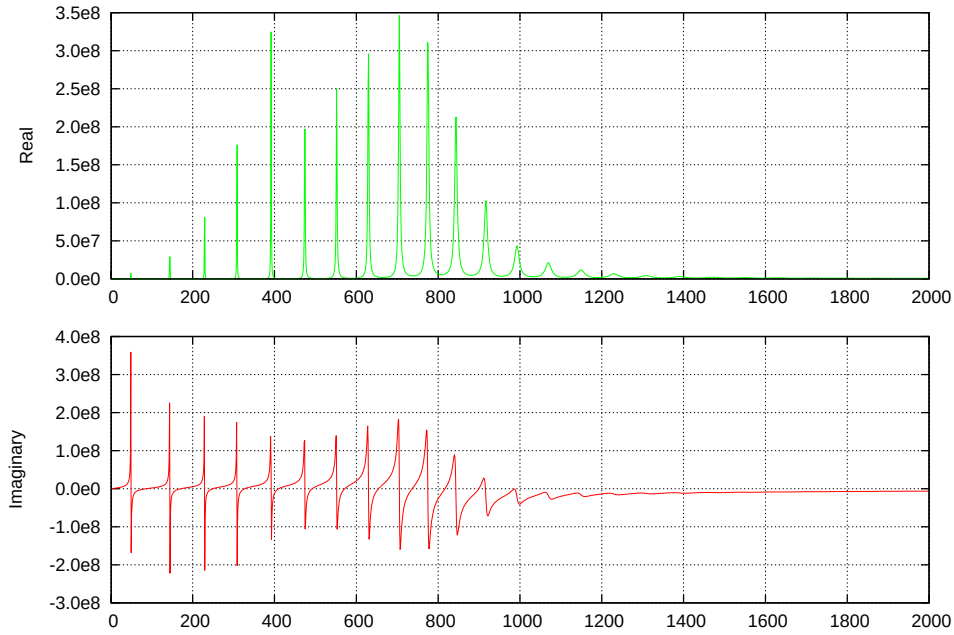

Figure 4.5: Components of the complex input impedance spectrum of the E$\flat$ natural trumpet.

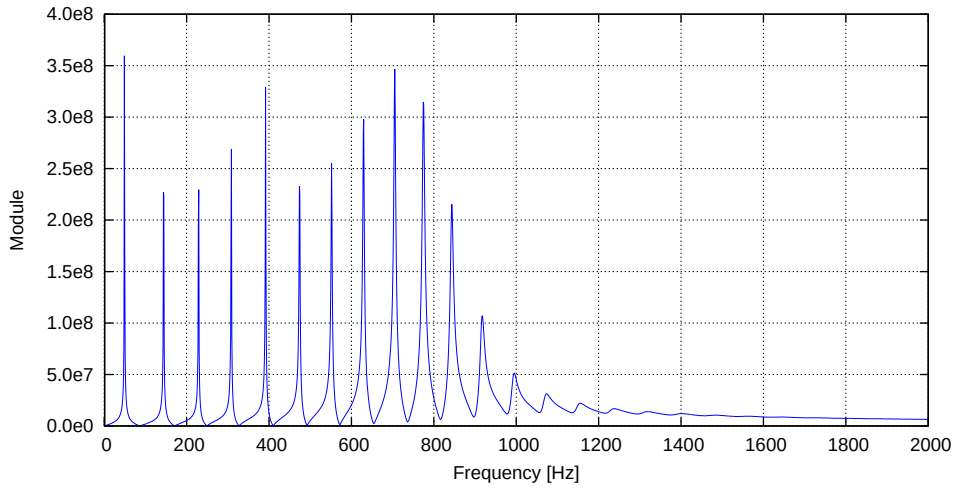

Figure 4.6: Module of the input impedance spectrum of the E$\flat$ natural trumpet.

The resonances, in proximity of which the musician can perform the notes, are

close to the Eb harmonic series.[7] Defining the deviation in cents of tone with respect to the frequencies of the notes as follows

$$\epsilon^c = 1200 \log \left(\frac{f_n^T}{f_n} \right) \tag{4.1}$$

it is possible to examine the tuning of the instrument, presented in Tab. 4.1.

	Frequency	**Note**	**Deviation**
f_I	49.49 Hz	G_1	+17 cents
f_{II}	144.05 Hz	D_3	-33 cents
f_{III}	228.97 Hz	Bb_3	-31 cents
f_{IV}	308.07 Hz	Eb_4	-17 cents
f_V	391.88 Hz	G_4	-1 cents
f_{VI}	474.17 Hz	Bb_4	+29 cents
f_{VII}	552.06 Hz	$C\#_5$	-7 cents
f_{VIII}	629.67 Hz	Eb_5	+21 cents
f_{IX}	705.19 Hz	F_5	+17 cents
f_X	774.83 Hz	G_5	-20 cents
f_{XI}	843.17 Hz	Ab_5	+26 cents
f_{XII}	915.47 Hz	Bb_5	-32 cents

Table 4.1: Resonances of the natural trumpet in Eb, with deviation from the theoretical frequencies related to the Eb harmonic series in equal temperament tuned at 440 Hz.

The deviation of the resonant frequencies from the theoretical frequency of each note of the Eb harmonic series seems to be dependant by the quality of the geometric model.[8] It is important to note that the tuning of a brass is a serious challenge and it was noticed that even in real instruments the first peak, excluding the pedal–tone, is shifted towards the half-tone immediately below.

With the purpose to obtain a suitable tuning starting from knowledge of the rough geometrical sizes of the instrument, the adopted strategy was that of vary the flaring constant of the bell and slightly change the length of the cylindrical piping. With these precautions it has been possible to readily reach a satisfactory tuning of the instrument (this can be considered *virtual lutherie*), obtaining the proper tuning without excessively altering the geometric sketch of the instrument.

To complete the acoustical characterization of the resonator, the minima of the input impedance spectrum are reported in Tab. 4.2.

[7] Is an exception the second resonance which results to be a D instead of Eb, but it is noted that is a characteristic of also detected in the real instruments.

[8] Moreover, being resonances calculated as the crossing, from positive to negative, of the imaginary part of the complex impedance spectrum (see Fig. 4.5), each resonant frequency is affected by an error of the order of the frequency step, as described in the Chap. 2.

	Frequency	Note	Deviation
f_I	86.50 Hz	F_2	-16 cents
f_{II}	171.08 Hz	F_3	-35 cents
f_{III}	249.36 Hz	B_3	+17 cents
f_{IV}	327.12 Hz	E_4	+13 cents
f_V	410.32 Hz	Ab_4	-21 cents
f_{VI}	492.18 Hz	B_4	-6 cents
f_{VII}	571.70 Hz	D_5	-47 cents
f_{VIII}	654.15 Hz	E_5	-13 cents
f_{IX}	736.44 Hz	$F\#_5$	-8 cents
f_X	816.72 Hz	Ab_5	-29 cents
f_{XI}	899.38 Hz	A_5	+38 cents

Table 4.2: Antiresonances of the natural trumpet in Eb, with deviation from the theoretical frequencies related to the nearest note in equal temperament tuned at 440 Hz.

The inverse Fourier transform of the input impedance, shown in Fig. 4.7, provides the impulse response of the resonator which, as detailed above, turns out to be not suitable for the time–domain simulation due to its decay time.

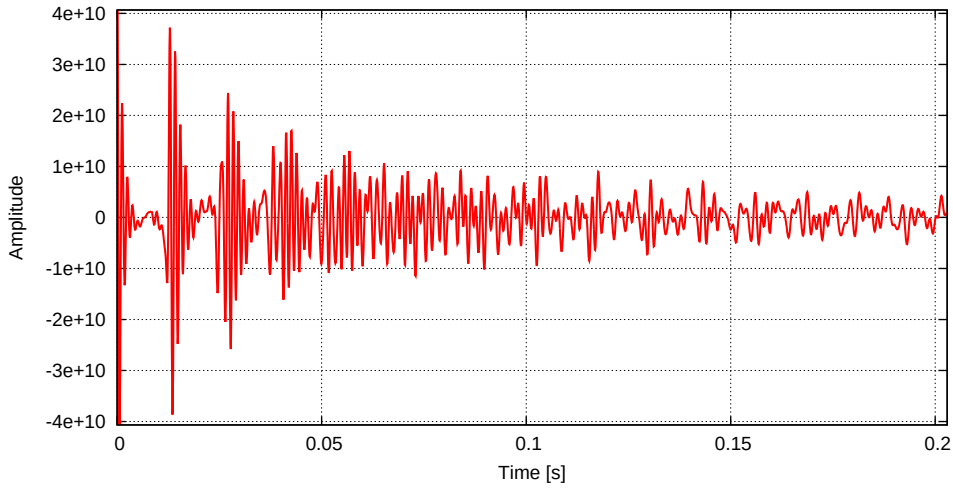

Figure 4.7: Impulse response of the Eb natural trumpet.

Reflection coefficient and reflection function

As described in the Chap. 3, the numerical simulations are based on defining the reflection coefficient (see Eq. 3.7), directly descending from the knowledge of the input impedance (see Figs. 4.8 and 4.9).

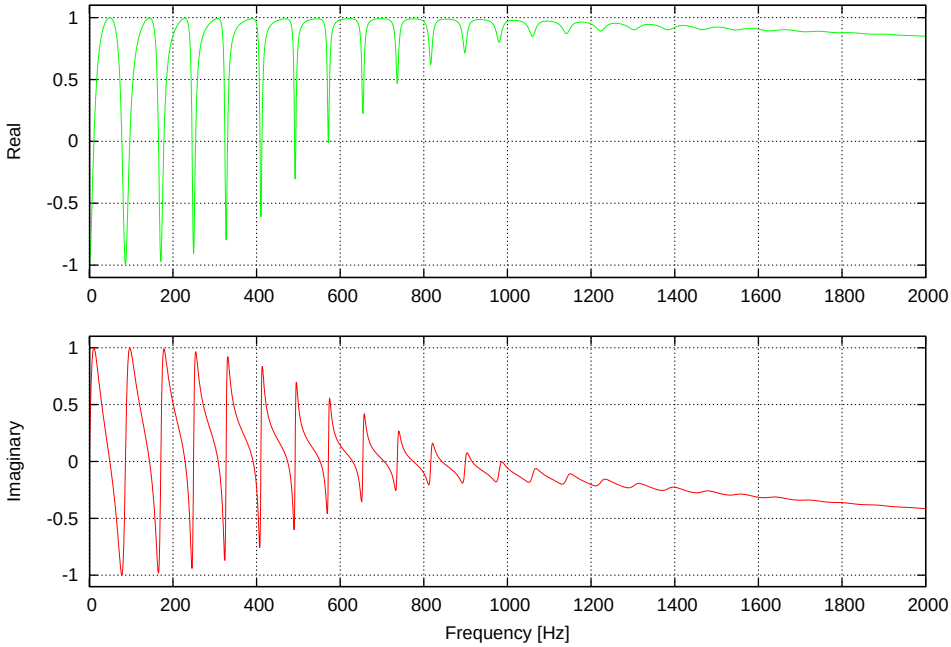

Figure 4.8: Components of the reflection coefficient of the E$\flat$ natural trumpet.

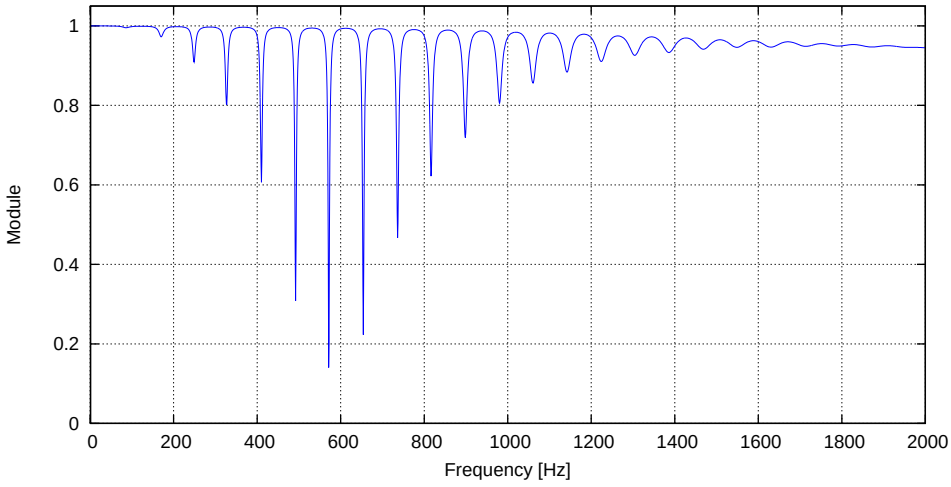

Figure 4.9: Module of the reflection coefficient of the E$\flat$ natural trumpet.

It is worth noting that the condition of passive resonator, expressed by the Eq. 3.8, is fully complied.

The reflection coefficient allows to isolate a single reflection inside the resonator, so that the decay time of its inverse Fourier transform, shown in Fig. 4.10, be shorter than the impulse response, in Fig. 4.7.

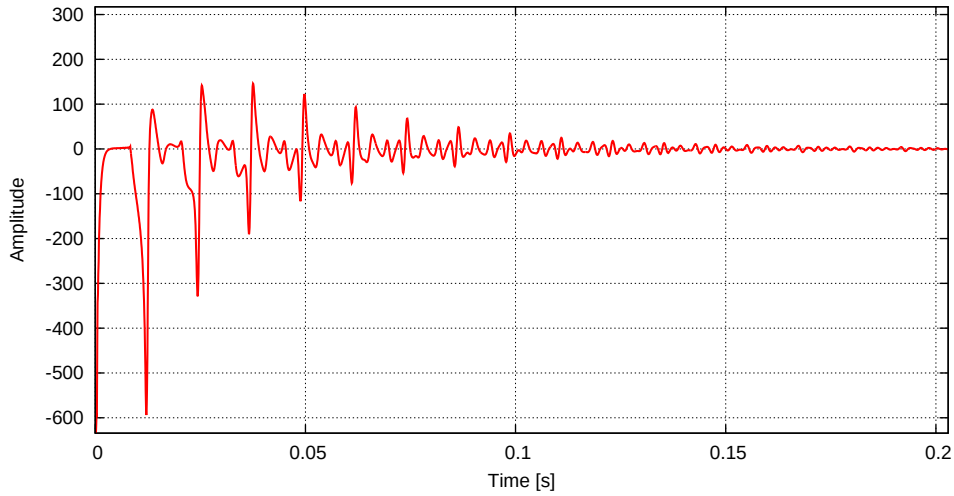

Figure 4.10: Reflection function of the E$\flat$ natural trumpet.

It seems important to emphasize that, unlike the cylindrical pipe, the decay time of the reflection function is is certainly not comparable with the fundamental period due to the complex shape of the resonator, nevertheless become such that the convolution integral has a faster convergence.

Embouchure-to-Microphone transfer function

The *Embouchure-to-Microphone* transfer function $\mathbf{E_2M}$ is achievable solving the Eq. 2.32, and its evaluation at suitable locations allows to assess the directivity pattern of both the resonances and the antiresonances (see Figs. 4.11 and 4.12).

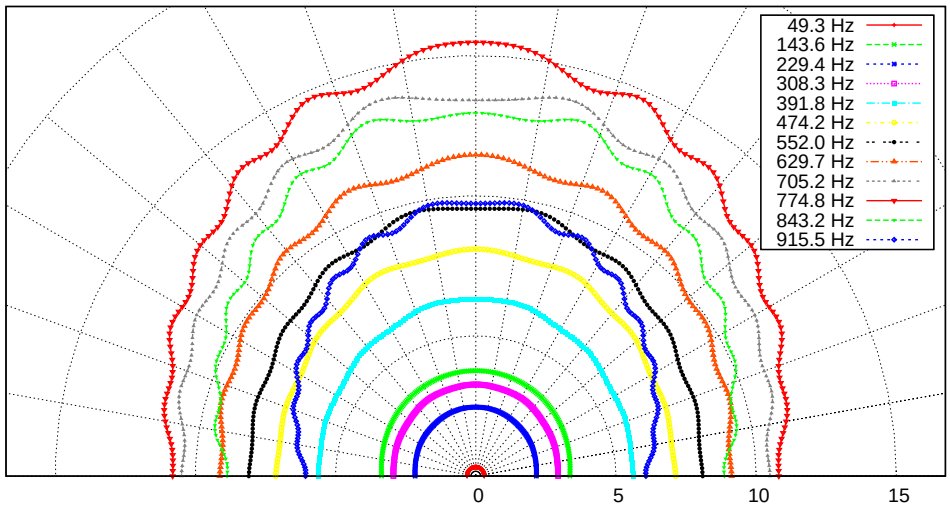

Figure 4.11: Resonances directivity patterns of the E$\flat$ natural trumpet, evaluated on an half–circle of virtual microphones located at a distance $r = 2$ m from the outlet section.

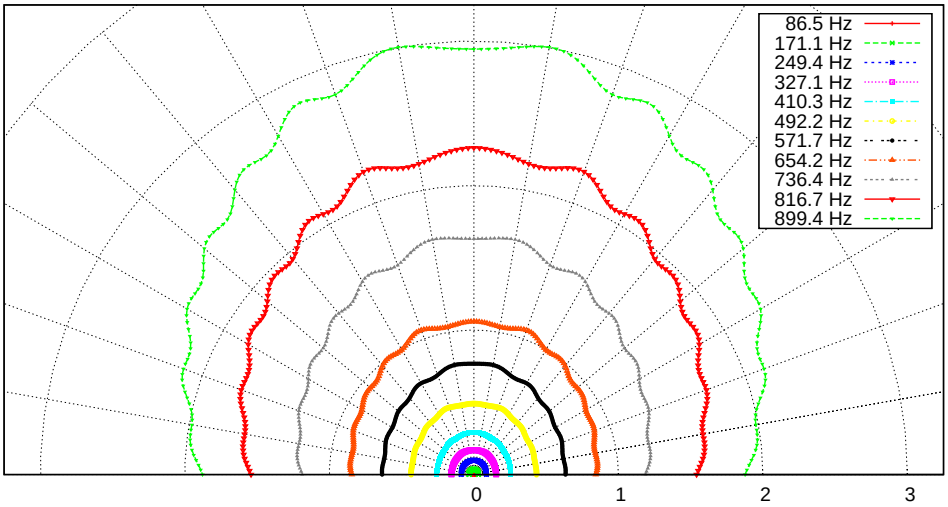

Figure 4.12: Antiresonances directivity patterns of the Eb natural trumpet, evaluated on an half–circle of virtual microphones located at a distance $r = 2$ m from the outlet section.

It is interesting to note that the behaviour of the directivity pattern at increasing frequencies related to the resonances manifests a maximum for the tenth peak, which results to be close to the first peak of the mouthpiece (see Fig. 4.13).

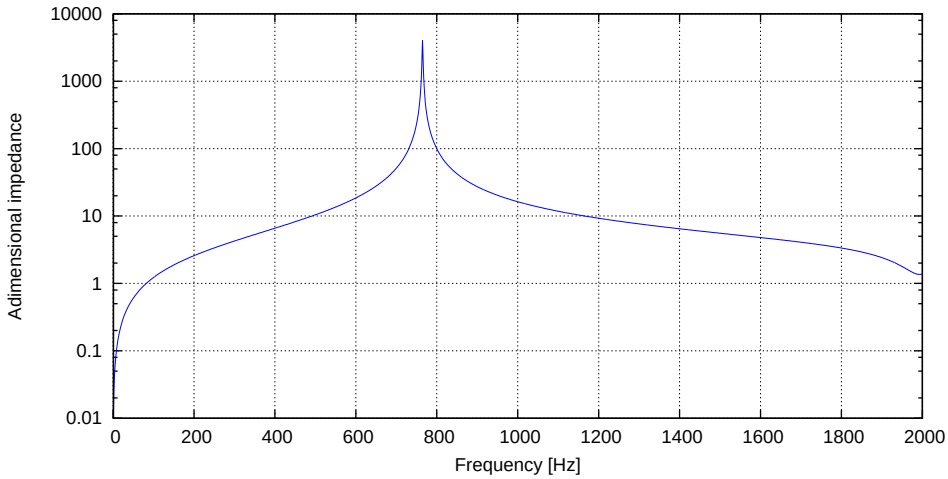

Figure 4.13: Input impedance spectrum divided by $\rho c/\mathcal{S}_{in}$ related to the mouthpiece of the Eb natural trumpet.

Let now consider a single virtual microphone located at a distance $r = 2$ m from the outlet section of the trumpet, with an offset $\alpha = 30°$ with respect to the longitudinal axis of the instrument, as shown in Fig. 4.14.

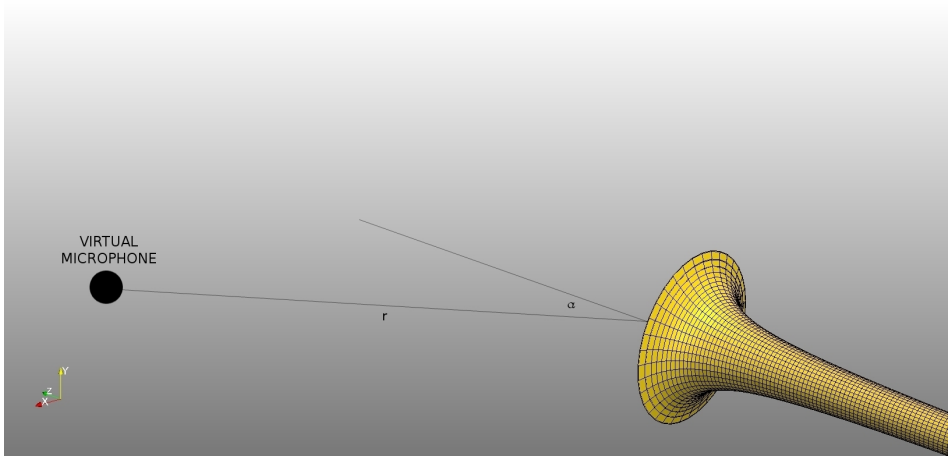

Figure 4.14: Position of the virtual microphone located at a distance $r = 2$ m from the outlet section of the trumpet, with an offset $\alpha = 30°$ with respect to the longitudinal axis of the E$\flat$ natural trumpet.

Since the problem is axisymmetric, the virtual microphone is representative of the entire circumference of radius $r\sin(\alpha)$, distant $r\cos(\alpha)$ from the outlet section of the trumpet. In this location the *Embouchure-to-Microphone* transfer function $\mathbf{E_2M}$ takes the shape of Fig. 4.15.

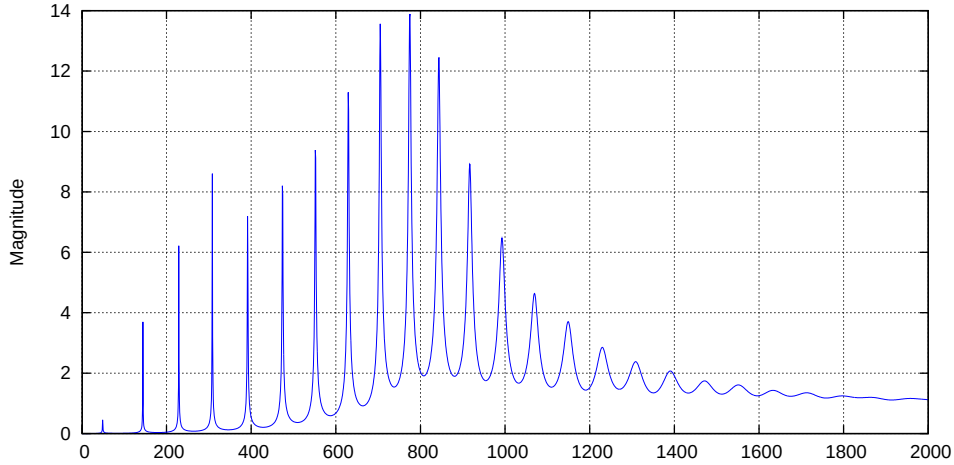

Figure 4.15: Magnitude of the *Embouchure-to-Microphone* transfer function divided by $1/\mathcal{S}_{in}$ related to a virtual microphone located at a distance $r = 2$ m from the outlet section of the trumpet, with an offset $\alpha = 30°$ with respect to the longitudinal axis of the E$\flat$ natural trumpet.

The Bode diagram of the *Embouchure-to-Microphone* transfer function $\mathbf{E_2M}$ is presented in Fig. 4.16.

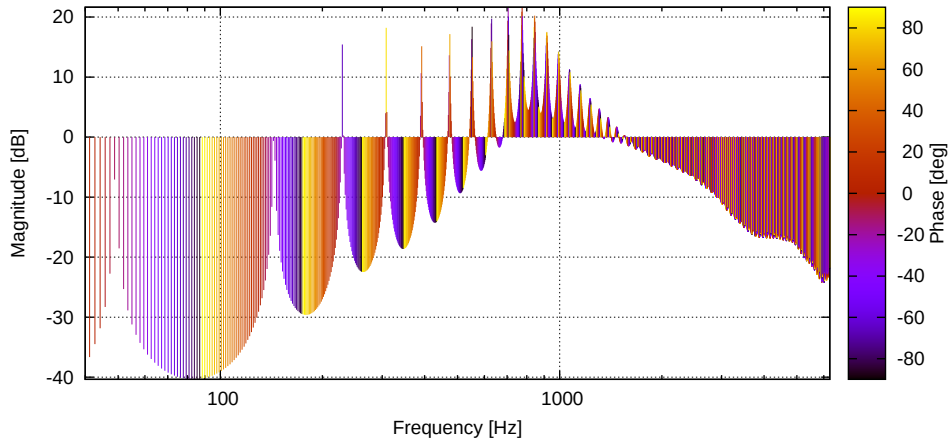

Figure 4.16: Bode diagram of the *Embouchure-to-Microphone* transfer function divided by $1/\mathcal{S}_{in}$ related to a virtual microphone located at a distance $r = 2.0$ m from the outlet section of the trumpet, with an offset $\alpha = 30^\circ$ with respect to the longitudinal axis of the Eb natural trumpet.

The pressure signal at the microphone location is given by the convolution between $e_2m(t)$, the inverse Fourier transform of $\mathbf{E_2M}$, and the inflow $u_{in}(t)$ (see Eq. 3.12): such inverse Fourier transform $e_2m(t)$, in Fig. 4.17, represents the impulse perceived at the virtual microphone.

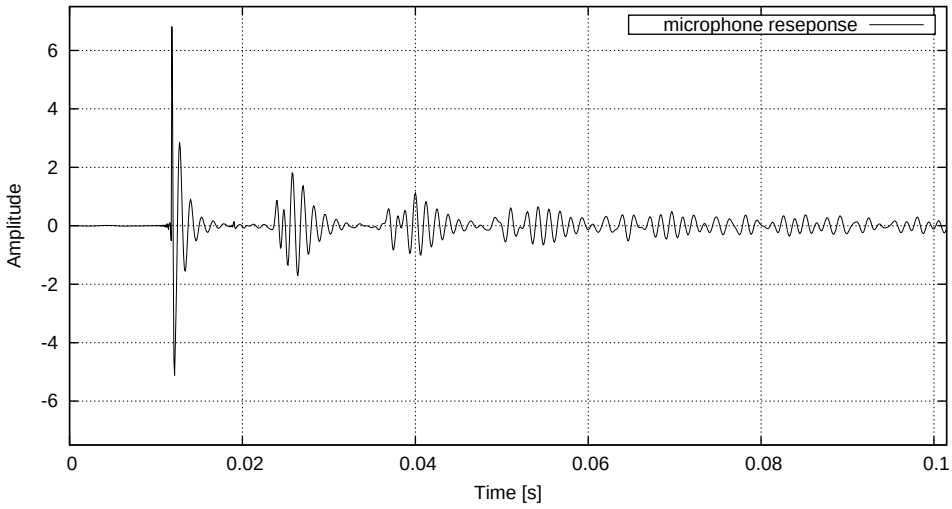

Figure 4.17: Microphone response related to a virtual microphone located at a distance $r = 2.0$ m from the outlet section of the trumpet, with an offset $\alpha = 30^\circ$ with respect to the longitudinal axis of the Eb natural trumpet.

Obviously such impulse response is shifted in the time–domain of the distance between the input section and the microphone multiplied by the sound velocity.

Embouchure-to-Listener transfer function

Considering a simple model of the head[9] located at distance $d = 3$ m from the outlet section of the instrument. The transfer function is evaluated, as illustrated in Fig. 4.18, at two antipodal location of the head.

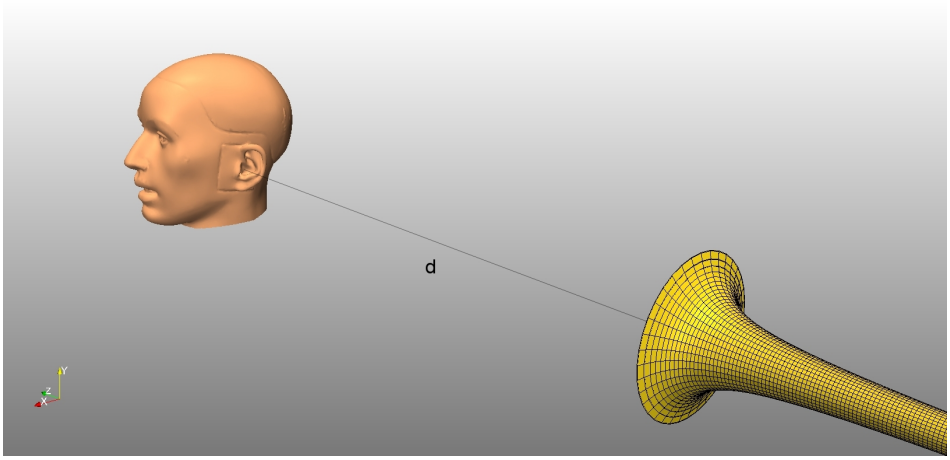

Figure 4.18: Position of the head with respect to the outlet section of the Eb natural trumpet.

The auralization of the sound, as described above (Eq. 2.46), is based on the knowledge of the *Embouchure-to-Listener* $\mathbf{E_2L}$ transfer function (see Fig. 4.19).

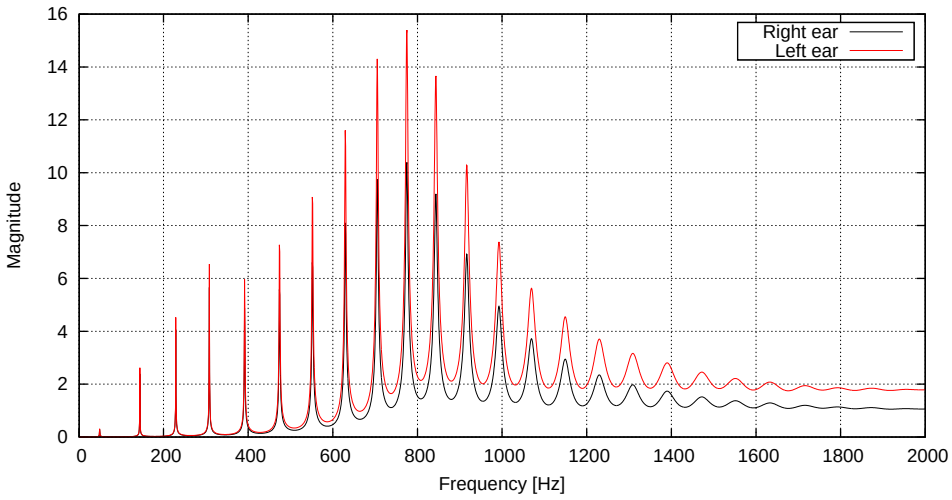

Figure 4.19: Magnitude of the *Embouchure-to-Listener* transfer function divided by $1/\mathcal{S}_{in}$ for the Eb natural trumpet related to a simplified model of head.

The Bode plot of the *Embouchure-to-Listener* transfer function $\mathbf{E_2L}$ is presented

[9] In the simulation the head is assumed to be a simple sphere of radius $r_{sph} = 8.75$ cm.

below, in Fig. 4.20.

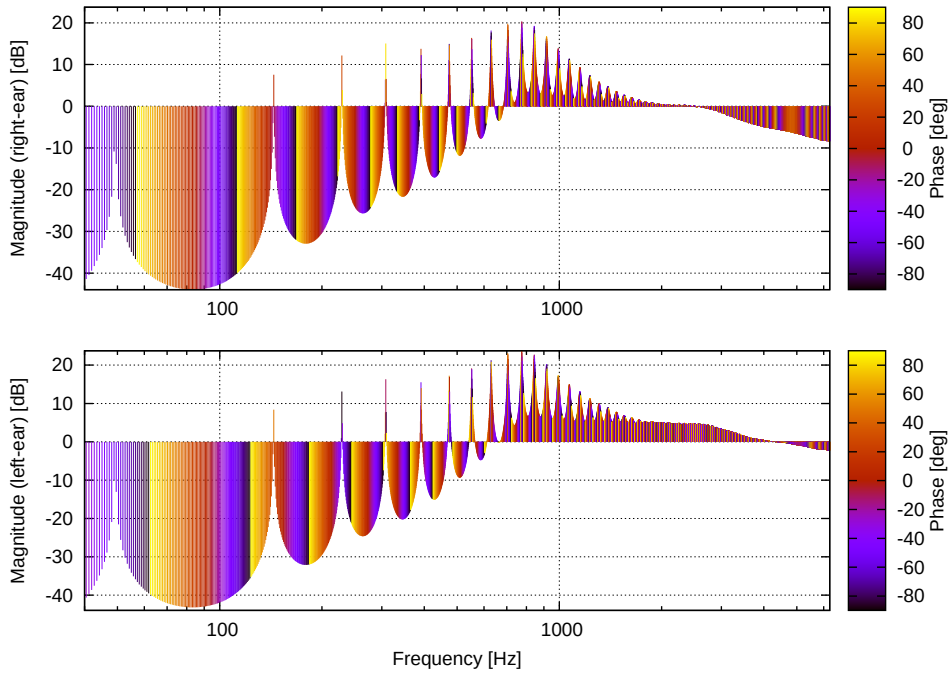

Figure 4.20: Bode diagram of the *Embouchure-to-Listener* transfer function divided by $1/\mathcal{S}_{in}$ for the E$\flat$ natural trumpet related to a simplified model of head.

The function $\mathbf{e_2l}(t)$, in Fig. 4.21, represents the impulse perceived by the listener

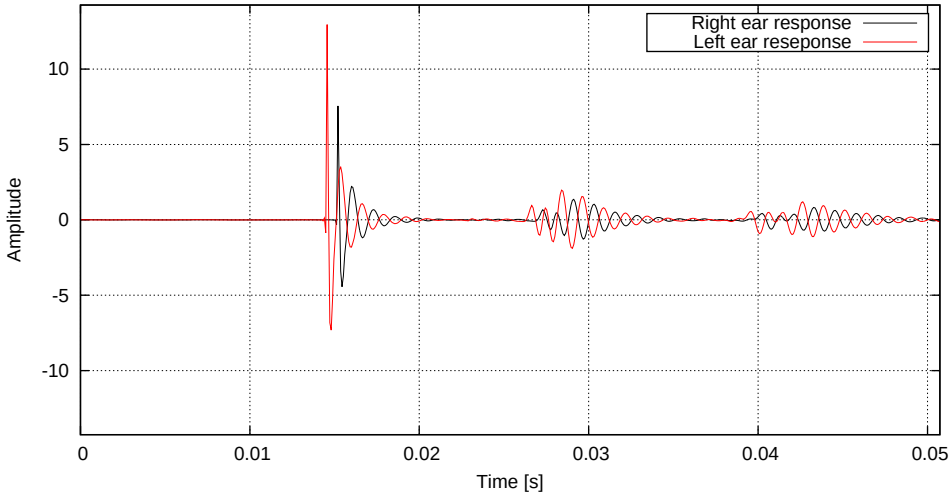

Figure 4.21: Response at the listener's ears, related to a simple model of head located on the instrument axis at distance $d = 3$ m with respect to the outlet section of the E$\flat$ natural trumpet.

In fact, as in the case of the virtual microphone, the pressure signal at the listener ears is given by the convolution between $e_2 l(t)$, the inverse Fourier transform of $\mathbf{E_2 L}$, and the inflow $u_{in}(t)$ (see Eq. 3.12). Even this time the impulse response is shifted in the time–domain of the distance between the input section and each ear multiplied by the sound velocity, consequently the peak–to–peak distance between the right–channel and the left–channel of Fig.4.21 multiplied by the sound velocity provides the spatial distance between the ears of the listener.

4.2 The system solution

4.2.1 Signals inside the embouchure

The step integration of the Eq. 3.26 provides simultaneously the displacement, the inflow and the pressure signal inside the embouchure, at the inlet section of the instrument. By a suitable choosing of the parameters of the Eq. 3.24, the virtual trumpet it is able to play several notes, all close to the resonant peaks of the input impedance spectrum (see Tab. 4.1).

The one degree of freedom model of the valve is characterized by the frequency response in Fig. 4.22.

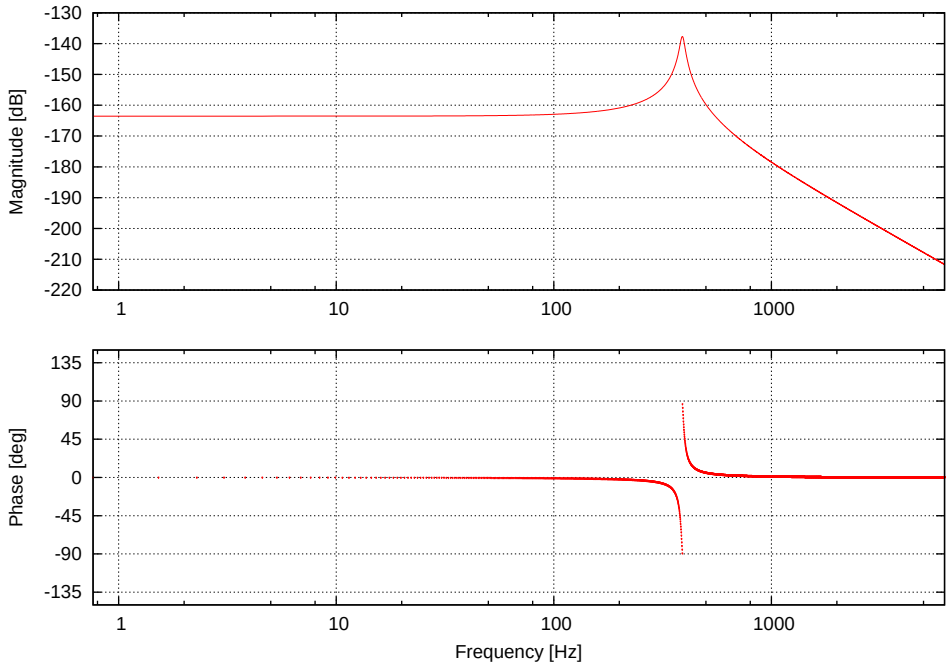

Figure 4.22: Bode diagram for the one degree of freedom model of the valve during the performance of the G_4 with the E$\flat$ natural trumpet.

The inverse Fourier transform of the valve frequency response, in Fig. 4.23,

provides the impulse response of the mechanical system.

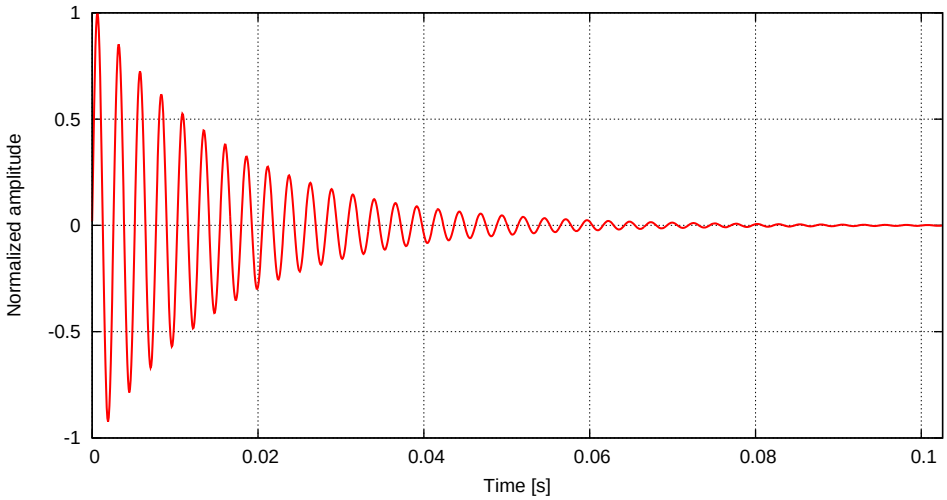

Figure 4.23: Normalized impulse response of the one degree of freedom model of the valve during the performance of the G_4 with the Eb natural trumpet.

The state variables inside the embouchure related to the performance of the G_4, 395.6 Hz pitched, are presented in Fig. 4.24.

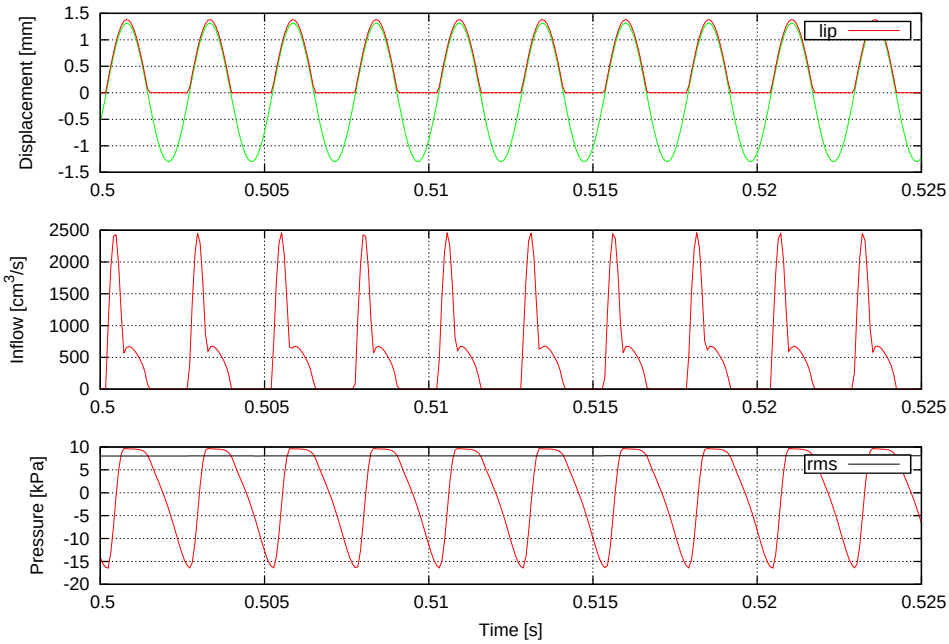

Figure 4.24: Lip displacement, inflow and pressure signal inside the embouchure during the performance of the G_4, 395.6 Hz pitched, with the Eb natural trumpet.

It is worth noting that the state variables, *i.e.* the lip's displacement $y(t)$, the inflow $u(t)$ and the pressure $p(t)$ exhibit behaviour fully consistent with what is available in literature [2, 50].

The analysis of the phases portrait (see Fig. 4.25) highlights the limit–cycle rotating clockwise around the center of the phases,[10] proving the stability of the solution.

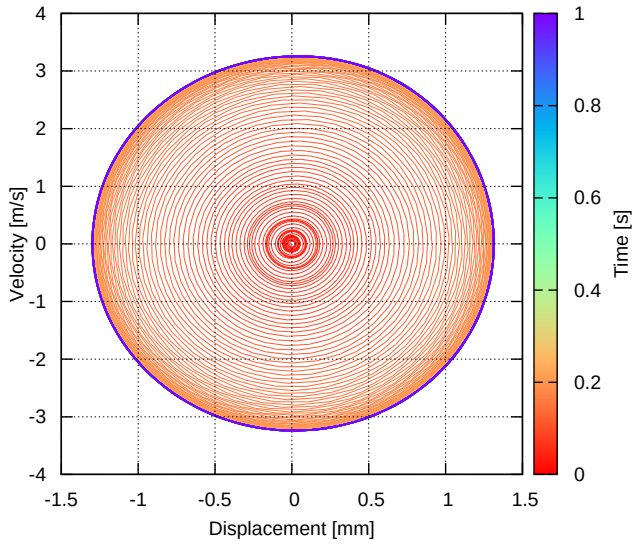

Figure 4.25: Phase–trajectory related to the performance of the G_4, 395.6 Hz pitched, with the E$\flat$ natural trumpet.

It seems essential to highlight that the occurrence of the limit–cycle is necessary and sufficient condition for the dynamic evolution of the system represented by the Eq. 3.12 to produce a pressure signal attributable to a sustained–sound: as will be shown in the Chap. 5, it depends on the combination of the parameters of the Eq. 3.24, *i.e.* the blowing pressure P_m and the mechanical characteristics of the valve, μ_L, g_L and ω_L, describing the motion of the lips.

4.2.2 Pressure at the microphone location

The signal at the virtual microphone location will be assessed for a microphone located at a distance $r = 2$ m from the outlet section of the trumpet, with an offset $\alpha = 30°$ with respect to the longitudinal axis of the instrument (see Fig. 4.14). The pressure signal at such microphone location related to the performance of the G_4, 395.6 Hz pitched, is presented in Fig. 4.26, and is evaluated using the Eq. 3.29.

[10] The phases–plane analysis will be detailed in the Chap. 5 (see Sect. 5.3.1).

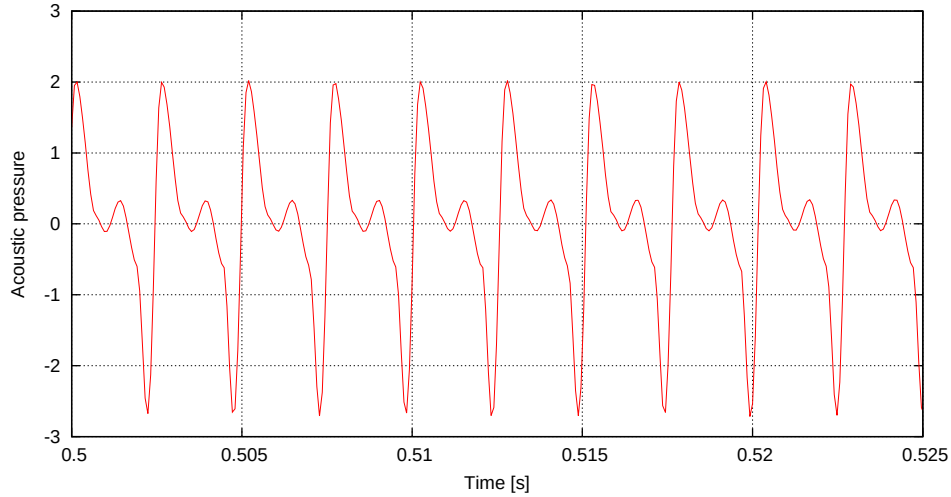

Figure 4.26: Pressure signal at microphone location during the performance of the G_4 with the E$\flat$ natural trumpet.

In the frequency–domain (see Fig. 4.27) it is evident that the signal spectrum is rich even at high frequency, which shows that it is essential to carry out the frequency analysis up to very high frequencies.

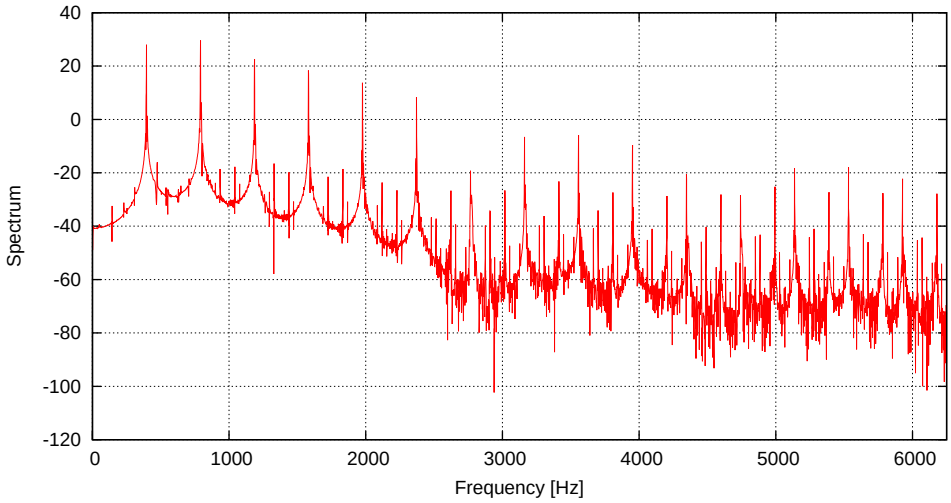

Figure 4.27: Pressure spectrum at microphone location related to the performance of the G_4 with the E$\flat$ natural trumpet.

It seems essential to point up, as shown in Fig. 4.28, that the coherence of the simulated waveform at the virtual microphone location with respect to a recorded waveform with an instrument of the same category, is remarkable.

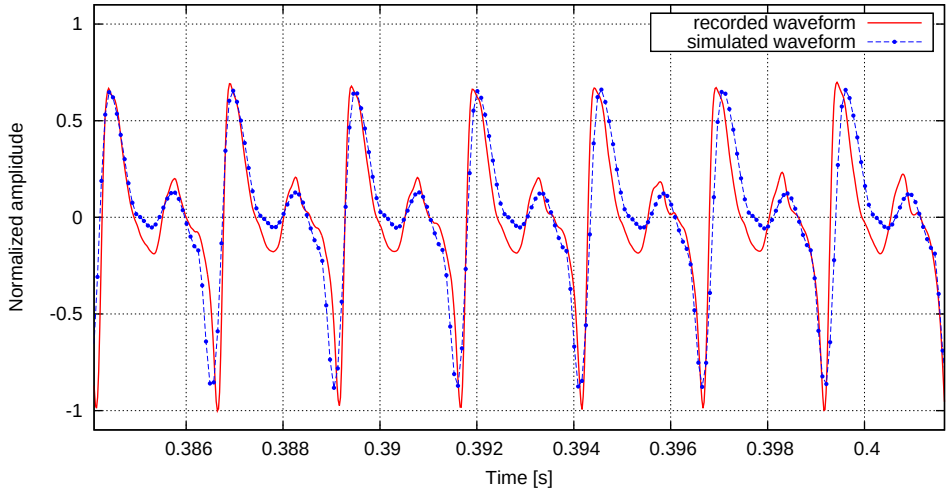

Figure 4.28: Comparison between recorded waveform (sampling frequency $F_s = 44100$ Hz) and simulated waveform at the microphone location.

4.2.3 The auralization

As seen above, the transfer function $\mathbf{E_2L}$ related to the listener ears was evaluated on a simple head model, specifically on two poles apart points of the sphere. This choice is particularly interesting, since it allows to have the greatest differences between the left and right channel of the stereophonic signal.

The pressure signals referred to both right and left ears is computed by solving the Eq. 3.31, and are presented in Fig. 4.29

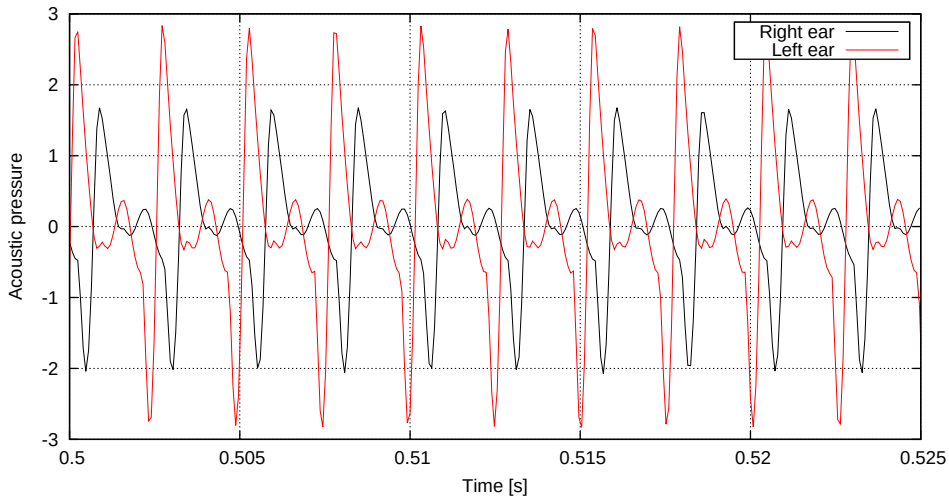

Figure 4.29: Pressure signal at the ears of the listener during the performance of the G_4 with the E$\flat$ natural trumpet.

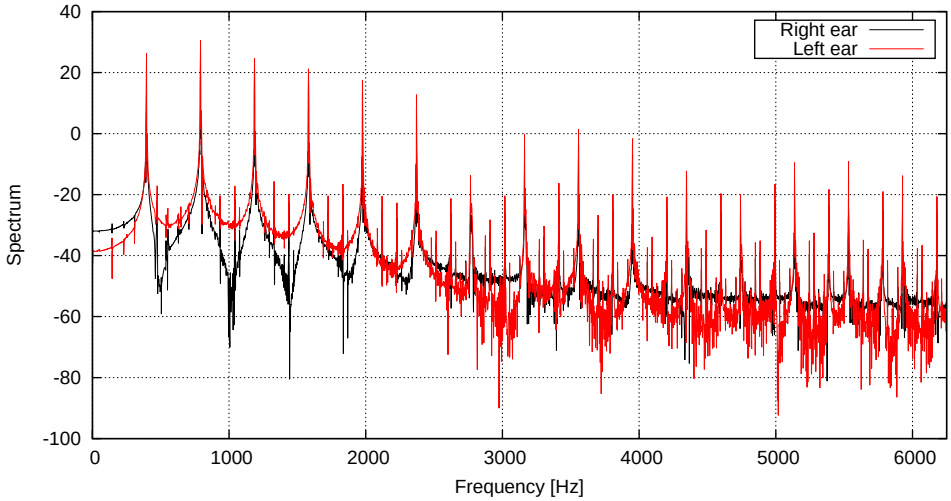

Figure 4.30: Pressure spectrum at the ears of the listener during the performance of the G_4 with the Eb natural trumpet.

4.3 Towards the real–time simulations

The exploitation of the physical models for the real–time sound synthesis can find several employment in the digital synthesizers or applications compatible with the consumer devices, as well as in the *hybrid* and *augmented* musical instruments design. The need of the scientific community of focusing the efforts on the real–time sound synthesis is also attributable to the recent development of several low–cost portable devices. It is worth noting that the interaction between the "computability" and the "playability" of the physical model turns out to be crucial in the real–time approach to the physical modeling.

Out below will be outlined an operating block diagrams representation of the acousto–elastic coupled system which represents the physical model of the brasses, and of the sound radiation.

4.3.1 Block diagram representation

In the *Feedback Control Theory* and in the *Signal Processing* fields, the classic diagram modeling consists of several interconnected blocks: each block represents a dynamic system and the all the blocks at once describe the overall dynamic. Each block has an input (or several inputs) and an output (or several outputs), and three basic elements can be identified, *i.e.*

- the **summing junction**, used to sum or subtract signals, is represented by a circle within which the signs "+" and "−" indicate the operations of addition or subtraction of the inputs;

- the **constant gain**, which is simply a scalar multiplier. It consists in a triangle block, and its output is equal to the input multiplied the value of the gain;

- the **transfer function**, representing the ratio between the output signal and the input signal, is sketched with a rectangle and contains the model of the transfer function.

By exploiting the abovementioned elements it is possible to achieve a suitable description of the system represented by the Eq. 3.24, in order to obtain the sound radiated at the virtual microphone and the auralized signal, making use of the Eqs. 2.31 and 2.45.

Let consider the dynamic of the acousto–elastic system. The player supplies a constant blowing pressure P_m: the latter combines with the time–varying acoustic pressure inside the embouchure $p(t)$ and both interact with the exciter, modeled as a simple valve (characterized by the inertial term μ_L, the viscous term g_L and the resonant frequency ω_L), providing the displacement $\xi(t)$, as shown in Fig. 4.31.

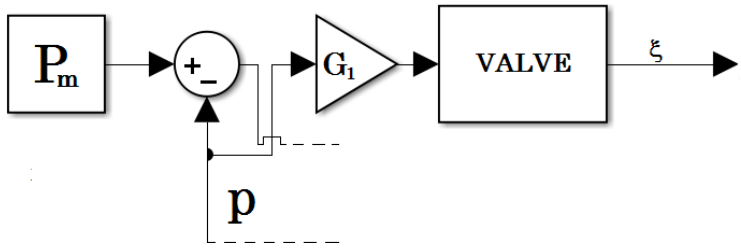

Figure 4.31: Block diagram for the valve motion $\xi(t)$, related to the physical model of a brass instrument.

The gain G_1 in Fig. 4.31, being μ_L the mass ratio, is defined in accordance with the Eq. 3.24 as

$$G_1 = -\mu_L^{-1} \tag{4.2}$$

As described by the Eq. 3.25 the resulting valve displacement $\xi(t)$ provides the lip movement $y(t)$, and the opening area $S(t)$ can be evaluated as a function of $y(t)$ (see Fig. 4.32).

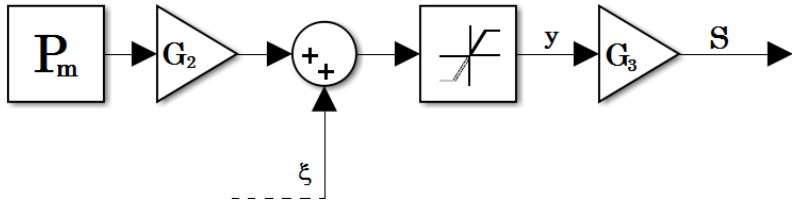

Figure 4.32: Block diagram for the opening area $S(t)$, related to the physical model of a brass instrument.

The gains G_2, according with the Eq. 3.25, and G_3 in Fig. 4.32 are given by the following

$$\begin{aligned} G_2 &= \left(\mu_L \omega_L^2\right)^{-1} \\ G_3 &= h_L \end{aligned} \tag{4.3}$$

being μ_L the mass ratio, ω_L the resonance of the lip and h_L the diameter of the inlet section of the embouchure.[11] Note that the saturation block downstream the summing junction, in Fig. 4.32, means that the lip displacement cannot assume negative values, as described by the Eq. 3.27.

The opening area $S(t)$ let transit the volume inflow $u_{in}(t)$ through the player lips (see Fig. 4.33), under the Bernoulli law.

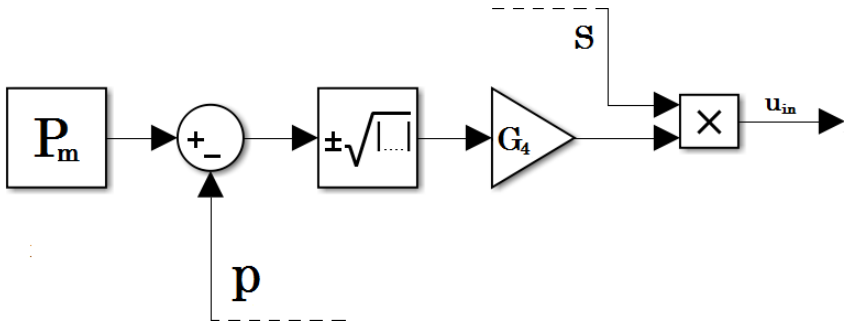

Figure 4.33: Block diagram for the inflow $u_{in}(t)$, related to the physical model of a brass instrument.

The gain G_4 of Fig. 4.33, derived from the Eq. 3.11, is defined as follows

$$G_4 = (2/\rho)^{1/2} \tag{4.4}$$

being ρ the air density.[12]

Finally, the volume inflow $u_{in}(t)$, in agreement with the Eq. 3.3 and with the notion of input impedance, contributes to the temporal variation of the acoustic pressure $p(t)$ inside the embouchure: moreover, with the knowledge of the *Embouchure–to–Microphone* transfer function $\mathbf{E_2M}$, one can obtain the pressure signal $p_m(t)$ at the virtual microphone (or several virtual microphones), whereas the *Embouchure–to–Listener* transfer function $\mathbf{E_2L}$ enables the achievement of the auralized signal, obtaining the pressure signal $\mathbf{p}_l(t)$ at the listener's ear (see Fig. 4.34).

[11] The shape of the area has been arbitrarily choosen (see Sect. 3.2.2).

[12] The block of Fig. 4.33 identified by the symbol "×" refers to the multiplication of the two inputs (see Eq. 3.11).

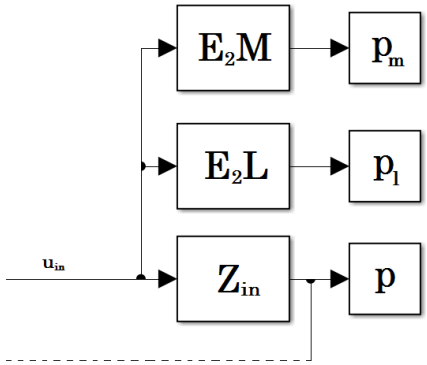

Figure 4.34: Block diagram for the pressure signal $p(t)$ at the inlet section of the instrument and for the sound radiation ($p_m(t)$ and $\mathbf{p}_l(t)$), related to the physical model of a brass instrument.

The block diagram related to the complete brass physical model with the sound propagation and auralization can be obtained by combining the subsystems of Figs. 4.31, 4.32, 4.33 and 4.34, and is sketched in Fig. 4.35.

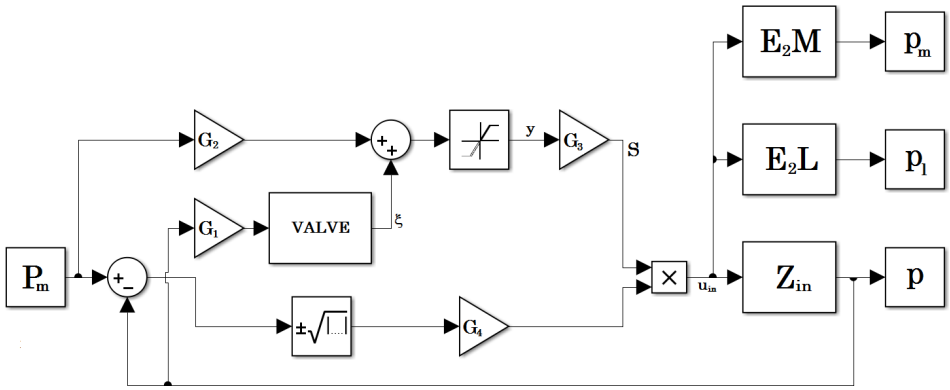

Figure 4.35: Block diagram for the physical model of a brass instrument with the sound propagation and auralization.

Continuous–time vs. discrete–time

With few precautions and modifications,[13] this schematic representation of brass instruments physical model may be used in both the continuous–time and in the discrete–time.

The continuous–time systems describe differential equations and employ the transfer function representation in the Laplace–domain, namely the s–domain, being

[13]It is worth noting that, *e.g.* in the first summing junction the output is driven by the output of the same line through the feedback path: in order to overcome this drawback, a *delay* on the feedback line must be placed.

$s = \alpha + i\omega$: a transfer function can be written as

$$H(s) = \frac{N(s)}{D(s)} = \frac{b_m s^m + b_{m-1} s^{m-1} + b_1 s + b_0}{a_n s^n + a_{n-1} s^{n-1} + a_1 s + a_0} \tag{4.5}$$

or in zero/pole/gain form as

$$H(s) = G \frac{(s - z_m) \dots (s - z_1)}{(s - p_n) \dots (s - p_1)} \tag{4.6}$$

Instead the discrete–time systems describe finite–differences equations making use of the transfer function representation in the z–domain. Actually the z–domain is the discrete counterpart of the s–domain. Indeed it is easy to note that, defining $z = e^{s\Delta t}$, the z–transform is proportional to the Laplace transform of continuous–time signal sampled every Δt seconds [78, 75, 1].

In addition it is easy do demonstrate that

$$z = e^{s\frac{\Delta t}{2}} = \frac{e^{s\frac{\Delta t}{2}}}{e^{-s\frac{\Delta t}{2}}} \approx \frac{1 + e^{s\frac{\Delta t}{2}}}{1 - e^{s\frac{\Delta t}{2}}} \tag{4.7}$$

being Δt the time step of the sampled continuous–time signal. It follows that the s–domain representation of a transfer function can be mapped into the z–domain by substitution

$$H(z) = H(s)|_{s=\frac{2}{\Delta T}\frac{z-1}{z+1}} = H\left(\frac{2}{\Delta T}\frac{z-1}{z+1}\right) \tag{4.8}$$

The Eq. 4.8 is the bilinear approximation, also referred to as the *Tustin*'s method.

Example As an example, let consider the model of the valve (see Fig. 4.31) described, as detailed above, by a simple second–order system. Its transfer function in the s–domain, imposing arbitrary values for g_l and ω^2 is given by the following

$$H_v(s) = \frac{1}{s^2 + 3 \cdot 10^2 s + 4 \cdot 10^6} \tag{4.9}$$

Using the Eq. 4.8 with a time step $\Delta t = 10^{-3}$, the z–domain representation of $H_v(s)$ turns out to be

$$H_v(z) = \frac{2.496 \cdot 10^{-7} z^2 + 4.992 \cdot 10^{-7} z + 2.496 \cdot 10^{-7}}{z^2 + 1.997 z + 0.997} \tag{4.10}$$

4.3.2 System realization

The block representation of the Fig. 4.35 implies the realization of the input impedance $\mathcal{Z}_{in}$, the *Embouchure–to–Microphone* transfer function $\mathbf{E_2M}$, aimed at the propagation of the signal to toward the virtual microphone, and the *Embouchure–to–Listener* transfer function $\mathbf{E_2L}$ for the signal auralization.

One can demonstrate that the bilinear approximation (see Eq. 4.8) preserves the stability of the frequency response, mapping every point of $H(s)$. Accordingly, a suitable Reduced–Order–Model (ROM) in the s–domain was used. Specifically, a representation [36, 37] of the abovementioned transfer functions was provided by the following

$$\mathbf{E}(s) = \mathbf{C}\,(s\mathbf{I} - \mathbf{A})^{-1}\,\mathbf{B} \tag{4.11}$$

It is worth noting that in all the analysed cases the realization has demonstrated to be stable using a few hundred of degrees–of–freedom (see Fig. 4.36).

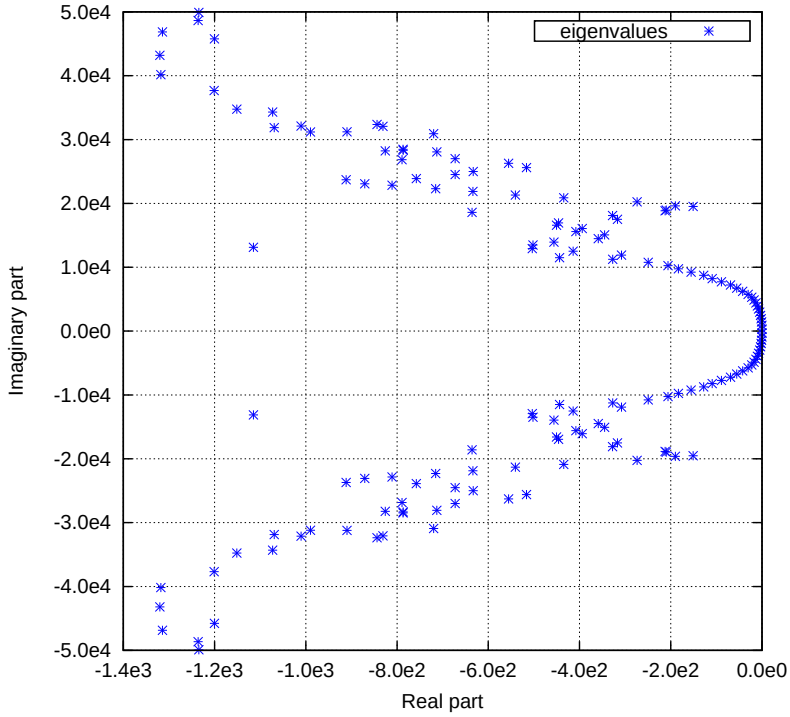

Figure 4.36: Eigenvalues of the matrix **A** (see Eq. 4.11) related to the realization of the input impedance $\mathcal{Z}_{in}$ of the natural Eb trumpet.

Starting from the Eq. 4.11, the N poles p_n and the M zeros z_m (see Eq. 4.6) are easy achievable and the discrete–time system can be provided by the Eq. 4.8.

CHAPTER 5

Exploration of the physical model parameters

The variety of playable notes is attributable to the mastery of the player to move on each of the harmonic sounds, typically from the 3rd to the 16th, and in this chapter the link between the mechanical characteristics of the lip and the emitted sounds will be explained, with emphasis on identifying all the signals peculiarity that may be considered musically relevant.

Particularly will be described the process leading to the characterization of the pressure signals at the inlet section, referring to the natural trumpet in Eb described in the Chap. 4. The aim of this part of the work is seeking, in the space of the coefficients of the Eq. 3.24, the spots that give rise to physically–*feasible* and *musically*–relevant sounds. The process leading to the identification of such spots passes through both physical and aesthetical considerations, digging the initial space with the purpose of reach the *performance* space which provide the *performance* sounds.

5.1 Sculpting the variables space

5.1.1 Initial premises

The sound synthesis through physical modeling may be intended to two issues, different and ostensibly contrasting. On one hand, the accurate reconstruction of both the physical phenomena concerning the act of playing and the pressure signals, with special attention to the correlation between phenomenon and perception. On the other hand, the modelation in a wider sense, offers the opportunity, *i.e.* of scanning the effect of a negative mass or a negative damping, as well listen the sound produced by a senseless geometry, namely scanning the space of the non–physical variables. In a certain sense, however, the proper modelation of the real phenomena

is essential prerequisite for the exploration of improbable realities. Moreover should be highlighted that the link between the two points of view lies in the artistic field, within which turns to be essential the exploration of new sonorities, for purposes of both the electronic music composition and the *hybrid* or *augmented* musical instruments design.

The time–domain simulation provide a time–varying signal given a prescribed combination of input data, identified within a mathematical domain. The domain characterization is no easy matter due to the limitations imposed by modeling itself, such as the degree–of–freedom reduction or the compatibility with the available computing resources. It is important to note that identification of the "quality" of the sounds, solution of the simulations, should involve a perceptual investigation. Instead, in the following will be outlined an attempt to objectively characterize the solutions of the physical model through a mathematical description.

Given this, turns out to be essential to formalize the terminology that will be used hereafter. Let so define

- **Variables space**: is the domain $\mathcal{X}$ of definition of the physical model in the space of the involved parameters. A prescribed location in the variables space consists of a combination of the parameters of the Eq. 3.24 and constitutes the input data set of the simulation;

- **Solutions space**: is the space $\mathcal{P}$, image of $\mathcal{X}$, of the time–varying signals generated by prescribed coordinates of the variables space. The solutions space contains several subspaces, among which is useful to identify:

  - the **hearing–range solutions**, which are characterized by a periodicity within the hearing–range;
  - the **sustained solutions**, *i.e.* with a steady–state characterized by self–sustained oscillations.
  - the **feasible solutions**, then which not involve absurd physical quantities, *i.e.* if are in accordance with the physics of the case study in terms of geometric values and performance praxis;
  - the **musical solutions**, whose timbrical properties in terms of attack–time transient and spectral fluctuation can ascribed to a brass instrument.[1]

- ***Performance* sounds**: are the solutions belonging the intersection of all the subspaces detailed above. Such sounds turn out to be attributable to the sounds performed by an experienced musician, with timbrical characteristics compliant with the real sounds. In addition the involved state variables are feasible in physical terms;

[1] These solutions can be considered by definition within the hearing–range.

- ***Performance* space**: is the subspace of the variable space the image of which is the space of the *performance* sounds.

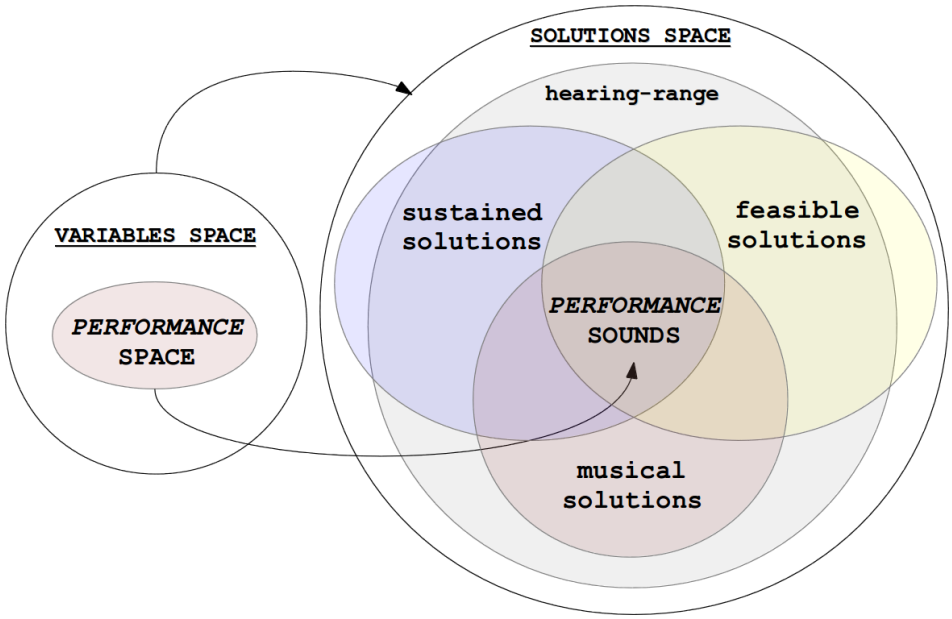

Figure 5.1: Identification of the *performance* sounds as superposition of subspaces in the global space of the solutions: sustained solutions, feasible solutions and musical solutions with the condition that the signal periodicity falls within the hearing–range.

With the purpose to identify the sounds that can be attributable to the musical instrument under examination, considering that playing a resonant aerophone consists in producing a sustained and controlled oscillation of the air column inside the instrument, and this is possible as long as the musician directly sustains the oscillation, *i.e.* the solution should be sustained (*sustained solutions* subspace). Moreover, the sustained solution must lead to a physically–feasible combination displacements, inflow and pressure at the inlet section of the instrument (*feasible solutions* subspace). In addition, the sounds should also be coherent in terms of spectral fluctuations and attack–time (*musical solutions* subspace).

The reason to consider the intersection of these subspaces (under the condition that the periodicity fall within the hearing–range) lies on the knowledge that the physical model may lead to the generation of solutions not referable to a brass instruments, some of which are exceptionally similar to membranophones and chordophones sounds: thus the timbrical characteristics identified in the subspace of the musical solutions are not sufficient to identify a brass–like sound.

Then a solution will be characterized as **sustained–sound** if it reaches self–sustained oscillations with periodicity within the hearing–range. In the event that the solution is musically relevant but is not sustained, will be referred to simple as **sound** on the condition that the periodicity falls within the hearing–range.

It is obvious as the identification of the solutions characteristics plays a key role. The interplay between mathematics, physics and music seems to be crucial, since the set of the solutions of the models equations turns out to be significantly larger than the set of the expected sounds.

5.1.2 Employed methodologies

First of all it is essential to specify that, since the qualitative aspects of the perceived sounds are closely linked to the signals across inlet section, everything that follows will be related to the variables inside the embouchure, computed as step–integration of the system formalized by the Eq. 3.12: indeed the propagation of the signal consists in a frequency–dependent linear filtering of the resulting inflow at the intake section of the instrument (see Eqs. 2.31 and 2.45).

For a given resonator,[2] the generic solution $p(t)$ of the system described by the Eq. 3.12 can be seen as a function $\mathcal{F}$ of domain $\mathcal{X}$

$$\mathcal{F} \quad : \quad \mathcal{X} \longrightarrow \mathcal{P}, \quad \mathcal{X} \in \mathbb{R}^4, \quad \mathcal{P} \in \mathbb{R} \tag{5.1}$$

Such a function, under certain hypothesis, can provide a time–varying pressure signal at the intake section of the embouchure. The latter is thus a function of the coefficients of the Eq. 3.24

$$p(t) = f\left(x^p\right) \tag{5.2}$$

being x^p the vector of the parameters related to the performance which identifies a locus on the domain $\mathcal{X}$

$$x^p = (\mu_L, g_L, \omega_L, P_m) \tag{5.3}$$

the latter having coordinates consisting of both the blowing pressure P_m and the mechanical properties of the valve representing the lips, *i.e.* the inertial term μ_L, the damping factor g_L, the resonant frequency of the lips ω_L.

In order to perform the exploration of the domain $\mathcal{X}$, let formalize the discrete four-dimensional space $\mathbf{X}$ consisting in a set of spots each one providing a solution of the Eq. 3.24:

$$\mathbf{X} := [\mathbf{x}_{pqrs}] = \left(\mu_{L_p}, g_{L_q}, \omega_{L_r}, P_{m_s}\right), \quad \begin{cases} p = 1, \ldots, N_{\mu_L} \\ q = 1, \ldots, N_{\mu_L} \\ r = 1, \ldots, N_{g_L} \\ s = 1, \ldots, N_{P_m} \end{cases} \tag{5.4}$$

being N_{μ_L}, N_{g_L}, N_{ω_L} and N_{P_m} the number of subdivisions of the domain related to

[2] As mentioned above, the space of the variables related to the natural trumpet in Eb, described above in the Chap. 4, will be analysed.

each variable. [3] In this view, it can be easily defined the function F of the discrete domain $\mathbf{X}$, such that

$$F \quad : \quad \mathbf{X} \longrightarrow \mathbf{P} \tag{5.5}$$

being $\mathbf{P} = F(\mathbf{X})$ the global discrete space of the solutions. The function F provides a generic pressure signal $\mathbf{p}_{pqrs}$ inside the embouchure

$$\mathbf{p}_{pqrs} = \mathbf{p}[n\Delta t] = \begin{pmatrix} p[\Delta t] \\ \vdots \\ p[N_S \Delta t] \end{pmatrix}, \quad n = 1, \ldots, N_s \tag{5.6}$$

with Δt the time step and N_s the total number of samples of the time–domain simulation. The target of the analysis is the identification $\mathbf{X}^\pi \subseteq \mathbf{X}$, defined as follows

$$\mathbf{X}^\pi := \left[\mathbf{x}_{p'q'r's'}\right] \quad : \quad \mathbf{P} = \mathbf{P}^\pi = \left[\mathbf{p}_{p'q'r's'}\right] \tag{5.7}$$

where $p' \leq p$, $q' \leq q$, $r' \leq r$, $s' \leq s$ and hence $\mathbf{P}^\pi \subseteq \mathbf{P}$ is the space of the *performance* sounds, being $\mathbf{p}_{p'q'r's'}$ the generic pressure signal inside the embouchure mirroring specified requirements both physical and musical. Such requirements, as will detailed below, identify three subspaces in the solutions space, *i.e.* the sustained solutions $\mathbf{P}^S$, the feasible solutions $\mathbf{P}^F$ and the the musical solutions $\mathbf{P}^M$. The intersection of the abovementioned subspaces gives to the space of the *performance* sounds.

Note that the criteria aimed at the recognition of the physical and the musical requirements should be construed as a tapering functions for the variables space $\mathbf{X}$, obtained as suitable filter functions W^* on the solutions space $\mathbf{P}$

$$\mathbf{P} \xrightarrow{W^*} \mathbf{P}^* \tag{5.8}$$

Accordingly the tapered variables space $\mathbf{X}^*$, can be obtained applying a specific criterion represented by W^* on the solutions space $\mathbf{P}$, *i.e.*

$$\mathbf{P}^* = F\left(\mathbf{X}^*\right) = W^* \left\langle F\left(\mathbf{X}\right)\right\rangle \tag{5.9}$$

where the meaning of the angle brackets is the filtering of the solutions related to the previous variables space.

Notice that the same methodologies aimed at the identification of the *performance* sounds are even oriented to identification of the aforementioned partial intersection spaces, via the backward usage of the filter functions W^*, namely

$$\mathbf{P} \xrightarrow{W^*_{-1}} \left(\mathbf{P} - \mathbf{P}^*\right) \tag{5.10}$$

[3] It is worth to point up that it seems not possible to predict neither the shape nor the boudaries of the variables space, but one can expect that the lips resonant frequency is close to the fundamental frequency of the signal as well as the adimensional damping $\zeta = g_L/2\omega_L$ must be such that the second order system not results over-damped. In order to achieve a qualitative but meaningful exploration of the variables space, it was imposed a bounding box compatible with computational resources.

and thus, as mentioned above, the complementary set $\mathbf{X}_c^*$ is such that

$$\mathbf{P}_c^* = \mathbf{P} - \mathbf{P}^* = W_{-1}^* \langle F(\mathbf{X}) \rangle \tag{5.11}$$

According to what have been explained, the process leading to the definition of $\mathbf{X}^\pi$, starting the identification of the *performance* sounds, substantially consists in the sequential filtering of the space of the solutions $\mathbf{P}$ through an adequate number of filtering functions

$$W^i, \quad i = \ldots, n_W \tag{5.12}$$

formalizing the characteristics of the *performance* sounds, such as the condition of sustained oscillations, as well as physical or aesthetical restrictions.

Noting lastly that, giving two generic W^{i_1} and W^{i_2} and defining

$$\begin{aligned} \mathbf{X}^{i_1} &: \mathbf{P}^{i_1} = W^{i_1} \langle F(\mathbf{X}) \rangle \\ \mathbf{X}^{i_2} &: \mathbf{P}^{i_2} = W^{i_2} \langle F(\mathbf{X}) \rangle \end{aligned} \tag{5.13}$$

it is easy to verify the equivalence

$$\mathbf{X}^{i_1} \cap \mathbf{X}^{i_2} = W^{i_1} \left\langle F\left(\mathbf{X}^{i_2}\right) \right\rangle = W^{i_2} \left\langle F\left(\mathbf{X}^{i_1}\right) \right\rangle \tag{5.14}$$

and therefore, in the seeking of the *performance* space $\mathbf{X}^\pi$, the order of the application of the several W^i is totally irrelevant.

The hearing–range

It is worth to point up that, regarding the *performance* space $\mathbf{X}^\pi$, it seems not possible make any predictions about neither its shape nor its boundaries.[4] Actually is worth formulate a hypothesis concerning the aim of the study. If the components of $\mathbf{x}_{pqrs}$ are positive real numbers, the solution of the system 3.24 can consist in a set of time–dependent variables and the dynamics of such variables mark the pressure signal inside the embouchure. Since the goal of this part of the work is the recognition of $\mathbf{X}^\pi$, via the identification and the characterization of the *performance* sounds space $\mathbf{P}^\pi$, one can immediately exclude the signals whose periodicity falls outside the hearing–range.

Notice that the one degree of freedom model of the valve, described in the Sect. 3.2.2, secures that the oscillation frequency of the latter, described by the auxiliary variable $\xi(t)$ (see Eq. 3.26), is mainly monochromatic, as opposed the pressure signal as well as the inflow signal, whose harmonic components are often predominant, in terms of amplitude, compared to the fundamental frequency. Since the fundamental frequency of the pressure signal inside the embouchure is the same of the oscillation

[4] Actually one can expect that the lips resonant frequency is close to the fundamental frequency of the signal as well as the adimensional damping $\zeta = g_L/2\omega_L$ must be such that the second order system not results over-damped.

of the valve, in convenient enumerate the local maxima (or minima) N^p of the displacement function $\xi(t)$ as fallows

$$N^P = N^P + 1, \quad \text{if} \quad \begin{cases} \xi[n] > \xi[n-1] \\ \xi[n] > \xi[n+1] \end{cases} \quad n = 1, \ldots, N_s - 1 \tag{5.15}$$

being N_s the total number of samples of the time–domain simulation, and impose, in order to discern if the signal falls within the hearing–range, the condition

$$T_{min} \leq \frac{n\Delta t}{N^p} \leq T_{max}, \quad \forall \mathbf{p}_{pqrs} \in \mathbf{P} \tag{5.16}$$

being $T_{max} = 1/f_{low}$, $T_{min} = 1/f_{up}$ with $f_{low} = 20$ Hz and $f_{up} = 20$ kHz. Actually, the event that the signal falls above the hearing–range is highly improbable, since the box constraint on the resonance frequency of the lip turns out to be much lower than the upper bound of the hearing–range. Moreover the sampling frequency is such that the Nyquist frequency is in the hearing–range. Given this, the condition expressed by the Eq. 5.16 should be considered in terms of its lower limit.

The Eq. 5.16 defines the the space $\mathbf{X}_{hr}$, subspace of $\mathbf{X}$, shown in Fig. 5.2.

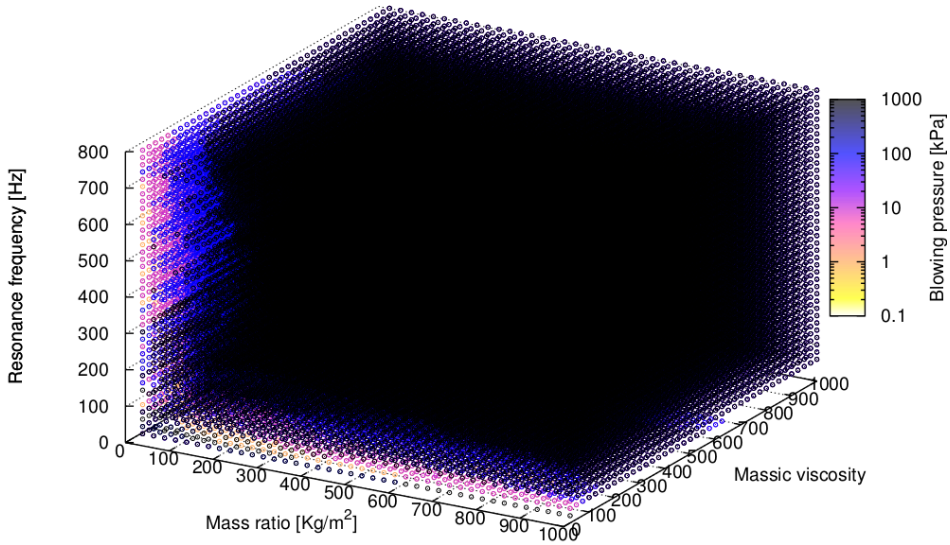

Figure 5.2: Variables space $\mathbf{X}_{hr}$ of the the natural Eb trumpet (obtained with the condition that the pressure signals must fall into the hearing–range), with the blowing pressure as parameter.

Noting that the space $\mathbf{X}_{hr}$ consists in a dense distribution of spots which seem slightly dug for high values of g_L. The analysis of Fig. 5.2 highlights that the spots $\mathbf{x}_{pqrs}$ seem tend to leave the bound of the domain for increasing blowing pressure P_m and increasing resonance frequency of the lip ω_L.

The assumption formalized with the Eq. 5.16 automatically ensures that the signal is periodic but, of course, does not provide information on the evolution of

the signal, meaning that an accurate analysis of the time evolution of the signals is needed in order to achieve the *performance* space.

Numerical stability

The basis of the simulation is the stability of the numerical scheme which leads to the generation of the pressure signals. Indeed the aim of find out criteria for the characterization of the sounds, the unconditioned numerical stability turns out to be essential. In order to ensure it, the Crank–Nicolson method [20, 22] was implemented. Such method is a combination of the forward Euler method and the backward Euler method and approximates the derivative as follows

$$\frac{y^{n+1} - y^n}{\Delta t} = \frac{H^{n+1} + H^n}{2} \tag{5.17}$$

being H^{n+1} and H^n respectively the forward and the backward Euler approximations for the derivative.

5.2 On the note detection

In music, a note is simply defined as a pitched sound, *i.e.* a sound event for which it is possible to define a fundamental frequency f_0.[5] Two issues are involved in the identification of a musical note, namely the recognition of the perceived pitch and the choice or the musical tuning, from which it is possible to unambiguously determine the note (name and octave), starting from the knowledge of the characteristics of the signal.

The pitch estimation is a popular topic in many fields of research, and if related to the musical sound appears to be a more complex topic. The pitch range can be wide, and the sound of the musical instruments vary a lot in terms of spectral content. The pitch perception is highly dependent on the harmonic composition of the signal and f_0 it rarely corresponds to the maximum of the signal spectrum.

The methods aimed at the estimation of the fundamental frequency f_0 (PDA, *pitch detection algorithms*) of monophonic sounds could be classified into time–domain and frequency–domain algorithms. In the time–domain algorithms the detection is provided by the inversion of the fundamental period, computed as the distance between alternate zero–crossing points, peak–to–peak distances, or slope periodicity of the signal.[6] Instead, the frequency–domain algorithms attempt to recognize the fundamental tone, by computing the spectrum of the signal within

[5] Psychoacoustic tests have also proved that the brain decodes the pitch of sound only if its duration is greater or equal than 10 milliseconds, whereas below this value the feeling is the same of an impulse.

[6] Another method consists in computing the autocorrelation function, defined as the sum of the pointwise absolute difference between the shifted signal and the original signal, identifying the fundamental period in correspondence with the minimum of the autocorrelation function

appropriately overlapped windows. Statistical frequency–domain methods, as neural networks and maximum likelihood estimators, was recently developed.

The frequency–domain algorithms turn out to be typically more accurate then the time–domain methods, but are computationally more expensive. On the contrary, the time–domain algorithms appear to be little less efficient in the case of complex waveforms, but are very easy to implement.

Should be noted that, as mentioned above, the waveform of $\xi(t)$ is mainly monochromatic, hence a peak–to–peak algorithm was implemented. The only shrewdness pertains the evaluation of the time instant T_k^c related to the local k-th peak, computed as the position of the vertex of the parabola defined by three points among which the central has the greater ordinate.

$$f_0^c[n] = \frac{1}{T_k^c - T_{k-1}^c}, \quad n = 1, ..., N, \quad k = 1, ..., N^P \tag{5.18}$$

where the superscript c indicates that the fundamental frequency is instantaneous. Indeed the identification of the note will entail the definition of two pitch frequencies, *i.e.* the current pitch $f_0^c[n]$, described above, and the mean pitch $f_0^m[n]$, obtained as the geometric mean value of the current pitch frequencies

$$f_0^m[n] = \sqrt[n]{\prod_{i=1}^{n} f_0^c[n]}, \quad i = 1, ..., n, \quad n = 1, ..., N_s \tag{5.19}$$

being n the current sample and N_s the total number of samples of the time–domain simulation. Note that the geometric mean, compared to the algebraic mean, is less affected by the presence of terms far from the group, typically distinctive of the transients, so provides a result closer to statistical mode. Furthermore in the step integration the n–th value of the geometric mean

$$f_0^m[n] = f_0^c[n-1]^{\frac{n-1}{n}} \cdot f_0^c[n]^{\frac{1}{n}} \quad n = 1, ..., N_s \tag{5.20}$$

seems converge to the perceived pitch lightly faster than the n–th value of the algebraic mean.

In Fig. 5.3, the time–history of both the current pitch and the mean pitch.

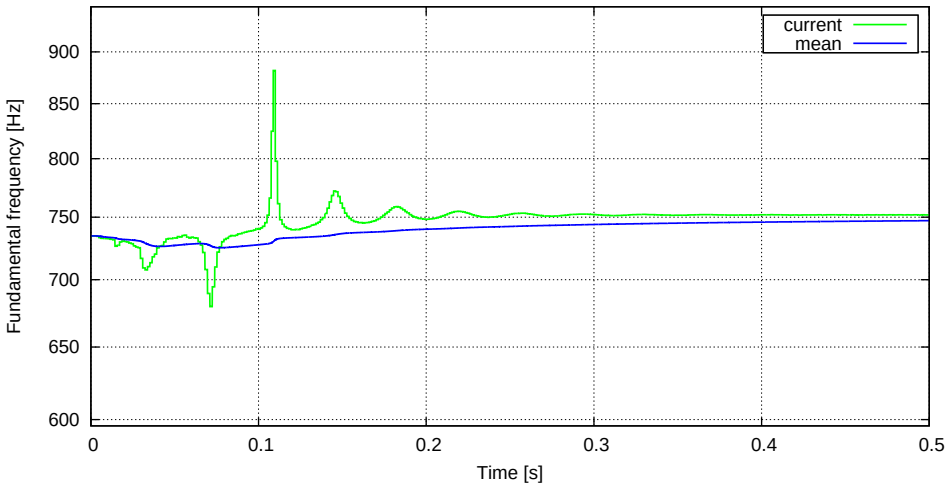

Figure 5.3: Current pitch and mean pitch detected with the time–domain algorithm: mean pitch detected 747.13 Hz for a simulation of 0.5 seconds.

Note that the mean pitch is affected by the length of the simulation so the relative errorsare lower as longer is the simulation, as shown in Fig. 5.4.

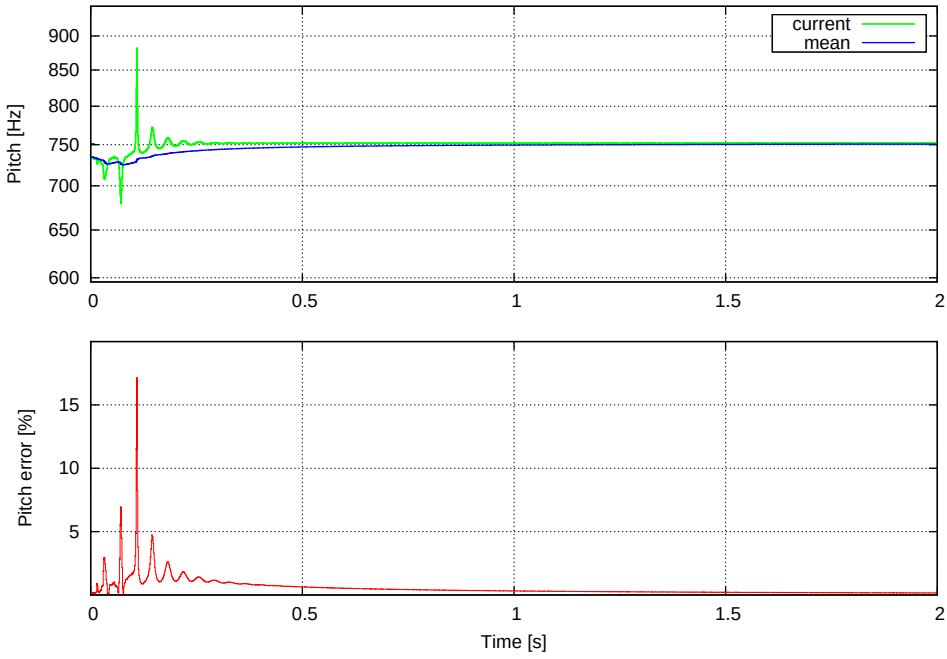

Figure 5.4: Current pitch and mean pitch detected with the time–domain algorithm: mean pitch detected 750.72 Hz for a simulation of 2.0 seconds.

The variables space $\mathbf{X}_{hr}$ of Fig. 5.2, using the sound pitch as parameter, is presented in Fig. 5.5.

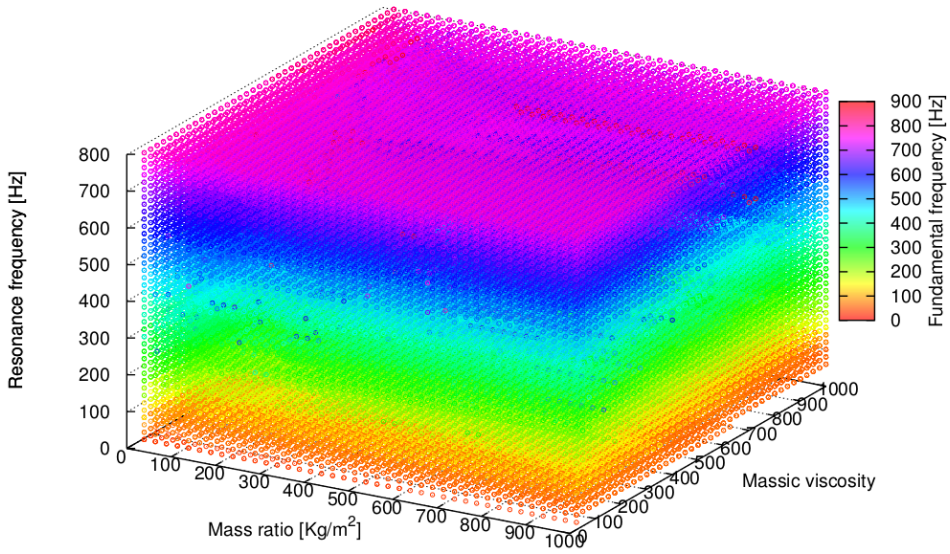

Figure 5.5: Variables space $\mathbf{X}_{hr}$ of the the natural Eb trumpet (obtained with the condition that the pressure signals must fall into the hearing–range), with the sound pitch as parameter.

The analysis of Fig. 5.5 evidences that the sound pitch is a quasi–linear function of the lip resonance frequency, but it was noticed that that the link between the latter and the pitch frequency highly complex.

For what concerns the musical tuning, it is essential to choose both tuning system the reference tuning frequency. Historically, the first important system is ascribed to Pythagoras, and consists in generate all the musical intervals from the pure perfect fifth,[7] *i.e.* the 3 : 2 ratio, as shown in Tab. 5.2.

Note	**C**	**D**	**E**	**F**	**G**	**A**	**B**	**C**
Ratio	1:1	9:8	81:64	4:3	3:2	27:16	243:128	2:1

Table 5.1: The C major scale obtained from the *pytagorean tuning*.

The *pytagorean tuning* tuning, particularly suitable for medieval and renaissance music, appears to be unsatisfactory for tonal music, and through the centuries many tuning systems were developed. Up to now the western music is based almost exclusively on the so-called *twelve–tone equal temperament*, or simply *equal temperament*. This tuning system divides the octave[8] into 12 parts, all of which are equal on a logarithmic scale. Denoting by f_0^I the fundamental frequency of a reference note, and f_0^{II},..., f_0^N the subsequent, it is necessary to calculate the ratio between

[7] This interval is choosen because it is the most consonant.

[8] The octave is defined as the distance between two sounds among which the high–pitched has the fundamental frequency twice with respect to the low–pitched.

two adjacent notes assuming it constant,[9] as shown below

$$\frac{f_0^{II}}{f_0^{I}} = \frac{f_0^{III}}{f_0^{II}} = \frac{f_0^{N}}{f_0^{N-1}} = k \tag{5.21}$$

By relating two non–adjacent notes one obtain

$$\frac{f_0^{N}}{f_0^{I}} = \frac{f_0^{N}}{f_0^{N-1}} \frac{f_0^{N-1}}{f_0^{N-2}} \ldots \frac{f_0^{II}}{f_0^{I}} = (N-1)k = k^{N-1} \tag{5.22}$$

Since the octave is the thirteenth note with respect to any reference note

$$\frac{f_0^{XIII}}{f_0^{I}} = 2 = k^{12} \quad \rightarrow k = \sqrt[12]{2} \tag{5.23}$$

Accordingly, each successive note is derived by multiplying or dividing the previous by the twelfth root of two. Once the relationship between the semitones is known, is necessary to establish the reference frequency from which derive all the notes of the tempered system. Until the 19th century there was no coordinated effort to set a standard in the field of music, but in 1939 an international conference suggested that the fifth A of the piano keyboard (see Fig. 5.6), A_4 which is the forty-ninth note of the piano keyboard, was tuned to $f_{A_4} = 440$ Hz.[10]

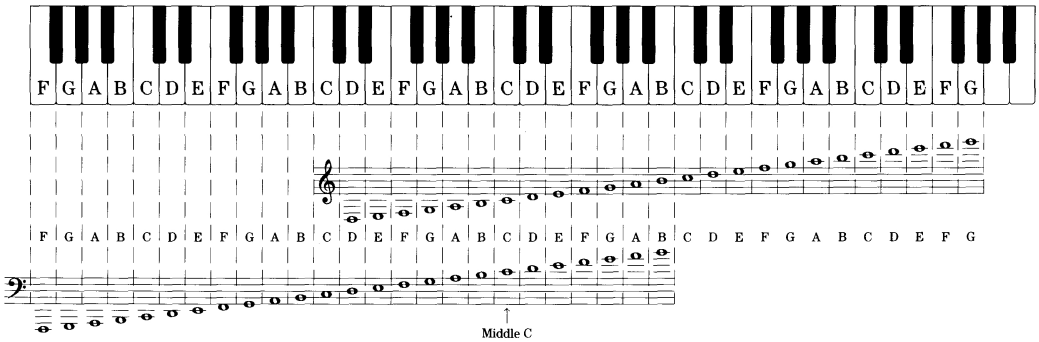

Figure 5.6: The piano keyboard.

At this stage, the following equation gives the order number of a generic note with respect to the piano keyboard.

$$n = 49 + 12log\left(\frac{f_0}{f_{A4}}\right) \tag{5.24}$$

The space $\mathbf{X}_{hr}$ is such that the physical model can produce signals characterized by a continue distribution of fundamental frequencies, as shown in Fig. 5.7.

[9] This hypothesis was first proposed by Aristoxenus of Tarentum in c. 320 BC.

[10] The standard had to be 439 Hz, but was changed because 440 is numerically easier to reproduce than the 439, which is a prime number.

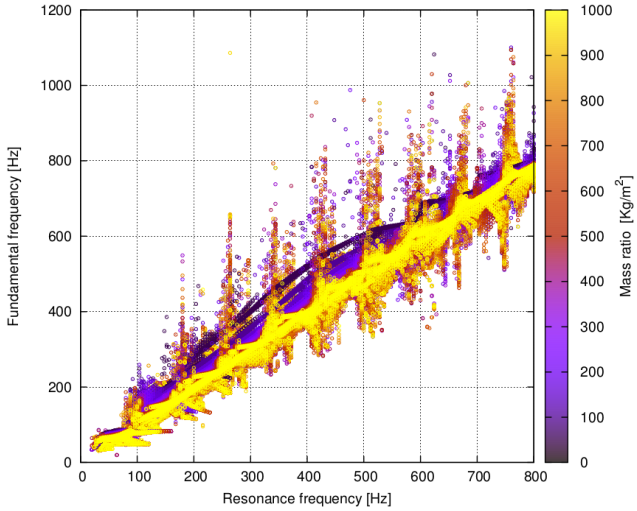

Figure 5.7: Fundamental frequency as a function of the lip resonance frequency with the mass ratio as parameter, related to the variables space $\mathbf{X}_{hr}$ of the natural Eb trumpet obtained by imposing the fundamental frequency within the hearing–range.

It seems that, for a given lip resonance frequency, the pitch of the signal is also weakly a function of the mass ratio μ_L, *i.e.* the greater the amount of vibrating mass, the less will be the fundamental frequency of the signal. Obviously one can expect that many of the solutions of Fig. 5.7 are not related to sounds, as will be detailed below.

5.3 Sounds and self–sustained oscillations

Once the periodicity of the signals is automatically ensured by imposing the condition expressed by the Eq. 5.16 it may be useful to swiftly predict the steady–state behaviour of the oscillations, since a sound correspond to the self–oscillations of the system.

The aim of this section is the identification, within the space of the solutions, of the space $\mathbf{P}^{\sigma}$. Such a space is the intersection between the space of the solution which fall within the hearing–range $\mathbf{P}_{hr}$, and the space $\mathbf{P}^{S}$ of the solutions which involve a sustained steady–state.

$$\mathbf{P}^{\sigma} = \mathbf{P}_{hr} \cap \mathbf{P}^{S} \tag{5.25}$$

It is important to note that the solution belonging the space $\mathbf{P}^{\sigma}$ are related to those that have been called the sustained–sounds.

When the musician start to play, more or less consciously, imposes a combination of the four parameters governing the Eq. 3.24, positioning in a definite location of the variables space $\mathbf{X}_{hr}$. If the blowing pressure overcome the inertia of the valve, an acoustic perturbation start travelling inside the resonator. Such a perturbation

is reflected by the bell and come back towards the embouchure. Depending on $\mathbf{x}_{pqrs}$ it can occur that that the system continuously loses energy, which is never restored and thus the oscillations decline and the system reaches a resting state. Contrariwise, if the energy source plumps the system, the self–sustained oscillations are established. Both the previous instances comply with the condition defined above with the Eq. 5.16, and just the signal observation provides information on the steady–state behaviour of the system.

5.3.1 Phases–plane analysis

Considering a generic steady–state solution of the system: if occurs that the velocity tends to vanish, the oscillations are destined to fade, *i.e.* the valve reaches a quasi–idle state. This condition refers to a solution of the system formalized by the Eq. 3.12 which not give rise to a sound, since the oscillations turns out to be non–sustained.

However the mere analysis of the velocity function $v(t) = \dot{\xi}(t)$ (see Eq. 3.25) is not enough to predict the dynamical behaviour of the system, since the stable periodic motion implies a periodic annulment of the velocity. Thereafter, a simultaneous observation of velocity and position is forcedly needful.

Let consider the Eq. 3.26, governing the dynamic of the lips motion. The definition of the auxiliary variable $\xi(t)$ of the Eq. 3.25, yields that $\dot{y} = \dot{\xi} = v$, hence

$$\begin{aligned} \frac{dv}{dt} &= \frac{d^2\xi}{dt^2} = f\left(\xi, \frac{d\xi}{dt}\right) = f(\xi, v) \\ \frac{d\xi}{dt} &= v = g(\xi, v) \end{aligned} \tag{5.26}$$

Combining the equations, with simple steps one can obtain

$$\frac{dv}{d\xi} = \frac{F(\xi, v)}{G(\xi, v)} \tag{5.27}$$

The (ξ,v)–plane is the phases–plane and the integral curve, the phase–trajectory, represents the solution of the equation. The direction of travel along the trajectories can then be assigned, moving to the right, in the direction of increasing ξ in the upper half of the (ξ,v)–plane and moving to the left, in the direction of decreasing ξ in the lower half of the (ξ,v)–plane. The centre of the phases–plane is the equilibrium point (0,0) and any stable self–sustained oscillation must clockwise rotate round this.

In the event that the oscillations becomes gradually smaller, may occur the spiral motion in the phases–plane may converge to the centre of the phases enclosing the latter, as illustrated in Fig. 5.8.

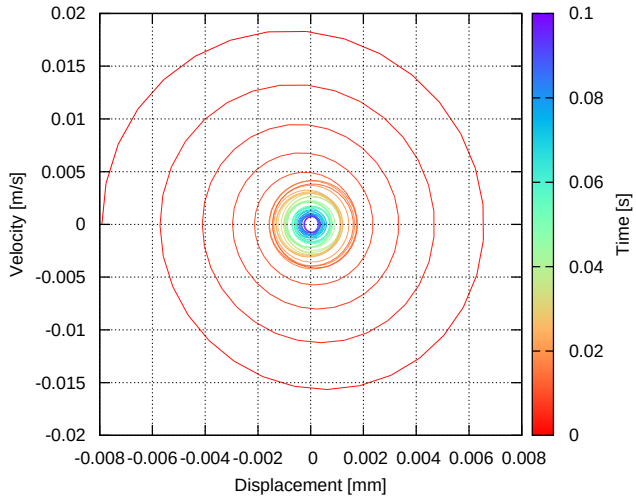

Figure 5.8: Phase–trajectory with converging spiral motion.

Moreover, as shown in Fig. 5.9, it is possible that the converging motion is such that the first spire does not enclose the equilibrium point.

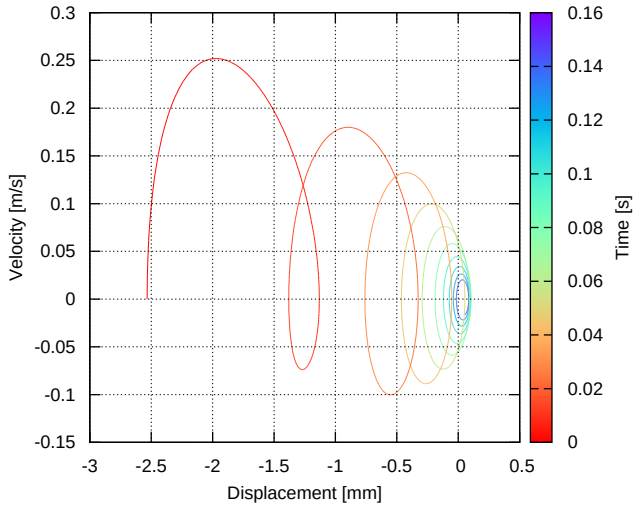

Figure 5.9: Phase–trajectory with converging–translating spiral motion.

Both the previous cases are referred to the condition that the inflow keeps the lip opened, and the latter is animated by decaying microfluctuations around a constant value. Furthermore, if the inflow tends to translate indefinitely the oscillating lip, as illustrated in Fig. 5.10, the spiral motion is divergent.

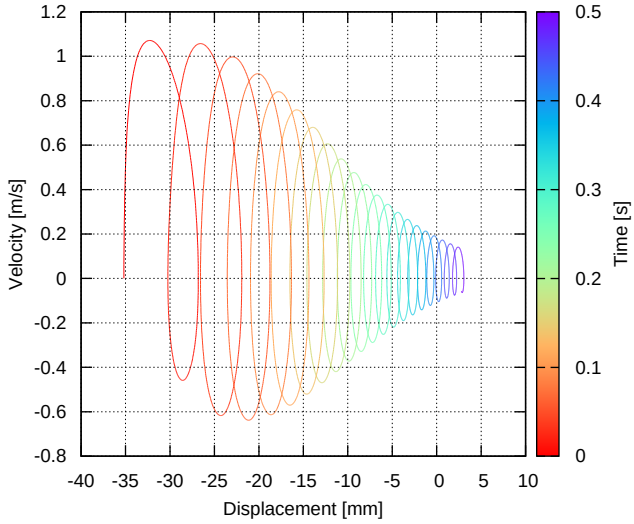

Figure 5.10: Phase–trajectory with diverging–translating spiral motion.

Instead, if the trajectory maintains indefinitely a clockwise rotation around the centre of the phases, as shown in Fig. 5.11

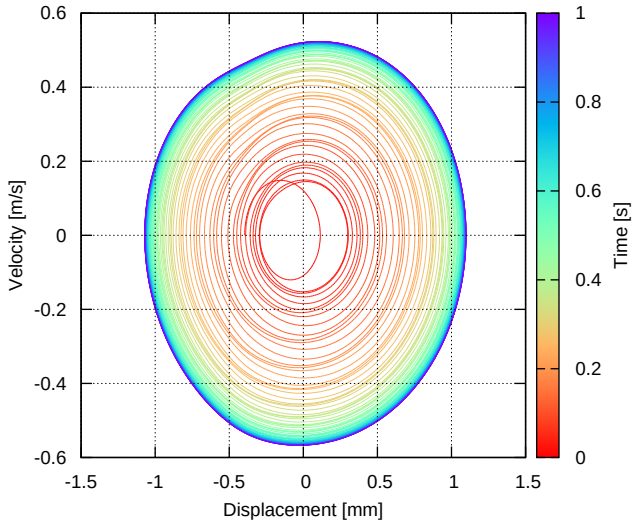

Figure 5.11: Phase–trajectory related to a self–oscillating dynamical system.

Notice that the cases of Figs. 5.8, 5.9 and 5.10, the acousto–elastic coupling can be considered *destructive*, whereas in the case of Fig. 5.11 the acousto–elastic coupling is *constructive* and the limit–cycle represents the steady–state

A criterion aimed at the recognition of the self–sustained solutions, cannot rely on the comparison between two consecutive spires, due to the unpredictable transient behaviour (see Fig. 5.12), and to the periodical contraction and relaxation of

the limit–cycle.

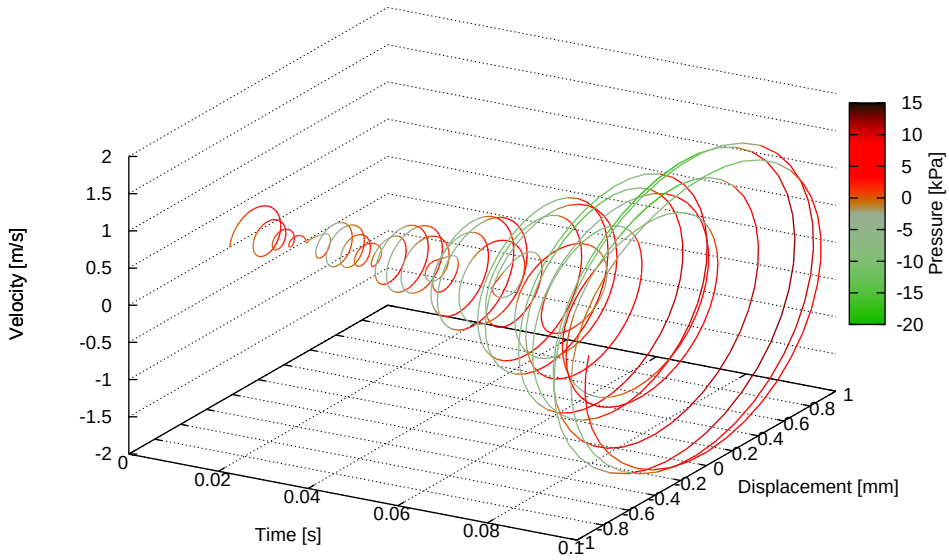

Figure 5.12: Phase–trajectory as function of the time related to a self–oscillating dynamical system during the transient.

However it was noticed that the observation of the system dynamics in the phases–plane may contribute to the establishment of a suitable criterion aimed at discarding the solution that will not reach a self–sustained steady–state. Note that the phase–trajectories with a limit–cycle must enclose the centre of the phases (see Fig. 5.11) but this is a necessary and not sufficient condition for achievement of the self–sustained oscillation because may occur that such oscillation manifest a decaying behaviour (see Fig. 5.8, Fig. 5.9).

In order to formalize these assumption, considering the generic k-th cycle and let define the the intercepts of the phase–trajectory with the axes $v = 0$ and $\xi = 0$ of each cycle as

$$\begin{aligned} \xi_k^+ &= [\xi]_{v_c^{max}}\,, \quad \xi_k^- = [\xi]_{v_c^{min}} \\ v_k^+ &= [v]_{\xi_c^{max}}\,, \quad v_k^- = [v]_{\xi_c^{min}} \end{aligned} \tag{5.28}$$

being ξ_c and v_c respectively the current displacement and the current velocity on the cycle. Since the limit–cycle solution must enclose the centre of the phases, the following condition

$$\frac{\xi_k^+}{\xi_k^-} < 0, \qquad \frac{v_k^+}{v_k^-} < 0 \tag{5.29}$$

must verified for each cycle of the steady–state.

In addition, in the event that the trajectory enclose the centre of the phases, one can define the phases radius r^ϕ as follows

$$r^\phi = \sqrt{\xi^2 + v^2} \tag{5.30}$$

and the area A_k^ϕ swept in clockwise direction by r^ϕ during the k-th cycle from an arbitrary origin θ_0^ϕ

$$A_k^\phi = \int_0^{2\pi} \int_0^{r^\phi} \rho^\phi d\rho^\phi d\theta^\phi \tag{5.31}$$

being

$$d\theta^\phi = \tan^{-1}\left(\frac{|dv|}{|d\xi|}\right) \tag{5.32}$$

As soon as the Eq. 5.29 is satisfied, the initial area A_0^ϕ of the limit–cycle can be defined. As detailed before, an assumption based on the observation of only two cycles cannot represent the oscillations destined to the collapse, since it may occur that the area of the k-th spire is less than the area of the $(k-1)$-th spire in the transient, or the oscillations increase and then decrease periodically in the steady–state. Thus is necessary to analyse the global time history of the spiral areas A_k^ϕ. With this purpose let define a reference area A_{min}^ϕ as follows

$$A_{min}^\phi = A_k^\phi, \quad \text{if} \quad A_k^\phi < A_{min}^\phi \tag{5.33}$$

It is easy to note that a solution can be considered leaving the limit–cycle if the area A_{min}^ϕ continuously decreases as long as the Eq. 5.29 is satisfied. To ensure a reliable recognition of the oscillations which tend to a rest state,[11] let define the index m such that

$$m = m + 1, \quad \text{if} \quad A_k^\phi < A_{min}^\phi, \quad \text{with} \quad m < M \tag{5.34}$$

Then, if m exceeds a prefixed appropriate value M, one can consider that the energy loss is irreversible, and the system will reach a quasi–resting state.

It is worth noting that if M is chosen too small, several self–oscillating solutions with irregular transients are rejected, while high values of M make the condition of Eq. 5.34 totally ineffective.

In addition, since this methodology is affected by the simulation length, it seems appropriate to impose that the spire enclosing the greater area A_{max} is greater than the first spire of the limit–cycle

$$A_{max}^\phi \geq A_0^\phi \tag{5.35}$$

with the purpose of exclude oscillating solutions with a manifest tendency to decay.

Notwithstanding such a methodology do not provides information concerning the trend of the oscillations to grow up. It is worth remembering that the model of the acousto–elastic dynamical system is such that even the solutions that reach the steady–state in infinite time are provided, *i.e.* at the moment, with the conditions described above, even the solution which *slowly* reach the steady–state, are

[11] Note that A_{min}^ϕ is constantly updated during the step integration.

considered. In the view of characterize the *performance* sounds, the hypothesis of self–sustained oscillations must be supplemented by the imposition of the temporal length within which the oscillation are established. In order to discard all the signals whose transient behaviour is not compatible with the brass instruments[12] let define the function a_n^ϕ as follows

$$a_n^\phi = \frac{A_{k-1}^\phi}{A_0^\phi} \quad \text{if} \quad \theta_n^\phi < \theta_0^\phi + 2k\pi, \quad k = 1, \ldots, K \tag{5.36}$$

Noting that the function a_n^ϕ describes the time–history of the complete spiral areas and is piecewise defined, since for all the duration of the clockwise revolution of r^ϕ related to the k–th spire the value of a_n^ϕ is constant.

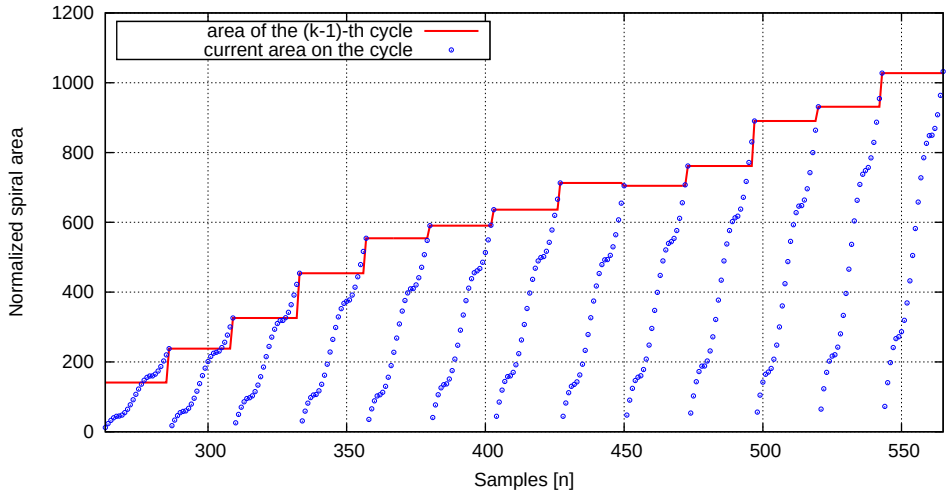

Figure 5.13: Time–history of the spiral areas A_k^ϕ divided by the initial area A_0^ϕ, related to a time window within which the signal grow up.

The current algebraic mean function $\bar{a}_n^\phi$ is

$$\bar{a}_n^\phi = \frac{1}{n} \sum_{i=1}^{n} a_i^\phi, \quad i = 1, \ldots, n, \quad n = 1, \ldots, N_s \tag{5.37}$$

being N_s the total number of samples, the standard deviation function σ_n^ϕ related to a_n^ϕ can be easily formalized as follows

$$\sigma_n^\phi = \sqrt{\frac{1}{n} \sum_{i=1}^{n} \left(a_i^\phi - \bar{a}_i^\phi \right)^2}, \quad i = 1, \ldots, n, \quad n = 1, \ldots, N_s \tag{5.38}$$

[12] Although the musicians have great possibilities of differentiate the sounds, performing notes characterized by different rapidity, typically the brasses have a slightly percussive sound.

and represent the amount of variation of a_n^ϕ with respect to its current mean value. Obviously, under the hypothesis that the limit–cycle exists and such limit–cycle is stable, after the transient the areas related to the k–th cycle will be stabilize around a constant values. This implies that

$$\sigma_n^\phi \to 0, \quad n \to \infty \tag{5.39}$$

i.e. the standard deviation function will begin to decrease until tend to zero for $t \to \infty$, hence in the steady–state will occur that

$$\sigma_n^\phi - \sigma_{n-1}^\phi < 0, \quad \forall n \geq n^s \tag{5.40}$$

being n^s the sample after which the solution can be considered stationary. Note that the condition formalized with the Eq. 5.40 is satisfied only in the presence of self–sustained oscillations (see Figs. 5.14 and 5.15).

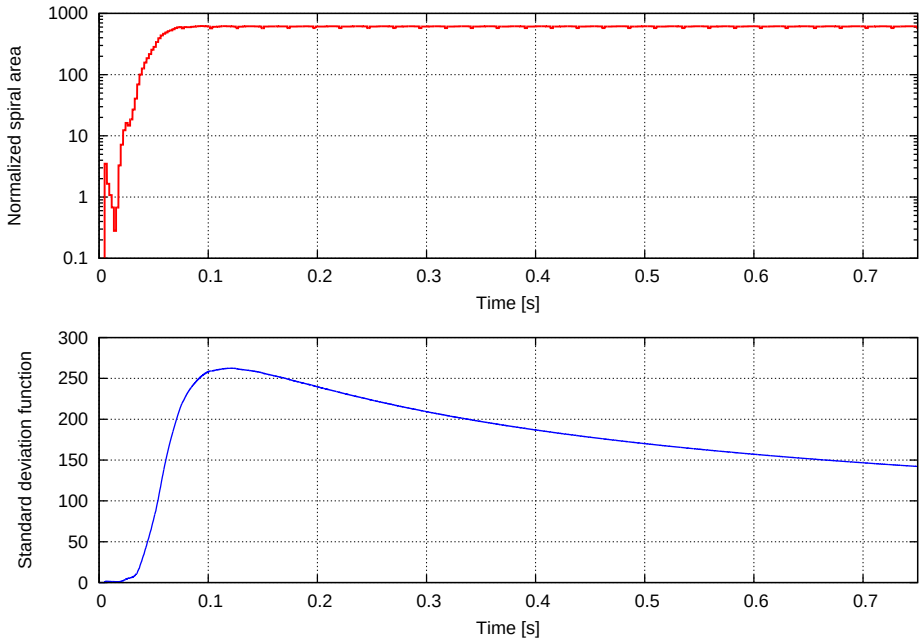

Figure 5.14: Time–history of the spiral areas A_k^ϕ divided by A_0^ϕ and standard deviation function σ_n^ϕ, related to a signal that reaches the steady–state.

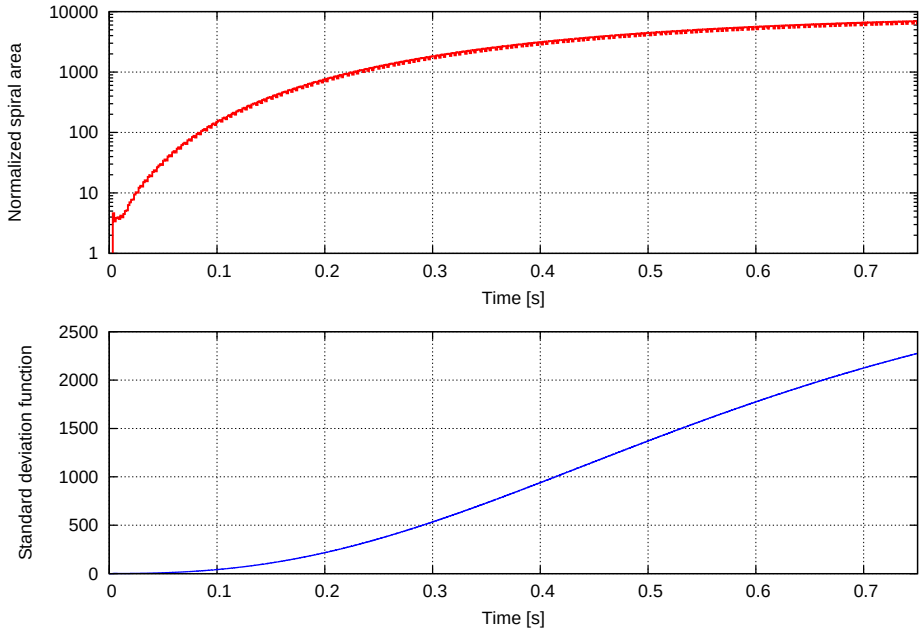

Figure 5.15: Time–history of the spiral areas A_k^ϕ divided by A_0^ϕ and standard deviation function σ_n^ϕ, related to a signal that does not reach the steady–state.

In the case of Fig. 5.15 the condition expressed by the Eq. 5.40 has been violated, and one can consider that the signal does not reach the steady–state in the length of the simulation.

In order to take into account this assumption, it is sufficient to simulate a reasonably long and impose at the end of the simulation the condition expressed by the Eq. 5.40, assuming that the steady–state should already have occurred, *i.e.*

$$\sigma_{N_s}^\phi - \sigma_{N_s-1}^\phi < 0 \tag{5.41}$$

In summary, the phases–plane overview provides valuable information about the system solution. Specifically the awareness that the sound of brasses is only provided by a self–sustained solution, *i.e.* is linked to the existence of the limit cycle,[13] offers the possibility of analyse the spiral areas and impose them a behaviour globally neither decreasing (Eq. 5.33) nor growing (Eq. 5.41), with the aim of ensure a self–sustained steady–state within a reasonable length of the simulation.

The variables space $\mathbf{X}^\sigma$, in Fig. 5.16, is strongly digged with respect to $\mathbf{X}_{hr}$ (see Fig. 5.2).

[13] As detailed above the limit cycle must enclose the centre of the phases.

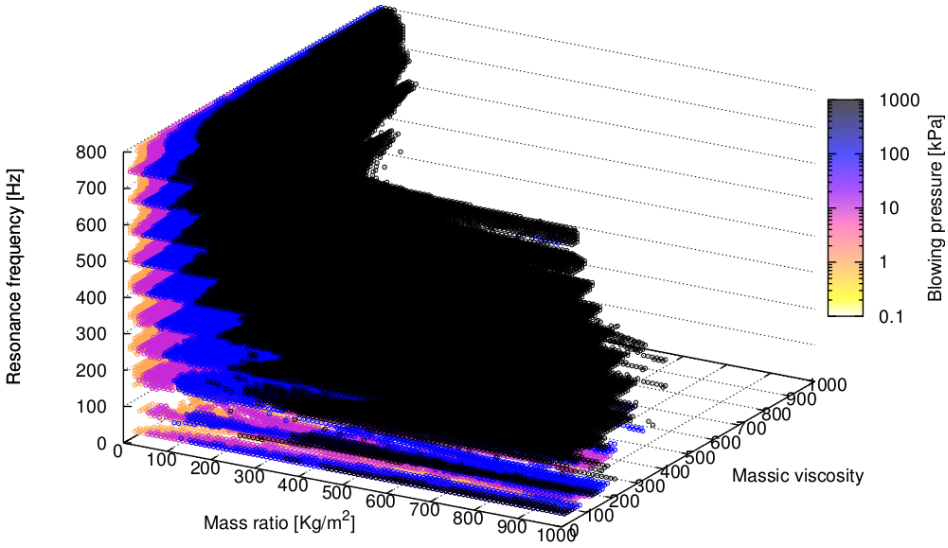

Figure 5.16: Variables space $\mathbf{X}^{\sigma}$ (sustained solutions within the hearing–range) of the natural Eb trumpet with the blowing pressure as parameter.

The discarded spots refer to both solutions that are not characterized by self–oscillations and the solution with a slow transient behaviour, which are not compatible with the sound of brasses. Notice that, using the sound pitch as parameter (see Fig. 5.17), one can note a discrete distribution of fundamental frequencies along the z–axis.

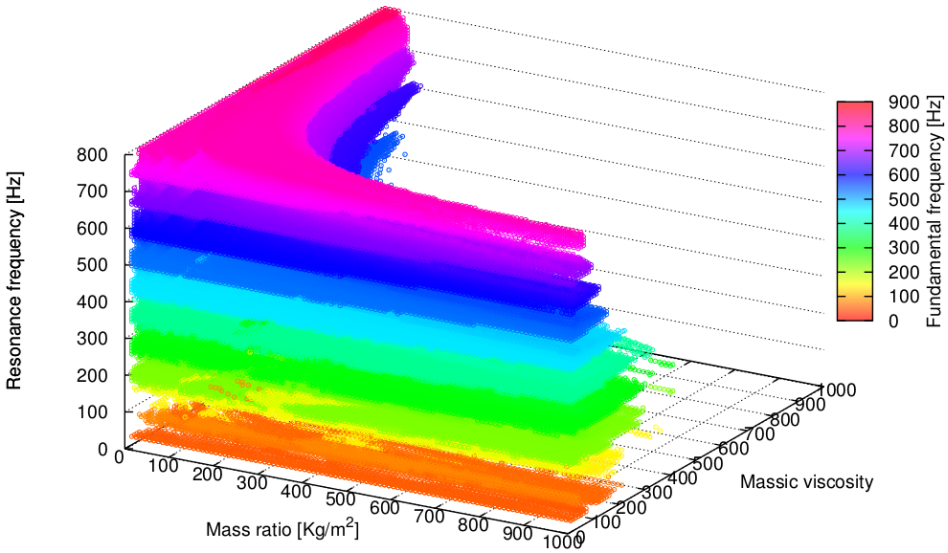

Figure 5.17: Variables space $\mathbf{X}^{\sigma}$ (sustained solutions within the hearing–range) of the natural Eb trumpet with the sound pitch as parameter.

The analysis of Fig. 5.17 suggests that the spots distribution seems gathering in coherent structures, and such structures are characterized by different pitches, being the latter close to the input impedance maxima, as shown in Fig. 5.18.

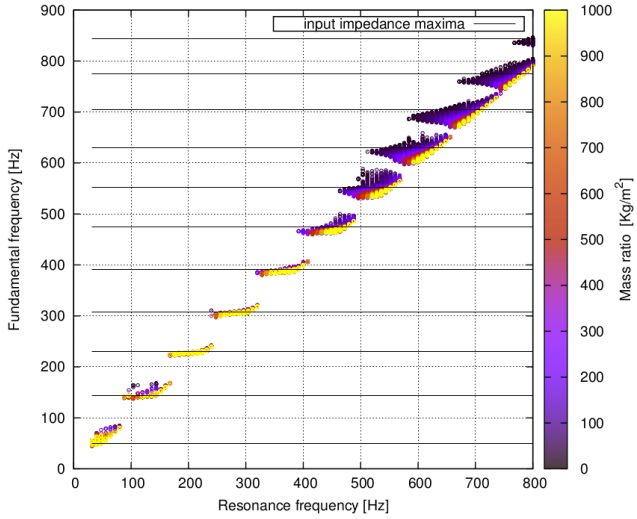

Figure 5.18: Sound pitch as a function of the lip resonance frequency with the mass ratio as parameter, related to the variables space $\mathbf{X}^S$ (sustained solutions within the hearing–range) of the natural Eb trumpet.

This phenomenon reflects the practice of the brasses, which reveals the impossibility to emit sounds near the minima of the input impedance spectrum.

5.4 The physics of the case study

In this section, the issues concerning the connection between the physical model and the physics of the case study will be discussed.[14]

Specifically will be examined the values that the blowing pressure can assume in a real performance of a brass instrument. Then will be formalized the lip behaviour during the playing. At last a kind of baric–efficiency will be introduced with the purpose of taking into account the effort of the musician during the performance.

The superposition of the abovementioned criteria defines the space $\mathbf{P}^F$ of the feasible solutions (see Sect. 5.1.1), and the intersection between $\mathbf{P}^S$ and $\mathbf{P}^F$, under the condition that the sounds fall within the hearing–range

$$\mathbf{P}_{hr} \cap (\mathbf{P}^S \cap \mathbf{P}^F) \tag{5.42}$$

gives rise to the space $\mathbf{P}^{\sigma\phi}$ of the feasible sustained–sounds $i.e$ the space of the solu-

[14] In terms of the state variables related to a real performance. Note that several artificial mouths can easily overcome the real performance techniques of the musical instruments.

tion characterized by self–sustained oscillations and periodicity within the hearing–range, coherent with the physics of the case study.

5.4.1 Blowing pressure

The blowing technique is the foundation of the trumpet playing, as well as the playing of any wind instruments. The characterization of the aerodynamic parameters involving the control of intra–oral pressure is a topic difficult to deal, due to the variable and impulsive nature of the act of playing. Several works [12, 33, 61, 34] focused the issue both theoretically and experimentally.

Certainly the blowing pressure affects the loudness of the sounds, sweeping values from about 1 kPa in the performance of the *pianissimo* reaching values up to 20 kPa for the *sforzatissimo*,[15] but it was also noticed that the entity of the blowing pressure is also closely linked to the pitch of the sound. In addition, as shown in Fig. 5.19, the connection between the sound characteristics and the blowing pressure is highly affected by the playing technique, or rather by the capabilities of the musician.

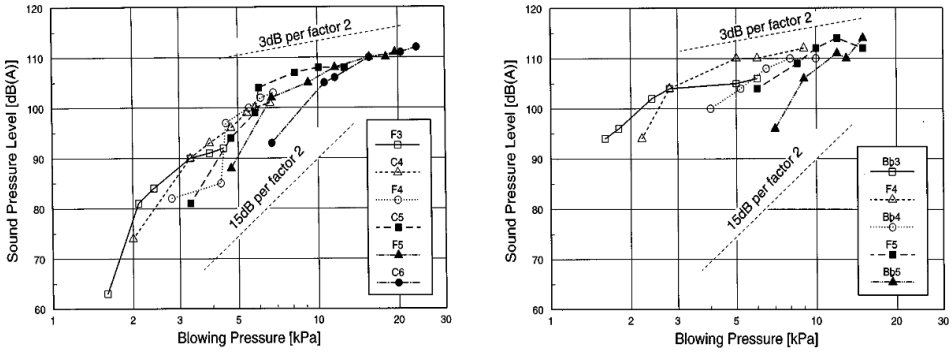

Figure 5.19: Measured sound pressure level as a function of blowing pressure for different notes played by two different musician [33].

Self–sustained oscillation may arise (see Fig. 5.16) from blowing pressures greater than those that can be produced by a musician,[16] as shown in Fig. 5.20.

[15] In musical notation respectively ***ppp*** and ***fff***.

[16] Additional exploration of the *performance* space carried out by the author have proved that the physical model works even with blowing pressures of the order of the GPa.

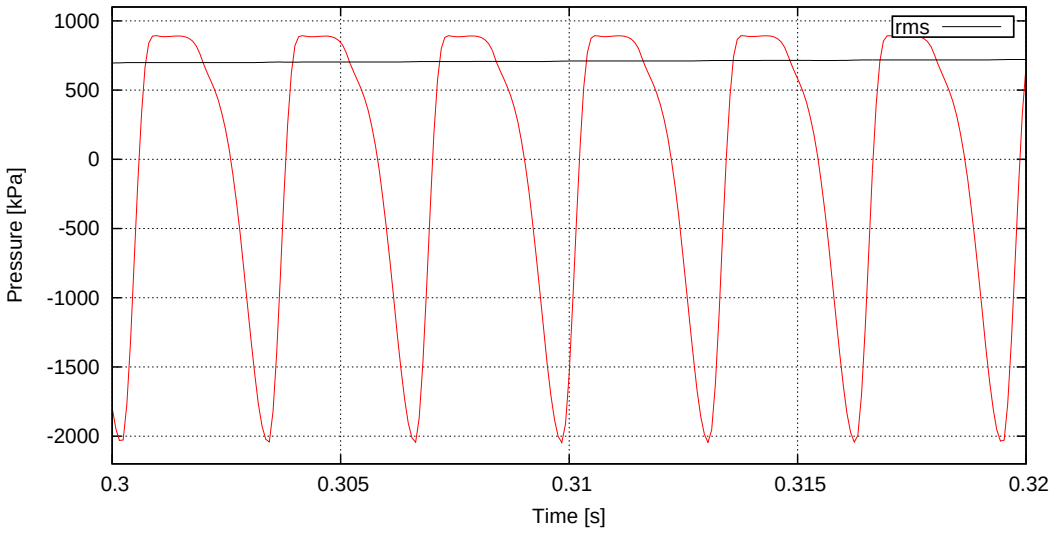

Figure 5.20: Pressure signal at the intake section of the natural Eb trumpet, obtained with a blowing pressure $P_m = 1$ MPa.

With the aim of characterize only the solutions compliant with the physics of the case study, it is necessary to assume that the blowing pressure must not go below 1 kPa and nor above 20 kPa (see Fig. 5.21).

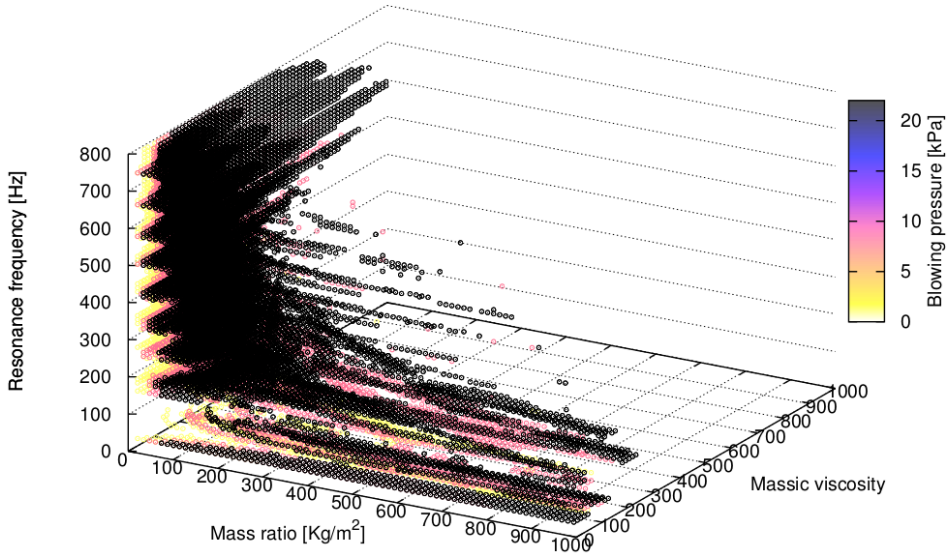

Figure 5.21: Variables space $\mathbf{X}^{\sigma}$ of the natural Eb trumpet with the blowing pressure as parameter, obtained bounding the values of the blowing pressure (1kPa $\leq P_m \leq$ 20kPa).

Just for convenience, let now remove the dependence of $\mathbf{x}_{pqrs}$ (see Eq. 5.4) from

P_m by choosing a single value of blowing pressure

$$P_m^* = 9 \text{ kPa} \tag{5.43}$$

This assumption decreases of a dimension the variables space,

$$[\mathbf{x}_{pqr}]_{s=s^*} = \left(\mu_{Lp}, g_{Lq}, \omega_{Lr}, P_m^*\right), \quad \begin{cases} p = 1, \ldots, N_{\mu_L} \\ q = 1, \ldots, N_{\mu_L} \\ r = 1, \ldots, N_{g_L} \\ s = s^* \end{cases} \tag{5.44}$$

making more handy the the analysis of the successive constraints.[17]

The variables space related to the single blowing pressure chosen, with the sound pitch as parameter, is presented in Fig. 5.22.

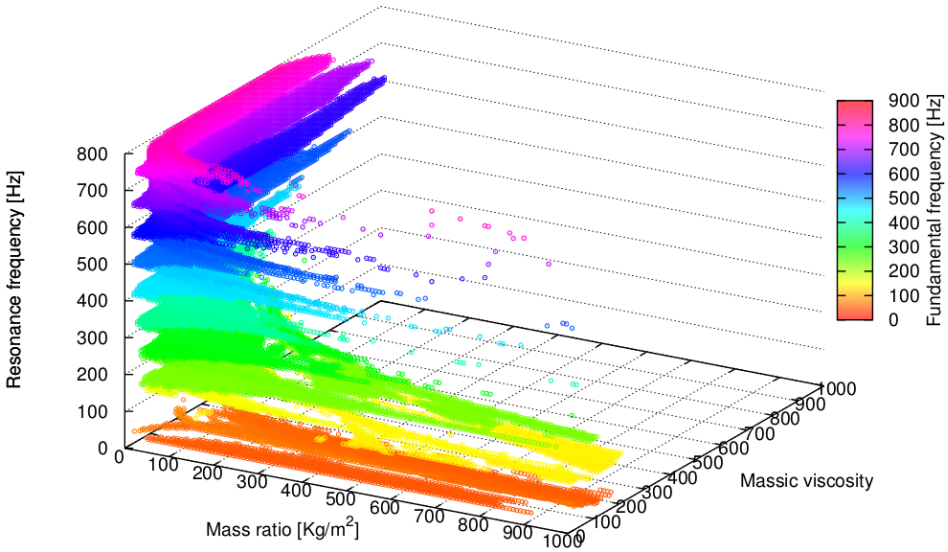

Figure 5.22: Variables space $\mathbf{X}^\sigma$ of the natural Eb trumpet with the sound pitch as parameter, obtained with the single value of blowing pressure $P_m = 9$ kPa.

Notice that the values of the adimensional damping factor

$$\zeta_{L_{pqr}} = \frac{g_{L_{pqr}}}{2\omega_{L_{pqr}}} \tag{5.45}$$

related to the solutions, do not exceed 0.15 for all the notes with the exception of the pedal–tone and the first note, as shown in Fig. 5.23.

[17] Obviously, the generality of the approach adopted in this chapter makes possible the application of the criteria presented in the next sections to all the values of blowing pressure $P_{m\,s}$.

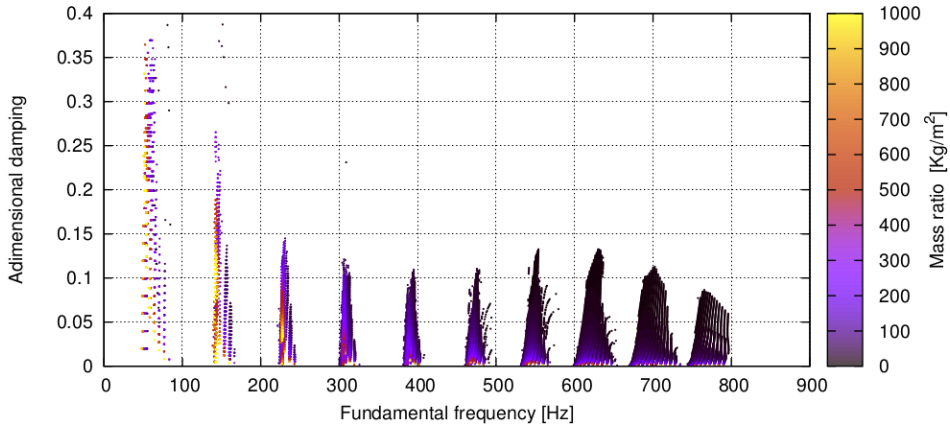

Figure 5.23: Adimensional damping factor as a function of the sound pitch with the mass ratio as a parameter, related to the variables space $\mathbf{X}^{\sigma}$ of the natural Eb trumpet, obtained with the single value of blowing pressure $P_m = 9$ kPa.

5.4.2 The lip behaviour

The motion of the lip inside the cup of the mouthpiece, which represents the excitation system, is a very complex phenomenon. In the reality the motion of the lip is such that it performs moderate shifts and is characterized by intermittent closure. It was noticed that the physical model, as will be detailed below, provides solutions that do not satisfy those conditions. In this section will be explained the methods aimed at constrain the exciter behaviour into the physical bounds.

Maximum displacement

The one–dimensional models traditionally [2] employed to describe the physics of the lips,[18] model these last making use of a linear spring forced by both the mouth pressure and the vibration of the air column. More sophisticated anatomy–based models [26] describe the lip motion through two nonlinear differential equations whose variables are the lip physical length and the inclination with respect to the plane defined by the cup of the mouthpiece.

Irrespective of the model, the lip displacement described by the variable $y(t)$ (see Eq. 3.24), in the practice is quite small, in the order of a few millimetres for the lowest notes and a few tenths of a millimetre for the higher. Nevertheless, as mentioned above, the physical model simulates self–sustained oscillations involving lip displacements far above the physical, as shown in Fig. 5.24.[19]

[18] Known as *outward–striking* and *upward–striking*.

[19] Actually it was noticed that the percentage of such solutions is really small.

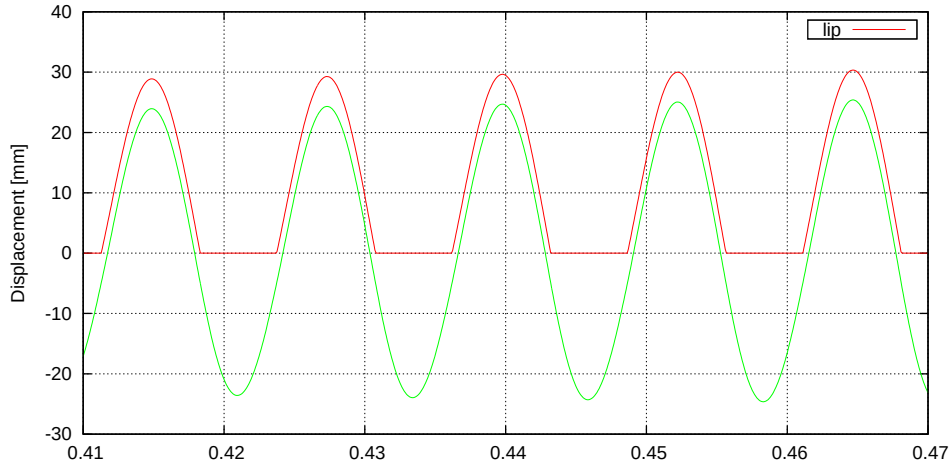

Figure 5.24: Oscillations $\xi(t)$ and lip displacement $y(t)$ related to a self–sustained solution without the constraint of the maximum displacement.

It was noticed that the maximum displacement of the lip decrease with the increasing of the sound pitch. Such a behaviour points up that wide movements at high frequencies are not conceivable, indeed the solutions characterized by displacements not even compatible with the geometric size of the mouthpiece are only related to the pedal–tone and the first two notes (G_1, D_3 and Bb_3). In addition, as evidenced in Fig. 5.25, correspond to plausible displacements many solution related to all the notes, this implies that it seem possible to bound the solutions within a range of displacement physically feasible.

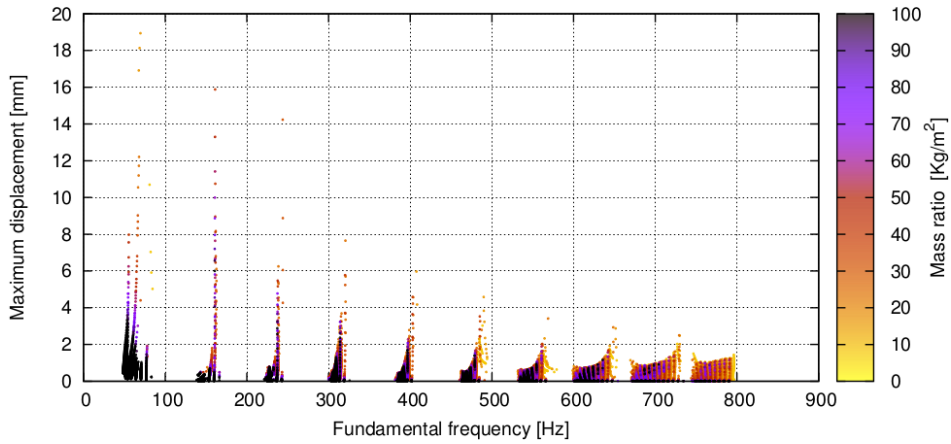

Figure 5.25: Maximum lip displacement as a function of the sound pitch with the mass ratio as a parameter, related to the variables space $\mathbf{X}^{\sigma}$ (sustained solutions within the hearing–range) of the natural Eb, with $P_m = 9$ kPa.

Notwithstanding some consideration must be done. First of all, as mentioned above, though the player lip has very small movements, much lower than the cup

size, it seems complicated to introduce a fixed value within which considering the displacement as acceptable. It is also awkward to establish an unambiguous rule to link the maximum admissible displacement to the other variables of the *performance* space, or rather to the pitch of the sound. Nevertheless, defining

$$\delta_y := \frac{\max[y(t)]}{R_{cup}} \tag{5.46}$$

being R_{cup} the radius of the mouthpiece cup, imposing the pure geometrical constraint

$$\delta_y < 1 \quad \forall t \tag{5.47}$$

seems reasonable with the purpose of excluding the solutions involving preposterous displacements, such as the one presented in Fig. 5.24, where one can see a maximum displacement of about 30 mm against a cup radius of less than a centimetre. The variables space plot of Fig. 5.26, using the pitch the maximum value of the maximum lip displacement δ_y as parameter, highlights a strong regularity in the distributions of the latter.

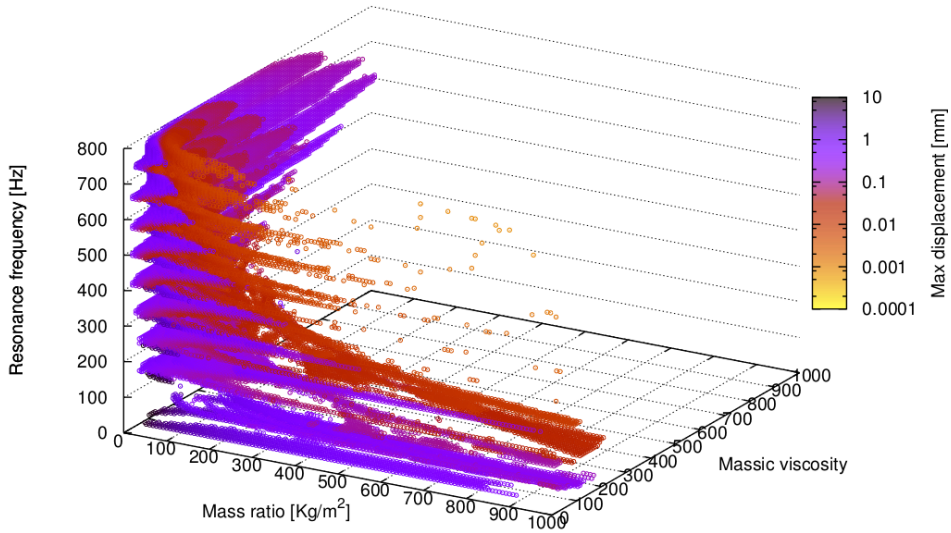

Figure 5.26: Variables space $\mathbf{X}^{\sigma}$ of the natural Eb, with $P_m = 9$ kPa, obtained constraining the maximum lip displacement, with the maximum lip displacement as parameter.

The *buzzing* issue

Several studies concerning the motion of the lips [25, 19, 83, 58, 15] have been carried out, many of these taking advantage from photographic techniques (see Fig. 5.27), in order to achieve a proper model for the time–dependent behaviour of both the upper and the lower lip.

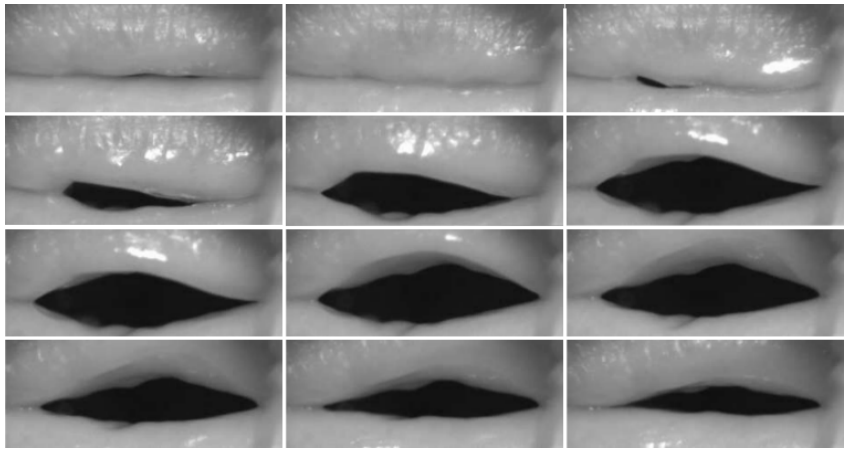

Figure 5.27: Series of images from a digital high–speed film visualizing the lip separation during the performance of a note with a brass instrument [15].

The self–oscillating motion of the musician lips during the performance of any note is characterized by intermittent closure, which implies the locking of the inflow through the player's lips: subsequently the pressure gradient, due to the blowing pressure P_m, between the player's mouth and the resonator is such that the lips open again starting over the loop.

Given the above, it was noticed that many of the solutions provided by the models, may be such that the lips never close. Moreover, it is worth noting that the vast majority of the high–pitched non–buzzing solutions are related to microfluctuations of the valve, as shown in Fig. 5.28.

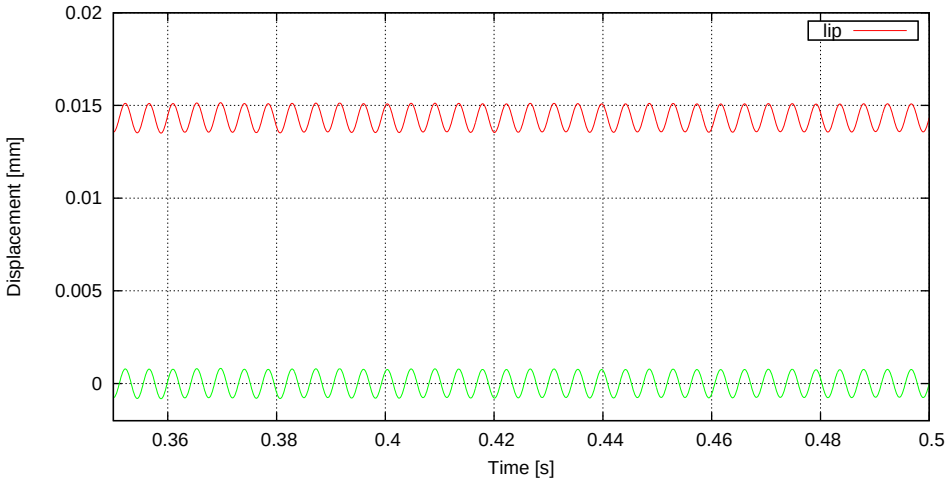

Figure 5.28: Oscillations $\xi(t)$ and lip displacement $y(t)$ related to a high–pitched non–buzzing solution.

Instead, as illustrated in Fig. 5.29 to the low–pitched non–buzzing solutions

pertain proper displacements, compatible with the physics of the case study.

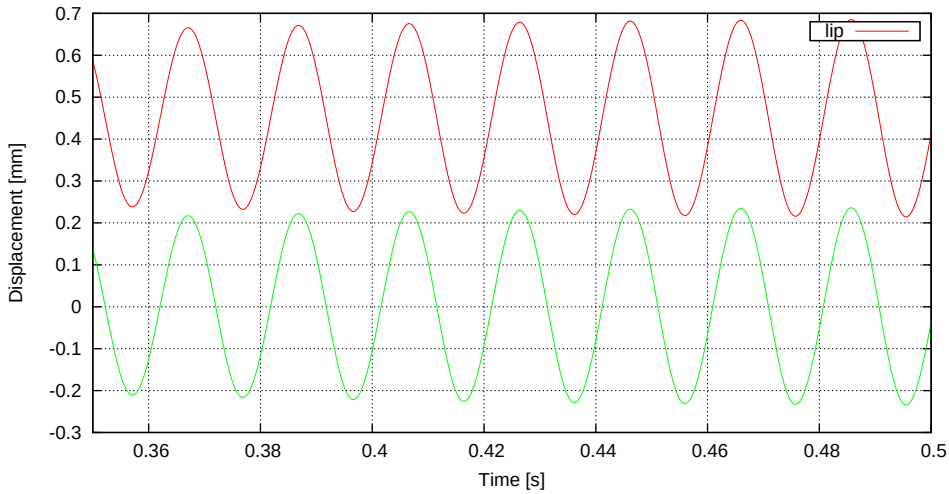

Figure 5.29: Oscillations $\xi(t)$ and lip displacement $y(t)$ related to a low–pitched non–buzzing solution.

In order to take into account the performing technique, admitted that the specific spot $\mathbf{x}_{pqr}$ in the variables space can be consistent with the mechanical properties of the lips, seems necessary to verify the simulated lips behaviour emulate the lifelike performance.

Note that, recalling the Eq. 3.25, a condition can easily be formalized in terms of phase–trajectory. In fact, the analysis of the Fig. 5.30 highlights that the valve motion keeps the lip opened if the limit–cycle of the phase–trajectory not include the initial condition.

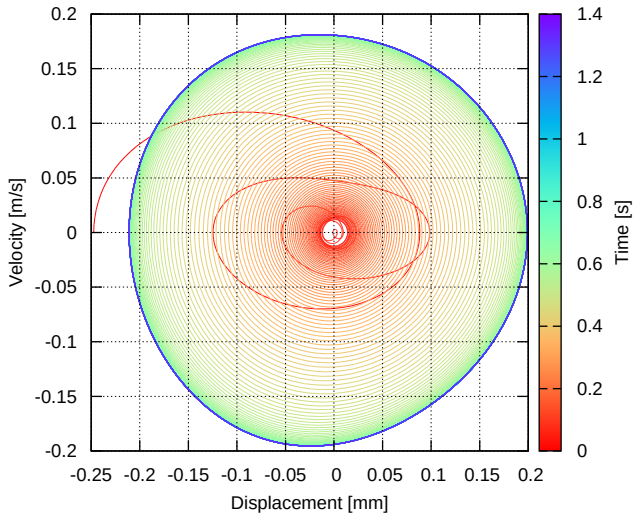

Figure 5.30: Phases–trajectory related to a non–buzzing solution.

Let so define a condition on the coefficient β_y in the lip reference system, aimed at the identification in the phases–plane of the horizontal distance between the limit–cycle the initial condition $(-P_m/(\mu\omega^2), 0)$, as follows

$$\beta_y := \frac{P_m}{\mu\omega^2} + \min\left[\xi(t)\right]_k, \quad \forall k > 1 \tag{5.48}$$

being k the reference number of the spire of the phase-trajectory. It is easy to note that the more decrease C_β, the more the lips tends to a buzzing behaviour. In these terms a slight regularity in the distribution of the spots in the space of the non–buzzing solutions, as shown in Fig. 5.31, may be found, meaning that the lower is the pitch frequency the greater is the distance between the limit–cycle and the coordinates of the initial conditions.

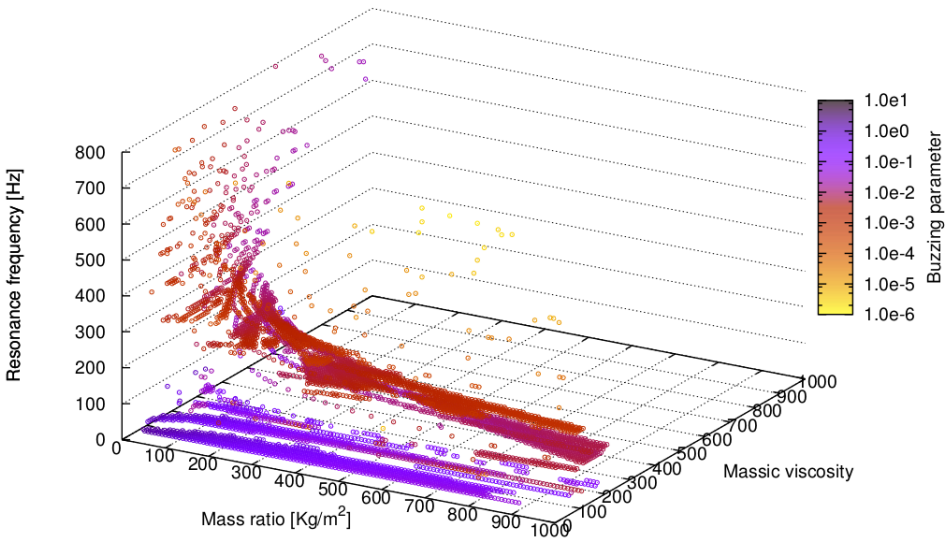

Figure 5.31: Non–buzzing solutions in the variables space $\mathbf{X}^\sigma$ of the natural Eb trumpet, with $P_m = 9$ kPa and constraint on the maximum lip displacement, with the buzzing coefficient β_y as parameter.

By giving a suitable condition on β_y (see Eq. 5.48), such as

$$\beta_y \leq 0 \tag{5.49}$$

the non–buzzing solution can be easily discarded. It is interesting to note that, as shown in Fig. 5.31 and Fig. 5.32, the discarded solution pertain almost to low–pitched sounds.

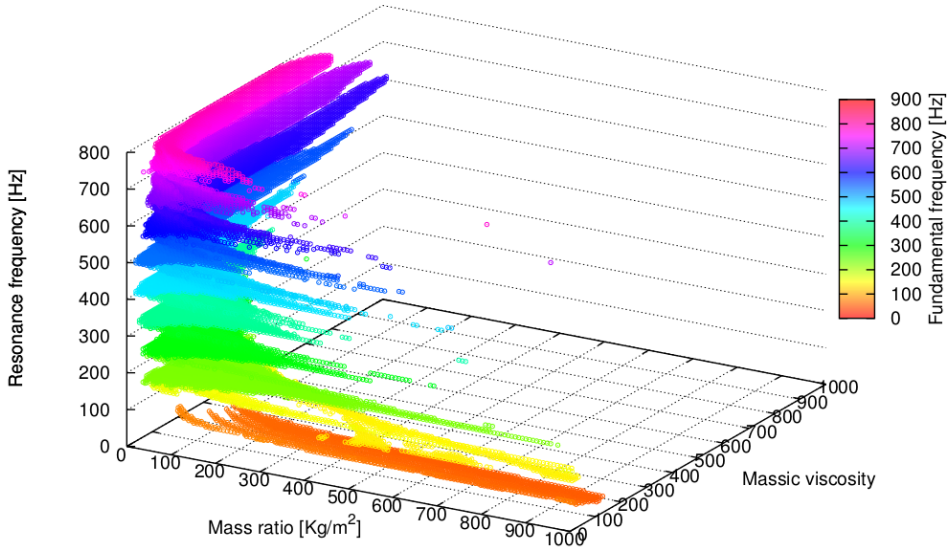

Figure 5.32: Buzzing solutions in the variables space $\mathbf{X}^{\sigma}$ of the natural Eb trumpet, with $P_m = 9$ kPa and constraint on the maximum lip displacement, with the sound pitch as parameter.

5.4.3 The pressure efficiency

The identification of a parameter aimed at taking into account the energetic content of the pressure signal come from the assumption that the goal of the musician during the performance is to emit the correct sound at the proper loudness with as little effort as possible. This consideration, as well as being compliant to the *principle of least action*,[20] is founded on the observation of the musical practice which often requires extreme duration. Let introduce a coefficient η_p with the purpose to take into account the baric restoration with respect to the blowing pressure during the performance. Since the pressure signal inside the embouchure is a zero–crossing periodic signal it seemed appropriate to define such coefficient as follow

$$\eta_P := \frac{1}{P_m}\sqrt{\frac{1}{T}\int_T [p(t)]^2 dt} = \frac{p_{rms}}{P_m} \tag{5.50}$$

being T the total time of the simulation.

It is interesting to highlights that, as shown in Fig. 5.33, the distribution η_p on the spots $\mathbf{x}_{pqr}$ manifest a remarkable regularity.

[20] In his *Accord de diffèrentes lois de la nature qui avaient jusqu'ici paru incompatibles* (1744), Pierre–Louis Moreau de Maupertuis asserts that "Nature is thrifty in all its actions", *i.e.* in all the changes that occur in the universe, the amount of action necessary for them is always the least possible.

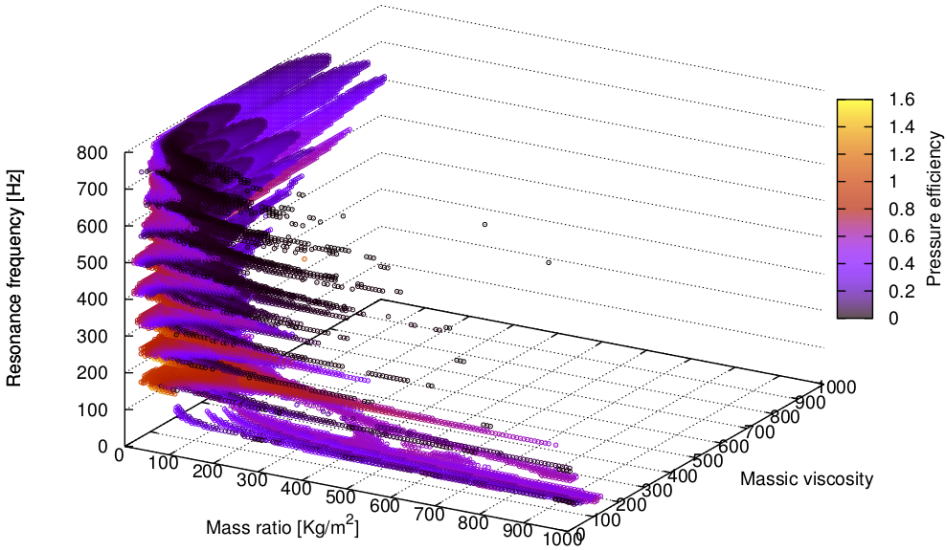

Figure 5.33: Variables space $\mathbf{X}^{\sigma}$ of the natural Eb trumpet, with $P_m = 9$ kPa and constraint on the lip behaviour (maximum displacement and *buzzing*), with the pressure efficiency η_P as parameter.

Moreover, as illustrated in Fig. 5.34, the pressure efficiency η_p is heavily linked to the maximum lip displacement, described above.

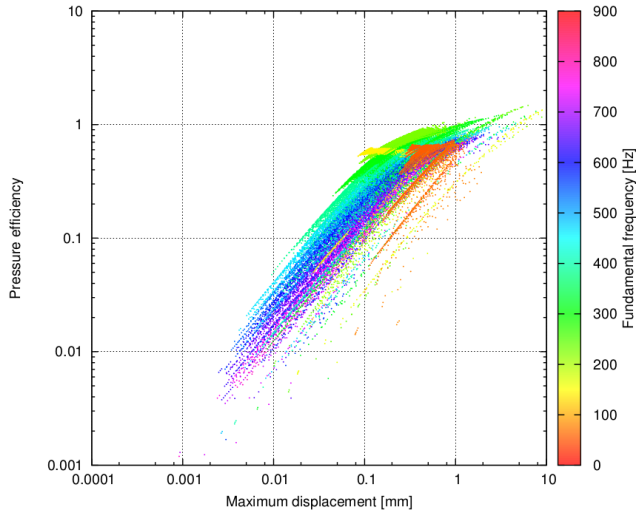

Figure 5.34: Pressure efficiency η_P as a function of the maximum lip displacement with the sound pitch as parameter, related to the variables space $\mathbf{X}^{\sigma}$ of the natural Eb trumpet, with $P_m = 9$ kPa and constraint on the lip behaviour (maximum displacement and *buzzing*).

It is also worth noting that the same note may be performed at different values of η_p, as shown in Fig. 5.35.

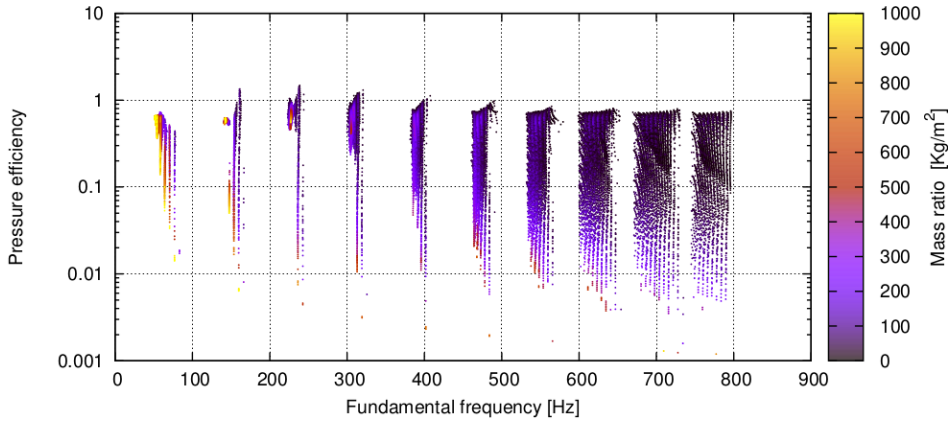

Figure 5.35: Pressure efficiency η_P as a function of the sound pitch with the mass ratio as parameter, related to variables space $\mathbf{X}^{\sigma}$ of the natural Eb trumpet, with P_m = 9 kPa and constraint on the lip behaviour (maximum displacement and *buzzing*).

The pressure efficiency described above is based on energetic observations, and assign a prefixed value beneath which considerate the performance strenuous is not straightforward: however, for the purpose of examine the effect of such parameter on the spot distribution in the variable space, let hypothesize that η_p should never fall one order of size below the unit

$$\eta_p \geq 0.1 \tag{5.51}$$

The variables space further constrained by η_p is presented in Fig. 5.36,

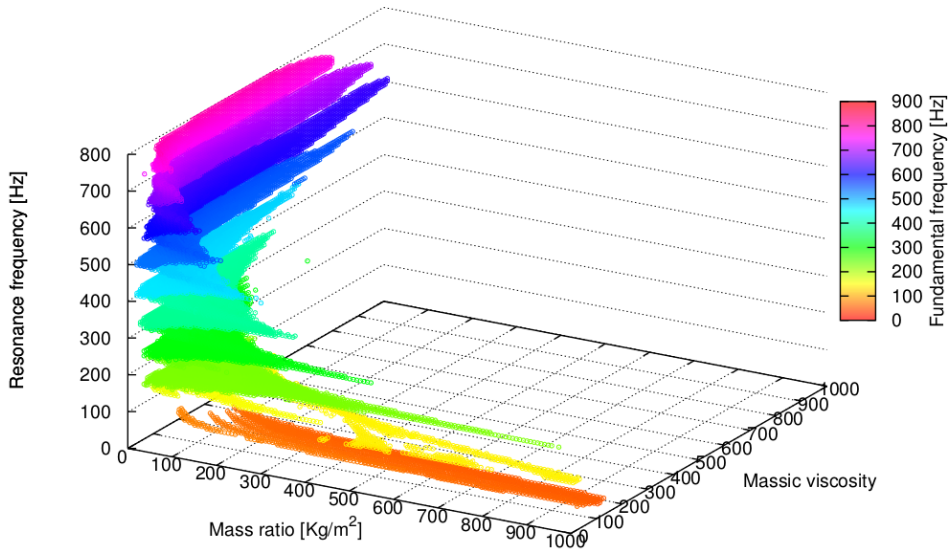

Figure 5.36: Variables space $\mathbf{X}^{\sigma\phi}$ of the natural Eb trumpet with P_m = 9 kPa (sustained solution within the hearing–range with all the physical constrains), with the sound pitch as parameter.

5.5 Musical properties of the solution

In this section will be derived the space of the *performance* sounds, via the identification of the musically–relevant properties of the solutions. Such properties concern the characteristics of the sounds in terms of perceived attack–time length and "cleanliness" of the note, being the latter derived from the analysis of the pitch fluctuations. Two criteria aimed at the control of the timbrical characteristics of the sound will be defined, giving rise to the musical solutions space $\mathbf{P}^M$, within which the abovementioned properties are prescribed.

The intersection between $\mathbf{P}^S$, $\mathbf{P}^F$, under the condition that such sounds fall within the hearing–range, and $\mathbf{P}^M$

$$\left[\mathbf{P}_{hr} \cap (\mathbf{P}^S \cap \mathbf{P}^F)\right] \cap \mathbf{P}^M \tag{5.52}$$

gives rise to the space $\mathbf{P}^\pi$ of the *performance* sounds, *i.e.* sustained oscillations within the hearing–range, physically feasible and attributable to a brass instrument.

5.5.1 Attack–time estimation

Believe that the waveform is the main discriminant for the recognition of musical sounds is a very common mistake. Actually, as demonstrated by several studies, the starting transient is of paramount importance in the differentiating the sounds performed by different instruments [52, 39, 85, 51].

There exist several definition of "attack–transient", since a sound event can be characterized by many types of non–stationarity. Typically it consist in burst of energy, which causes a fast change of the sound characteristics and can contain non-periodic components with a greater involvement of high–frequency components [69]. Lot of methods aimed at the attack–transient detection were developed, and such techniques frequently lead to significantly different results. The main strategies for the identification of the transient can summarized into three classes [21]. To the first class pertain the algorithms based on the linear prediction: such time–domain methods are based on the identification of a suitable resonating filter through which it is possible to recognize the bulk of the energy of the excitation signal which is exactly located at the transient. The second group of methods extract from the signal the sinusoidal part and identify the bursts of energy, specific of the attack transients, from the residual signal. Lastly, the third class of methods, the so–called *STN* (Sines–Transients–Noise) models, hypothesize explicit models for the transient behaviour and consider the signals as the superposition of a sinusoidal part, a transient and the residual component.

In this work its identification comes from the necessity to distinguish the sounds that are perceived as "*wah*" (long attack–times) from those that are perceived "*dah*" (short attack–times).[21] With this purpose let recall the Eq. 5.38, representing the

[21] Obviously there are an infinite number of sounds with different attack–times, and these two onomatopoeias have the sole purpose to give the impression of the percussive effect of the sounds.

standard deviation function related to the spiral areas enclosed by the phases–trajectory: since σ_n^ϕ is positive definite and by definition $\sigma_1^\phi = 0$, it must be that $\sigma_2 - \sigma_1 > 0$. If the Eq. 5.40 is satisfied there must be at least a maximum between $n = 1$ and $n \to \infty$. The absolute maximum of σ_n^ϕ occurs at $t^{\sigma_{max}^\phi}$ and from here the transient can be considered extinguished, since the limit–cycle stabilizes or fluctuates around a constant mean value. Such a time instant occurs at the sample

$$n^{\sigma_{max}^\phi} = \arg\max\left(\sigma_n^\phi\right) \tag{5.53}$$

thus at the time

$$t^{\sigma_{max}^\phi} = n^{\sigma_{max}^\phi}\Delta t \tag{5.54}$$

The behaviour of the standard deviation function σ_n^ϕ up to the time instant $t^{\sigma_{max}^\phi}$ can be approximated by a generic sigmoid function, such as

$$S(t) = \frac{\max\left(\sigma_n^\phi\right)}{1 + c_1 e^{(-c_2 t + c_3)}} \tag{5.55}$$

being c_1, c_2 and c_3 suitable coefficients minimizing the L^2 norm between σ_n^ϕ and the discrete representation of $S(t)$ between the origin and $t^{\sigma_{max}^\phi}$. The second derivative of $S(t)$, *i.e.* the change of concavity of the sigmoid function, crosses the zero at the time instant τ_ϕ when the function a_n^ϕ (see Eq. 5.36) almost reaches the maximum value, as shown in Fig. 5.37.

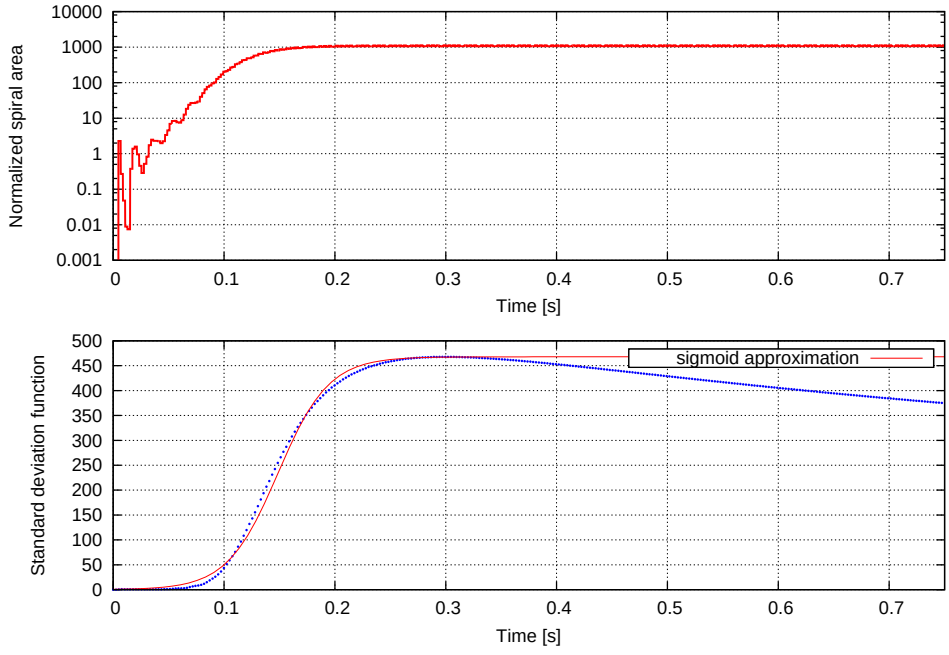

Figure 5.37: Time–history of the spiral areas A_k^ϕ divided by the initial area A_0^ϕ, standard deviation function σ_n^ϕ and sigmoid approximation, related to a self–sustained signal.

Then τ_ϕ will be considered as the attack–transient, and for the symmetry of $S(t)$

$$\tau_\phi = \frac{t^{\sigma^\phi_{max}}}{2} = \frac{\Delta t}{2}\left[\arg\max\left(\sigma^\phi_n\right)\right] \tag{5.56}$$

The distribution of the τ_ϕ in the variables space is quite regular (see Fig. 5.38).

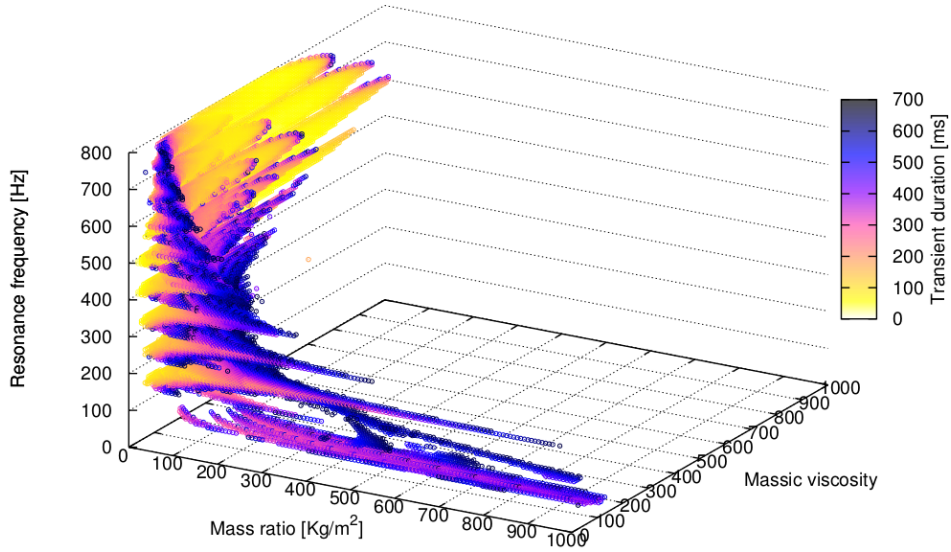

Figure 5.38: Variables space $\mathbf{X}^{\sigma\phi}$ of the natural Eb trumpet with $P_m = 9$ kPa, with the attack–time τ_ϕ as parameter.

Noting that the attack time is linked to the sound pitch, as shown in Fig. 5.39, and can be noted even a dependence from the adimensional damping factor, especially for the high–pitched sounds.

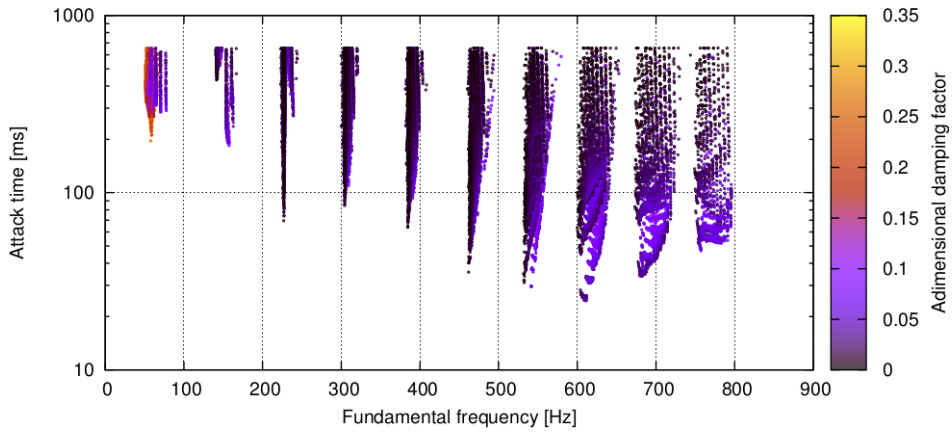

Figure 5.39: Attack time as a function of the sound pitch, with the adimensional damping factor as parameter, related to the variables space $\mathbf{X}^{\sigma\phi}$ of the natural Eb trumpet with $P_m = 9$ kPa.

It seems not easy to establish an univocal value of τ_ϕ with the purpose of identify the sound of the brasses, since it is strongly dependent by the dynamic of the performance, as summarized in Tab. 5.2

	Trombone	**Trumpet**
pianissimo	70-250 ms	40-60 ms
fortissimo	40-50 ms	25-35 ms

Table 5.2: Typical ranges of attack–times of the trombone and the modern trumpet related to the dynamics *pianissimo* and *fortissimo*.

Thus it is reasonable to impose a suitable range, as

$$25 \text{ ms} \leq \tau_\phi \leq 250 \text{ ms} \tag{5.57}$$

The variables space results now further restricted, as shown in Fig. 5.40.

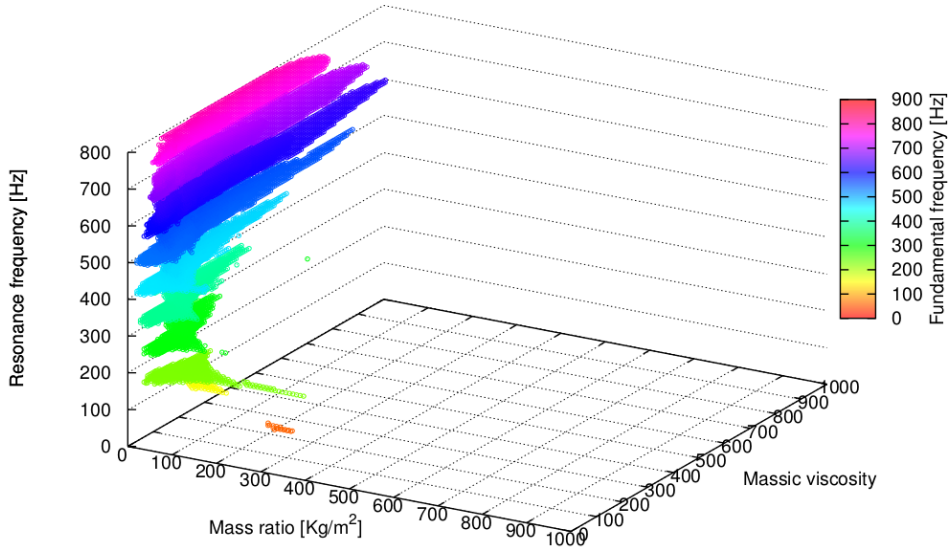

Figure 5.40: Variables space $\mathbf{X}^{\sigma\phi}$ of the natural Eb trumpet with $P_m = 9$ kPa, constrained with a maximum and minimum attack–time 25 ms $\leq \tau_\phi \leq$ 250 ms, with the sound pitch as parameter.

It is interesting to note that the pedal–tone almost disappear, this could mean that is quite improbable to play this note within the imposed range of attack–times.

5.5.2 Pitch quality factor

The motion of contraction and relaxation of the limit–cycle leads to the fluctuation of the spectral components of the sound: such fluctuations confers authenticity, since the perception of the sounds is highly related the spectral dynamics.

As explained above, the pitch of the simulated sounds is *runtime* estimated as the geometric mean of a current pitch (see Fig. 5.41), computed as the inverse of the fundamental period (see Eqs. 5.18 and 5.19).

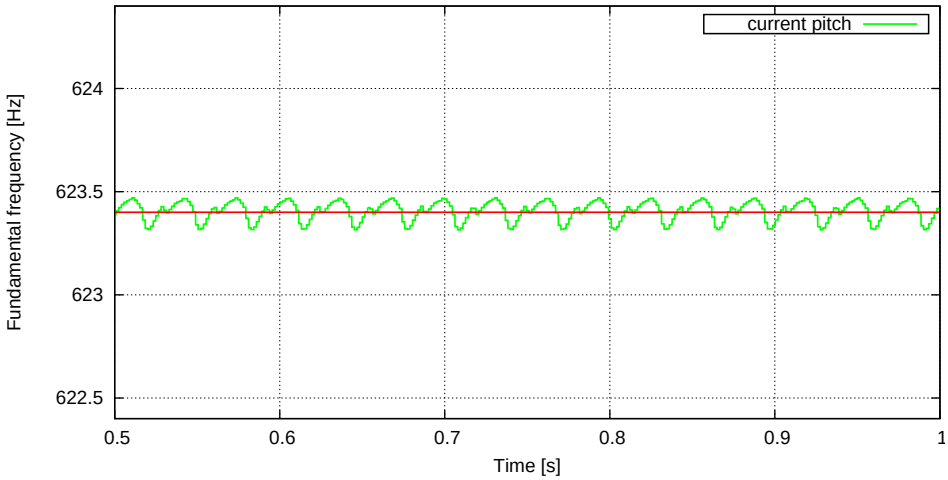

Figure 5.41: Pitch fluctuation related to the Eb_5 performed with the natural Eb.

Since the perceived frequency increase an octave with every doubling in frequency, the absolute value of the amplitude of pitch oscillations appears to be almost meaningless. Indeed an amplitude range of few Hertz proves to be imperceptible for high–pitched sounds and quite discernible for low–pitched sounds.

It is also worth noting that the estimation of the pitch fluctuation must be carried out downstream of the attack–time since, as detailed above, from the starting of the sound up to the end of the attack–transient, high–frequency components are involved [69] (see Figs. 5.3 and 5.4).

Given this, with the aim of quantify the amplitude of the pitch oscillations let consider the maximum value $f^c_{0\,max}$ and the minimum value $f^c_{0\,min}$ of the current pitch downstream of the attack–time, and let define the pitch precision ε^{f_0} as follows

$$\varepsilon^{f_0} = \max\left[\left(\frac{f_0}{f^c_{0\,min}}\right), \left(\frac{f^c_{0\,max}}{f_0}\right)\right]_{t>\tau_\phi} \tag{5.58}$$

being f_0 the mean pitch evaluated at the end of the simulation. Using ε^{f_0}, recalling the Eq. 5.23, it is possible to express the precision in terms of half–tones. Let hypothesize that for a good sound,[22] the range of oscillation of the current pitch with respect to de sound pitch must not exceed the quarter–tone,[23] by the imposition of

$$\varepsilon^{f_0} \leq \sqrt[24]{2} \tag{5.59}$$

[22] As detailed before, the meaning of "good" must be intended in the view of seeking of the *performance* sounds.

[23] With assumption can be justified that starting form the half–tone a change of note is percieved.

This assumption allows to discard the solutions, as the one in Fig. 5.42, whose current pitch f_0^c falls outside the tolerance.

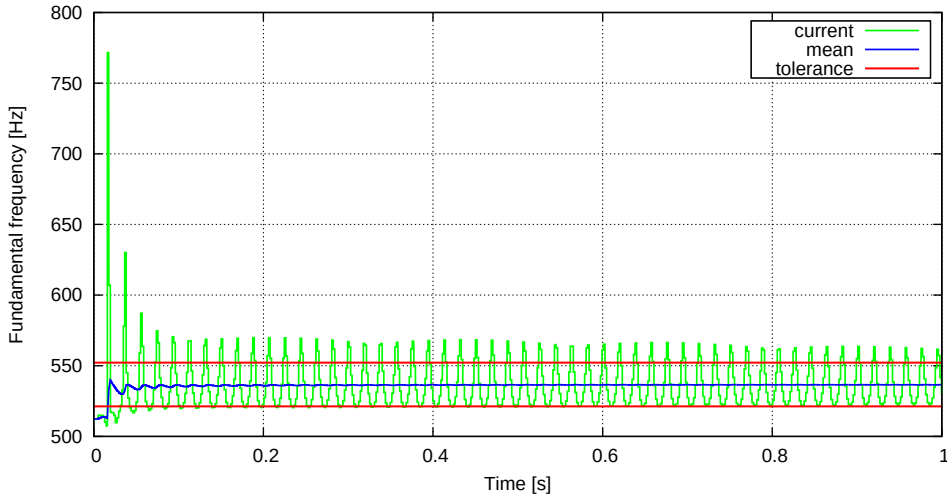

Figure 5.42: Pitch fluctuation falling outside the prescribed tolerance of a quarter–tone, related to a note performed by the natural Eb trumpet.

Noting that in terms of phase–trajectory, such solution are related to the periodical change of limit cycle, as shown in Fig. 5.43

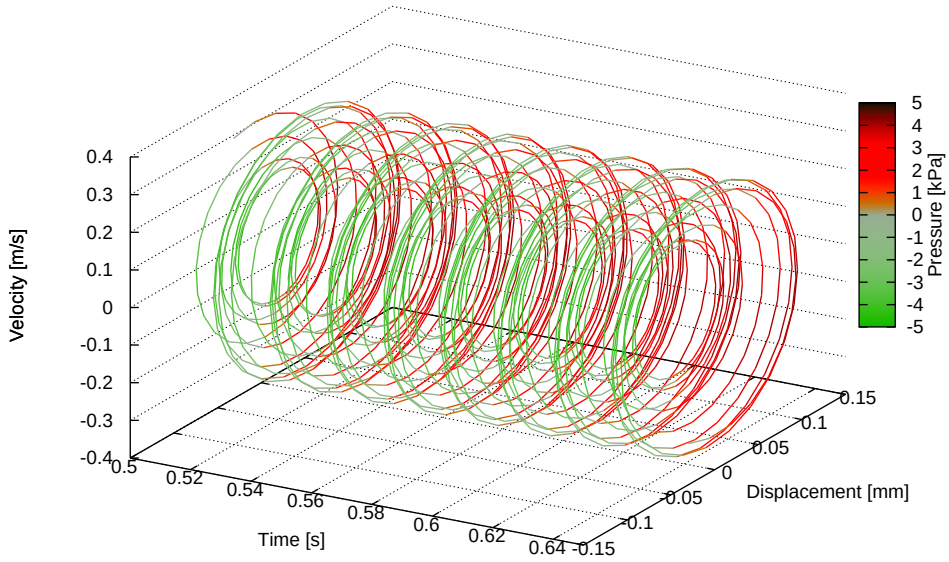

Figure 5.43: Phase–trajectory of a sound whose pitch fluctuation fall outside the prescribed tolerance of a quarter–tone, related to a note performed by the natural Eb trumpet.

5.6 The *performance* space

In the previous sections several criteria aimed at the recognition of the *performance* sounds have been developed. Such criteria have enabled the identification of several subspaces, within the global space of the parameter of the Eq. 3.24, which lead to time–dependent solutions characterized by

- periodicity within the hearing–range;
- self–sustained oscillations in the steady–state;
- feasible involved state variables;
- sounds relevant in terms of timbrical characteristics.

It is worth noting that the identification of the subspaces of $\mathcal{X}$ satisfying the above-mentioned characteristics is aimed at the research of the the *performance* space $\mathcal{X}^{\pi}$ which represents the set of the locations of the space of the parameters in which is positioned an experienced musician during the performance. A summary of the criteria is listed in Tab. 5.3.

Subspace	Motivation	Description	Formalization
$\mathbf{X}_{hr}$	Periodicity within the hearing–range	*Runtime* checking of the peaks (maxima)	Eq. 5.16
$\mathbf{X}^{S}$	Self–sustained oscillations in the steady–state	Phase–trajectory spiral areas analysis	Eqs. 5.33 and 5.41
$\mathbf{X}^{F}$	Feasible values of blowing pressure	Constraining the variables space	Eq. 5.43
	Lip displacement limited by the geometry	*Runtime* checking of the lip displacement	Eq. 5.47
	Buzzing behaviour of the lips (intermittent closing and opening)	Verification of the initial conditions inclusion by the phase–trajectory	Eq. 5.49
	Minimal musician effort	Checking of a suitable energetic index	Eq. 5.51
$\mathbf{X}^{M}$	Proper maximum attack–time length	Analysis of the standard deviation function	Eqs. 5.38 and 5.57
	Stable spectral behaviour (pitch oscillations)	Restriction of the maximum range of the pitch fluctuation	Eq. 5.59

Table 5.3: Summary of the criteria used for the recognition of the *performance* sounds.

The *performance* space of the natural Eb trumpet is so obtained by applying all the conditions of Tab. 5.3, and is presented in Fig. 5.44.

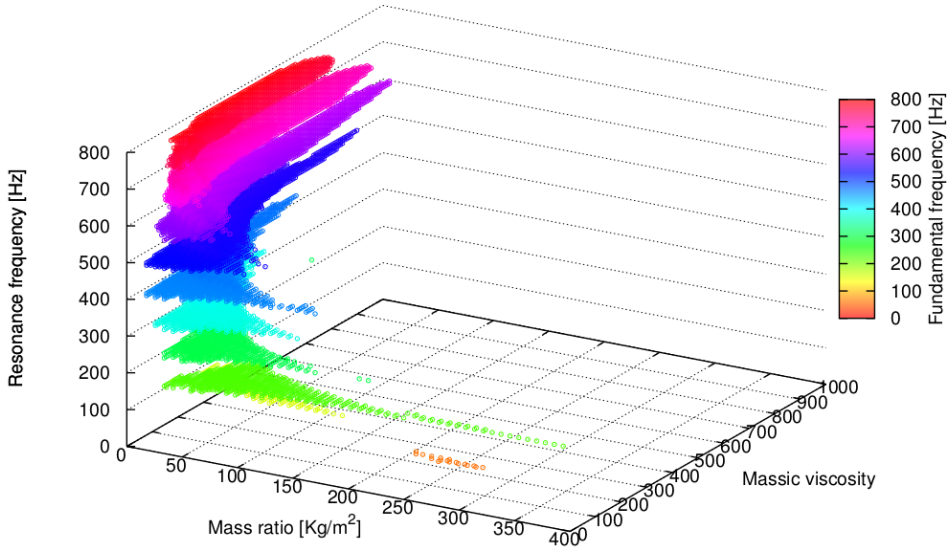

Figure 5.44: *Performance* space $\mathbf{X}^{\pi} = \left[\mathbf{P}_{hr} \cap (\mathbf{P}^{S} \cap \mathbf{P}^{F})\right] \cap \mathbf{P}^{M}$ of the natural Eb trumpet.

Note that the spots $\mathbf{x}_{pqr}$[24] of the *performance* space $\mathbf{X}^{\pi}$ manifest an asymptotic behaviour with respect to both the mass ratio μ_L and the massic viscosity g_L. The location related to the *performance* sounds are, in the (μ_L,g_L)–plane, superiorly limited by an hyperbola with the exception of the pedal–tone as shown in Fig. 5.45.

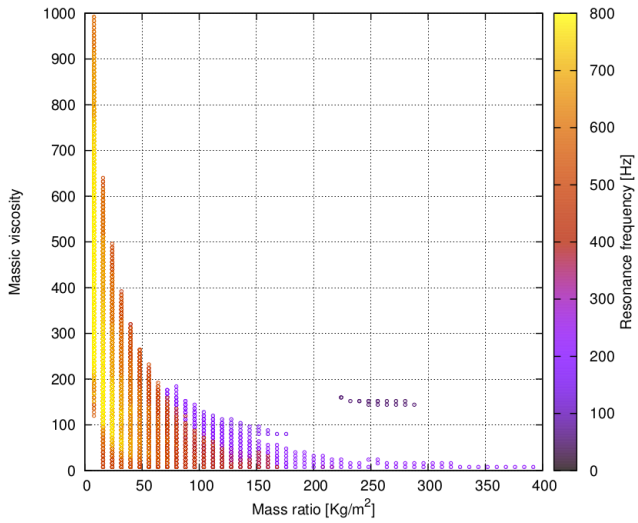

Figure 5.45: *Performance* space of the natural Eb trumpet: massic viscosity as a function of the mass ratio with the lip resonance frequency as parameter.

[24]The dependence of $\mathbf{x}_{pqrs}$ from P_m is removed by the imposition of a single value of blowing pressure $P_m = 9$ kPa (see Sect. 5.4.1).

Furthermore the distribution of the $\mathbf{x}_{pqr}$, as illustrated in Figs. 5.46 and 5.46 is such that coherent and separated structures are formed.

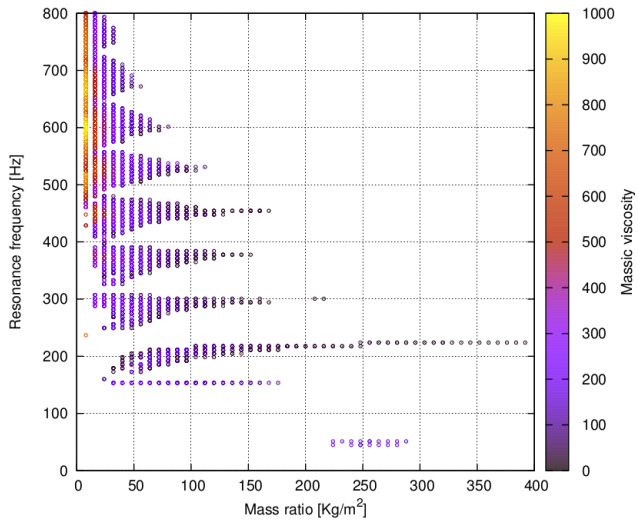

Figure 5.46: *Performance* space of the natural Eb trumpet: lip resonance frequency as a function of the mass ratio with the massic viscosity as parameter.

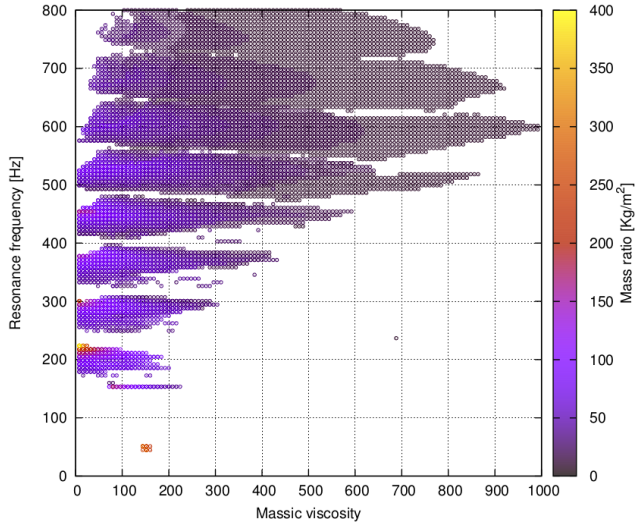

Figure 5.47: *Performance* space of the natural Eb trumpet: lip resonance frequency as a function of the massic viscosity with the mass ratio as parameter.

Such structures, as mentioned above, share common pitches as is evident from the analysis of Fig. 5.44, close to the maxima of the input impedance spectrum (see Fig. 5.18).

CHAPTER 6

The sound as an optimization problem

In this chapter will be defined an optimization problem for the identification, within the *performance* space, of the location that provides a solutions complying prefixed characteristics. Such characteristics deal with both physics of the involved state variables and the timbrical characteristics of the sound, and can be described with the criteria detailed in the Chap. 5.

6.1 Generalities

Seeking the coordinates in the *performance* space corresponding to a prefixed note, for a given blowing pressure, is not too easy. Indeed one can note that moving in the direction of the lips resonance frequency, small shifts can have large pitch variations, this because exist several directions of the space such that the function $\mathcal{F}$ (see Eq. 5.5) is discontinuous. The treatment of this issue as an optimization problem, allows to identify a certain sound starting from the selection of its characteristics.

A generic optimization problem (see App. C) yields the minimization of an objective function $J(\mathbf{x})$, while both the N_g inequality constraints $g_i(\mathbf{x})$ and the N_h equality constraints $h_j(\mathbf{x})$ are satisfied. In the event of N_J multiple objectives, one can be define an aggregate function $J^A(\mathbf{x})$ containing all the k–th objectives, each one adequately weighed. It is worth noting that instead of solving the constrained problem, it is possible to define a pseudo–objective function $\bar{J}(\mathbf{x})$ including the inequality constraints through the so–called *penalty function* method. Once the optimization problem is formulated, a numerical strategy for the optimum solution research must be used.[1]

[1] In this work the minimization is provided by a genetic algorithm. The used algorithm is based on the `FORTRAN` Genetic Algorithm (GA) by David L. Carroll.

In the following, both the single–objective and the multi–objective approaches will be detailed: the formalization of the objective functions and the constraints related to the case study is addressed using the criteria described in the Chap. 5.

6.2 Single–objective optimization

Since the target of the musician is the intonation of the note[2] it seems reasonable to set as the objective function the distance between the sound pitch f_0 and a target pitch f_0^T, hence

$$J(\mathbf{x}) = \frac{|f_0^T - f_0|}{f_0^T} \tag{6.1}$$

Regarding the constraints, note that if the time–varying pressure signal inside the embouchure violates the condition expressed by the Eqs. 5.16, 5.34, 5.35 and 5.41, the solution is automatically discarded and a penalty value is consequently given to the function $J(\mathbf{x})$. The Eqs. 5.47, 5.49 and 5.51 define the same number of constraints which ensure that the sound is *feasible* in physical terms: such constraint can be formalized as follows

$$\begin{aligned} g_1(\mathbf{x}) &= \delta_y - 1 < 0 \\ g_2(\mathbf{x}) &= \beta_y \leq 0 \\ g_3(\mathbf{x}) &= \frac{1}{10\eta_P} - 1 \leq 0 \end{aligned} \tag{6.2}$$

The Eqs. 5.57 and 5.59 provide the control on the sound properties (attack–transient and spectral fluctuations), and the following constraints are imposed

$$\begin{aligned} g_4(\mathbf{x}) &= \frac{\tau_\phi}{\tau_\phi^{max}} - 1 \leq 0 \\ g_5(\mathbf{x}) &= \frac{\epsilon_{f_0}}{\epsilon_{f_0}^{max}} - 1 \leq 0 \end{aligned} \tag{6.3}$$

6.2.1 Seeking *a note*: the G_4

As an example let impose as target frequency, in the Eq. 6.1, the frequency of the note G_4 which turns out to be the fourth peak of the input impedance spectrum of the E$\flat$ natural trumpet.

The maximum imposed attack–time length is ${\tau_\phi}^{max} = 250$ ms and the maximum pitch oscillation must be bounded in a quarter of tone, *i.e.* ${\varepsilon^{f_0}}_{max} = \sqrt[24]{2}$ (see Eq. 6.3) after the attack–transient. Must be also complied the constraints on the lip behaviour, *i.e.* on the maximum displacement and on the intermittent closure (see Eq. 6.2).

[2] Actually the intonation is just one of the targets, jointly the proper loudness and expression, then it would seem appropriate to set an optimization problem involving multiple objectives.

The convergence, as shown in Fig. 6.1, is achieved in about 500 generations, which is equivalent to $15 \cdot 10^3$ objective function evaluations, having been imposed a population size of 30 individuals.

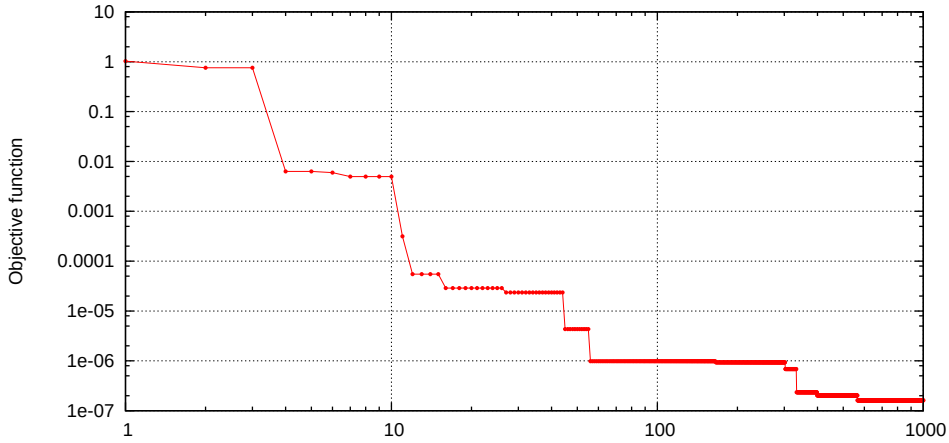

Figure 6.1: Convergence of the genetic algorithm for the single–objective optimization problem.

The progress of the variables with increasing iterations is illustrated in Fig. 6.2.

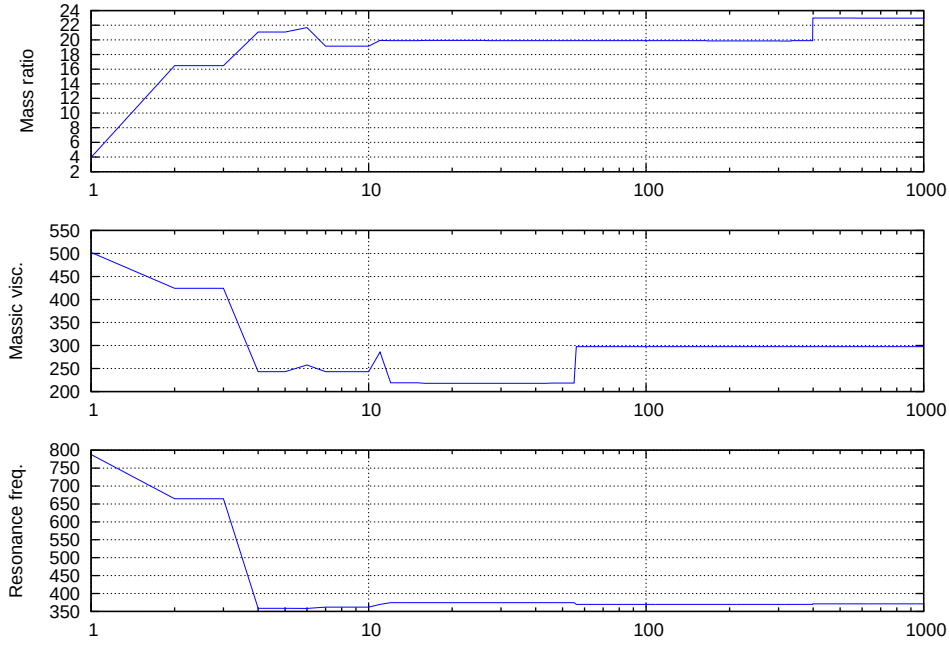

Figure 6.2: Progress of the design variables as a function of the index of generation for the single–objective optimization problem.

The optimal vector related to the single–objective optimization, in Tab. 6.1, is

such that the optimal point falls within the *performance* space (see Figs. 5.44, 5.46, 5.45 and 5.47).

μ_L	g_L	ω_L
22.97	297.4	2332

Table 6.1: Optimal solution of the single–objective optimization.

The optimal vector leads to an optimal solution whose characteristics are presented in Tab. 6.2.

f_0	391.76 Hz
δ_y	< 1
β_y	< 0
η_P	0.7181
τ_ϕ	146.67 ms
ϵ_{f_0}	1.0010

Table 6.2: Summary of the characteristics of the solution related to the optimal point of the single–objective optimization.

The state variables, *i.e.* the displacement, the inflow and the pressure at the inlet section of the instrument, as well as the time history of the sound pitch are presented in Figs. 6.3 and 6.4.

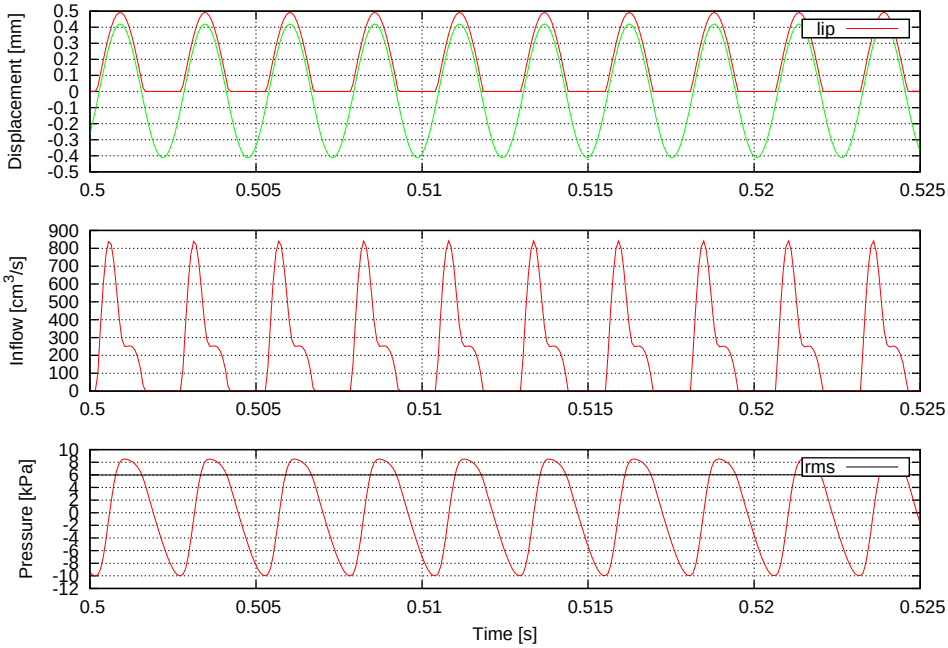

Figure 6.3: Optimal solution of a multi–objective optimization problem: lip displacement, inflow and pressure signal inside the embouchure related to the performance of the a G_4 with the E$\flat$ natural trumpet.

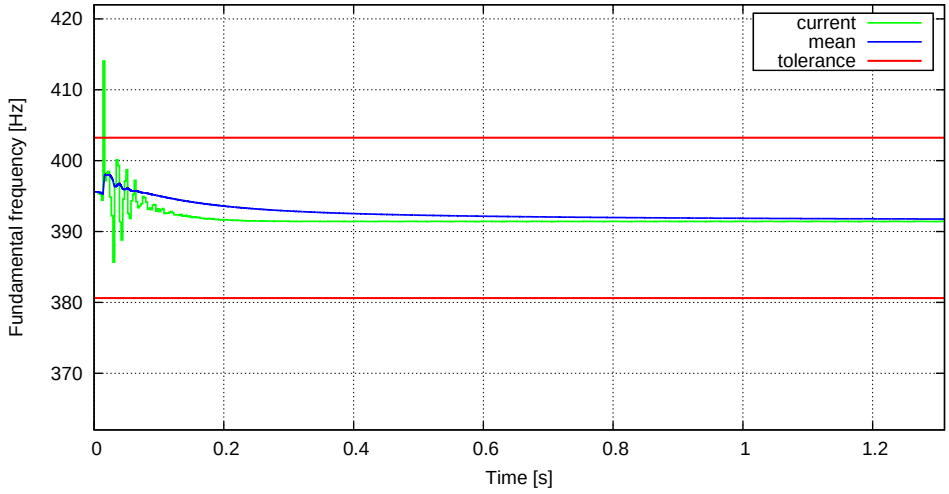

Figure 6.4: Optimal solution of the single–objective optimization problem: current pitch, mean pitch and tolerance related to the performance of the a G_4 with the E$\flat$ natural trumpet.

The sound is radiated to a virtual microphone located at distance $r = 2$ m with respect to the outlet section, with an offset $\alpha = 30°$ with respect to its longitudinal axis (see Sects. 2.3.1 and 3.3): the resulting waveform and the spectrum are shown in Figs. 6.5 and 6.6.

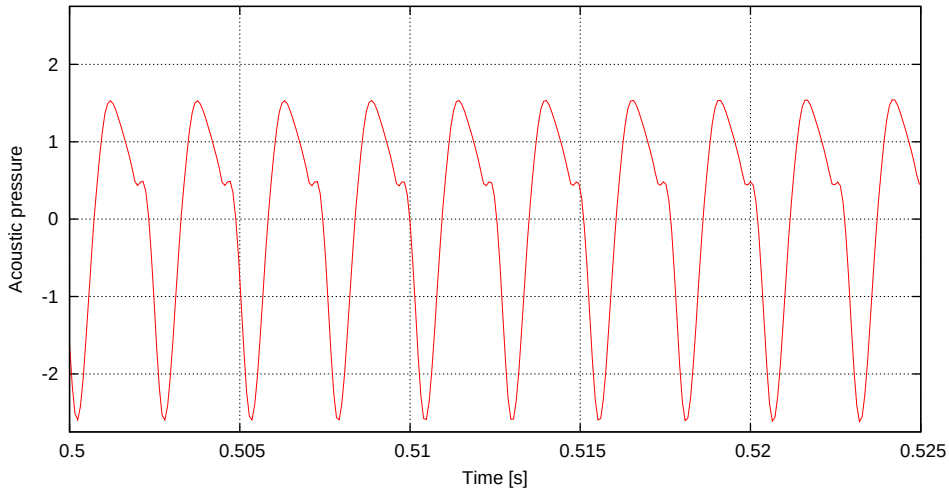

Figure 6.5: Optimal solution of the single–objective optimization problem: pressure signal at the virtual microphone located at distance $r = 2$ m with respect to the outlet section of the instrument, with an offset $\alpha = 30°$ with respect to its longitudinal axis, during the performance of the a G_4 with the E$\flat$ natural trumpet.

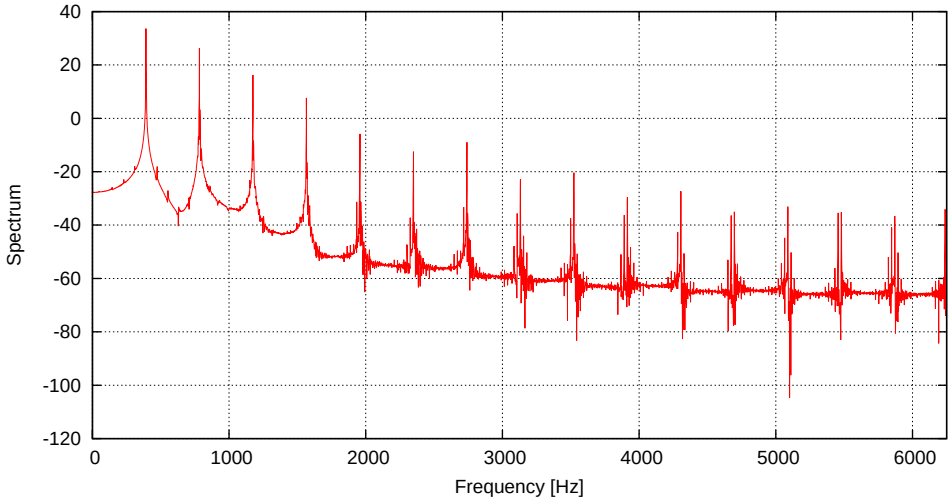

Figure 6.6: Optimal solution of the single–objective optimization problem: pressure spectrum at the virtual microphone located at distance $r = 2$ m with respect to the outlet section of the instrument, with an offset $\alpha = 30^\circ$ with respect to its longitudinal axis, during the performance of the a G_4 with the E$\flat$ natural trumpet.

Let now consider a simple model of head (see Sects. 2.3.2 and 3.3): the auralized signal related to two antipodal location of the head model located on the instrument axis at distance $d = 3$ m with respect to the outlet section of the resonator, is presented below with its pressure spectrum (see Figs. 6.7 and 6.8).

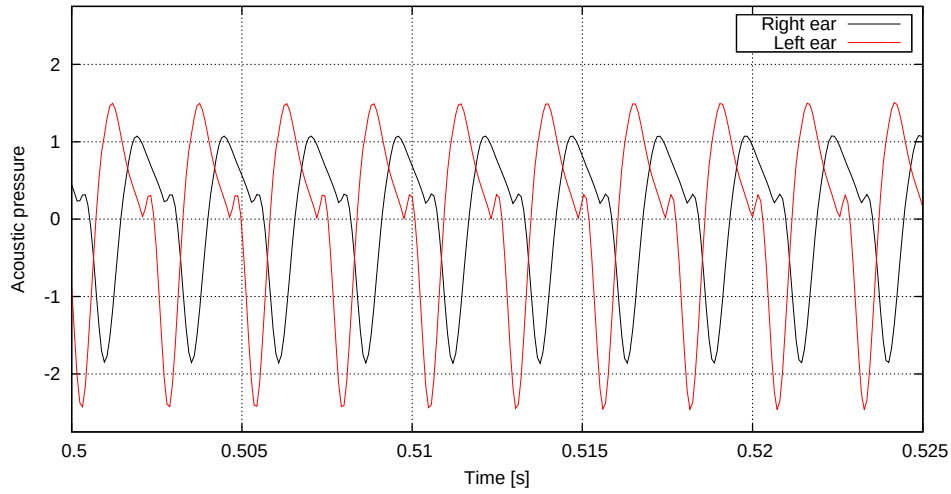

Figure 6.7: Optimal solution of the single–objective optimization problem: pressure signal at the ears of the listener related to a simple model of head located on the instrument axis at distance $d = 3$ m with respect to the outlet section of the resonator, during the performance of the a G_4 with the E$\flat$ natural trumpet.

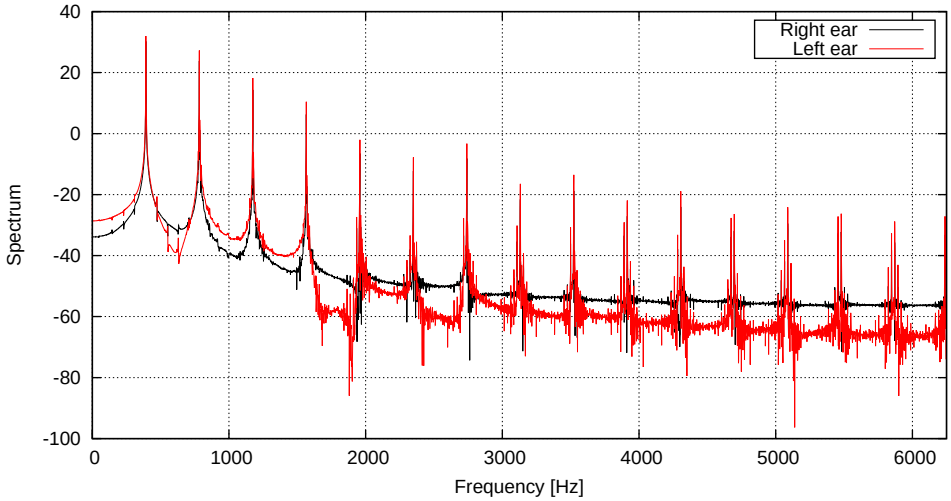

Figure 6.8: Optimal solution of the single–objective optimization problem: pressure spectrum at the ears of the listener related to a simple model of head located on the instrument axis at distance $d = 3$ m with respect to the outlet section of the resonator, during the performance of the a G_4 with the Eb natural trumpet.

6.3 Multi–objective optimization

The single–objective optimization problem, that has just been described, allows to find within the *performance space* the location which provides a signal with a prescribed pitch. Nevertheless the musical praxis requires a huge variety of emphasis during the performance, as the accents and the articulation, then the intonation (see Eq. 6.1) cannot be the only goal of the musician. The dynamic accents, for example, impose the control on the attack–time of the sound.[3]

Accordingly, it seems appropriate to treat the constraint $g_4(\mathbf{x})$ (see Eq. 6.3) as additional objective function, by imposing a target attack–time τ_ϕ^T. Furthermore the minimization of the musician effort (the constraint $g_5(\mathbf{x})$ of the Eq. 6.3), by maximizing η_P, is equally desirable.

$$\begin{aligned} J_1(\mathbf{x}) &= \frac{|f_0^T - f_0|}{f_0^T} \\ J_2(\mathbf{x}) &= \frac{|\tau_\phi^T - \tau_\phi|}{\tau_\phi^T} \\ J_3(\mathbf{x}) &= \frac{1}{\eta_P} \end{aligned} \tag{6.4}$$

The objectives $J_1(\mathbf{x})$, $J_2(\mathbf{x})$ and $J_3(\mathbf{x})$ are the goal of the multi–objective optimization problem, and the pseudo–objective function $\bar{J}(\mathbf{x})$ is completed by the definition

[3]The tonguing technique can help the the brass player to have a control on the attack–time of the sounds.

of the following constraints

$$\begin{aligned} g_1(\mathbf{x}) &= \delta_y - 1 < 0 \\ g_2(\mathbf{x}) &= \beta_y \leq 0 \\ g_3(\mathbf{x}) &= \frac{\epsilon_{f_0}}{\epsilon_{f_0}^{max}} - 1 \leq 0 \end{aligned} \tag{6.5}$$

with the aim of control the lip behaviour and the spectral fluctuations.

6.3.1 Seeking *the note*: the C$\#_5$

Let impose as target frequency, in the $J_1(\mathbf{x})$ of the Eq. 6.4, the frequency of the note C$\#_5$, *i.e.* the seventh peak of the input impedance spectrum of the Eb natural trumpet, whereas the target attack–time is ${\tau_\phi}^T = 50$ ms. Constrain the problem the conditions on the lip behaviour and the maximum pitch oscillation, which must be bounded within a quarter of tone, *i.e.* ${\varepsilon^{f_0}}_{max} = \sqrt[24]{2}$ (see Eq. 6.3).

The convergence, as shown in Fig. 6.9, is achieved in about 40 generations, that is equivalent to $12 \cdot 10^2$ objective function evaluations, having been imposed a population size of 30 individuals, as in the previous case.

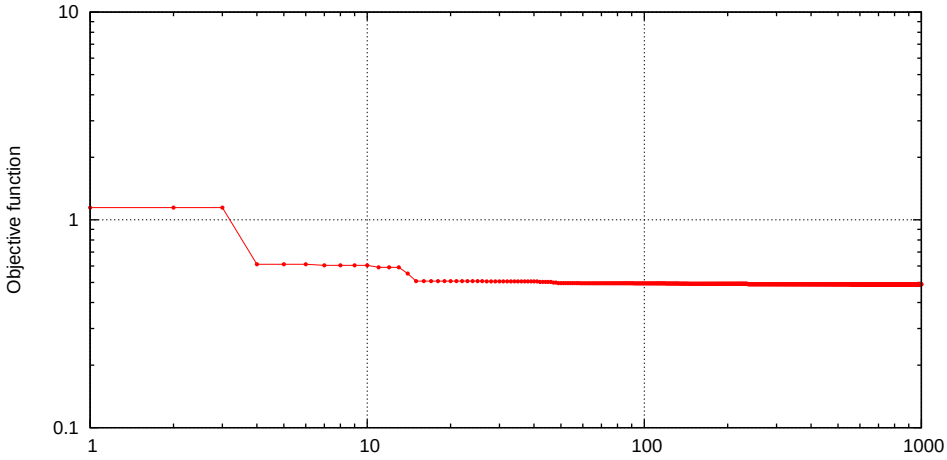

Figure 6.9: Convergence of the genetic algorithm for the multi–objective optimization problem.

It is important to note that the iterations needed for the convergence is slightly smaller with respect to the single–objective optimization, this because the co-domain is significantly restricted due to the identification of several objective functions.

Even in this case, as illustrated in Fig. 6.10, the optimal point falls within the *performance* space.

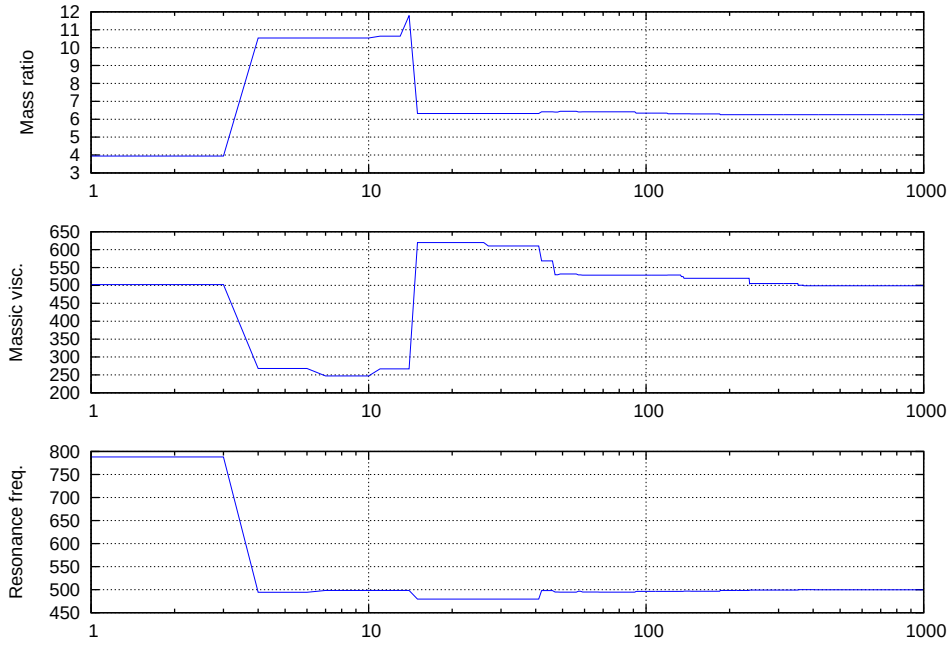

Figure 6.10: Progress of the design variables as a function of the index of generation for the multi–objective optimization problem.

The optimal vector related to the multi–objective optimization, in Tab. 6.3, is within the *performance* space (see Figs. 5.44, 5.46, 5.45 and 5.47).

μ_L	g_L	ω_L
6.250	498.1	3140

Table 6.3: Optimal solution of the multi–objective optimization.

The optimal vector leads to an optimal solution whose characteristics are presented in Tab. 6.4.

f_0	548.52 Hz
δ_y	< 1
β_y	< 0
η_P	0.7509
τ_ϕ	49.985 ms
ϵ_{f_0}	1.0014

Table 6.4: Summary of the characteristics of the solution related to the optimal point of the multi–objective optimization.

The lip displacement, the inflow and the pressure at the inlet section of the instrument are presented in Fig. 6.11 and the time history of the sound pitch is in Fig. 6.12.

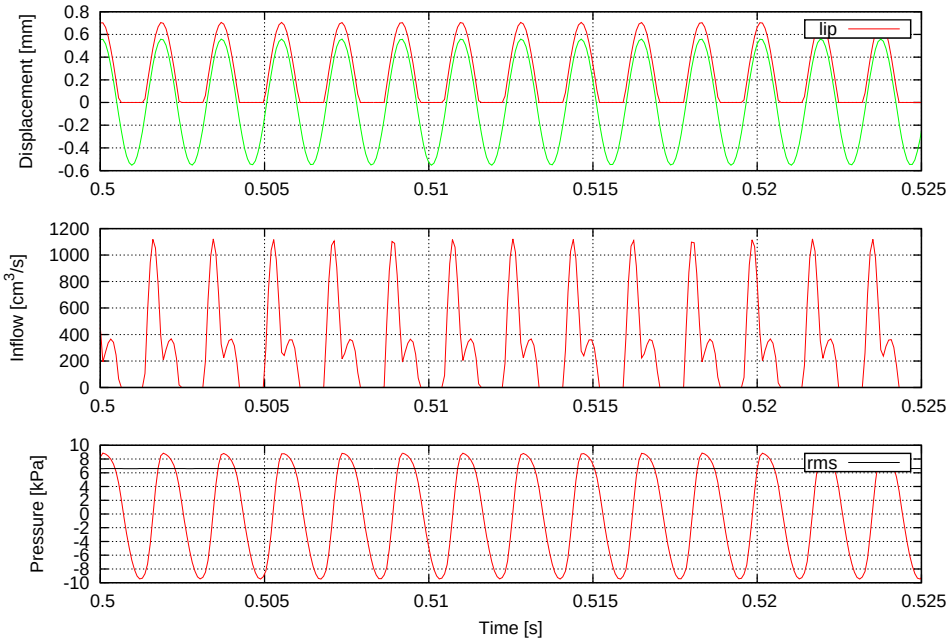

Figure 6.11: Optimal solution of a multi–objective optimization problem: lip displacement, inflow and pressure signal inside the embouchure related to the performance of the a C#$_5$ with the Eb natural trumpet.

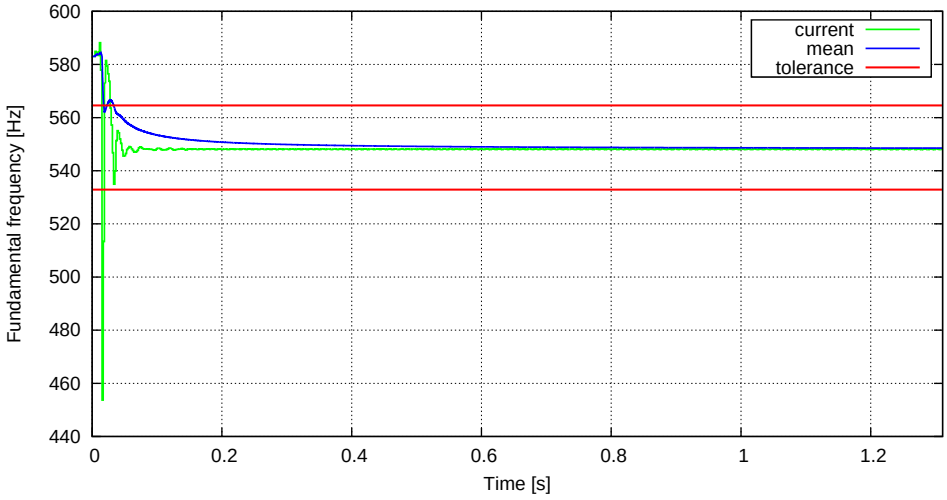

Figure 6.12: Optimal solution of a multi–objective optimization problem: current pitch, mean pitch and tolerance related to the performance of the a C#$_5$ with the Eb natural trumpet.

Let now radiate the sound, as done before, to a virtual microphone located at distance $r = 2$ m with respect to the outlet section, with an offset $\alpha = 30°$ with

respect to its longitudinal axis (see Sects. 2.3.1 and 3.3): the waveform and the pressure spectrum are shown in Figs. 6.13 and 6.14.

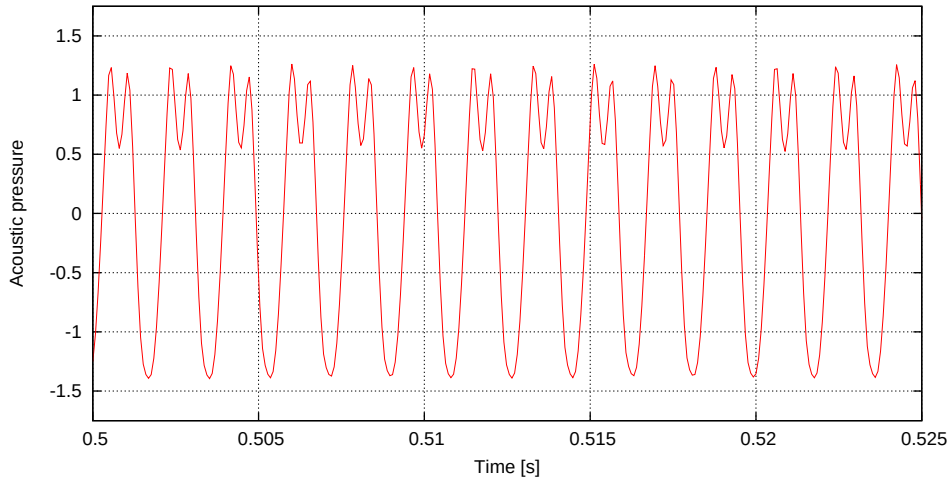

Figure 6.13: Optimal solution of the multi–objective optimization problem: pressure signal at the virtual microphone located at distance $r = 2$ m with respect to the outlet section of the instrument, with an offset $\alpha = 30^\circ$ with respect to its longitudinal axis, during the performance of the a C$\#_5$ with the Eb natural trumpet.

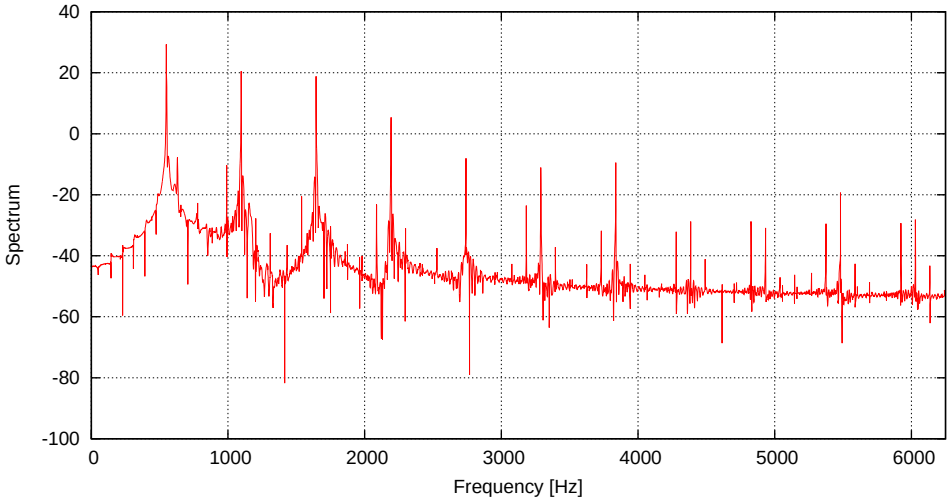

Figure 6.14: Optimal solution of the multi–objective optimization problem: pressure spectrum at the virtual microphone located at distance $r = 2$ m with respect to the outlet section of the instrument, with an offset $\alpha = 30^\circ$ with respect to its longitudinal axis, during the performance of the a C$\#_5$ with the Eb natural trumpet.

The auralized signal (see Sects. 2.3.2 and 3.3) related to two antipodal location of the head model located on the instrument axis at distance $d = 3$ m with respect

to the outlet section of the resonator, is presented below with its pressure spectrum (see Figs. 6.15 and 6.16).

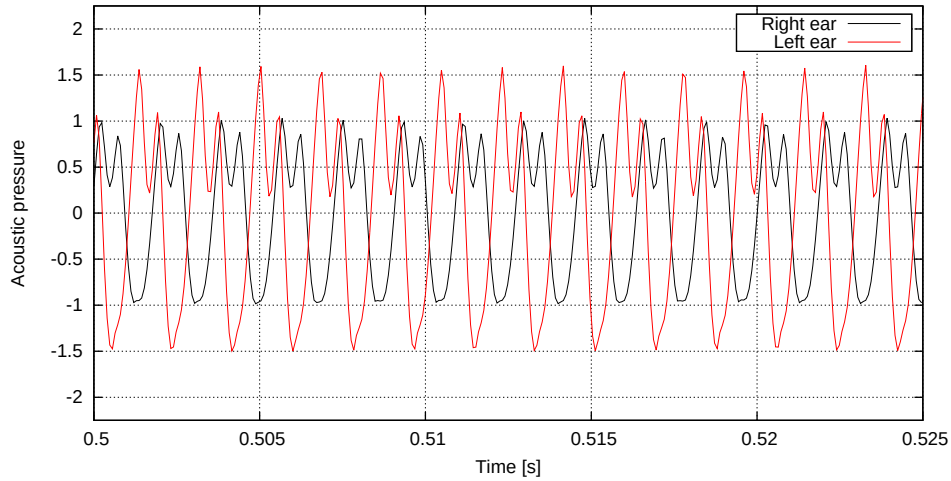

Figure 6.15: Optimal solution of the multi–objective optimization problem: pressure signal at the ears of the listener related to a simple model of head located on the instrument axis at distance $d = 3$ m with respect to the outlet section of the resonator, during the performance of the a C$\#_5$ with the E$\flat$ natural trumpet.

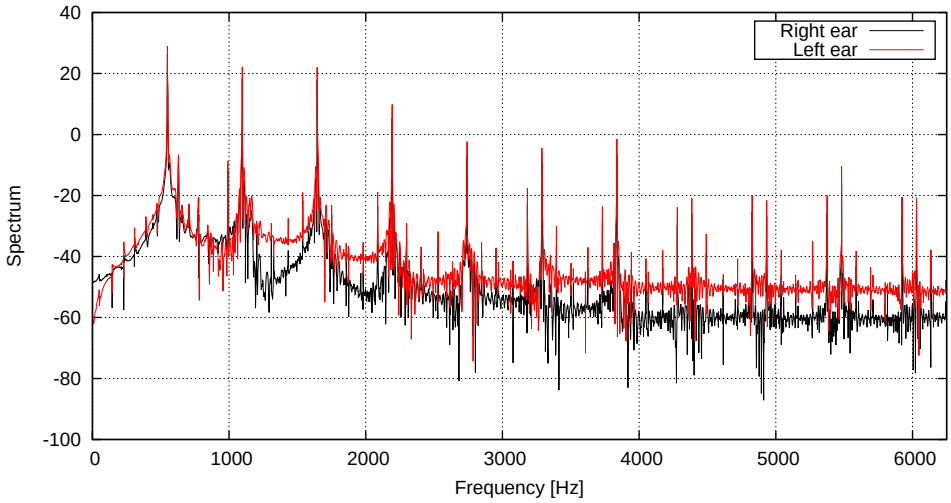

Figure 6.16: Optimal solution of the multi–objective optimization problem: pressure spectrum at the ears of the listener related to a simple model of head located on the instrument axis at distance $d = 3$ m with respect to the outlet section of the resonator, during the performance of the a C$\#_5$ with the E$\flat$ natural trumpet.

Part IV

Finale

CHAPTER 7

Conclusions and future works

In this chapter will be presented a brief summary of the addressed work. Afterwards a few suggestions for eventual future developments will be presented.

7.1 Completed tasks

This research dealt with the sound synthesis through physical modeling, and within the work have been developed models and methodologies for the time–domain simulation of the wind instruments. The aim of the research lies on the possibility to achieve valuable sounds for electronic music compositions, and to explore new features of the design of hybrid and augmented musical instruments. Another crucial aspect has been the characterization of the solution of the physical model of the brass instruments.

The proposed methodology has as the starting point that which has been called virtual lutherie, *i.e.* the integrated modeling of the instrument response and the propagation and scattering within the hall where the performance takes place. Starting from the geometric model, the acoustical characteristics of the resonator and the surroundings was carried out by exploiting the integral representation of the acoustic fields through the Kirchhoff–Helmholtz Integral Equation (KHIE) in the frequency–domain, and the numerical solution was provided by a zeroth–order Boundary Element Method (BEM). The pipe is considered ideally closed, and its frequency response is evaluated by imposing a pure Neumann boundary conditions at the inlet section. This is equivalent to considering the resonator forced by a flat spectrum and is compliant with the definition of frequency response, since a flat spectrum is provided by a time–impulse force. The solution has been evaluated at the inlet section of the instrument in order to achieve the input impedance which completely

characterize the resonator since provides information on the sound pressure intensity at a given frequency. Have been made several comparisons and convergence analysis between the numerical solutions and the approximated analytical solution of the Webster's horn equation: in all the analysed cases, the agreement is excellent. The BEM solution of the KHIE were also evaluated at several locations of the acoustic field with the aim of derive the propagation transfer functions and reconstruct sound radiated by the instrument towards the environment: such transfer functions are related to both the locations of virtual microphones (*Embouchure–to–Microphone* transfer function) or the antipodal points of a rigid sphere representing the listener's head (*Embouchure–to–Listener* transfer function).

The solution of the acousto–elastic coupling between the resonator and the exciter was carried out in the time–domain. A wide literature provides valuable models of exciters for the single–reed–instruments (clarinets and saxophones), the double–reed–instruments (oboe, bassoon, *etc.*), the jet–driven instruments (flutes, flue organ pipes, *etc.*) and brasses (trumpet, trombone, flughelhorn, *etc.*). The solution consists in convolving the inflow with a time–domain function describing the resonator. The impulse response, inverse Fourier transform of the input impedance, is not useful in the time–domain simulation due to its wide decay–time: according to the literature the reflection function, inverse Fourier transform of the reflection coefficient (directly derived from the input impedance), was used with the purpose of implement an efficient step integration aimed at the delayed–time simulations.

A complete time–domain solution has been detailed for an interesting case study, *i.e.* the natural Eb trumpet. Very ancient instrument, it is a valveless brass and the variety of playable notes is attributable to the mastery of the player to move on each of the harmonic sounds. Starting from the geometric model, based on a modern replica, the acoustical characterization was carried out via BEM and the comparison with the tuning of real instruments is fully consistent. The step integration has led to the evaluation of the state variables (displacements, inflow and pressure signal at the inlet section of the instrument) for a suitable performance condition and the radiated sound compared with a recorded sound manifests an excellent agreement. A suitable block diagram aimed at the physical model exploitation for real–time application has been presented, and the algorithm has demonstrated to be accurate and efficient in offline calculation. The utilization of meta-models for the representation of the acoustic transfer functions with a finite number of states has been also described.

The solutions of the brasses physical model has been characterized: several subspaces within the global space of the solutions have been identified and such subspaces are related to different properties of the generated signals in terms of physical feasibility and timbrical characterization. The identification of the solutions characteristics provides the space of the performance, *i.e.* the set of the locations in the space of the parameters governing the model where an experienced musician is placed when performs a note. This method allows to predict the combinations of the equations parameters corresponding to a sound complying prescribed characteristics both physical and timbrical.

The criteria developed for the characterization of the brass physical model solutions have been exploited for the formalization of both a single–objective and a multi–objective optimization problems. The optimal solutions, achieved with a genetic algorithm, are related to physically feasible sounds with prescribed timbrical characteristics.

7.2 Future research

The developed models and methodologies have led to more than satisfactory results regarding the time–domain simulation of the wind instruments. An adequate acoustical characterization has allowed to obtain proper transfer functions which have led to excellent timbrical reconstructions of the radiated sounds. Moreover it has been developed an effective block diagram representation for the physical model that reveals the opportunity to exploit it for real–time applications.

Nevertheless some aspects are still to be explored, and such issues can be divided into two classes, *i.e*

- the **models improvement**, specifically the investigation on the connection between the timbrical reconstruction and both the fluid–dynamic and the structural effect on the instruments, *e.g*
  - the influence of the viscous and thermal boundary layer, and the effect of thermal gradients inside the resonator;
  - the nonlinear effects of the shock–waves propagation inside the resonator, *i.e.* during the performance of loudness sounds especially in the brass instruments;
  - the Helmholtz resonator effect caused by the pronunciation of vowels during the blowing into the embouchure: this aspect seems to be crucial for the simulation of musical instruments such as the *didgeridoo*;
  - the connection between the acoustical properties of the resonator and both the wall vibration and the wall impedance.
- the realization of **real–time devices**, *e.g.* physical–models–based synthesizers or equipment aimed at the design of *hybrid* or *augmented* musical instruments, as well as applications for consumer devices.

The importance of further develop this research lies on the possibility to put beside the valuable sound synthesis techniques currently employed, the methodologies based on physical modeling which allow to explore the limits of expressive space of both the existing instruments and the virtual or innovative musical instruments.

Part V

Appendices

APPENDIX A

Kirchhoff-Helmholtz Integral Equation

The acoustic perturbations through a homogeneous, inviscid, non–heat conducting and compressible fluid can be described with the wave equation. Under the hypothesis that the medium is initially stationary, the wave equation can be expressed in term of potential φ as follows

$$\nabla^2\varphi - \frac{1}{c^2}\frac{\partial^2\varphi}{\partial t^2} = \sigma \tag{A.1}$$

being c the sound velocity and σ the contribution of the nonlinear terms, defined as

$$\sigma = \frac{1}{c^2}\left[(c^2 - a^2)\nabla^2\varphi + 2\nabla\varphi \cdot \frac{\partial\nabla\varphi}{\partial t} + \frac{\nabla\varphi}{2} \cdot \nabla|\nabla\varphi|^2\right] \tag{A.2}$$

with a the local sound velocity. Under the hypothesis of small acoustic perturbations it is possible to assume

$$\sigma = 0 \tag{A.3}$$

In the frequency–domain, for a simple harmonic of angular pulsation ω the potential φ can be expressed as

$$\tilde{\varphi} = \varphi e^{i\omega t} \tag{A.4}$$

Combining the Eqs. A.1 and A.4 one obtain

$$\nabla^2\tilde{\varphi} + k^2\tilde{\varphi} = 0 \tag{A.5}$$

being $k = \omega/c$ the wavenumber or reduced–frequency. Let now define the fundamental G such that

$$\nabla^2 G + k^2 G\left(\mathbf{x}, \mathbf{x}_*\right) = \delta\left(\mathbf{x} - \mathbf{x}_*\right) \tag{A.6}$$

The Eq. A.6 must satisfy the Sommerfeld radiation condition, *i.e.*

$$G = \mathcal{O}\left(r^{-\alpha}\right), \quad \alpha > 0, \quad r = ||\mathbf{x} - \mathbf{x}_*|| \tag{A.7}$$

The solution of the Eq. A.6 is the Green function

$$G(\mathbf{x}, \mathbf{x}_*) = -\frac{1}{4\pi r} e^{-ikr} = G_0 e^{-ikr} \tag{A.8}$$

being $r = ||\mathbf{x} - \mathbf{x}_*||$ with $\mathbf{x}_*$ the observation point, and G_0 the free-field Green's function. Let now define the fluid domain $\mathcal{V}$ bounded by the surface $\mathcal{S}_B$ of a body and a spherical surface $\mathcal{S}_\infty$ of radius R that encloses the body, with $R \to \infty$ and let consider the system defined by the Eqs. A.5 and A.6

$$\begin{cases} \nabla^2 \tilde{\varphi} + k^2 \tilde{\varphi} = 0 \\ \nabla^2 G + k^2 G\left(\mathbf{x}, \mathbf{x}_*\right) = \delta\left(\mathbf{x} - \mathbf{x}_*\right) \end{cases} \tag{A.9}$$

By subtracting the second of the Eq. A.9 multiplied by $\tilde{\varphi}$ from the first of the Eq. A.9 multiplied by G, integrating on the volume $\mathcal{V}$ one obtain

$$\iiint_{\mathcal{V}} \left(G\nabla^2 \tilde{\varphi} - \tilde{\varphi}\nabla^2 G\right) d\mathcal{V} = -\iiint_{\mathcal{V}} \tilde{\varphi}\delta\left(\mathbf{x} - \mathbf{x}_*\right) d\mathcal{V} \tag{A.10}$$

The second Green's identity,[1] considering the normals n internal and using the *Dirac* delta selective property, [2], implies that

$$\oint_{\mathcal{S}_B} \left(G\frac{\partial \tilde{\varphi}}{\partial n} - \tilde{\varphi}\frac{\partial G}{\partial n}\right) d\mathcal{S} + \oint_{\mathcal{S}_\infty} \left(G\frac{\partial \tilde{\varphi}}{\partial n} - \tilde{\varphi}\frac{\partial G}{\partial n}\right) d\mathcal{S} = E_* \tilde{\varphi}_* \tag{A.12}$$

The contribution of the integral on $\mathcal{S}_\infty$ tends to zero due to the Sommerfeld radiation condition

$$\tilde{\varphi} = \mathcal{O}\left(r^{-\alpha}\right), \quad \alpha \geq 1, \quad r = ||\mathbf{x} - \mathbf{x}_*|| \tag{A.13}$$

hence the Eq. A.12, making explicit the spatial dependences, becomes

$$E(\mathbf{x}_*)\tilde{\varphi}(\mathbf{x}_*) = \oint_{\mathcal{S}_B} \left(G(\mathbf{x}, \mathbf{x}_*)\frac{\partial \tilde{\varphi}(\mathbf{x}_*)}{\partial n} - \tilde{\varphi}(\mathbf{x}_*)\frac{\partial G(\mathbf{x}, \mathbf{x}_*)}{\partial n}\right) d\mathcal{S} \tag{A.14}$$

[1] Given two arbitrary functions f and g both at least two times differentiable, one has

$$\int_{\mathcal{V}} \left(f\nabla^2 g - g\nabla^2 f\right) dV = \int_{\mathcal{S}=\partial\mathcal{V}} (g\nabla f - f\nabla g) \cdot \mathbf{n} dS \tag{A.11}$$

[2] By definition, for a given h with compact support

$$\int_\Omega h(x)\delta\left(x - x_0\right) = h\left(x_0\right)$$

being the domain function $E(\mathbf{x})$ such that

$$E(\mathbf{x}_*) = \begin{cases} 0, & \forall \mathbf{x}_* \notin \mathcal{S}_B, \notin \mathcal{V} \\ 1, & \forall \mathbf{x}_* \notin \mathcal{S}_B, \in \mathcal{V} \\ \Omega/4\pi, & \forall \mathbf{x}_* \in \mathcal{S}_B \end{cases} \tag{A.15}$$

where Ω represents the solid angle and for regular point one have that

$$\Omega = 2\pi \tag{A.16}$$

Combining the Eqs. A.8 and A.14 can be expressed in terms of the free-field Green's function G_0

$$E_*\tilde{\varphi}_* = \oint_{\mathcal{S}_B} \left(G_0 \frac{\partial \tilde{\varphi}}{\partial n} - \tilde{\varphi} \frac{\partial G_0}{\partial n} + ik\tilde{\varphi} G_0 \frac{\partial r}{\partial n} \right) e^{-ikr} d\mathcal{S} \tag{A.17}$$

Considering the Laplace variable $s = \sigma + i\omega$ and imposing $\theta = r/c$, the Eq. A.17 becomes

$$E_*\tilde{\varphi}_* = \oint_{\mathcal{S}_B} \left(G_0 \frac{\partial \tilde{\varphi}}{\partial n} - \tilde{\varphi} \frac{\partial G_0}{\partial n} + s\tilde{\varphi} G_0 \frac{\partial r}{\partial n} \right) e^{-s\theta} d\mathcal{S} \tag{A.18}$$

The Eq. A.18 represents the equation for the velocity potential, known as Kirchhoff–Helmholtz Integral Equation (KHIE).

APPENDIX B

Boundary Element Method for acoustic problems

The Boundary Element Method (BEM), also referred to as the *panels–method*, is based on the discretization of the bodies surface $\mathcal{S}$ into N_e panels. In general, in order to reduce an integro–differential problem to and algebraic problem, one can define the unknown function u as a linear combination of N global shape–functions Ψ multiplied by the value of u in the collocation points, *i.e.*

$$u(\xi) \approx \sum_{n=1}^{N} u_n \Psi_n(\xi) \tag{B.1}$$

The evaluation of the coefficients with the knowledge of the boundary conditions provides the approximate solution of the problem.

Let now consider the following integro–differential acoustic problem

$$E_* \tilde{\varphi}_* = \oint_{\mathcal{S}_B} \left(G_0 \frac{\partial \tilde{\varphi}}{\partial n} - \tilde{\varphi} \frac{\partial G_0}{\partial n} + ik\tilde{\varphi} G_0 \frac{\partial r}{\partial n} \right) e^{-ikr} d\mathcal{S} \tag{B.2}$$

being the domain function E_* equal to 1, 1/2, or 0, if the solution is respectively evaluated in the field $\mathcal{V}$, on the body surface $\mathcal{S}_B = \partial\mathcal{V}$ or out of the domain.

The scalar potential function $\tilde{\varphi}$ and its normal derivative $\tilde{\chi}$ can be expressed with the Eq. B.1 as follows

$$\begin{aligned} \tilde{\varphi}(\mathbf{x}) &= \sum_{j=1}^{N_\varphi} \tilde{\varphi}_j \mathbf{M}_j^{\varphi}(\mathbf{x}) \\ \tilde{\chi}(\mathbf{x}) &= \sum_{j=1}^{N_\chi} \tilde{\chi}_j \mathbf{M}_j^{\chi}(\mathbf{x}) \end{aligned} \tag{B.3}$$

being $\tilde{\varphi}_j$ and $\tilde{\chi}_j$ the values that $\tilde{\varphi}$ and $\tilde{\chi}$ assume in the collocation point $\mathbf{x}_j$, whereas $\mathbf{M}_j^{\varphi}(\mathbf{x})$ and $\mathbf{M}_j^{\chi}(\mathbf{x})$ are the global shape–functions such that $\sum_j \mathbf{M}_j = 1$. Assuming that $\mathbf{M}_j^{\varphi}(\mathbf{x}) = \mathbf{M}_j^{\chi}(\mathbf{x})$, for for each point $\mathbf{x}_m$ the Eq. B.2 can be written as follows

$$\begin{aligned} E_m\varphi_m = &\sum_{j=1}^{N_e} \oint_{\mathcal{S}_B} G_0 e^{-s\theta} \mathbf{M}_j^{\chi} \chi_j d\mathcal{S} \\ &- \sum_{j=1}^{N_e} \oint_{\mathcal{S}_B} \left(\frac{\partial G_0}{\partial n} - s G_0 \frac{\partial r}{\partial n} \right) e^{-s\theta} \mathbf{M}_j^{\varphi} \varphi_j d\mathcal{S} \end{aligned} \tag{B.4}$$

that is the general form of the discretization of the boundary integral equation.

In the zeroth–order approximation for the unknown the values of $\tilde{\varphi}$ and $\tilde{\chi}$ are assumed to be constant equal to the value at the centroid of the panel. The terms of the Eq. B.2 can be written as follows

$$\begin{aligned} \int_{\mathcal{S}_B} G_0 \tilde{\chi} e^{-ikr} d\mathcal{S}_B &\approx \sum_{j=1}^{N} B_{ij} \tilde{\chi} e^{-ikr_{ij}} \\ -\int_{\mathcal{S}_B} \tilde{\varphi} \frac{\partial G_0}{\partial n} e^{-ikr} d\mathcal{S}_B &\approx \sum_{j=1}^{N} C_{ij} \tilde{\varphi}_j e^{-ikr_{ij}} \\ \int_{\mathcal{S}_B} ik\tilde{\varphi} G_0 \frac{\partial r}{\partial n} e^{-ikr} d\mathcal{S}_B &\approx \sum_{j=1}^{N} D_{ij} ik \tilde{\varphi}_j e^{-ikr_{ij}} \end{aligned} \tag{B.5}$$

with influence coefficients

$$\begin{aligned} B_{ij} &= \int_{\mathcal{S}_j} G_{0ij} d\mathcal{S}_j \\ C_{ij} &= -\int_{\mathcal{S}_j} \frac{\partial G_{0ij}}{\partial n} d\mathcal{S}_j \\ D_{ij} &= \int_{\mathcal{S}_j} G_{0ij} \frac{\partial r_{ij}}{\partial n} d\mathcal{S}_j \end{aligned} \tag{B.6}$$

Using the Eqs. B.5 and B.6, the Eq. B.2 becomes

$$E_j \tilde{\varphi}_j = \sum_{j=1}^{N} B_{ij} \tilde{\chi}_j e^{-ikr_{ij}} + \sum_{j=1}^{N} C_{ij} \tilde{\varphi}_j e^{-ikr_{ij}} + \sum_{j=1}^{N} D_{ij} ik \tilde{\varphi}_j e^{-ikr_{ij}} \tag{B.7}$$

In the Eq. B.7 the terms B_{ij} and C_{ij} represent respectively the source and doublet integral: it is worth noting that if the panels can be represented with portions of hyperbolic paraboloid, the sources and doublets integral are known. Let assume that the surface $\mathcal{S}_B = \partial\mathcal{V}$ is discretized into N quadrangular panels: defining the generic $\mathbf{x}$ in the local system (ξ, η)

$$\mathbf{x} = \mathbf{p}_0 + \xi\mathbf{p}_1 + \eta\mathbf{p}_2 + \xi\eta\mathbf{p}_3 \tag{B.8}$$

being $\xi \in [-1,1]$ and $\eta \in [-1,1]$. The position of the four vertices is given by the following

$$\mathbf{x}_{s_\xi, s_\eta} = \mathbf{p}_0 + s_\xi \mathbf{p}_1 + s_\eta \mathbf{p}_2 + s_\xi s_\eta \mathbf{p}_3 \tag{B.9}$$

with $s_\xi = \pm 1$ and $s_\eta = \pm 1$. Combining the Eqs. B.8 and B.9 one can obtain the relation between $\mathbf{p}_0$, $\mathbf{p}_1$, $\mathbf{p}_2$, $\mathbf{p}_3$ with the vertices coordinates. Defining

$$\mathbf{r} = \mathbf{p}_0 + \xi \mathbf{p}_1 + \eta \mathbf{p}_2 + \xi\eta \mathbf{p}_3 - \mathbf{x}_k \tag{B.10}$$

being ξ and η the local integration variables, it is possible to derive the source integral I_D and the doublet integral I_D as follows

$$\begin{aligned} I_S = B_{ij} &= \int_{-1}^{1}\int_{-1}^{1} -\frac{1}{4\pi r}||\mathbf{a}_1 \times \mathbf{a}_2|| d\xi d\eta \\ I_D = C_{ij} &= \int_{-1}^{1}\int_{-1}^{1} -\frac{\mathbf{r}\cdot\mathbf{n}}{4\pi r^3}||\mathbf{a}_1 \times \mathbf{a}_2|| d\xi d\eta = \\ &- \int_{-1}^{1}\int_{-1}^{1} \frac{\mathbf{r}\cdot\mathbf{a}_1 \times \mathbf{a}_2}{4\pi r^3} \end{aligned} \tag{B.11}$$

with $r = ||\mathbf{r}||$. The basis vectors can be expressed as

$$\begin{aligned} \mathbf{a}_1 &= \frac{\partial \mathbf{x}}{\partial \xi} = \mathbf{p}_1 + \eta \mathbf{p}_3 \\ \mathbf{a}_2 &= \frac{\partial \mathbf{x}}{\partial \eta} = \mathbf{p}_2 + \xi \mathbf{p}_3 \end{aligned} \tag{B.12}$$

and the related normal is

$$\mathbf{n} = \frac{\mathbf{a}_1 \times \mathbf{a}_2}{||\mathbf{a}_1 \times \mathbf{a}_2||} \tag{B.13}$$

Considering now a generic panel p: the value of $\tilde{\varphi}_p$, knowing the value of the domain function E, is provided by the Eq. B.7

$$\frac{1}{2}\tilde{\varphi}_p = \sum_{q=1}^{N} B_{pq}\tilde{\chi}_q e^{-ikr_{pq}} + \sum_{q=1}^{N} C_{pq}\tilde{\varphi}_q e^{-ikr_{pq}} + \sum_{q=1}^{N} D_{pq} ik \tilde{\varphi}_q e^{-ikr_{pq}} \tag{B.14}$$

being the influence coefficients defined by the Eq. B.6. Starting from the Eq. B.14 one can define the vector $\underline{\tilde{\varphi}}$ of the values $\tilde{\varphi}$ representing the velocity potential at the centroids of the N panels, and the vector $\underline{\tilde{\chi}}$ of the values $\tilde{\chi}$ related to the N panels

$$\underline{\tilde{\varphi}} = \begin{bmatrix} \tilde{\varphi}_1 \\ \vdots \\ \tilde{\varphi}_N \end{bmatrix}, \quad \underline{\tilde{\chi}} = \begin{bmatrix} \tilde{\chi}_1 \\ \vdots \\ \tilde{\chi}_N \end{bmatrix} \tag{B.15}$$

Let now define the matrix $\underline{Z}$ such that its generic element is

$$Z_{pq} = \int_{\mathcal{S}_q} G_{0pq} e^{-ikr_{pq}} d\mathcal{S}_q = B_{pq} e^{-ikr_{pq}} \tag{B.16}$$

and the matrix $\underline{Y}$

$$\begin{aligned} Y_{pq} &= \frac{1}{2}\int_{\mathcal{S}_q} \frac{\partial G_{0pq}}{\partial n} e^{-ikr_{pq}} d\mathcal{S}_q - \int_{\mathcal{S}_q} G_{0pq} \frac{\partial r_{pq}}{\partial n} ike^{-ikr_{pq}} d\mathcal{S}_q \\ &= \frac{1}{2} - C_{pq}e^{-ikr_{pq}} - ikD_{pq}e^{-ikr_{pq}} \end{aligned} \tag{B.17}$$

Combining the Eqs. B.15, B.16 and B.17, the Eq. B.14 becomes

$$\underline{Y}\underline{\tilde{\varphi}} = \underline{Z}\underline{\tilde{\chi}} \tag{B.18}$$

and allows to evaluate the N values of velocity potential on the discretized body surface $\mathcal{S}_B$.

Let now consider the solution for a generic location of the volume $\mathbf{V}$ identified by the vector $\mathbf{x}_*$. The integral representation of $\tilde{\varphi}$ is defined by the following

$$\tilde{\varphi}(\mathbf{x}_*) = \sum_{q=1}^{N} B_{\mathbf{x}_* q}\tilde{\chi}_q e^{-ikr_{\mathbf{x}_* q}} + \sum_{q=1}^{N} C_{\mathbf{x}_* q}\tilde{\varphi}_q e^{-ikr_{\mathbf{x}_* q}} + \sum_{q=1}^{N} D_{\mathbf{x}_* q} ik\tilde{\varphi}_q e^{-ikr_{\mathbf{x}_* q}} \tag{B.19}$$

Considering the vector $\underline{\tilde{\varphi}}^M$ representing the velocity potential in M locations of the domain $\mathcal{V}$

$$\underline{\tilde{\varphi}}^M = \begin{bmatrix} \tilde{\varphi}_1^M \\ \vdots \\ \tilde{\varphi}_N^M \end{bmatrix} \tag{B.20}$$

and the matrix $\underline{Z}^M$ such that

$$Z_{pq}^M = \int_{\mathcal{S}_q} G_{0pq}^M e^{-ikr_{pq}} d\mathcal{S}_q = B_{pq}e^{-ikr_{pq}} \tag{B.21}$$

Note that for a given location p identified with the vector $\mathbf{x}_{*p}$ with $1 \leq p \leq M$ the free–field Green's function with respect to the generic panel q is given by the following

$$G_{0pq}^M = -\frac{1}{4\pi||\mathbf{x}_q - \mathbf{x}_{*p}||} \tag{B.22}$$

Let introduce the matrix $\underline{S}^M$

$$\begin{aligned} S_{pq} &= \int_{\mathcal{S}_q} \frac{\partial G_{0pq}^M}{\partial n} e^{-ikr_{pq}^M} d\mathcal{S}_q - \int_{\mathcal{S}_q} G_{0pq}^M \frac{\partial r_{pq}^M}{\partial n} ike^{-ikr_{pq}^M} d\mathcal{S}_q \\ &= C_{pq}e^{-ikr_{pq}^M} - ikD_{pq}e^{-ikr_{pq}^M} \end{aligned} \tag{B.23}$$

Combining the Eqs. B.15, B.21 and B.23, the Eq. B.19 becomes

$$\underline{\tilde{\varphi}}^M = \underline{Z}^M\underline{\tilde{\chi}} + \underline{S}^M\underline{\tilde{\varphi}} \tag{B.24}$$

APPENDIX C

Optimization problems

The generic optimization problem yields the minimization of an objective function, or multiple objective functions, while all the constraints are satisfied. The problem can be formalized as follows

$$\begin{aligned} \text{minimize } & [J_1(\mathbf{x}), ..., J_K(\mathbf{x})], && k = 1, ..., N_J \text{ and } \mathbf{x} \in \mathcal{D} \\ \text{bounds } & x_n^L \leq x_n \leq x_n^U, && n = 1, ..., N_x \\ \text{subject to } & g_i(\mathbf{x}) \leq 0, && i = 1, ..., N_g \\ \text{and } & h_j(\mathbf{x}) = 0, && j = 1, ..., N_h \end{aligned} \tag{C.1}$$

being $J_k(\mathbf{x})$ the k–th *objective function* with $\mathbf{x}$ the vector containing the N_x *design variables* bounded by x_n^L and x_n^U in the *design space* $\mathcal{D}$, $g_i(\mathbf{x})$ the N_g *inequality constraints* and $h_j(\mathbf{x})$ the N_h *equality constraints*. The set of $\mathbf{x}$ in the n–dimensional design space $\mathcal{D}$ which satisfy the constraints is called the *feasible set*.

Omitting the *multiple–criteria decision analysis* (Pareto optimization) methods, the objective function can be processed by defining a single objective function $J^A(\mathbf{x})$ containing all the objective functions $J_k(\mathbf{x})$ by using suitable weight coefficients λ_k

$$J^A(\mathbf{x}) = \sum_{k=1}^{N_J} \lambda_k J_k(\mathbf{x}) \tag{C.2}$$

where the weight vector λ generally respect the following rule

$$\sum_{k=1}^{N_J} \lambda_k = 1 \tag{C.3}$$

Combining the Eqs. C.1 and C.2, and neglecting the N_h equality constraints $h_j(\mathbf{x})$

$$\begin{aligned} \text{minimize } & J^A(\mathbf{x}), && \mathbf{x} \in \mathcal{D} \\ \text{bounds } & x_n^L \leq x_n \leq x_n^U, && n = 1, ..., N_x \\ \text{subject to } & g_i(\mathbf{x}) \leq 0, && i = 1, ..., N_g \end{aligned} \tag{C.4}$$

The treatment of the inequality constraints $g_i(\mathbf{x})$ can be addressed by using several techniques. One of these consists in solving the original constrained problem formalized with the Eq. C.4 by defining a pseudo–objective function $\bar{J}(\mathbf{x})$ including all the inequality constraints: the idea is to combine the objective function $J^A(\mathbf{x})$ and the N_g inequality constraints $g_i(\mathbf{x})$ so that even the constraints violation is minimized. This strategy is the so–called *penalty function method* and provides the solution of the original constrained problem by solving an unconstrained one.

The unconstrained optimization problem for the Eq. C.4, addressed with the quadratic penalty function can be defined as follows

$$\bar{J}(\mathbf{x}) = J^A(\mathbf{x}) + \frac{1}{\epsilon} \sum_{i=1}^{N_g} \max\left[0, g_i(\mathbf{x})\right]^2 \tag{C.5}$$

being $1/\epsilon$ the penalty parameter, with $\epsilon < 1$: the smaller is ϵ the greater is the penalty. The constrained problem of the Eq. C.4 reduces to

$$\begin{aligned} \text{minimize } & \bar{J}(\mathbf{x}), && \mathbf{x} \in \mathcal{D} \\ \text{bounds } & x_n^L \leq x_i \leq x_n^U && n = 1, ..., N_x \end{aligned} \tag{C.6}$$

Once the optimization problem is formulated, must be used a numerical technique in order to find its solution: a wide scenario of optimization algorithms can be found in the literature.

Bibliography

[1] Kakhkhor Abdijalilov and Haim Grebel. Z-transform theory and FDTD stability. *IEEE Transactions on Antennas and Propagation*, 52:2950–2954, 2004.

[2] S Adachi and M Sato. Time–domain simulation of sound production in the brass instrument. *The Journal of the Acoustical Society of America*, 97(June), 1995.

[3] Joaquim Agullo. Alternatives to the impulse response h(t) to describe the acoustical behavior of conical ducts, 1988.

[4] A Almeida, Christophe Vergez, R Caussé, and Xavier Rodet. Physical study of double-reed instruments for application to sound-synthesis. 2002.

[5] Andre Almeida, Christophe Vergez, and René Caussé. Quasi-static non-linear characteristics of double-reed instruments. July 2006.

[6] N. Amir, U Shimony, and G. Rosenhouse. A discrete model for tubular acoustic systems with varying cross–section - the direct and inverse problems. *ACUSTICA*, 81(Part 2. EXPERIMENTS):463–474, 1995.

[7] D Arfib. Digital synthesis of complex spectra by means of multiplication of non linear distorted sine waves. *Audio Engineering Society Convention 59*, 1978.

[8] Anthony Baines. Brass instruments: their history and development. 1993.

[9] G Bartolozzi, R D'Amico, A Pratellesi, and M Pierini. An Efficient Method for Selecting CHIEF Points. In *International Conference on Structural Dynamics*, number July, pages 4–6, 2011.

[10] JW Beauchamp. Additive Synthesis of Harmonic Musical Tones. *Journal of the Audio Engineering Society*, 1966.

[11] Daniel Bernoulli. *Sur le son et sur les tons des tuyaux d'orgues différemment construits.* 1764.

[12] A Bouhuys. Lung volumes and breathing patterns in wind-instrument player. *Journal of applied physiology (Bethesda, Md. : 1985)*, 19:967–975, 1964.

[13] F Brackhane. Perception tests with a replica of von Kempelen's speaking machine. (1):122–125, 2009.

[14] Fabian Brackhane and Jürgen Trouvain. What makes "Mama" and "Papa" acceptable? - Experiments with a replica of von Kempelen's speaking machine. In *International Speech Production Seminar (ISSP 2008) Proceedings*, pages 329–332, 2008.

[15] Seona Bromage. Visualisation of the lip motion of brass instrument players, and investigations of an artificial mouth as a tool for comparative studies of instruments. 2007.

[16] IL Chen, JT Chen, and MT Liang. Analytical study and numerical experiments for radiation and scattering problems using the CHIEF method. *Journal of Sound and Vibration*, 2001.

[17] JM Chowning. The synthesis of complex audio spectra by means of frequency modulation. *Computer Music Journal*, 1977.

[18] P Comerford. Simulating an organ with additive synthesis. *Computer Music Journal*, 1993.

[19] David C. Copley. A stroboscopic study of lip vibrations in a trombone, 1996.

[20] J Crank and P Nicolson. A practical method for numerical evaluation of solutions of partial differential equations of the heat-conduction type. *Mathematical Proceedings of the Cambridge Philosophical Society*, 43(01):207–226, 1947.

[21] Laurent Daudet. A review on techniques for the extraction of transients in musical signals. *Computer Music Modeling and Retrieval*, 2006.

[22] EJ Davison. A High-Order Crank–Nicholson Technique for Solving Differential Equations. *The Computer Journal*, pages 195–197, 1967.

[23] Patricio De La Cuadra. *The sound of oscillating air jets: physics, modeling and simulation in slute-like instruments.* PhD thesis, 2005.

[24] Patricio De La Cuadra, Christophe Vergez, and Benoit Fabre. Visualization and analysis of jet oscillation under transverse acoustic perturbation. *Journal of Flow Visualization and Image Processing*, November 2008.

[25] Philippe Depalle (Author) and Xavier Rodet (Author). A physical model of lips and trumpet. *Collected Work: Proceedings: International Computer Music Conference, San Jose, California, October 14-18, 1992. Pages: 132-135. (AN: 1992-08542).*, 1992.

[26] Riccardo Di Federico and Gianpaolo Borin. Synthesis of the trumpet tone based on physical models. *International Computer Music Conference*, 1997.

[27] Kees Van Den Doel and DK Pai. Modal synthesis for vibrating objects. *Audio Anectodes. AK Peter, Natick, MA*, pages 1–8, 2003.

[28] Peter Downey. The renaissance slide trumpet: Fact or fiction? *Early Music*, 12:26–33, 1984.

[29] Pauline Eveno and JP Dalmont. Comparisons between models and measurements of the input impedance of brass instruments bells. In *Forum Acusticum 2011*, 2011.

[30] S Félix, JP Dalmont, and CJ Nederveen. Effects of bending portions of the air column on the acoustical resonances of a wind instrument. *The Journal of the Acoustical Society of America*, 2012.

[31] S. Félix and V. Pagneux. Multimodal analysis of acoustic propagation in three-dimensional bends. *Wave Motion*, 36:157–168, 2002.

[32] N H Fletcher. Autonomous vibration of simple pressure-controlled valves in gas flows. *The Journal of the Acoustical Society of America*, 93(4):2172, 1993.

[33] NH Fletcher and A Tarnopolsky. Blowing pressure, power, and spectrum in trumpet playing. *The Journal of the Acoustical Society ...*, 105(April 1998):874–881, 1999.

[34] V Fréour, R Caussé, and IA Cossette. Simultaneous measurements of pressure, flow and sound during trumpet playing. *10ème Congrès Français d' Acoustique*, pages 12–16, 2010.

[35] B Gazengel, J Gilber, N Amir, and J Gilbert. Time Domain Simulation of Single Reed wind Instrumet. From Measured Input Impedance to the Syntesis Signal. Where are the Traps? *Acta acustica*, 3(October):445–472, 1995.

[36] GL Ghiringhelli and P Mantegazza. Interpolation extrapolation and modeling of unsteady linear(ized) aerodynamic forces. In *International Forum on Aeroelasticity and Structural Dynamics*, 1993.

[37] R Gori, F Pausilli, M D Pavel, and Massimo Gennaretti. State-Space Rotor Aeroelastic Modeling for Real-Time Helicopter Flight Simulation. *Advanced Materials Research*, pages 451–459, 2014.

[38] A. Gotouda, T. Yamaguchi, K. Okada, T. Matsuki, S. Gotouda, and N. Inoue. Influence of playing wind instruments on activity of masticatory muscles. *Journal of Oral Rehabilitation*, 34:645–651, 2007.

[39] John M. Grey. Perceptual evaluations of synthesized musical instrument tones, 1977.

[40] T Helie, Christophe Vergez, T Hélie, J Lévine, and X Rodet. Inversion of a physical model of a trumpet. In *International Computer Music Conference*, volume 3, 1999.

[41] HLF Helmholtz. *On the Sensations of Tone as a Physiological Basis for the Theory of Music*. 1885.

[42] a. Hirschberg, J. Gilbert, a. P.J. Wijnands, and a. M.C. Valkering. Musical aero-acoustics of the clarinet. *Le Journal de Physique IV*, 04:C5–559–C5–568, 1994.

[43] Gregory Howland. *Woodwind Air Columns in the Time Domain*. PhD thesis, 2007.

[44] U Iemma. Singing Integrals or wind instruments modeling using Boundary Integral Equations. *Acoustics 2008*, pages 3907–3912, 2008.

[45] U Iemma, V Marchese, and R Gori. AcouSTO-a new open-source project for acoustic simulation. *16th International Congress on Sound and Vibration*, 2009.

[46] David A. Jaffe and Julius O. Smith. Extensions of the Karplus-Strong Plucked-String Algorithm. *Computer Music Journal*, 7(2):56, January 1983.

[47] Kevin Karplus and Alex Strong. Digital Synthesis of Plucked-String and Drum Timbres. *Computer Music Journal*, 7(2):43, January 1983.

[48] CR Kipp and RJ Bernhard. Prediction of acoustical behavior in cavities using an indirect boundary element method. *... and Acoustics*, 1987.

[49] B Kolbrek. Horn Theory: An Introduction, Part. *Audio Xpress*, 2008.

[50] Bernhard Krach, Stefan Petrausch, and Rudolf Rabenstein. Digital sound synthesis of brass instruments by physical modeling. In *Conference on Digital Audio Effects (DAFx)*, pages 101–106, 2004.

[51] Shona Logie and John Chick. Upward and downward slurred transients on brass instruments: Why is one not simply the inverse of the other? *10ème Congrès Français d' Acoustique*, pages 12–16, 2010.

[52] David Luce. Physical Correlates of Brass-Instrument Tones, 1967.

[53] Charles A Macaluso and Jean-Pierre Dalmont. Trumpet with near-perfect harmonicity: design and acoustic results. *The Journal of the Acoustical Society of America*, 129:404–414, 2011.

[54] P Manning. *Electronic and computer music*. 2013.

[55] P. a. Martin. On Webster's horn equation and some generalizations. *The Journal of the Acoustical Society of America*, 116(3):1381, 2004.

[56] ME McIntyre. On the oscillations of musical instruments. *The Journal of the Acoustical Society of America*, 74, 1983.

[57] Marin Mersenne. *Harmonie Universelle*. Facsimil e edition, 1636.

[58] Mark A Neal, Orlando Richards, D Murray Campbell, and Joël Gilbert. Study of the reed mechanism of brass instruments using an artificial mouth. In *Proceedings of the International Symposium on Musical Acoustics*, 2001.

[59] Harry F Olson. Elements of acoustical engineering. 1957.

[60] Harry F Olson. *Music, Physics and Engineering*. 1967.

[61] JF Petiot and Franck Teissier. Comparative analysis of brass wind instruments with an artificial mouth: first results. *Acta Acustica united with Acustica*, 2003.

[62] PB Pickett. *An investigation of active tonal spectrum control as applied to the modern trumpet*. PhD thesis, 1998.

[63] Emilie Poirson, Jean-François Petiot, and Joël Gilbert. Study of the brightness of trumpet tones. *The Journal of the Acoustical Society of America*, 118:2656–2666, 2005.

[64] Bernd Pompino-Marschall. Von Kempelen et al. - Remarks on the history of articulatory–acoustic modelling. *ZAS Papers in Linguistics*, pages 145–159, 2005.

[65] Markus Raquet and Klaus Martius. Benninck Meets Sander: A Comparison of Two Early Seventeenth-Century Trumpets. *Historic Brass Society Journal*, 13:52–66, 2001.

[66] John William Strutt Rayleigh. *The theory of sound*. Dover, rep edition, 1894.

[67] SW W Rienstra and Avraham Hirschberg. *An introduction to acoustics*. 2004.

[68] C Roads. A tutorial on non-linear distortion or waveshaping synthesis. *Computer Music Journal*, 1979.

[69] T. D. Rossing. *Springer Handbook of Acoustics*. 2007.

[70] Thomas D Rossing. Woodwind Instruments. In *The science of sound*, pages 213–229. Addison-Wesley Publishing Company, 1991.

[71] H A Schenck. Improved Integral Formulation for Acoustic Radiation Problems. *Journal of the Acoustical Society of America*, 44(1):41–89, 1967.

[72] Lorenzo Seno. Perchè i modelli fisici sono necessari. 2002.

[73] AF Seybert and TK Rengarajan. The high-frequency radiation of sound from bodies of arbitrary shape. *Journal of Vibration, Acoustics, Stress, and Reliability in Design*, 1987.

[74] JO Smith and Xavier Serra. *PARSHL: An analysis/synthesis program for non-harmonic sounds based on a sinusoidal representation.* 1987.

[75] Steven W. Smith. The z-Transform. In *The Scientist and Engineer's Guide to Digital Signal Processing*, pages 605–630. 1997.

[76] GW Stewart and RB Lindsay. Acoustics: a text on theory and applications. 1930.

[77] T Stilson and J Smith. Alias-free digital synthesis of classic analog waveforms. *Proc. International Computer Music Conference*, 1996.

[78] Dennis M. Sullivan. Z-transform theory and the FDTD method. *IEEE Transactions on Antennas and Propagation*, 44:28–34, 1996.

[79] T. H. Tarnoczy. The Speaking Machine of Wolfgang von Kempelen, 1949.

[80] S Terrien, R Auvray, and Benoit Fabre. Numerical resolution of a physical model of flute-like instruments: comparison between different approaches. *Proceedings of the Acoustics 2012*, (April):1179–1184, 2012.

[81] MP Verge, R Caussé, and B Fabre. Jet oscillations and jet drive in recorder-like instruments. *Acta acustica*, 1994.

[82] C Vergez, A Almeida, René Causse, and X Rodet. Toward a Simple Physical Model of Double-Reed Musical Instruments: Influence of Aero-Dynamical Losses in the Embouchure on the Coupling Between the Reed and the Bore of the Resonator. *Acta Acustica united with Acustica*, 89:964–973, 2003.

[83] Christophe Vergez and X Rodet. Model of the Trumpet Functioning: Real-time Simulation and Experiments with an Artificial Mouth. *PROCEEDINGS-INSTITUTE OF ACOUSTICS*, 1997.

[84] I Xenakis. *Formalized music: thought and mathematics in composition.* 1992.

[85] S Yoshikawa. Acoustical behavior of brass player's lips. *The Journal of the Acoustical Society of America*, 97:1929–1939, 1995.